Using Motion Primitives to Rapidly Design Trajectories in Multi-Body Systems

by

Thomas Raymond Smith

B.S., University of Illinois Urbana-Champaign, 2018

M.S., University of Colorado Boulder, 2020

A thesis submitted to the

Faculty of the Graduate School of the

University of Colorado in partial fulfillment

of the requirements for the degree of

Doctor of Philosophy

Ann and H.J. Smead Department of Aerospace Engineering Sciences

2023

Committee Members:

Prof. Natasha Bosanac, Chair

Dr. Kathryn Davis

Prof. Morteza Lahijanian

Prof. Jay McMahon

Dr. Christopher Spreen

Smith, Thomas Raymond (Ph.D., Aerospace Engineering Sciences)

Using Motion Primitives to Rapidly Design Trajectories in Multi-Body Systems

Thesis directed by Prof. Natasha Bosanac

Space exploration is a catalyst for technology development and the cornerstone of a future in which humans have established a sustainable presence in cislunar space; propellant depots facilitate a growing space economy; fleets of small spacecraft explore celestial bodies throughout the solar system; and advanced space telescopes assembled in space continue to unravel the history of the universe. In pursuit of this future, trajectory design serves as a critical technology by extending the capabilities of current spacecraft, supporting mission concept development for future spacecraft, and enabling complex spacecraft operations in chaotic multi-body environments. The increasing number and variety of spacecraft that are expected to operate within cislunar space and other multi-body gravitational environments throughout the solar system necessitates the continued development of strategies for rapid trajectory design and design space exploration. In the field of robotics, similar needs have been addressed using motion primitives that capture the fundamental building blocks of motion and are used to rapidly construct complex paths. Inspired by this concept, this work leverages motion primitives to construct a framework for rapid and informed spacecraft trajectory design in a multi-body gravitational system. First, motion primitives of fundamental solutions, e.g., selected periodic orbits and their stable and unstable manifolds, are generated via clustering to form a discrete summary of segments of the phase space. Graphs of motion primitives are then constructed and searched to produce primitive sequences that form candidate initial guesses for transfers of distinct geometries. Finally, continuous transfers are computed from each initial guess using multi-objective constrained optimization and collocation. This approach is demonstrated by constructing an array of geometrically distinct transfers in the Earth-Moon circular restricted three-body problem with impulsive maneuvers.

Dedication

To my mother (Mary) and my brothers (James, Nick, and Doug), your unconditional love and support continually lifts me up and allows me to reach for the stars.

In loving memory of

my father and my grandparents:

Jim Smith

Francis & Virginia Borio

Raymond & Mary Ruth Smith

Acknowledgements

I would first like to sincerely thank my advisor, Professor Bosanac, for your immeasurable support and guidance. Thank you for continuously challenging and encouraging me to think critically; to ask insightful questions; to be confident in my knowledge; and ultimately, to become a better researcher and person. You have helped me gain a deep understanding of astrodynamics, the research process, and the art of storytelling. I would also like to thank each of my committee members for your invaluable feedback on this work. In addition, I want to thank all of my previous teachers, professors, and mentors that have shaped my academic and professional career. Next, I would like to thank my family for always being my rock and standing by my side in all seasons of life. This achievement would not have been possible without your love, encouragement, and support; I owe everything to all of you. My experience at CU has also been incredible and I cherish all of the friendships I have made during my time in Boulder. I would like to especially thank the past and current members of the Bosanac Group: Stefano, Ian, Jack, Kristen, Giuliana, Renee, and Sai. It has been a privilege to go through this experience with each of you and thank you all for your friendship and support. I would also like to thank my friends at CU outside of the Bosanac Group, particularly Damennick, Jordan, Sam, David, Jesse, and Anna. Thank you for all the good times, fun memories, and support along this journey. Finally, I would like to gratefully acknowledge the Graduate Assistantship in Areas of National Need Fellowship and the NASA Space Technology Research Fellowship (NSTRF Grant 80NSSC19K1155) for funding this work; as part of the NSTRF, I want to give a special thanks to Dr. Christopher Spreen for all of your feedback and support as my NASA collaborator as well as Dr. Robert Pritchett for supporting this work.

Contents

Chapter

Tables

Table

Figures

Figure

Chapter 1

Introduction

Due to an increasing number of spacecraft planned to operate in the chaotic regimes of multi-body gravitational systems, traditional Keplerian motion is often insufficient for preliminary trajectory design. Currently, spacecraft trajectory design in multi-body systems involves separating a mission itinerary into distinct phases, determining candidate trajectory segments for each phase, and connecting these segments to discover a nearby continuous solution. However, current methodologies require manual exploration of a complex multi-dimensional solution space that is nontrivial, mission specific, and time-consuming for a human analyst. To address this challenge, this dissertation research focuses on the use of motion primitives, a concept from robotics and motion planning, to summarize the solution space in a multi-body system via fundamental, yet representative, building blocks of motion. Motion primitives provide a means of summarizing the solution space to reduce the burden on a human analyst and are leveraged to rapidly construct complex trajectories in a multi-body gravitational environment.

1.1 Motivation

Leveraging the mutual gravitational influence of multiple celestial bodies significantly increases the complexity of the spacecraft trajectory design space for a transfer design scenario. In a restricted two-body model, conic sections are the main building blocks of motion for trajectory design. However, in a restricted three-body model, a variety of interesting and complex fundamental solutions are present throughout the system including equilibrium points, periodic orbits, quasi-periodic orbits, and hyperbolic invariant manifolds [101, 61]. These solutions govern natural flow throughout the multi-body system.

Fundamental solutions have previously been used to design complex trajectories to enable new and innovative mission concepts in the Sun-Earth system. In 1978, the International Sun-Earth Explorer-3 (ISEE-3) became the first spacecraft to insert into a halo orbit around the Sun-Earth L_1 libration point [25]. Since the launch of ISEE-3, the Solar and Heliospheric Observatory (SOHO), the Advanced Composition Explorer (ACE), and other spacecraft have also been placed in orbits around the Sun-Earth L_1 libration point to study solar activity and improve forecasting for space weather events that impact Earth [53, 95, 24]. In addition, the Genesis spacecraft leveraged the natural dynamics of the Sun-Earth system to collect solar wind particle samples while in orbit around L_1 and then L_2 on its return to Earth to enable a daytime recovery [67]. More recently, the James Webb Space Telescope (JWST) inserted into a halo orbit around the Sun-Earth L_2 libration point and the Nancy Grace Roman Space Telescope is also planned to orbit around L_2 by the mid to late 2020s [36, 10]. Building on the success of past and current missions, there are a large number of future mission concepts proposed in the upcoming decades for a variety of solar observatories and advanced space telescopes to operate throughout the Sun-Earth system. In each of these missions or mission concepts, innovative trajectory solutions leveraging multi-body dynamics enable the placement of spacecraft in key regions of high scientific interest.

In addition to exploring the Sun-Earth system, there is a strong and growing interest in leveraging multi-body dynamics for cislunar exploration. Analyzing the underlying dynamics governing

motion in the Earth-Moon system is critical for developing spacecraft trajectories that may seem nonintuitive but enable effective and efficient exploration of the system. The Hiten spacecraft was the first spacecraft to utilize a low-energy transfer from Earth to a lunar orbit in order to recover the mission after experiencing orbital injection errors [5]. Additionally, the Acceleration, Reconnection, Turbulence, and Electrodynamics of the Moon's Interaction with the Sun (ARTEMIS) spacecraft leveraged a transfer between orbits around L_1 and L_2 in the Earth-Moon system as an extension to the THEMIS mission [28]. Finally, the Artemis Program and Gateway is an international effort that plans to establish a sustainable human presence in cislunar space by constructing an orbital outpost, currently planned in a near-rectilinear halo orbit (NRHO) in the Earth-Moon system, that will serve as a waypoint for lunar surface access and deep space transport [97]. As a precursor to Gateway, the Cislunar Autonomous Positioning System Technology Operations and Navigation Experiment (CAPSTONE) spacecraft recently inserted into an Earth-Moon L_2 southern NRHO and is currently testing and validating procedures for operating within cislunar space in an NRHO [15]. This discussion of mission examples is not an exhaustive list of all the past, present, and future missions that are enabled by leveraging multi-body dynamics; however, these missions demonstrate the increasing interest in exploiting the natural dynamical structures that govern motion in a multi-body system to enable innovative scientific explorations of the solar system.

1.2 Previous Contributions

1.2.1 Spacecraft Trajectory Design in Multi-Body Systems

A challenging aspect of trajectory design in multi-body systems is developing a systematic, rapid, and robust process for initial guess construction. An initial guess for a spacecraft trajectory is commonly constructed in a simplified dynamical model that adequately represents a desired environment. The difficulty of constructing an initial guess is dependent on the complexity of the solution space and the quality of the initial guess impacts the ability to recover a feasible solution. Even in a low-fidelity approximation of a multi-body gravitational environment, such as the circular

restricted three-body problem (CR3BP), the available design space is large and analytical solutions do not exist [101]. Despite the lack of a generalized analytical solution, the CR3BP is commonly used to model the motion of a spacecraft for preliminary trajectory design in a multi-body system.

Historical context is important for understanding the modern use of the CR3BP for spacecraft trajectory design in multi-body systems. The three-body problem has been a focus of study since Sir Issac Newton published the law of universal gravitation in *Principia* in 1687 [4]. Building on Newton's foundational work, Leonhard Euler presented the first formulation of the CR3BP and the existence of the collinear equilibrium points in 1772; during the same year, Joseph-Louis Lagrange discovered the existence of the triangular equilibrium points in addition to the collinear solutions [4]. Years later in 1836, Carl Gustav Jacob Jacobi formulated an integral of motion in the CR3BP, commonly known as the Jacobi constant, which led to George Hill introducing the concept of zero velocity surfaces and allowable regions of motion in 1878 [4]. These results and discoveries provided invaluable insight for studying motion in the CR3BP. Inspired by these developments, the foundational work of Henri Poincaré on the three-body problem at the end of the 19th century and the beginning of the 20th century led to the development of modern dynamical systems theory and chaos theory [4]. Poincaré established that there is not a generalized analytical solution to the CR3BP because no additional integrals of motion exist in the system and also established the existence of an infinite number of periodic orbits in the CR3BP [4]. His work focused on a geometric and qualitative study of the differential equations governing a dynamical system, which inspired a plethora of researchers to study motion in the CR3BP as well as other dynamical systems throughout the last century.

The application of dynamical systems theory to trajectory design in multi-body systems has enabled the development of systematic analysis and design techniques in chaotic environments. In 1967, Szebehely [101] published a foundational and comprehensive book on the study of motion in the CR3BP titled *Theory of Orbits: The Restricted Problem of Three Bodies*. In 1968, Conley [16] characterized transitory and non-transitory behaviors of the flow in the CR3BP near the collinear libration points to motivate the design of low-energy transfers between the Earth and Moon. Llibre

et al. [65] studied the transversality of invariant manifolds associated with L_2 Lyapunov orbits in the CR3BP and Gómez et al. [33] presented a collection of works on the use of dynamical systems techniques for studying dynamics and exploring mission design near libration points in the CR3BP. Building on foundations in dynamical systems theory, Lo [66], Howell et al. [49], Koon et al. [60], and Gómez et al. [32] pioneered the use of natural transport mechanisms in the CR3BP to systematically study the natural motion of small celestial bodies and design complex transfer trajectories in multi-body systems. These foundational techniques have led to the current state-of-the-art for trajectory design in multi-body systems where dynamical insight into the solution space obtained from dynamical systems theory is used to guide the design process. A vast number of researchers, with only a few cited here, have since developed innovative trajectory design techniques that extend the application of dynamical systems theory to increasingly complex design problems [102, 80, 20, 39, 8]. However, the increasing complexity and number of future mission concepts that leverage multi-body dynamics continues to drive a need for rapid trajectory design strategies that reduce the burden on, and expertise required by, a human trajectory designer.

In multi-body systems, one current approach to rapid trajectory design begins with generating a large database of solutions discretized along families of known fundamental solutions such as periodic and quasi-periodic orbits [27, 81, 109]. Similarly, analysis of the natural transport of spacecraft and celestial bodies throughout a multi-body system leverages the generation of stable and unstable manifolds of periodic and quasi-periodic orbits [61]. Specialized design tools then support the exploration and analysis of these families of solutions to identify trajectory segments that are assembled to form an initial guess for a trajectory [22, 41, 40, 38, 94, 109]. However, searching over a large and complex design space may impede analysis because it requires significant time and resources from a human-in-the-loop.

A foundational technique in dynamical systems theory developed by Poincaré and leveraged extensively in current rapid trajectory design strategies is a first return map, which is commonly referred to as a Poincaré map [4, 61]. A Poincaré map provides a discrete and lower dimensional description of motion in a continuous dynamical system [85, 61]. The first step in generating a

Poincaré map is to define a surface of section that is transverse to the flow. Then, initial conditions for a set of trajectories are seeded and propagated within the system. Finally, each intersection of each trajectory with the selected surface of section is recorded and produces the resulting Poincaré map. The resulting map reveals insight into the structure, or lack thereof, of the associated motion in the dynamical system and therefore may simplify analysis of the solution space.

Poincaré maps are typically employed to select trajectory segments that are used to form an initial guess for a trajectory in a multi-body system. For example, a Poincaré map may be used to identify heteroclinic connections between two periodic orbits via their stable and unstable manifolds [61, 39]. However, identifying connections between arcs via a Poincaré map is challenging when considering spatial motion, motion at different energy levels, and a large number of trajectories. Furthermore, it may be difficult for a human analyst to select an appropriate surface of section without sufficient a priori knowledge and experience. Finally, identifying connections between arcs from a Poincaré map typically involves manual processes, does not supply information about the geometry of the resulting initial guess, and it may be challenging to efficiently conduct an expansive exploration of the solution space for a transfer scenario. Accordingly, new strategies are required for simplifying the analysis of the design space and reducing the burden on a human analyst with the goal of supporting effective exploration and use of natural motion for increasingly complex mission concepts, mission extensions, and real-time operations as well as the study of natural transport in multi-body gravitational environments.

An initial guess constructed for a complex trajectory in a multi-body system to support a mission concept is typically comprised of a sequence of discontinuous trajectory segments. Due to the complexity of the nonlinear dynamics in a chaotic gravitational environment, a differential corrections algorithm is commonly employed to recover a continuous solution from a discontinuous initial guess [17, 6]. A variety of numerical methods, such as multiple shooting or collocation, may be used within a corrections algorithm to solve the trajectory design problem [17]. The ability to recover a continuous solution heavily depends on the quality of the initial guess; however, it may also be influenced by the selected numerical method.

Collocation schemes have been employed in corrections algorithms to compute end-to-end trajectories in multi-body systems for a variety of applications [78, 35, 87]. Collocation is commonly used due to its robustness with respect to the quality of an initial guess, which is particularly important for being able to consistently recover continuous trajectories even when starting from a poor initial guess [17]. The basin of convergence for a corrections problem leveraging collocation is typically wider than when leveraging multiple shooting because collocation methods often involve more design parameters and are not constrained by explicit propagation [17, 83]. Rather, a solution to a dynamical system is recovered using collocation by approximating the solution as sets of piecewise polynomials that satisfy the system dynamics at collocation nodes. Parrish and Scheeres [83] demonstrated the robustness of collocation by designing low-thrust optimal trajectories between periodic orbits in the CR3BP given an initial guess of random noise. Previous applications of collocation have enabled robust recovery of continuous trajectories and motivates the continued use of collocation schemes for recovering complex trajectories in multi-body systems [78, 35, 87, 83].

1.2.2 Clustering in Astrodynamics

Clustering is an unsupervised learning method for separating the members of a dataset into groups based on a defined set of features [46]. In this work, clustering algorithms are leveraged to summarize fundamental solutions in the CR3BP. The utility of clustering algorithms in grouping solutions to nonlinear dynamical systems has been demonstrated by a variety of researchers. For instance, spectral clustering has been employed by Hadjighasem et al. [44] to identify coherent Lagrangian vortices from a set of trajectories within a dynamical system. In astrodynamics, the partition-based clustering algorithm, k-means, has been used by Nakhjiri and Villac [74] to identify regions of bounded motion on a Fast Lyapunov Indicator (FLI) map in both the circular and elliptic restricted three-body problems and by Villac et al. [110] to group periodic orbits near small bodies, such as asteroids, in an augmented Hill's three-body problem. In addition, Bosanac [9] and Bonasera and Bosanac [7] have applied hierarchical density-based clustering methods to Poincaré maps in the CR3BP to group trajectories with similar geometries to facilitate analysis

in the trajectory design process. These applications of clustering all demonstrate the value of a data-driven approach to grouping members of a family or set of trajectories in a chaotic dynamical system based on a defined set of features.

1.2.3 Motion Primitives for Motion Planning

To support continued advancement in trajectory design, the concept of a motion primitive is used in this work to summarize sets of trajectories in a multi-body system. This concept has been explored extensively in robotic motion planning, transportation applications, and human body gesture analysis [29, 54, 79, 90, 112]. In each of these fields, motion primitives are used to decompose complex actions or paths into a finite set of representative components, either via analytical or data-driven techniques such as clustering.

Motion primitives have been used in various disciplines to construct a reduced basis set of path segments, actions, configurations, or behaviors that reflects the characteristics of a solution space; however, the exact definition of a motion primitive depends on the field of application [29, 54, 79, 90, 112]. In robotic motion planning, motion primitives may be defined as sets of control inputs that result in a common desired behavior, such as a circular path or an aggressive turn [79]. Similarly, in transportation applications, motion primitives may be defined as steering and velocity profiles that result in different basic driving tasks such as a lane change or lane keeping [112]. A set of Euler angles may be used in human body gesture analysis to define motion primitives as fundamental limb configurations [90]. Frazzoli defines trajectory primitives in the context of autonomous vehicle motion planning as a set of path segments that capture the characteristics of the solution space, support complex path construction, and support extraction of key state description parameters [29]. Based on these examples, a motion primitive set is defined in this research as a set of arcs that capture the characteristics of a larger set of trajectories and support assembly of an initial guess for a more complex path in a multi-body system.

Motion primitive sets are an effective tool often leveraged in motion planning to construct complex paths throughout an environment [117, 63]. Frazzoli et al. [30] compute a finite library

of trim and maneuver primitives and leverage the library of primitives for motion planning. In their investigation, a motion plan is defined as a sequence of concatenated motion primitives where a finite-state machine, denoted as a Maneuver Automaton, is represented as a graph and governs how primitives can be concatenated in a given sequence; a graph is a network of nodes connected by either directed or undirected edges, where each edge is assigned an associated weight. Grymin et al. [37] reframe the motion planning problem as a graph search problem, a common technique in robotics and motion planning, by constructing a graph of reachable states in the environment connected by primitives selected from a precomputed library. Previous applications of primitive-based motion planning in robotics, such as the studies discussed here, motivate an exploration of applying a graph-based approach to initial guess construction in a multi-body system.

1.2.4 Motion Planning in Astrodynamics

The utility of leveraging graph-based searches for initial trajectory design in astrodynamics has been demonstrated by a variety of researchers. Tsirogiannis [105] explored a graph-based methodology for designing impulsive transfers between periodic orbits in the CR3BP using Dijkstra's algorithm. Trumbauer and Villac [104] developed an automated heuristic search-based framework for redesigning trajectories onboard a spacecraft in the CR3BP by leveraging precomputed dynamical structures, periapsis Poincaré maps, and the A* search algorithm. Das-Stuart et al. [18] formulated a search-based trajectory design framework that constructs an initial guess in the low-thrust enabled CR3BP using known dynamical structures, reinforcement learning, and Dijkstra's algorithm. Parrish [82] leveraged a graph-based approach for computing optimal continuous-thrust trajectories in the two-body problem using the A* search algorithm. More recently, Bruchko and Bosanac [14] leveraged probabilistic roadmap generation and Dijkstra's algorithm to autonomously generate transfers between Lyapunov orbits in the CR3BP. Each of these methods effectively leverage different solution space discretization approaches as well as automated graph-based search methods; however, these contributions collectively demonstrate the value of simplifying the continuous trajectory design problem by reframing it as a discrete graph search problem.

1.3 Dissertation Overview

To support continued advancement in rapid trajectory design strategies and reduce the burden on a human analyst during the trajectory design process, the main goal of this dissertation is to develop a new approach for rapidly constructing an initial guess for a spacecraft trajectory in a multi-body system by leveraging motion primitives and dynamical systems theory. To support a proof of concept, motion primitives of fundamental solutions, e.g., selected periodic orbits and their stable and unstable manifolds, are generated via clustering to form a discrete summary of segments of the phase space. Graphs of motion primitives are then constructed and searched to produce primitive sequences that form candidate initial guesses for transfers. Finally, continuous maneuver-enabled transfers are computed from each initial guess using multi-objective constrained optimization and collocation. Distinct sequences of motion primitives are then used to construct trajectories of distinct geometries and explore the solution space.

1.3.1 Organization

The research presented in this dissertation is structured in the following manner:

Chapter 2: Dynamical models are used to approximate the motion of a spacecraft due to the mutual gravitational influence of multiple celestial bodies. This chapter presents an overview of the CR3BP as well as a point mass ephemeris model. Both of these dynamical models are used in the primitive-based trajectory design framework presented in this work. In addition, the reference frame transformations used in each model are defined and numerical propagation is discussed for computing trajectories in each model.

Chapter 3: Fundamental solutions in the CR3BP often support the construction of initial guesses for complex trajectories in a chaotic multi-body gravitational environment. This chapter presents a detailed overview of the methods used to compute the equilibrium points, periodic orbit families, and hyperbolic invariant manifolds associated with periodic orbits in the CR3BP; each fundamental type of solution is leveraged to inform the primitive-based trajectory design framework.

Chapter 4: In a multi-body system, a spacecraft trajectory is typically computed by solving a two-point boundary value problem using multiple shooting or collocation methods. Collocation is used in this work for numerically correcting transfers because it is often more robust with respect to the quality of an initial guess compared to multiple shooting. This chapter presents a detailed overview of a free variable and constraint vector formulation of collocation used to transform the trajectory design problem into a parameter design problem and robustly compute continuous solutions from primitive-based initial guesses.

Chapter 5: Generalizable and exact analytical criteria for grouping solutions along a set of trajectories in a multi-body system according to both qualitative and quantitative characteristics do not currently exist. Thus, clustering techniques are employed in this investigation to group similar trajectories and construct summarizing sets of motion primitives. This chapter presents an overview of the clustering techniques leveraged in this work.

Chapter 6: Rapid trajectory design in multi-body systems often leverages individual arcs along natural dynamical structures that exist in an approximate dynamical model, such as the CR3BP. To reduce the complexity of this analysis in a chaotic gravitational environment, motion primitive sets are constructed to represent the finite geometric, stability, and/or energetic characteristics exhibited by sets of trajectories. This chapter presents and demonstrates the motion primitive construction process developed to summarize fundamental solutions in the CR3BP.

Chapter 7: The increasing number and variety of spacecraft that are expected to operate within cislunar space and other multi-body gravitational environments throughout the solar system necessitates the continued development of strategies for rapid trajectory design and design space exploration. In this chapter, the primitive-based trajectory design framework is presented and demonstrated by evaluating a planar transfer design scenario from an L_1 Lyapunov orbit to an L_2 Lyapunov orbit in the Earth-Moon CR3BP with impulsive maneuvers.

Chapter 8: The primitive-based initial guess construction framework presented in Chapter 7 enables rapid generation of trajectories with distinct geometries for a transfer design scenario. In this chapter, a variety of transfer design scenarios are explored to demonstrate the utility of this

approach for preliminary trajectory design in multi-body systems. A more expansive exploration of the planar transfer design scenario from an L_1 Lyapunov orbit to an L_2 Lyapunov orbit with impulsive maneuvers is conducted. In addition, a spatial transfer design scenario from an L_1 northern halo orbit to an L_2 northern halo orbit with impulsive maneuvers is explored. Finally, a subset of the transfer design space between an L_2 southern NRHO and selected distant retrograde orbits (DRO) is explored due to the recent interest in the use of NRHOs for cislunar exploration.

Chapter 9: This chapter summarizes the work completed in this dissertation. In addition, recommendations for future investigations and applications of the primitive-based trajectory design framework are discussed.

1.3.2 Contributions

The primary contributions of this investigation to the astrodynamics community are as follows:

(1) Development of a motion primitive construction process that leverages consensus clustering to summarize periodic orbit families and trajectories along hyperbolic invariant manifolds associated with periodic orbits in the CR3BP. This contribution may support summarizing the complex solution space admitted by a multi-body system and reducing the analytical workload of a trajectory designer during the trajectory design process.

(2) Development of a modular primitive-based initial guess construction framework that enables rapid generation of trajectories with distinct geometries and efficient design space exploration in multi-body systems. The examples evaluated in this investigation demonstrate that motion primitives can support rapid initial guess construction for spacecraft trajectories in the CR3BP. Furthermore, distinct primitive sequences support rapid exploration of the associated design space via the design of geometrically distinct trajectories. The presented approach contributes to addressing the challenges present in current manual design methodologies when attempting to identify different geometric solutions for a design scenario, particularly in the case of spatial design scenarios at high energy levels.

(3) Formulation of a robust corrections procedure that leverages collocation and multi-objective optimization to recover continuous maneuver-enabled trajectories that balance geometrically resembling a primitive-based initial guess with reducing impulsive maneuver requirements. The corrections process presented in this work builds upon previous collocation formulations by incorporating it into a multi-objective optimization scheme that explicitly encourages the recovery of a trajectory that geometrically resembles the initial guess.

Construction of this new rapid trajectory design strategy for multi-body systems may potentially support rapid mission concept development and efficient response to post-launch trajectory design scenarios, such as time-critical contingencies and development of mission extension options.

Chapter 2

Dynamical Models

This work focuses on the design of spacecraft trajectories in multi-body gravitational systems. To support initial guess construction, the CR3BP is used as an approximate model of the motion of a spacecraft due to the mutual gravitational influence of two primary celestial bodies, such as the Earth and Moon. Despite being a low-fidelity approximation of a multi-body system, the CR3BP admits a variety of fundamental dynamical structures that may be leveraged for preliminary trajectory design. These fundamental solutions provide insight into the solution space in a higher fidelity approximation of the space environment, such as a point mass ephemeris model. Accordingly, a trajectory in a multi-body system is often first constructed in the CR3BP and then transitioned into a high-fidelity model for use in the mission design process. This chapter presents an overview of the CR3BP as well as a point mass ephemeris model. Both of these dynamical models are used in the primitive-based trajectory design framework presented in this work. Furthermore, the reference frame transformations used in each model are defined and numerical propagation is discussed for computing trajectories in each model.

2.1 Circular Restricted Three-Body Problem

2.1.1 Model Overview

The CR3BP is used to approximate the motion of a spacecraft, P_3, under the gravitational influences of two primary celestial bodies, P_1 and P_2. Initially, consider the general three-body problem consisting of P_1, P_2, and P_3 where all three bodies are considered point masses and the only forces acting on each body are the gravitational attraction forces from the other two bodies. The CR3BP relies on the assumption that P_3 possesses a negligible mass compared to P_1 with constant mass $\tilde{M}_1$ as well as P_2 with constant mass $\tilde{M}_2$, where $\tilde{M}_1 \geq \tilde{M}_2$ and the tilde notation denotes a dimensional quantity [101]. Therefore, the center of mass of the system lies on the line between P_1 and P_2. Furthermore, P_1 and P_2 are an isolated two-body problem and consequently follow conics about their mutual barycenter. Finally, P_1 and P_2 are assumed to travel on circular orbits about their mutual barycenter [101]. The plane containing the motion of P_1 and P_2 is defined as the XY-plane of a general inertial frame, $\mathcal{I}$. This inertial reference frame is defined by placing its origin at the barycenter of the system with axes $\{\hat{\boldsymbol{X}}, \hat{\boldsymbol{Y}}, \hat{\boldsymbol{Z}}\}$; throughout this work, vectors are denoted in bold and the $\hat{(\cdot)}$ notation denotes a unit vector. Figure 2.1 displays the configuration of the multi-body system in the general inertial frame with $\hat{\boldsymbol{Z}}$ directed out of the page to complete the right-handed orthogonal triad. The spacecraft P_3 is able to move freely in space where $\tilde{\boldsymbol{r}}_{\boldsymbol{3}}$ is the position of P_3 with respect to the origin of $\mathcal{I}$, $\tilde{\boldsymbol{r}}_{\boldsymbol{1,3}}$ is the position of P_3 with respect to P_1, and $\tilde{\boldsymbol{r}}_{\boldsymbol{2,3}}$ is the position of P_3 with respect to P_2. Following these assumptions and definitions, the equations of motion for P_3 in the CR3BP are derived.

2.1.2 Equations of Motion

Newtonian mechanics is used to derive the equations of motion for a spacecraft in the CR3BP. First, consider the general three-body problem as mentioned in Section 2.1.1. The negative gravitational potential of P_3 per unit mass is defined as

$$\tilde{U}_3 = \frac{\tilde{G}\tilde{M}_1}{\tilde{r}_{1,3}} + \frac{\tilde{G}\tilde{M}_2}{\tilde{r}_{2,3}} \tag{2.1}$$

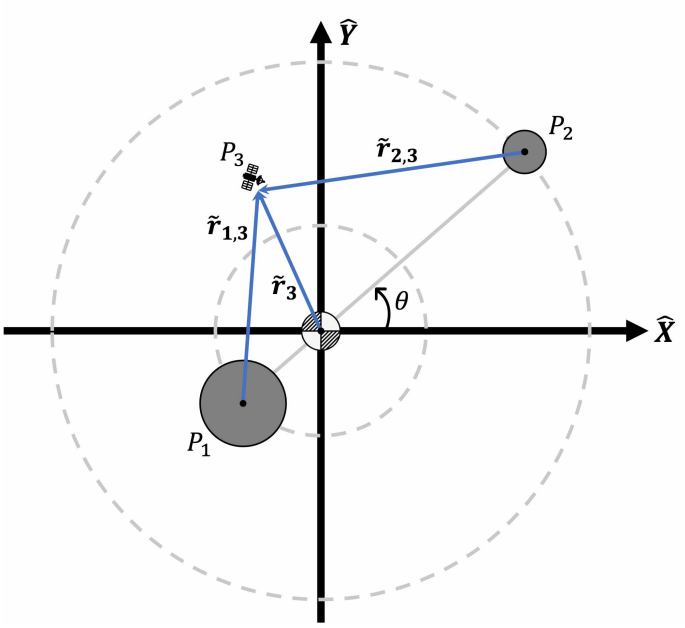

Figure 2.1: Configuration of P_1, P_2, and P_3 in the inertial frame $\mathcal{I} : \{\hat{\boldsymbol{X}}, \hat{\boldsymbol{Y}}, \hat{\boldsymbol{Z}}\}$ for the CR3BP.

where $\tilde{G}$ is the universal gravitational constant, $\tilde{r}_{1,3} = ||\tilde{\boldsymbol{r}}_{\mathbf{1,3}}||$ is the distance of P_3 with respect to P_1, $\tilde{r}_{2,3} = ||\tilde{\boldsymbol{r}}_{\mathbf{2,3}}||$ is the distance of P_3 with respect to P_2, and $||\cdot||$ denotes the l^2-norm [101]. Then, the inertial acceleration of P_3 due to P_1 and P_2 is equal to the gradient of Equation 2.1 and is therefore computed as

$$\tilde{\boldsymbol{r}}_{\mathbf{3}}'' = \boldsymbol{\nabla}\tilde{U}_3 = \frac{\partial \tilde{U}_3}{\partial \tilde{\boldsymbol{r}}_{\mathbf{3}}} = \frac{-\tilde{G}\tilde{M}_1}{\tilde{r}_{1,3}^3}\tilde{\boldsymbol{r}}_{\mathbf{1,3}} - \frac{\tilde{G}\tilde{M}_2}{\tilde{r}_{2,3}^3}\tilde{\boldsymbol{r}}_{\mathbf{2,3}} \tag{2.2}$$

where the $(\cdot)'$ notation denotes a time derivative with respect to an inertial observer and the vectors are expressed independent of a coordinate system [101]. Equation 2.2 can be rewritten as 3 scalar second-order ordinary differential equations (ODEs) that describe the motion of P_3 in the general three-body problem. However, there are an additional 3 scalar second-order ODEs to describe the motion of P_1 as well as another 3 scalar second-order ODEs to describe the motion of P_2. Therefore, a complete description of the motion of P_3 in the general three-body problem requires the use of 9 second-order ODEs which may be reformulated as 18 single-order ODEs [101]. A set of 10 integrals of motion may be defined due to the conservation of linear momentum, angular momentum, and energy in the closed system; however, 18 constants are needed to solve the general three-body

problem analytically [101]. The absence of a generalized analytical solution in the three-body problem motivates the study and use of a simplified restricted three-body problem, such as the CR3BP. Despite the simplifications, there is also no generalized analytical solution in the CR3BP but it does provide a simpler approximation of a three-body system. The CR3BP is an appropriate model for many physical environments found in the solar system, such as star-planet-moon, star-planet-spacecraft, and planet-moon-spacecraft systems. Leveraging the CR3BP to study motion in a three-body system simplifies the equations of motion, reduces the complexity of analysis, and enables identification of particular solutions despite the lack of a generalized closed-form solution [101].

Applying the assumptions of the CR3BP, the equations of motion for P_3 defined in Equation 2.2 are simplified by using characteristic length, mass, and time quantities for nondimensionalization and to express the problem as a function of a single system parameter [101, 61]. The characteristic parameter for length, l^*, is selected as the assumed constant distance between P_1 and P_2. The characteristic parameter for mass, m^*, is equal to the total mass of the system, i.e., $m^* = \tilde{M}_1 + \tilde{M}_2$, and the mass ratio of the multi-body system is then defined as

$$\mu = \frac{\tilde{M}_2}{m^*} \tag{2.3}$$

Finally, the characteristic parameter for time, t^*, is defined such that the nondimensional period of the primary system is equal to 2π. Both P_1 and P_2 are assumed to move in circular orbits about the barycenter of the system with a mean motion equal to

$$\tilde{n} = \left(\frac{\tilde{G} m^*}{{l^*}^3} \right)^{\frac{1}{2}} \tag{2.4}$$

[89]. Consequently, t^* is defined as

$$t^* = \frac{1}{\tilde{n}} = \left(\frac{{l^*}^3}{\tilde{G} m^*} \right)^{\frac{1}{2}} \tag{2.5}$$

to produce a nondimensional period of 2π for the primary system. Using these characteristic quantities to normalize the variables in Equation 2.2, the nondimensional equations of motion for

P_3 in the CR3BP with respect to an inertial observer are defined as

$$\boldsymbol{r_3''} = \frac{-(1-\mu)}{r_{1,3}^3}\boldsymbol{r_{1,3}} - \frac{\mu}{r_{2,3}^3}\boldsymbol{r_{2,3}} \tag{2.6}$$

These equations of motion depend only on the mass ratio of the multi-body system and are therefore only a function of a single system parameter. The characteristic quantities and mass ratio computed for the Earth-Moon and Sun-Earth CR3BP systems are provided in Table 2.1 [76, 75, 106]. In this work, trajectories are only computed in the Earth-Moon and Sun-Earth systems; however, the nondimensional form of the equations of motion provides a useful formulation to efficiently study motion in a variety of multi-body systems by simply adjusting the value of μ.

Table 2.1: Characteristic quantities and mass ratio computed for the Earth-Moon and Sun-Earth CR3BP systems.

Parameter	Earth-Moon	Sun-Earth
l^*	3.84400×10^5 km	$1.495978706996262 \times 10^8$ km
m^*	$6.046804167273307 \times 10^{24}$ kg	$1.988803216221062 \times 10^{30}$ kg
t^*	$3.751902588926273 \times 10^5$ s	$5.022635348636394 \times 10^6$ s
μ	$1.215058535056245 \times 10^{-2}$	$3.003480640226780 \times 10^{-6}$

Next, a rotating frame is defined to reformulate the equations of motion for P_3 in the CR3BP with respect to a rotating observer. In the inertial frame, the positions of P_1 and P_2 depend on time; however, a rotating reference frame is defined to remove this explicit dependence on time and produce an autonomous system [101]. The rotating frame, $\mathcal{R}$, is defined by placing its origin at the barycenter of the system, i.e., coincident with the origin of $\mathcal{I}$, with axes $\{\hat{\boldsymbol{x}}, \hat{\boldsymbol{y}}, \hat{\boldsymbol{z}}\}$: $\hat{\boldsymbol{x}}$ is directed from P_1 to P_2, $\hat{\boldsymbol{z}}$ is aligned with the orbital angular momentum vector of the primary system which is parallel to $\hat{\boldsymbol{Z}}$, and $\hat{\boldsymbol{y}}$ completes the right-handed orthogonal triad [101]. Therefore, the angle between $\hat{\boldsymbol{x}}$ and $\hat{\boldsymbol{X}}$ at a nondimensional time, t, is defined as

$$\theta = nt + \theta_0 \tag{2.7}$$

where θ is labeled in Figure 2.1, $n = \tilde{n}t^*$ is unity, and θ_0 is the initial value of θ. Figure 2.2 displays the configuration of the multi-body system in the rotating frame with $\hat{\boldsymbol{z}}$ directed out of the page.

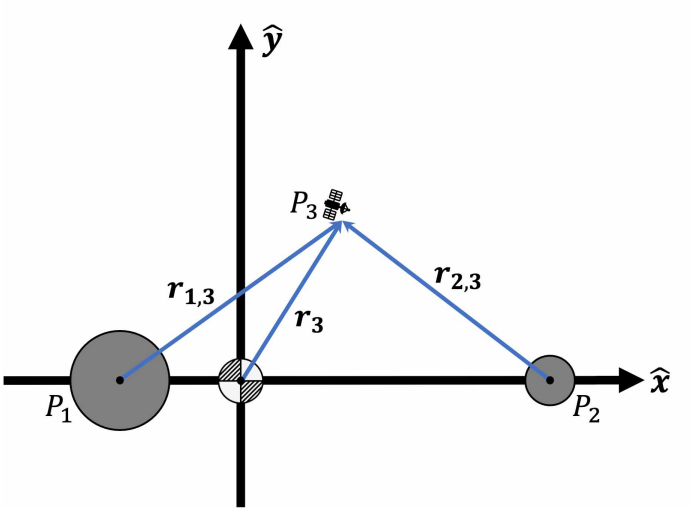

Figure 2.2: Configuration of P_1, P_2, and P_3 in the rotating frame $\mathcal{R} : \{\hat{\boldsymbol{x}}, \hat{\boldsymbol{y}}, \hat{\boldsymbol{z}}\}$ for the CR3BP.

The transport theorem is used to define the equations of motion for P_3 in the rotating frame [93]. First, the time derivative of $\boldsymbol{r_3}$ with respect to an inertial observer fixed in $\mathcal{I}$ is equal to

$$\boldsymbol{r_3'} = \dot{\boldsymbol{r}}_3 + \left(\boldsymbol{\omega_{\mathcal{R}/\mathcal{I}}} \times \boldsymbol{r_3}\right) \tag{2.8}$$

where the $(\dot{\cdot})$ notation denotes a time derivative with respect to a rotating observer fixed in $\mathcal{R}$ and $\boldsymbol{\omega_{\mathcal{R}/\mathcal{I}}}$ is the angular velocity of $\mathcal{R}$ with respect to $\mathcal{I}$. Applying transport theorem again, the time derivative of $\boldsymbol{r_3'}$ with respect to an inertial observer fixed in $\mathcal{I}$ is defined as

$$\boldsymbol{r_3''} = \dot{(\boldsymbol{r_3'})} + \left(\boldsymbol{\omega_{\mathcal{R}/\mathcal{I}}} \times \boldsymbol{r_3'}\right) = \ddot{\boldsymbol{r}}_3 + 2\left(\boldsymbol{\omega_{\mathcal{R}/\mathcal{I}}} \times \dot{\boldsymbol{r}}_3\right) + \left(\boldsymbol{\omega_{\mathcal{R}/\mathcal{I}}} \times \left(\boldsymbol{\omega_{\mathcal{R}/\mathcal{I}}} \times \boldsymbol{r_3}\right)\right) \tag{2.9}$$

Equating Equations 2.6 and 2.9 and then solving for $\ddot{\boldsymbol{r}}_3$ results in the following equations of motion for P_3 in the CR3BP with respect to a rotating observer fixed in $\mathcal{R}$:

$$\ddot{\boldsymbol{r}}_3 = -2\left(\boldsymbol{\omega_{\mathcal{R}/\mathcal{I}}} \times \dot{\boldsymbol{r}}_3\right) - \left(\boldsymbol{\omega_{\mathcal{R}/\mathcal{I}}} \times \left(\boldsymbol{\omega_{\mathcal{R}/\mathcal{I}}} \times \boldsymbol{r_3}\right)\right) - \frac{(1-\mu)}{r_{1,3}^3}\boldsymbol{r_{1,3}} - \frac{\mu}{r_{2,3}^3}\boldsymbol{r_{2,3}} \tag{2.10}$$

Thus far, the nondimensional equations of motion for P_3 have been derived in the CR3BP with respect to an inertial observer fixed in $\mathcal{I}$ (Equation 2.6) and with respect to a rotating observer fixed in $\mathcal{R}$ (Equation 2.10) expressed independent of a coordinate system.

The equations of motion for P_3 with respect to an inertial observer fixed in $\mathcal{I}$, as defined in Equation 2.6, may be evaluated by expressing the nondimensional positions of P_1, P_2, and P_3 in $\mathcal{I}$. The position of P_3 in $\mathcal{I}$ is defined as

$$^{\mathcal{I}}\boldsymbol{r_3} = X\hat{\boldsymbol{X}} + Y\hat{\boldsymbol{Y}} + Z\hat{\boldsymbol{Z}} \tag{2.11}$$

where, when included, the left superscript notation for a vector denotes the Cartesian coordinate system in which the vector is expressed. Furthermore, the position of the center of mass of the system is defined as

$$(1-\mu)\boldsymbol{r_1} + \mu\boldsymbol{r_2} = \boldsymbol{0} \tag{2.12}$$

where $\boldsymbol{r_1}$ is the position of P_1, $\boldsymbol{r_2}$ is the position of P_2, and $\boldsymbol{0}$ is the zero vector with respect to the origin of $\mathcal{I}$. When $\theta = 0$, Equation 2.12 is satisfied by $^{\mathcal{I}}\boldsymbol{r_1} = -\mu\hat{\boldsymbol{X}}$ and $^{\mathcal{I}}\boldsymbol{r_2} = (1-\mu)\hat{\boldsymbol{X}}$. Therefore, due to the circular motion of P_1 and P_2, $^{\mathcal{I}}\boldsymbol{r_1}$ and $^{\mathcal{I}}\boldsymbol{r_2}$ may more generally be computed as

$$\begin{aligned} ^{\mathcal{I}}\boldsymbol{r_1} &= (-\mu\cos\theta)\hat{\boldsymbol{X}} + (-\mu\sin\theta)\hat{\boldsymbol{Y}} + 0\hat{\boldsymbol{Z}} \\ ^{\mathcal{I}}\boldsymbol{r_2} &= ((1-\mu)\cos\theta)\hat{\boldsymbol{X}} + ((1-\mu)\sin\theta)\hat{\boldsymbol{Y}} + 0\hat{\boldsymbol{Z}} \end{aligned} \tag{2.13}$$

and, consequently, $^{\mathcal{I}}\boldsymbol{r_{1,3}}$ and $^{\mathcal{I}}\boldsymbol{r_{2,3}}$ are computed as

$$\begin{aligned} ^{\mathcal{I}}\boldsymbol{r_{1,3}} &= {}^{\mathcal{I}}\boldsymbol{r_3} - {}^{\mathcal{I}}\boldsymbol{r_1} = (X+\mu\cos\theta)\hat{\boldsymbol{X}} + (Y+\mu\sin\theta)\hat{\boldsymbol{Y}} + Z\hat{\boldsymbol{Z}} \\ ^{\mathcal{I}}\boldsymbol{r_{2,3}} &= {}^{\mathcal{I}}\boldsymbol{r_3} - {}^{\mathcal{I}}\boldsymbol{r_2} = (X-(1-\mu)\cos\theta)\hat{\boldsymbol{X}} + (Y-(1-\mu)\sin\theta)\hat{\boldsymbol{Y}} + Z\hat{\boldsymbol{Z}} \end{aligned} \tag{2.14}$$

Finally, Equation 2.6 is evaluated using Equation 2.14 and results in the following set of scalar second-order ODEs in the inertial frame $\mathcal{I}$:

$$\begin{aligned} X'' &= \frac{-(1-\mu)}{r_{1,3}^3}(X+\mu\cos\theta) - \frac{\mu}{r_{2,3}^3}(X-(1-\mu)\cos\theta) \\ Y'' &= \frac{-(1-\mu)}{r_{1,3}^3}(Y+\mu\sin\theta) - \frac{\mu}{r_{2,3}^3}(Y-(1-\mu)\sin\theta) \\ Z'' &= \frac{-(1-\mu)}{r_{1,3}^3}Z - \frac{\mu}{r_{2,3}^3}Z \end{aligned} \tag{2.15}$$

As previously discussed, there is no generalized analytical solution in the CR3BP for the motion of P_3; however, the motion of P_3 in $\mathcal{I}$ may be computed via numerical propagation using Equation 2.15 given an initial state and time for P_3 [101, 61].

The motion of a spacecraft in the CR3BP is more commonly computed and analyzed in the rotating frame due to the removal of the explicit time dependence. The equations of motion for P_3 with respect to a rotating observer fixed in $\mathcal{R}$, as defined in Equation 2.10, may be evaluated by expressing the nondimensional positions of P_1, P_2, and P_3 in $\mathcal{R}$. The position of P_3 in $\mathcal{R}$ is defined as

$$^{\mathcal{R}}\boldsymbol{r_3} = x\hat{\boldsymbol{x}} + y\hat{\boldsymbol{y}} + z\hat{\boldsymbol{z}} \tag{2.16}$$

Then, to express $\boldsymbol{r_1}$ and $\boldsymbol{r_2}$ in the rotating frame, $^{\mathcal{I}}\boldsymbol{r_1}$ and $^{\mathcal{I}}\boldsymbol{r_2}$ are transformed into the coordinates of the rotating frame using a single axis rotation about $\hat{\boldsymbol{Z}}$ [93]. The corresponding rotation matrix is defined as

$$\left[\boldsymbol{C^{\mathcal{RI}}}\right] = \begin{bmatrix} cos(\theta) & sin(\theta) & 0 \\ -sin(\theta) & cos(\theta) & 0 \\ 0 & 0 & 1 \end{bmatrix} \tag{2.17}$$

where the right superscript notation denotes the target coordinate system followed by the source coordinate system from left to right; throughout this work, matrices are denoted in bold and encompassed by brackets. Therefore, the positions of P_1 and P_2 are computed in the rotating frame as

$$\begin{aligned} ^{\mathcal{R}}\boldsymbol{r_1} &= \left[\boldsymbol{C^{\mathcal{RI}}}\right]^{\mathcal{I}}\boldsymbol{r_1} = -\mu\hat{\boldsymbol{x}} + 0\hat{\boldsymbol{y}} + 0\hat{\boldsymbol{z}} \\ ^{\mathcal{R}}\boldsymbol{r_2} &= \left[\boldsymbol{C^{\mathcal{RI}}}\right]^{\mathcal{I}}\boldsymbol{r_2} = (1-\mu)\hat{\boldsymbol{x}} + 0\hat{\boldsymbol{y}} + 0\hat{\boldsymbol{z}} \end{aligned} \tag{2.18}$$

and are consequently fixed in $\mathcal{R}$ as expected. As displayed in Figure 2.2, $^{\mathcal{R}}\boldsymbol{r_{1,3}}$ and $^{\mathcal{R}}\boldsymbol{r_{2,3}}$ may then be computed as

$$\begin{aligned} ^{\mathcal{R}}\boldsymbol{r_{1,3}} &= {}^{\mathcal{R}}\boldsymbol{r_3} - {}^{\mathcal{R}}\boldsymbol{r_1} = (x+\mu)\hat{\boldsymbol{x}} + y\hat{\boldsymbol{y}} + z\hat{\boldsymbol{z}} \\ ^{\mathcal{R}}\boldsymbol{r_{2,3}} &= {}^{\mathcal{R}}\boldsymbol{r_3} - {}^{\mathcal{R}}\boldsymbol{r_2} = (x-1+\mu)\hat{\boldsymbol{x}} + y\hat{\boldsymbol{y}} + z\hat{\boldsymbol{z}} \end{aligned} \tag{2.19}$$

Finally, Equation 2.10 is evaluated using Equations 2.16 and 2.19 where $^{\mathcal{R}}\boldsymbol{\omega_{\mathcal{R}/\mathcal{I}}} = 1\hat{\boldsymbol{z}}$ and $^{\mathcal{R}}\dot{\boldsymbol{r}}_{\boldsymbol{3}} =$

$\dot{x}\hat{\boldsymbol{x}} + \dot{y}\hat{\boldsymbol{y}} + \dot{z}\hat{\boldsymbol{z}}$, resulting in the following set of scalar second-order ODEs in the rotating frame $\mathcal{R}$:

$$\begin{aligned}
\ddot{x} &= 2\dot{y} + x - \frac{(1-\mu)(x+\mu)}{r_{1,3}^3} - \frac{\mu(x-1+\mu)}{r_{2,3}^3} \\
\ddot{y} &= -2\dot{x} + y - \frac{(1-\mu)y}{r_{1,3}^3} - \frac{\mu y}{r_{2,3}^3} \\
\ddot{z} &= -\frac{(1-\mu)z}{r_{1,3}^3} - \frac{\mu z}{r_{2,3}^3}
\end{aligned} \tag{2.20}$$

A pseudo-potential function, U^*, may then be defined by inspection to produce a compact form of these equations of motion as

$$\ddot{x} = 2\dot{y} + \frac{\partial U^*}{\partial x} \qquad \ddot{y} = -2\dot{x} + \frac{\partial U^*}{\partial y} \qquad \ddot{z} = \frac{\partial U^*}{\partial z} \tag{2.21}$$

where

$$U^* = \frac{1}{2}(x^2 + y^2) + \frac{(1-\mu)}{r_{1,3}} + \frac{\mu}{r_{2,3}} \tag{2.22}$$

[101, 61]. As previously discussed, there is no generalized analytical solution to the CR3BP. Instead, the motion of P_3 in $\mathcal{R}$ may be computed via numerical propagation using Equation 2.21 given an initial state for P_3. However, there are a variety of fundamental solutions in the CR3BP that may be computed numerically, such as equilibrium points, periodic orbits, quasi-periodic orbits, and hyperbolic invariant manifolds [101, 61].

2.1.3 Jacobi Constant

A constant of motion, commonly referred to as the Jacobi constant, exists in the CR3BP and is inversely proportional to the total energy of P_3 in the rotating reference frame [101]. The CR3BP admits a constant of motion because the equations of motion for P_3 defined in Equation 2.21 are Hamiltonian and autonomous [61]. The Jacobi constant may be derived directly using the equations of motion [101, 61]. The time derivative of the specific kinetic energy of P_3 in the rotating frame is defined as

$$\frac{d}{dt}\left(\frac{1}{2}v^2\right) = \frac{d}{dt}\left(\frac{1}{2}\left(\dot{x}^2 + \dot{y}^2 + \dot{z}^2\right)\right) = \dot{x}\ddot{x} + \dot{y}\ddot{y} + \dot{z}\ddot{z} \tag{2.23}$$

where v is the magnitude of the velocity of P_3 in $\mathcal{R}$. Substituting Equation 2.21 into Equation 2.23 results in the following equation:

$$\frac{d}{dt}\left(\frac{1}{2}v^2\right) = \dot{x}\left(2\dot{y} + \frac{\partial U^*}{\partial x}\right) + \dot{y}\left(-2\dot{x} + \frac{\partial U^*}{\partial y}\right) + \dot{z}\left(\frac{\partial U^*}{\partial z}\right) = \frac{\partial U^*}{\partial x}\dot{x} + \frac{\partial U^*}{\partial y}\dot{y} + \frac{\partial U^*}{\partial z}\dot{z} \quad (2.24)$$

where the right-hand side of Equation 2.24 is equal to the total time derivative of U^*. Therefore, Equation 2.24 is simplified as

$$\frac{d}{dt}\left(\frac{1}{2}v^2\right) = \frac{d}{dt}\left(U^*\right) \quad (2.25)$$

Finally, integrating both sides and introducing the constant of integration produces the following definition for the Jacobi constant:

$$C_J = 2U^* - v^2 \quad (2.26)$$

The Jacobi constant is inversely proportional to the total energy of P_3 in $\mathcal{R}$; therefore, increases in C_J correspond to decreases in energy and vice versa [61]. This quantity is invaluable for validating numerical propagation of trajectories, supplying insight into allowable regions of motion, and providing heuristics for maneuver design in the CR3BP [101, 61].

2.1.4 Zero Velocity Surfaces

The energy of a spacecraft in the rotating frame of the CR3BP provides insight into its allowable regions of motion throughout the system. In the CR3BP, the value of C_J is constant for the motion of P_3 in $\mathcal{R}$ unless a propulsion system is used to alter its energy [101, 61]. At a fixed Jacobi constant, there are possible motions of P_3 that are bounded by surfaces where $v = 0$ [61]. The velocity of P_3 in $\mathcal{R}$ would need to transition from real to imaginary for P_3 to cross through a boundary of motion, which is not physically possible. Therefore, the boundaries of motion in $\mathcal{R}$ for a natural trajectory, commonly referred to as zero velocity surfaces (ZVS), are formed by the set of points in the configuration space that satisfy the following equation for a fixed value of C_J:

$$2U^* - C_J = 0 \quad (2.27)$$

Regions bounded by a zero velocity surface where v is imaginary are identified as forbidden regions of motion. Figure 2.3 displays an example of a zero velocity surface computed in the Earth-Moon

CR3BP at $C_J = 3.05$; the Earth and Moon are plotted to scale and forbidden regions of motion are colored in gray. Figures 2.3a and 2.3b display the intersection of the zero velocity surface with the xy- and xz-planes of $\mathcal{R}$, respectively. The zero velocity surface appears as zero velocity curves (ZVC) when viewed in either plane. Based on the ZVCs displayed in Figure 2.3, P_3 may move in the local vicinity of both the Earth and Moon with bounds on its minimum/maximum x, y, and z coordinates. However, P_3 must travel near the vicinity of the Moon in order to reach exterior regions of the system that lie outside the ZVS when $C_J = 3.05$. Examining the zero velocity surfaces at distinct values of C_J provides a trajectory designer with invaluable insight into the constraints on the natural motion of P_3 in the vicinity of P_1 and P_2 as well as the manner in which changes in energy impact the allowable regions of motion in the configuration space of the CR3BP.

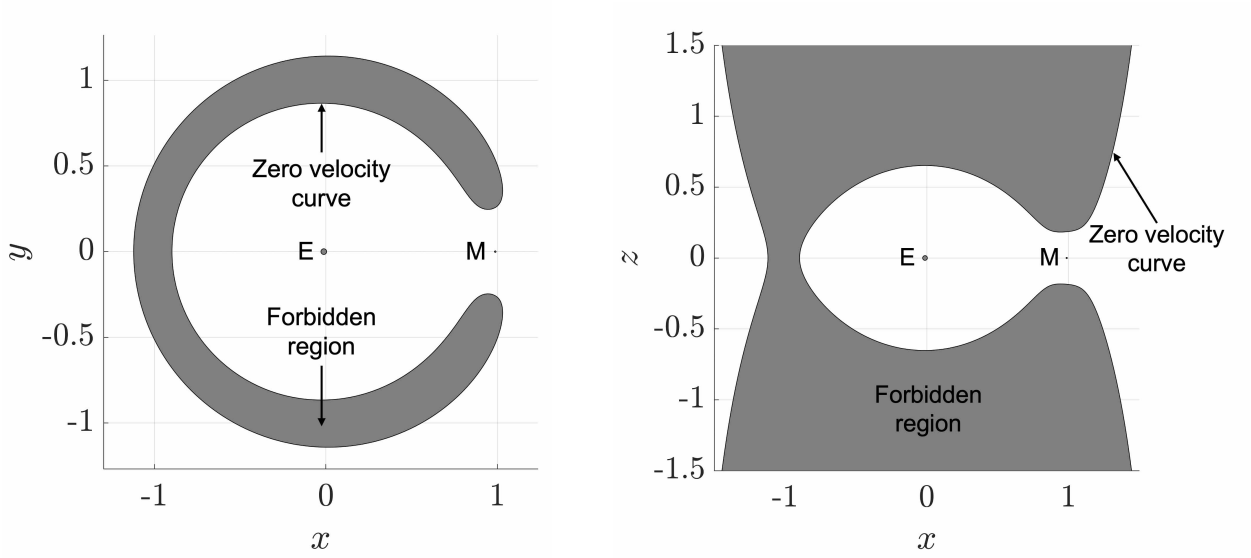

(a) Zero velocity curve in the xy-plane of $\mathcal{R}$ at $C_J = 3.05$.

(b) Zero velocity curve in the xz-plane of $\mathcal{R}$ at $C_J = 3.05$.

Figure 2.3: Example of a zero velocity surface computed in the Earth-Moon CR3BP at $C_J = 3.05$.

2.1.5 Jacobian Matrix

In a dynamical system, the Jacobian matrix of the dynamics characterizes the first-order response of the system to perturbations in the phase space relative to a reference solution [12, 85]. Consider a state $\boldsymbol{q}$ in a nonlinear, autonomous dynamical system where the equations of motion are defined as $\dot{\boldsymbol{q}} = \boldsymbol{f}(\boldsymbol{q})$. The Jacobian matrix of the dynamics is then defined as

$$[\boldsymbol{A}] = \frac{\partial \boldsymbol{f}(\boldsymbol{q})}{\partial \boldsymbol{q}} \tag{2.28}$$

where $[\boldsymbol{A}]$ may be evaluated along a reference solution. The Jacobian is constant if the reference solution is a stationary state; however, the Jacobian is time-varying if the reference solution is a trajectory. Evaluating the Jacobian matrix of the dynamics along a reference solution is critical for understanding the qualitative behavior of nearby solutions.

A Jacobian matrix is derived to characterize the first-order response of the CR3BP to perturbations in the phase space relative to a reference trajectory. In this work, the motion of a spacecraft in the CR3BP is computed with respect to a rotating observer fixed in $\mathcal{R}$ as defined in Equation 2.21. The nondimensional rotating state vector of P_3 expressed in $\mathcal{R}$ is defined as ${}^{\mathcal{R}}\boldsymbol{q} = [x, y, z, \dot{x}, \dot{y}, \dot{z}]^{\mathrm{T}}$ where ${}^{\mathcal{R}}\dot{\boldsymbol{q}} = {}^{\mathcal{R}}\boldsymbol{f}(\boldsymbol{q}) = [\dot{x}, \dot{y}, \dot{z}, \ddot{x}, \ddot{y}, \ddot{z}]^{\mathrm{T}}$. Therefore, given the equations of motion for P_3 presented in Equation 2.21, $[\boldsymbol{A}]$ is defined as

$$[\boldsymbol{A}] = \begin{bmatrix} 0 & 0 & 0 & 1 & 0 & 0 \\ 0 & 0 & 0 & 0 & 1 & 0 \\ 0 & 0 & 0 & 0 & 0 & 1 \\ U^*_{xx} & U^*_{xy} & U^*_{xz} & 0 & 2 & 0 \\ U^*_{xy} & U^*_{yy} & U^*_{yz} & -2 & 0 & 0 \\ U^*_{xz} & U^*_{yz} & U^*_{zz} & 0 & 0 & 0 \end{bmatrix} \tag{2.29}$$

where

$$
\begin{aligned}
U^*_{xx} &= \frac{\partial^2 U^*}{\partial x^2} = 1 + \frac{3(1-\mu)(x+\mu)^2}{r_{1,3}^5} - \frac{1-\mu}{r_{1,3}^3} + \frac{3\mu(x-1+\mu)^2}{r_{2,3}^5} - \frac{\mu}{r_{2,3}^3} \\
U^*_{yy} &= \frac{\partial^2 U^*}{\partial y^2} = 1 + \frac{3(1-\mu)y^2}{r_{1,3}^5} - \frac{1-\mu}{r_{1,3}^3} + \frac{3\mu y^2}{r_{2,3}^5} - \frac{\mu}{r_{2,3}^3} \\
U^*_{zz} &= \frac{\partial^2 U^*}{\partial z^2} = \frac{3(1-\mu)z^2}{r_{1,3}^5} - \frac{1-\mu}{r_{1,3}^3} + \frac{3\mu z^2}{r_{2,3}^5} - \frac{\mu}{r_{2,3}^3} \\
U^*_{xy} &= \frac{\partial^2 U^*}{\partial x \partial y} = \frac{3(1-\mu)(x+\mu)y}{r_{1,3}^5} + \frac{3\mu(x-1+\mu)y}{r_{2,3}^5} \\
U^*_{xz} &= \frac{\partial^2 U^*}{\partial x \partial z} = \frac{3(1-\mu)(x+\mu)z}{r_{1,3}^5} + \frac{3\mu(x-1+\mu)z}{r_{2,3}^5} \\
U^*_{yz} &= \frac{\partial^2 U^*}{\partial y \partial z} = \frac{3(1-\mu)yz}{r_{1,3}^5} + \frac{3\mu yz}{r_{2,3}^5}
\end{aligned}
\tag{2.30}
$$

This definition of $[\boldsymbol{A}]$ for the CR3BP (formulated with respect to a rotating observer fixed in $\mathcal{R}$) is used in subsequent chapters for fundamental solution analysis and differential corrections.

2.2 Point Mass Ephemeris Model

2.2.1 Model Overview

Transitioning a trajectory from a lower fidelity model, such as the CR3BP, into a point mass ephemeris model is an important step in designing a trajectory in a realistic model of a multi-body gravitational system. A point mass ephemeris model incorporates the gravitational influence of N bodies (P_1, P_2, ..., P_N) where each body is assumed to be a point mass [106]. The first body in the system (P_1) is denoted as the central primary body, the second body (P_2) is denoted as the secondary primary body, and the third body (P_3) is denoted as the spacecraft. If $N > 3$, the remaining $N - 3$ bodies are denoted as perturbing bodies. Similar to the CR3BP, the spacecraft is assumed to possess a negligible mass and therefore does not impact the motion of the primary bodies. However, no assumptions are made about the motion of each body. Rather, the state of each celestial body is obtained from ephemerides using the SPICE Toolkit developed by the Navigation and Ancillary Information Facility (NAIF) at the NASA Jet Propulsion Laboratory (JPL) [1, 2]. Figure 2.4 displays the configuration of the multi-body system in an inertial frame, $\mathcal{E}$, with axes $\{\hat{\boldsymbol{X}}_{\boldsymbol{\mathcal{E}}}, \hat{\boldsymbol{Y}}_{\boldsymbol{\mathcal{E}}}, \hat{\boldsymbol{Z}}_{\boldsymbol{\mathcal{E}}}\}$; besides P_1 and P_3, only one additional primary body is included in Figure

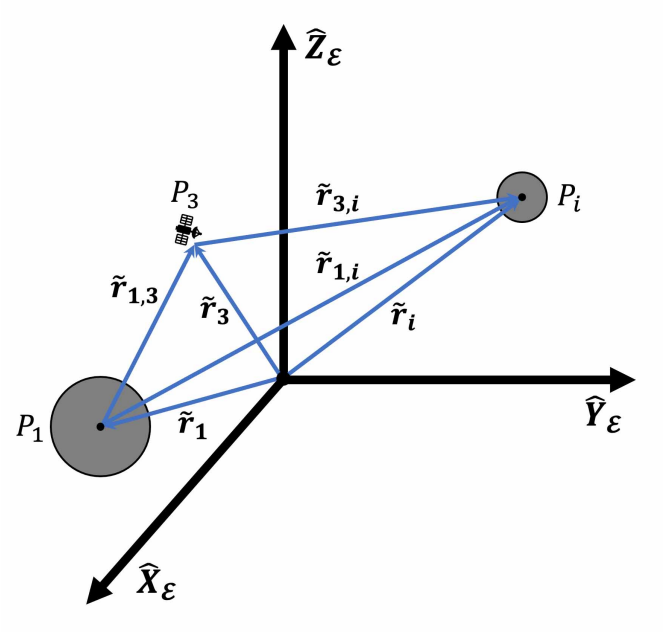

Figure 2.4: Configuration of P_1, P_3, and P_i in the inertial frame $\mathcal{E} : \{\hat{\boldsymbol{X}}_{\boldsymbol{\mathcal{E}}}, \hat{\boldsymbol{Y}}_{\boldsymbol{\mathcal{E}}}, \hat{\boldsymbol{Z}}_{\boldsymbol{\mathcal{E}}}\}$ for a point mass ephemeris model.

2.4 and labeled generically as P_i to simplify visualization of the multi-body system. Following these assumptions and definitions as well as the notation introduced in Section 2.1, the equations of motion for P_3 in a point mass ephemeris model are derived. Trajectories computed in a point mass ephemeris model may serve as a foundation for evaluating motion in even higher fidelity models of a multi-body system that incorporate additional common perturbations present in the space environment.

2.2.2 Equations of Motion

The equations of motion for a spacecraft in a point mass ephemeris model are derived relative to the central primary body and in an inertial frame using Newtonian mechanics [106]. From Newton's law of universal gravitation, the gravitational attraction force applied to P_j due to P_i is defined as

$$\boldsymbol{F_{i,j}} = \frac{-\tilde{G}\tilde{M}_i\tilde{M}_j}{\tilde{r}_{i,j}^3}\tilde{\boldsymbol{r}}_{\boldsymbol{i,j}} \tag{2.31}$$

where $\tilde{G}$ is the universal gravitational constant, $\tilde{M}_i$ is the mass of P_i, $\tilde{M}_j$ is the mass of P_j, $\tilde{\boldsymbol{r}}_{\boldsymbol{i,j}}$ is the position of P_j with respect to P_i, and $\tilde{r}_{i,j} = ||\tilde{\boldsymbol{r}}_{\boldsymbol{i,j}}||$ is the distance of P_j with respect to P_i [106]. Applying Newton's laws of motion to P_1 and P_3, the inertial acceleration of P_1 is defined as

$$\tilde{\boldsymbol{r}}_{\mathbf{1}}'' = \frac{\tilde{G}\tilde{M}_3}{\tilde{r}_{1,3}^3}\tilde{\boldsymbol{r}}_{\mathbf{1,3}} + \sum_{i=2, i\neq 3}^{N} \frac{\tilde{G}\tilde{M}_i}{\tilde{r}_{1,i}^3}\tilde{\boldsymbol{r}}_{\mathbf{1},\boldsymbol{i}} \tag{2.32}$$

and the inertial acceleration of P_3 is defined as

$$\tilde{\boldsymbol{r}}_{\mathbf{3}}'' = \frac{-\tilde{G}\tilde{M}_1}{\tilde{r}_{1,3}^3}\tilde{\boldsymbol{r}}_{\mathbf{1,3}} + \sum_{i=2, i\neq 3}^{N} \frac{\tilde{G}\tilde{M}_i}{\tilde{r}_{3,i}^3}\tilde{\boldsymbol{r}}_{\mathbf{3},\boldsymbol{i}} \tag{2.33}$$

Therefore, the inertial acceleration of P_3 relative to P_1 is defined as

$$\tilde{\boldsymbol{r}}_{\mathbf{1,3}}'' = \tilde{\boldsymbol{r}}_{\mathbf{3}}'' - \tilde{\boldsymbol{r}}_{\mathbf{1}}'' = \frac{-\tilde{G}(\tilde{M}_1 + \tilde{M}_3)}{\tilde{r}_{1,3}^3}\tilde{\boldsymbol{r}}_{\mathbf{1,3}} + \sum_{i=2, i\neq 3}^{N} \tilde{G}\tilde{M}_i \left(\frac{\tilde{\boldsymbol{r}}_{\mathbf{3},\boldsymbol{i}}}{\tilde{r}_{3,i}^3} - \frac{\tilde{\boldsymbol{r}}_{\mathbf{1},\boldsymbol{i}}}{\tilde{r}_{1,i}^3} \right) \tag{2.34}$$

Finally, the assumption that $\tilde{M}_3$ is negligible compared to the mass of each primary body in the system is applied and Equation 2.34 simplifies to

$$\tilde{\boldsymbol{r}}_{\mathbf{1,3}}'' = \frac{-\tilde{G}\tilde{M}_1}{\tilde{r}_{1,3}^3}\tilde{\boldsymbol{r}}_{\mathbf{1,3}} + \sum_{i=2, i\neq 3}^{N} \tilde{G}\tilde{M}_i \left(\frac{\tilde{\boldsymbol{r}}_{\mathbf{3},\boldsymbol{i}}}{\tilde{r}_{3,i}^3} - \frac{\tilde{\boldsymbol{r}}_{\mathbf{1},\boldsymbol{i}}}{\tilde{r}_{1,i}^3} \right) \tag{2.35}$$

where $\tilde{G}\tilde{M}_i$ is the standard gravitational parameter of P_i. Equation 2.35 presents the dimensional equations of motion for P_3 relative to P_1 in a point mass ephemeris model with respect to an inertial observer and expressed independent of a coordinate system.

To evaluate the motion of P_3 relative to P_1 in a point mass ephemeris model, the equations of motion presented in Equation 2.35 are nondimensionalized. The equations are nondimensionalized to improve the numerical conditioning of the system. The nondimensional standard gravitational parameter of P_i is computed as

$$GM_i = \tilde{G}\tilde{M}_i \frac{{t^*}^2}{{l^*}^3} \tag{2.36}$$

where l^* and t^*, as defined in Section 2.1.2, are the characteristic quantities computed for a reference CR3BP system. The reference CR3BP system is selected based on P_1 and P_2 in the point mass ephemeris model. However, it is important to note that $\tilde{M}_1$ is not assumed to be greater than $\tilde{M}_2$ in the ephemeris model; therefore, the order/numbering of these primary bodies in the reference

CR3BP system is established based on their masses as formulated in Section 2.1. Furthermore, l^* and t^* are used to nondimensionalize the position and velocity vectors of each body in the system. Finally, the resulting nondimensional equations of motion for P_3 relative to P_1 with respect to an inertial observer are defined as

$$\boldsymbol{r}_{\mathbf{1,3}}'' = \frac{-GM_1}{r_{1,3}^3}\boldsymbol{r}_{\mathbf{1,3}} + \sum_{i=2, i\neq 3}^{N} GM_i \left(\frac{\boldsymbol{r}_{\mathbf{3,}\boldsymbol{i}}}{r_{3,i}^3} - \frac{\boldsymbol{r}_{\mathbf{1,}\boldsymbol{i}}}{r_{1,i}^3} \right) \tag{2.37}$$

Thus far, the nondimensional equations of motion for P_3 relative to P_1 have been expressed independent of a coordinate system.

To compute the motion of P_3, Equation 2.37 is expressed in the Cartesian coordinates of a primary-centered inertial frame that uses the axes of the International Celestial Reference Frame (ICRF) [86]. The ICRF is an inertial frame with its origin placed at the barycenter of the solar system and its axes are computed based on the precise locations of a set of extragalactic radio sources [86]. A primary-centered inertial frame is then defined by using the center of a primary body and the axes of the ICRF. For the remainder of this work, assume the inertial frame $\mathcal{E}$ is aligned with the axes of the ICRF and its origin is shifted to the position of P_1. Therefore, the state of each body in the system is expressed relative to P_1. The nondimensional position of P_3 relative to P_1 in $\mathcal{E}$ is defined as

$${}^{\mathcal{E}}\boldsymbol{r}_{\mathbf{1,3}} = X\hat{\boldsymbol{X}}_{\boldsymbol{\mathcal{E}}} + Y\hat{\boldsymbol{Y}}_{\boldsymbol{\mathcal{E}}} + Z\hat{\boldsymbol{Z}}_{\boldsymbol{\mathcal{E}}} \tag{2.38}$$

and the nondimensional position of P_i relative to P_1 in $\mathcal{E}$ is defined as

$${}^{\mathcal{E}}\boldsymbol{r}_{\mathbf{1,}\boldsymbol{i}} = X_i\hat{\boldsymbol{X}}_{\boldsymbol{\mathcal{E}}} + Y_i\hat{\boldsymbol{Y}}_{\boldsymbol{\mathcal{E}}} + Z_i\hat{\boldsymbol{Z}}_{\boldsymbol{\mathcal{E}}} \tag{2.39}$$

where $\tilde{X}_i$, $\tilde{Y}_i$, and $\tilde{Z}_i$ are obtained at a given epoch and then nondimensionalized to obtain X_i, Y_i, and Z_i. In this work, the Development Ephemeris (DE) file DE421 is used in SPICE to retrieve the state of each desired celestial body at each epoch during numerical propagation [1, 2]. Finally, the nondimensional position of P_i relative to P_3 in $\mathcal{E}$ is computed as

$${}^{\mathcal{E}}\boldsymbol{r}_{\mathbf{3,}\boldsymbol{i}} = {}^{\mathcal{E}}\boldsymbol{r}_{\mathbf{1,}\boldsymbol{i}} - {}^{\mathcal{E}}\boldsymbol{r}_{\mathbf{1,3}} = (X_i - X)\hat{\boldsymbol{X}}_{\boldsymbol{\mathcal{E}}} + (Y_i - Y)\hat{\boldsymbol{Y}}_{\boldsymbol{\mathcal{E}}} + (Z_i - Z)\hat{\boldsymbol{Z}}_{\boldsymbol{\mathcal{E}}} \tag{2.40}$$

These relative position vectors are then used in the following set of nondimensional, scalar second-order ODEs expressed in the inertial frame $\mathcal{E}$:

$$\begin{aligned} X'' &= \frac{-GM_1}{r_{1,3}^3}X + \sum_{i=2,i\neq 3}^{N} GM_i\left(\frac{(X_i - X)}{r_{3,i}^3} - \frac{X_i}{r_{1,i}^3}\right) \\ Y'' &= \frac{-GM_1}{r_{1,3}^3}Y + \sum_{i=2,i\neq 3}^{N} GM_i\left(\frac{(Y_i - Y)}{r_{3,i}^3} - \frac{Y_i}{r_{1,i}^3}\right) \\ Z'' &= \frac{-GM_1}{r_{1,3}^3}Z + \sum_{i=2,i\neq 3}^{N} GM_i\left(\frac{(Z_i - Z)}{r_{3,i}^3} - \frac{Z_i}{r_{1,i}^3}\right) \end{aligned} \tag{2.41}$$

There is no generalized analytical solution for the motion of P_3 in a point mass ephemeris model; however, the motion of P_3 relative to P_1 may be computed in $\mathcal{E}$ via numerical propagation using Equation 2.41 and ephemerides given an initial state and epoch for P_3 [106]. In this work, a reference epoch is specified as a Gregorian calendar date in Coordinated Universal Time (UTC). SPICE is then used to convert the reference epoch from UTC into ephemeris time, equivalent to the seconds past the J2000 epoch and denoted as $\tilde{t}_{\mathrm{E}_{\mathrm{ref}}}$ [106, 76]; the J2000 epoch corresponds to January 1, 2000, at 12:00:00.000 Barycentric Dynamical Time (TDB). Therefore, the epoch corresponding to the nondimensional time t measured from the reference epoch is equal to

$$\tilde{t}_{\mathrm{E}} = \tilde{t}_{\mathrm{E}_{\mathrm{ref}}} + tt^* \tag{2.42}$$

which enables the state of each desired celestial body to be obtained using SPICE at each instance of t when propagating a trajectory in a point mass ephemeris model.

2.2.3 Jacobian Matrix

A Jacobian matrix is derived to characterize the first-order response of a point mass ephemeris model to perturbations in the phase space relative to a reference trajectory. The nondimensional inertial state vector of P_3 relative to P_1 expressed in $\mathcal{E}$ is defined as ${}^{\mathcal{E}}\boldsymbol{q}_{\boldsymbol{\mathcal{E}}} = [X, Y, Z, X', Y', Z']^{\mathrm{T}}$ where ${}^{\mathcal{E}}\boldsymbol{q}'_{\boldsymbol{\mathcal{E}}} = {}^{\mathcal{E}}\boldsymbol{f}(\boldsymbol{q}_{\boldsymbol{\mathcal{E}}}, t) = [X', Y', Z', X'', Y'', Z'']^{\mathrm{T}}$. Given the equations of motion for P_3 presented in Equation 2.41, the Jacobian is time-varying because the system is nonautonomous and is therefore

defined as

$$[\boldsymbol{A}(t)] = \begin{bmatrix} 0 & 0 & 0 & 1 & 0 & 0 \\ 0 & 0 & 0 & 0 & 1 & 0 \\ 0 & 0 & 0 & 0 & 0 & 1 \\ \frac{\partial X''}{\partial X} & \frac{\partial X''}{\partial Y} & \frac{\partial X''}{\partial Z} & 0 & 0 & 0 \\ \frac{\partial Y''}{\partial X} & \frac{\partial Y''}{\partial Y} & \frac{\partial Y''}{\partial Z} & 0 & 0 & 0 \\ \frac{\partial Z''}{\partial X} & \frac{\partial Z''}{\partial Y} & \frac{\partial Z''}{\partial Z} & 0 & 0 & 0 \end{bmatrix} \tag{2.43}$$

where

$$\begin{aligned} \frac{\partial X''}{\partial X} &= \frac{GM_1}{r_{1,3}^5}\left(3X^2 - r_{1,3}^2\right) + \sum_{i=2, i\neq 3}^{N} \frac{GM_i}{r_{3,i}^5}\left(3(X_i - X)^2 - r_{3,i}^2\right) \\ \frac{\partial Y''}{\partial Y} &= \frac{GM_1}{r_{1,3}^5}\left(3Y^2 - r_{1,3}^2\right) + \sum_{i=2, i\neq 3}^{N} \frac{GM_i}{r_{3,i}^5}\left(3(Y_i - Y)^2 - r_{3,i}^2\right) \\ \frac{\partial Z''}{\partial Z} &= \frac{GM_1}{r_{1,3}^5}\left(3Z^2 - r_{1,3}^2\right) + \sum_{i=2, i\neq 3}^{N} \frac{GM_i}{r_{3,i}^5}\left(3(Z_i - Z)^2 - r_{3,i}^2\right) \\ \frac{\partial X''}{\partial Y} &= \frac{\partial Y''}{\partial X} = \frac{3GM_1XY}{r_{1,3}^5} + \sum_{i=2, i\neq 3}^{N} \frac{3GM_i(X_i - X)(Y_i - Y)}{r_{3,i}^5} \\ \frac{\partial X''}{\partial Z} &= \frac{\partial Z''}{\partial X} = \frac{3GM_1XZ}{r_{1,3}^5} + \sum_{i=2, i\neq 3}^{N} \frac{3GM_i(X_i - X)(Z_i - Z)}{r_{3,i}^5} \\ \frac{\partial Y''}{\partial Z} &= \frac{\partial Z''}{\partial Y} = \frac{3GM_1YZ}{r_{1,3}^5} + \sum_{i=2, i\neq 3}^{N} \frac{3GM_i(Y_i - Y)(Z_i - Z)}{r_{3,i}^5} \end{aligned} \tag{2.44}$$

This definition of $[\boldsymbol{A}(t)]$ for a point mass ephemeris model (formulated with respect to an inertial observer fixed in $\mathcal{E}$) is used in subsequent chapters for differential corrections. Due to the nonautonomous structure of a point mass ephemeris model, the following partial derivatives of the equations of motion with respect to time are also used for differential corrections:

$$\begin{aligned} \frac{\partial X''}{\partial t} &= \sum_{i=2, i\neq 3}^{N} GM_i\left(\frac{X_i'}{r_{3,i}^3} - \frac{3(X_i - X)({}^{\mathcal{E}}\boldsymbol{r}_{\boldsymbol{3,i}}^{\mathrm{T}}\,{}^{\mathcal{E}}\boldsymbol{r}_{\boldsymbol{1,i}}')}{r_{3,i}^5} - \frac{X_i'}{r_{1,i}^3} + \frac{3X_i({}^{\mathcal{E}}\boldsymbol{r}_{\boldsymbol{1,i}}^{\mathrm{T}}\,{}^{\mathcal{E}}\boldsymbol{r}_{\boldsymbol{1,i}}')}{r_{1,i}^5}\right) \\ \frac{\partial Y''}{\partial t} &= \sum_{i=2, i\neq 3}^{N} GM_i\left(\frac{Y_i'}{r_{3,i}^3} - \frac{3(Y_i - Y)({}^{\mathcal{E}}\boldsymbol{r}_{\boldsymbol{3,i}}^{\mathrm{T}}\,{}^{\mathcal{E}}\boldsymbol{r}_{\boldsymbol{1,i}}')}{r_{3,i}^5} - \frac{Y_i'}{r_{1,i}^3} + \frac{3Y_i({}^{\mathcal{E}}\boldsymbol{r}_{\boldsymbol{1,i}}^{\mathrm{T}}\,{}^{\mathcal{E}}\boldsymbol{r}_{\boldsymbol{1,i}}')}{r_{1,i}^5}\right) \\ \frac{\partial Z''}{\partial t} &= \sum_{i=2, i\neq 3}^{N} GM_i\left(\frac{Z_i'}{r_{3,i}^3} - \frac{3(Z_i - Z)({}^{\mathcal{E}}\boldsymbol{r}_{\boldsymbol{3,i}}^{\mathrm{T}}\,{}^{\mathcal{E}}\boldsymbol{r}_{\boldsymbol{1,i}}')}{r_{3,i}^5} - \frac{Z_i'}{r_{1,i}^3} + \frac{3Z_i({}^{\mathcal{E}}\boldsymbol{r}_{\boldsymbol{1,i}}^{\mathrm{T}}\,{}^{\mathcal{E}}\boldsymbol{r}_{\boldsymbol{1,i}}')}{r_{1,i}^5}\right) \end{aligned} \tag{2.45}$$

2.3 Reference Frame Transformations

Examining the motion of a spacecraft with respect to different reference frames provides various perspectives on the behavior and properties of a trajectory [101, 61]. For example, in the CR3BP, the inertial frame is particularly useful for understanding the motion of all three bodies in the system as an explicit function of time. On the other hand, the rotating frame is used to effectively visualize the motion of P_3 relative to P_1 and P_2 which are fixed in $\mathcal{R}$. Therefore, the rotating frame is particularly useful for identifying conjunctions with the P_1-P_2 line, eclipses, resonances, and particular solution geometries that are not easily identified in the inertial frame [101, 61]. Given the utility of analyzing trajectories in both an inertial frame and a rotating frame, this section provides an overview of the reference frame transformations used in this work for trajectories generated in the CR3BP and a point mass ephemeris model.

2.3.1 Transformations between an Inertial Frame and a Rotating Frame

In this subsection, transformations of a state vector are derived between a general inertial frame and a general rotating frame. Assume a general inertial frame is defined as $\mathcal{A}$ with axes $\{\hat{\boldsymbol{a}}_1, \hat{\boldsymbol{a}}_2, \hat{\boldsymbol{a}}_3\}$ and a general rotating frame is defined as $\mathcal{B}$ with axes $\{\hat{\boldsymbol{b}}_1, \hat{\boldsymbol{b}}_2, \hat{\boldsymbol{b}}_3\}$. Given these definitions, a rotation matrix constructed between $\mathcal{A}$ and $\mathcal{B}$ may be defined as

$$\left[\boldsymbol{C}^{\mathcal{AB}}\right] = \begin{bmatrix} {}^{\mathcal{A}}\hat{\boldsymbol{b}}_1 & {}^{\mathcal{A}}\hat{\boldsymbol{b}}_2 & {}^{\mathcal{A}}\hat{\boldsymbol{b}}_3 \end{bmatrix} \tag{2.46}$$

where each axis of $\mathcal{B}$ is expressed in the coordinates of $\mathcal{A}$ [93]. Then, the position and velocity of an arbitrary object with respect to a rotating observer fixed in $\mathcal{B}$ are defined as $\boldsymbol{r}$ and $\dot{\boldsymbol{r}}$, respectively. Applying transport theorem, the transformation of a rotating state vector expressed in $\mathcal{B}$ into the corresponding inertial state vector expressed in $\mathcal{A}$ is defined as

$$\begin{aligned} {}^{\mathcal{A}}\boldsymbol{r} &= \left[\boldsymbol{C}^{\mathcal{AB}}\right] {}^{\mathcal{B}}\boldsymbol{r} \\ {}^{\mathcal{A}}\boldsymbol{r}' &= \left[\boldsymbol{C}^{\mathcal{AB}}\right]\left[{}^{\mathcal{B}}\boldsymbol{\omega}_{\mathcal{B}/\mathcal{A}}\right]_{\mathrm{x}} {}^{\mathcal{B}}\boldsymbol{r} + \left[\boldsymbol{C}^{\mathcal{AB}}\right] {}^{\mathcal{B}}\dot{\boldsymbol{r}} = \left[\dot{\boldsymbol{C}}^{\mathcal{AB}}\right] {}^{\mathcal{B}}\boldsymbol{r} + \left[\boldsymbol{C}^{\mathcal{AB}}\right] {}^{\mathcal{B}}\dot{\boldsymbol{r}} \end{aligned} \tag{2.47}$$

where $[\cdot]_{\mathrm{x}}$ denotes a skew-symmetric matrix computed from the provided vector, $\left[{}^{\mathcal{B}}\boldsymbol{\omega}_{\mathcal{B}/\mathcal{A}}\right]_{\mathrm{x}} {}^{\mathcal{B}}\boldsymbol{r} = {}^{\mathcal{B}}\boldsymbol{\omega}_{\mathcal{B}/\mathcal{A}} \times {}^{\mathcal{B}}\boldsymbol{r}$, and $\left[\dot{\boldsymbol{C}}^{\mathcal{AB}}\right] = \left[\boldsymbol{C}^{\mathcal{AB}}\right]\left[{}^{\mathcal{B}}\boldsymbol{\omega}_{\mathcal{B}/\mathcal{A}}\right]_{\mathrm{x}}$ [119, 93, 26]. This system of equations may be

rewritten in matrix form as

$$\begin{bmatrix} {}^{\mathcal{A}}\boldsymbol{r} \\ {}^{\mathcal{A}}\boldsymbol{r}' \end{bmatrix} = \begin{bmatrix} \left[\boldsymbol{C}^{\mathcal{AB}}\right] & [\boldsymbol{0}_{3\times3}] \\ \left[\dot{\boldsymbol{C}}^{\mathcal{AB}}\right] & \left[\boldsymbol{C}^{\mathcal{AB}}\right] \end{bmatrix} \begin{bmatrix} {}^{\mathcal{B}}\boldsymbol{r} \\ {}^{\mathcal{B}}\dot{\boldsymbol{r}} \end{bmatrix} \tag{2.48}$$

and, similarly, the inverse transformation is defined as

$$\begin{bmatrix} {}^{\mathcal{B}}\boldsymbol{r} \\ {}^{\mathcal{B}}\dot{\boldsymbol{r}} \end{bmatrix} = \begin{bmatrix} \left[\boldsymbol{C}^{\mathcal{AB}}\right]^{\mathrm{T}} & [\boldsymbol{0}_{3\times3}] \\ \left[\dot{\boldsymbol{C}}^{\mathcal{AB}}\right]^{\mathrm{T}} & \left[\boldsymbol{C}^{\mathcal{AB}}\right]^{\mathrm{T}} \end{bmatrix} \begin{bmatrix} {}^{\mathcal{A}}\boldsymbol{r} \\ {}^{\mathcal{A}}\boldsymbol{r}' \end{bmatrix} \tag{2.49}$$

These expressions provide simple equations to convert between a rotating state vector expressed in a general rotating frame and the corresponding inertial state vector expressed in a general inertial frame.

2.3.2 Transformations in the CR3BP

The inertial frame $\mathcal{I}$ and the rotating frame $\mathcal{R}$ are the primary frames of interest in the CR3BP. In this work, trajectories in the CR3BP are computed and analyzed in $\mathcal{R}$ using Equation 2.21 and then, if applicable, transformed into $\mathcal{I}$ to study the resulting motion with respect to an inertial observer. The nondimensional rotating state vector of P_3 expressed in $\mathcal{R}$ is defined as

$${}^{\mathcal{R}}\boldsymbol{q} = \begin{bmatrix} {}^{\mathcal{R}}\boldsymbol{r_3} \\ {}^{\mathcal{R}}\dot{\boldsymbol{r}}_{\boldsymbol{3}} \end{bmatrix} \tag{2.50}$$

and the nondimensional inertial state vector of P_3 expressed in $\mathcal{I}$ is defined as

$${}^{\mathcal{I}}\boldsymbol{q_{\mathcal{I}}} = \begin{bmatrix} {}^{\mathcal{I}}\boldsymbol{r_3} \\ {}^{\mathcal{I}}\boldsymbol{r}_{\boldsymbol{3}}' \end{bmatrix} \tag{2.51}$$

Furthermore, $\left[\boldsymbol{C}^{\mathcal{IR}}\right]$ is defined as

$$\left[\boldsymbol{C}^{\mathcal{IR}}\right] = \left[\boldsymbol{C}^{\mathcal{RI}}\right]^{\mathrm{T}} = \begin{bmatrix} {}^{\mathcal{I}}\hat{\boldsymbol{x}} & {}^{\mathcal{I}}\hat{\boldsymbol{y}} & {}^{\mathcal{I}}\hat{\boldsymbol{z}} \end{bmatrix} = \begin{bmatrix} cos(\theta) & -sin(\theta) & 0 \\ sin(\theta) & cos(\theta) & 0 \\ 0 & 0 & 1 \end{bmatrix} \tag{2.52}$$

from Equation 2.17 and ${}^{\mathcal{R}}\boldsymbol{\omega}_{\boldsymbol{\mathcal{R}/\mathcal{I}}} = 1\hat{\boldsymbol{z}}$ as defined in Section 2.1.2. Finally, recall that $\theta = nt + \theta_0$ where $n = 1$. Using these definitions in Equations 2.48 and 2.49, the procedures for computing the reference frame transformations between $\mathcal{R}$ and $\mathcal{I}$ in the CR3BP are summarized as follows:

Rotating to Inertial Frame

Given: A nondimensional trajectory in $\mathcal{R}$ defined relative to the origin of $\mathcal{R}$ from an initial time, t_1, to a final time, t_2.

(1) Define θ_0 and select a center point fixed in $\mathcal{R}$ (e.g., the origin of $\mathcal{R}$, P_1, P_2).

(2) Shift the position of each state along the trajectory such that it is defined with respect to the position of the selected center point in $\mathcal{R}$.

(3) For each value of $t \in [t_1, t_2]$:

   (a) Compute $\left[\boldsymbol{C}^{\mathcal{IR}}\right]$ and $\left[\dot{\boldsymbol{C}}^{\mathcal{IR}}\right]$.

   (b) Use Equation 2.48 to transform the shifted state at t from $\mathcal{R}$ to $\mathcal{I}$.

Inertial to Rotating Frame

Given: A nondimensional trajectory in $\mathcal{I}$ defined relative to the origin of $\mathcal{I}$ from an initial time, t_1, to a final time, t_2.

(1) Define θ_0 and select a center point fixed in $\mathcal{R}$ (e.g., the origin of $\mathcal{R}$, P_1, P_2).

(2) For each value of $t \in [t_1, t_2]$:

   (a) Compute $\left[\boldsymbol{C}^{\mathcal{IR}}\right]$ and $\left[\dot{\boldsymbol{C}}^{\mathcal{IR}}\right]$.

   (b) Use Equation 2.49 to transform the state at t from $\mathcal{I}$ to $\mathcal{R}$.

(3) Shift the position of each transformed state along the trajectory such that it is defined with respect to the position of the selected center point in $\mathcal{R}$.

2.3.3 Transformations in a Point Mass Ephemeris Model

The inertial frame $\mathcal{E}$ and the rotating frame $\mathcal{R}$ are the primary frames of interest in a point mass ephemeris model. In this work, trajectories in a point mass ephemeris model are computed in $\mathcal{E}$ using Equation 2.41; in addition, $\mathcal{R}$ is used when transitioning a trajectory from the CR3BP

into an ephemeris model and when comparing trajectories computed in each dynamical model. The axes of $\mathcal{E}$ are aligned with the axes of the ICRF and its origin is shifted to the position of P_1 while $\mathcal{R}$ is defined instantaneously at a given epoch based on the reference CR3BP system. Recall from Section 2.2.2, the reference CR3BP system is selected based on the masses of the central and secondary primary bodies in the point mass ephemeris model. To avoid confusion between the ephemeris model and the reference CR3BP system, P_1 and P_2 for the reference CR3BP system are instead denoted as P_A and P_B, respectively. Therefore, the axes of $\mathcal{R}$ are defined instantaneously at a given epoch as

$$\begin{aligned} \hat{\boldsymbol{x}} &= \hat{\tilde{\boldsymbol{r}}}_{\mathbf{A,B}} \\ \hat{\boldsymbol{z}} &= \hat{\tilde{\boldsymbol{h}}}_{\mathbf{A,B}} = \frac{\tilde{\boldsymbol{r}}_{\mathbf{A,B}} \times \tilde{\boldsymbol{r}}'_{\mathbf{A,B}}}{||\tilde{\boldsymbol{r}}_{\mathbf{A,B}} \times \tilde{\boldsymbol{r}}'_{\mathbf{A,B}}||} \\ \hat{\boldsymbol{y}} &= \hat{\boldsymbol{z}} \times \hat{\boldsymbol{x}} \end{aligned} \tag{2.53}$$

where $\tilde{\boldsymbol{r}}_{\mathbf{A,B}}$ is the position vector from P_A to P_B and $\tilde{\boldsymbol{h}}_{\mathbf{A,B}}$ is the orbital angular momentum vector of P_B about P_A. Using these definitions, reference frame transformations between $\mathcal{R}$ and $\mathcal{E}$ are defined.

The procedures for computing the reference frame transformations between $\mathcal{R}$ and $\mathcal{E}$ are formulated for a point mass ephemeris model. The nondimensional rotating state vector of P_3 relative to the origin of $\mathcal{R}$ and expressed in $\mathcal{R}$ is defined in Equation 2.50. The nondimensional inertial state vector of P_3 relative to P_1 and expressed in $\mathcal{E}$ is defined as

$${}^{\mathcal{E}}\boldsymbol{q}_{\boldsymbol{\mathcal{E}}} = \begin{bmatrix} {}^{\mathcal{E}}\boldsymbol{r}_{\mathbf{1,3}} \\ {}^{\mathcal{E}}\boldsymbol{r}'_{\mathbf{1,3}} \end{bmatrix} \tag{2.54}$$

Furthermore, $\left[\boldsymbol{C}^{\boldsymbol{\mathcal{E}\mathcal{R}}}\right]$ is defined instantaneously at a given epoch using Equation 2.53 as

$$\left[\boldsymbol{C}^{\boldsymbol{\mathcal{E}\mathcal{R}}}\right] = \begin{bmatrix} {}^{\mathcal{E}}\hat{\boldsymbol{x}} & {}^{\mathcal{E}}\hat{\boldsymbol{y}} & {}^{\mathcal{E}}\hat{\boldsymbol{z}} \end{bmatrix} \tag{2.55}$$

Finally, the instantaneous dimensional angular velocity of $\mathcal{R}$ with respect to $\mathcal{E}$ expressed in $\mathcal{R}$ is defined as

$${}^{\mathcal{R}}\tilde{\boldsymbol{\omega}}_{\boldsymbol{\mathcal{R}/\mathcal{E}}} = \frac{||\tilde{\boldsymbol{r}}_{\mathbf{A,B}} \times \tilde{\boldsymbol{r}}'_{\mathbf{A,B}}||}{\tilde{r}^2_{\mathrm{A,B}}} \hat{\boldsymbol{z}} \tag{2.56}$$

[106]. The motion of P_{A} and P_{B} is not assumed to be circular in an ephemeris model and therefore ${}^{\mathcal{R}}\tilde{\boldsymbol{\omega}}_{\boldsymbol{\mathcal{R}}/\boldsymbol{\mathcal{E}}}$ is not constant and must be recalculated at each epoch. It is also important to note that dimensional vectors are utilized in the computation of both $\left[\boldsymbol{C}^{\boldsymbol{\mathcal{E}\mathcal{R}}}\right]$ and ${}^{\mathcal{R}}\tilde{\boldsymbol{\omega}}_{\boldsymbol{\mathcal{R}}/\boldsymbol{\mathcal{E}}}$ due to the instantaneous definition of $\mathcal{R}$ at each epoch. Using these definitions in Equations 2.48 and 2.49, the procedures for computing the reference frame transformations between $\mathcal{R}$ and $\mathcal{E}$ in a point mass ephemeris model are summarized as follows:

Rotating Frame to Primary-Centered Inertial Frame

Given: A nondimensional trajectory in $\mathcal{R}$ defined relative to the origin of $\mathcal{R}$ from an initial epoch, $\tilde{t}_{\mathrm{E}_1}$, to a final epoch, $\tilde{t}_{\mathrm{E}_2}$.

(1) Shift the position of each state along the trajectory such that it is defined with respect to the position of P_1 in $\mathcal{R}$. Note: If $\tilde{M}_1 \geq \tilde{M}_2$, P_1 corresponds to P_{A} in the reference CR3BP system; otherwise, P_1 corresponds to P_{B}.

(2) For each value of $\tilde{t}_{\mathrm{E}} \in [\tilde{t}_{\mathrm{E}_1}, \tilde{t}_{\mathrm{E}_2}]$:

   (a) Compute the instantaneous characteristic quantities for the reference CR3BP system and dimensionalize the shifted state at $\tilde{t}_{\mathrm{E}}$.

   (b) Compute $\left[\boldsymbol{C}^{\boldsymbol{\mathcal{E}\mathcal{R}}}\right]$ and $\left[\dot{\boldsymbol{C}}^{\boldsymbol{\mathcal{E}\mathcal{R}}}\right]$.

   (c) Use Equation 2.48 to transform the dimensional shifted state at $\tilde{t}_{\mathrm{E}}$ from $\mathcal{R}$ to $\mathcal{E}$.

(3) Nondimensionalize each transformed shifted state along the trajectory using the characteristic quantities for the reference CR3BP system. Note: The characteristic quantities used in this step are the constant quantities computed for the reference CR3BP system, i.e., not instantaneous values computed based on epoch.

Primary-Centered Inertial Frame to Rotating Frame

Given: A nondimensional trajectory in $\mathcal{E}$ defined relative to the origin of $\mathcal{E}$ from an initial epoch, $\tilde{t}_{\mathrm{E}_1}$, to a final epoch, $\tilde{t}_{\mathrm{E}_2}$.

(1) Dimensionalize each state along the trajectory using the characteristic quantities for the reference CR3BP system. Note: The characteristic quantities used in this step are the constant quantities computed for the reference CR3BP system, i.e., not instantaneous values computed based on epoch.

(2) For each value of $\tilde{t}_{\mathrm{E}} \in [\tilde{t}_{\mathrm{E}_1}, \tilde{t}_{\mathrm{E}_2}]$:

   (a) Compute $\left[\boldsymbol{C}^{\mathcal{ER}}\right]$ and $\left[\dot{\boldsymbol{C}}^{\mathcal{ER}}\right]$.

   (b) Use Equation 2.49 to transform the dimensional state at $\tilde{t}_{\mathrm{E}}$ from $\mathcal{E}$ to $\mathcal{R}$.

   (c) Compute the instantaneous characteristic quantities for the reference CR3BP system and nondimensionalize the transformed state at $\tilde{t}_{\mathrm{E}}$.

(3) Shift the position of each nondimensional transformed state along the trajectory such that it is defined with respect to the origin of $\mathcal{R}$. Note: If $\tilde{M}_1 \geq \tilde{M}_2$, P_1 corresponds to P_{A} in the reference CR3BP system; otherwise, P_1 corresponds to P_{B}.

2.4 Numerical Propagation

Trajectories for a spacecraft in the CR3BP and a point mass ephemeris model are computed using numerical propagation due to the lack of generalized analytical solutions [101, 61]. Given an initial condition, the equations of motion for a spacecraft derived in the CR3BP and in an ephemeris model in Sections 2.1 and 2.2, respectively, each define an initial value problem. In this work, MATLAB® is used as the main computing platform for numerical analysis [69]. However, the GNU Scientific Library (GSL) is used in C++ and interfaced with MATLAB® to solve the initial value problem for each dynamical model and numerically propagate trajectories [88]. In GSL, the Runge-Kutta Prince-Dormand 8/9 method is used for explicit numerical integration with a relative tolerance of 10^{-13} and an absolute tolerance of 10^{-14}.

Note:

In this work, trajectories in the CR3BP are computed with respect to a rotating observer fixed in $\mathcal{R}$ as previously discussed in this chapter. When applicable, trajectories are transformed from

$\mathcal{R}$ into $\mathcal{I}$ for visual evaluation. Therefore, in all subsequent chapters, assume all vectors associated with trajectory analysis in the CR3BP are expressed in $\mathcal{R}$ unless stated otherwise. Similarly, in all subsequent chapters, assume all vectors associated with trajectory analysis in a point mass ephemeris model are expressed in $\mathcal{E}$ unless stated otherwise. Given these assumptions, the left superscript notation introduced in this chapter to denote the Cartesian coordinate system in which a vector is expressed is omitted from subsequent chapters to simplify notation. Table 2.2 provides a summary of this note for each dynamical model.

Table 2.2: Notation used for each dynamical model throughout the remainder of the dissertation, unless stated otherwise.

Dynamical Model	State	Equations of Motion
CR3BP	$\boldsymbol{q} = [x, y, z, \dot{x}, \dot{y}, \dot{z}]^{\mathrm{T}}$	$\dot{\boldsymbol{q}} = \boldsymbol{f}(\boldsymbol{q}) = [\dot{x}, \dot{y}, \dot{z}, \ddot{x}, \ddot{y}, \ddot{z}]^{\mathrm{T}}$
Ephemeris	$\boldsymbol{q}_{\mathcal{E}} = \left[X, Y, Z, X', Y', Z'\right]^{\mathrm{T}}$	$\boldsymbol{q}'_{\mathcal{E}} = \boldsymbol{f}(\boldsymbol{q}_{\mathcal{E}}, t) = \left[X', Y', Z', X'', Y'', Z''\right]^{\mathrm{T}}$

Chapter 3

Fundamental Solutions in the CR3BP

Fundamental solutions in the CR3BP often support the construction of initial guesses for complex trajectories in a chaotic multi-body gravitational environment. The CR3BP admits a variety of fundamental dynamical structures, such as equilibrium points, periodic orbits, quasi-periodic orbits, and hyperbolic invariant manifolds [101, 61]. In the CR3BP, the stability of each equilibrium point supplies insight into the behavior of the nearby flow that may be leveraged in trajectory design. For instance, periodic and quasi-periodic orbits centered around equilibrium points support identifying candidates for mission and staging orbits whereas their hyperbolic invariant manifolds may approximate natural transport mechanisms throughout the system [61, 32, 50]. Due to the lack of generalized analytical solutions, numerical methods are employed to compute and analyze these types of motion. This chapter presents a detailed overview of the methods used to compute the equilibrium points, periodic orbit families, and hyperbolic invariant manifolds associated with periodic orbits in the CR3BP; each fundamental type of solution is leveraged in this work to inform the primitive-based trajectory design framework.

3.1 First-Order Variational Equations of Motion

Studying the global behavior of motion in a nonlinear dynamical system is often complex and challenging, particularly in the absence of a generalized analytical solution [85, 101, 61]. Therefore, a common analysis technique is to linearize the nonlinear dynamics about a reference solution to study the behavior of motion in the local vicinity of the solution [85]. In this section, the first-order variational equations of motion are derived in the CR3BP. Consider a reference trajectory denoted as $\boldsymbol{q}^*(t)$ where the nonlinear equations of motion in the CR3BP are denoted as $\dot{\boldsymbol{q}} = \boldsymbol{f}(\boldsymbol{q})$. The first-order Taylor series expansion of $\boldsymbol{f}(\boldsymbol{q})$ about $\boldsymbol{q}^*(t)$ is defined as

$$\dot{\boldsymbol{q}}(t) \approx \dot{\boldsymbol{q}}^*(t) + \left.\frac{\partial \boldsymbol{f}(\boldsymbol{q})}{\partial \boldsymbol{q}}\right|_{\boldsymbol{q}^*(t)} (\boldsymbol{q}(t) - \boldsymbol{q}^*(t)) \tag{3.1}$$

where $\boldsymbol{q}(t) = \boldsymbol{q}^*(t) + \boldsymbol{\delta q}(t)$ and higher-order terms are ignored because $\boldsymbol{\delta q}(t)$ is assumed to be a small perturbation relative to the reference trajectory at each instance of t [85]. This expression simplifies to

$$\boldsymbol{\delta}\dot{\boldsymbol{q}}(t) \approx [\boldsymbol{A}]\big|_{\boldsymbol{q}^*(t)} \boldsymbol{\delta q}(t) \tag{3.2}$$

where $[\boldsymbol{A}]$ is the Jacobian matrix of the dynamics defined in Section 2.1.5. Therefore, Equation 3.2 produces the first-order variational equations of motion in the CR3BP about a reference trajectory.

The first-order variational equations of motion are a linear approximation of the evolution of a perturbation applied to a reference trajectory [85, 61]. From the fundamental theorem for linear systems, the solution to Equation 3.2 is defined as

$$\boldsymbol{\delta q}(t) = [\boldsymbol{\Phi}(t, t_1)]\boldsymbol{\delta q}(t_1) \tag{3.3}$$

where $[\boldsymbol{\Phi}(t, t_1)]$ is referred to as the state transition matrix (STM), a linear mapping from a perturbation at time t_1 to a perturbation at time t relative to the reference trajectory [85, 61]. Using Equations 3.2 and 3.3, the evolution of the STM is derived as

$$\left[\dot{\boldsymbol{\Phi}}(t, t_1)\right] = [\boldsymbol{A}]\big|_{\boldsymbol{q}^*(t)} [\boldsymbol{\Phi}(t, t_1)] \quad \text{s.t.} \quad [\boldsymbol{\Phi}(t_1, t_1)] = [\boldsymbol{I}] \tag{3.4}$$

where $[\boldsymbol{I}]$ is the identity matrix with the same shape as the STM. Therefore, the evolution of the STM is governed by $[\boldsymbol{A}]$ evaluated along the reference trajectory and may be numerically

propagated from t_1 to t given its initial condition as the identity matrix at t_1 [85, 61]. Finally, the STM admits a variety of useful properties, such as

$$\begin{aligned}[\boldsymbol{\Phi}(t_1, t_2)] &= [\boldsymbol{\Phi}(t_2, t_1)]^{-1} \\ [\boldsymbol{\Phi}(t_3, t_1)] &= [\boldsymbol{\Phi}(t_3, t_2)][\boldsymbol{\Phi}(t_2, t_1)]\end{aligned} \tag{3.5}$$

which hold for any instances of t [61]. The results for the first-order variational equations of motion presented in this section provide a foundation for analyzing motion in the local vicinity of fundamental solutions in the CR3BP.

3.2 Equilibrium Points

3.2.1 Location of the Equilibrium Points

There are five equilibrium points in the CR3BP when formulated in the rotating frame; the equilibrium points are commonly referred to as libration or Lagrange points and denoted as L_i for $i \in [1, 5]$ [101, 61]. In an autonomous dynamical system, an equilibrium point is a stationary state in the system such that the time derivative of the state is equal to the zero vector [85]. Consequently, an object placed at an equilibrium point will remain at that point for all time unless an external perturbation is applied. In the CR3BP, defining the equations of motion for P_3 with respect to a rotating observer results in an autonomous system. Therefore, $\boldsymbol{q}^*$ is an equilibrium point in the CR3BP if $\boldsymbol{f}(\boldsymbol{q}^*) = \boldsymbol{0}$. Applying these conditions to the equations of motion for P_3, as defined in Equation 2.21, results in the following system of equations:

$$\begin{aligned}\ddot{x} &= \frac{\partial U^*}{\partial x} = x - \frac{(1-\mu)(x+\mu)}{r_{1,3}^3} - \frac{\mu(x-1+\mu)}{r_{2,3}^3} = 0 \\ \ddot{y} &= \frac{\partial U^*}{\partial y} = y - \frac{(1-\mu)y}{r_{1,3}^3} - \frac{\mu y}{r_{2,3}^3} = 0 \\ \ddot{z} &= \frac{\partial U^*}{\partial z} = -\frac{(1-\mu)z}{r_{1,3}^3} - \frac{\mu z}{r_{2,3}^3} = 0\end{aligned} \tag{3.6}$$

By inspection, $z = 0$ must be true for all L_i in order for the condition $\ddot{z} = 0$ to hold. Therefore, all five libration points are located in the xy-plane of $\mathcal{R}$ and Equation 3.6 may be rewritten as

$$\begin{aligned} x - \frac{(1-\mu)(x+\mu)}{r_{1,3}^3} - \frac{\mu(x-1+\mu)}{r_{2,3}^3} &= 0 \\ y\left(1 - \frac{(1-\mu)}{r_{1,3}^3} - \frac{\mu}{r_{2,3}^3}\right) &= 0 \end{aligned} \tag{3.7}$$

This resulting system of equations may then be used to solve for the x and y coordinates of each L_i by evaluating two different cases: $y = 0$ and $y \neq 0$.

The first three libration points (L_1, L_2, L_3) are computed for the case where $y = 0$ and referred to as the collinear libration points. Assuming $y = 0$, Equation 3.7 is simplified as

$$f(x) = x - \frac{(1-\mu)(x+\mu)}{((x+\mu)^2)^{\frac{3}{2}}} - \frac{\mu(x-1+\mu)}{((x-1+\mu)^2)^{\frac{3}{2}}} = 0 \tag{3.8}$$

where the roots of $f(x)$ correspond to the x coordinates of L_1, L_2, and L_3. Due to the complexity of $f(x)$, Newton's method is employed to solve for the roots of this function. Given an initial guess $x = x_1$, Newton's method is a numerical root-finding algorithm that iteratively updates the value of x until the condition $f(x) = 0$ is satisfied to within a desired numerical tolerance [106]. The update equation used in Newton's method is defined as

$$x_{i+1} = x_i - f(x_i)\left(\frac{df(x)}{dx}\bigg|_{x_i}\right)^{-1} \tag{3.9}$$

where x_i is the current value of x and x_{i+1} is the updated value of x for the next iteration of the algorithm. Based on the geometry of the CR3BP in the rotating frame, there are three regions to consider along $\hat{\boldsymbol{x}}$: Region 1 where $-\mu < x < 1-\mu$, Region 2 where $x > 1-\mu$, and Region 3 where $x < -\mu$ [101]. Therefore, Newton's method may be applied to Equation 3.8 by initializing x within Region 1, 2, or 3 to compute the x-coordinate of L_1, L_2, or L_3, respectively. Table 3.1 lists the computed x-coordinate of each collinear libration point in the Earth-Moon CR3BP; furthermore, Figure 3.1 displays each collinear libration point as a red diamond in $\mathcal{R}$ for the Earth-Moon CR3BP. The Earth and Moon are displayed as gray circles and plotted to scale.

The final two libration points (L_4, L_5) are computed for the case where $y \neq 0$ and referred to as the triangular or equilateral libration points. In this case, the system of equations presented

Table 3.1: x-coordinate of each libration point in the Earth-Moon CR3BP.

Libration Point	Earth-Moon
	x
L_1	0.836915127047076
L_2	1.155682164448510
L_3	-1.005062645702342
L_4/L_5	0.487849414649438

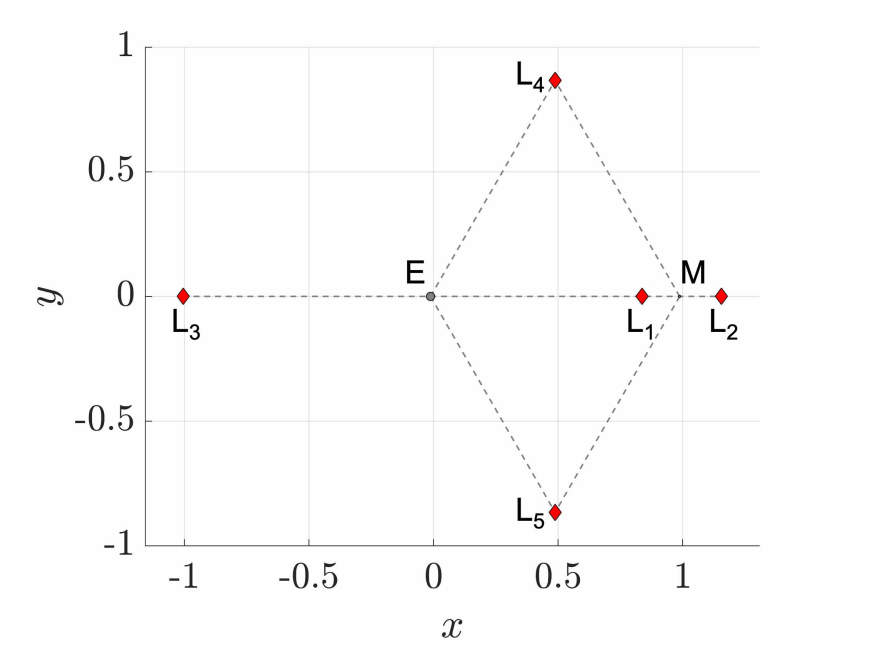

Figure 3.1: Locations of the libration points in $\mathcal{R}$ for the Earth-Moon CR3BP.

in Equation 3.7 may be rewritten as

$$\begin{aligned} x\left(1-\frac{(1-\mu)}{r_{1,3}^3}-\frac{\mu}{r_{2,3}^3}\right)-\frac{\mu(1-\mu)}{r_{1,3}^3}+\frac{\mu(1-\mu)}{r_{2,3}^3}=0 \\ y\left(1-\frac{(1-\mu)}{r_{1,3}^3}-\frac{\mu}{r_{2,3}^3}\right)=0 \end{aligned} \tag{3.10}$$

By inspection, this system of equations is satisfied when $r_{1,3} = r_{2,3} = 1$. The nondimensional distance between P_1 and P_2 in the CR3BP is also equal to unity. Therefore, the configuration of P_1, P_2, and P_3 forms an equilateral triangle at each triangular libration point. Given this condition

and the fixed positions of P_1 and P_2 in $\mathcal{R}$, $x = 0.5 - \mu$ for both L_4 and L_5, $y = \sqrt{3}/2$ for L_4, and $y = -\sqrt{3}/2$ for L_5. Table 3.1 lists the computed x-coordinate of the triangular libration points in the Earth-Moon CR3BP; furthermore, Figure 3.1 displays each triangular libration point as a red diamond in $\mathcal{R}$ for the Earth-Moon CR3BP.

Examining the ZVSs in relation to the libration points of the CR3BP provides insight into the allowable regions of motion in $\mathcal{R}$ within different energy regimes [101, 61]. The Jacobi constant at each libration point is denoted as $C_{J_{L_i}}$ where $C_{J_{L_1}} > C_{J_{L_2}} > C_{J_{L_3}} > C_{J_{L_{4/5}}}$ [61]. As discussed in Section 2.1.4, examining the ZVSs in the CR3BP at distinct values of C_J provides critical insight into the constraints on the natural motion of P_3 in $\mathcal{R}$. Figure 3.2 displays the evolution of the ZVCs in the xy-plane of $\mathcal{R}$ computed in the Earth-Moon CR3BP at various values of C_J; the Earth and Moon are plotted to scale and forbidden regions of motion are colored in gray. When $C_J > C_{J_{L_1}}$, P_3 is not able to naturally transfer between the vicinity of P_1 and P_2 as evident from the forbidden regions of motion displayed in Figure 3.2a at $C_J = 3.2500$ in the Earth-Moon system [61]. However, the allowable regions of motion around P_1 and P_2 increase in size as C_J is decreased and eventually intersect at L_1 when $C_J = C_{J_{L_1}}$; this region is often referred to as the L_1 gateway [61]. An example where the L_1 gateway is open is displayed in Figure 3.2b at $C_J = 3.1780$ in the Earth-Moon system. In this regime, P_3 is able to naturally transfer between the two primary bodies via the L_1 gateway. As C_J is decreased further, the L_2 gateway is formed at $C_J = C_{J_{L_2}}$ and then the L_3 gateway is formed at $C_J = C_{J_{L_3}}$ [61]. In Figure 3.2c, P_3 may depart the vicinity of both primary bodies through the L_2 gateway; however, in Figure 3.2d, P_3 may depart the vicinity of both primary bodies through either the L_2 or L_3 gateway. Finally, as C_J is decreased even further, the forbidden regions of motion continue to shrink in the xy-plane of $\mathcal{R}$ and coalesce at L_4/L_5 when $C_J = C_{J_{L_{4/5}}}$ [61]. The motion of P_3 is then unconstrained in the xy-plane of $\mathcal{R}$ when $C_J < C_{J_{L_{4/5}}}$ but its out-of-plane motion is still constrained. This qualitative analysis of the ZVSs in relation to the libration points of the CR3BP provides information about the energy regimes in which natural trajectories are bounded in the vicinity of a primary body, may transfer between the vicinity of P_1 and P_2, or may depart the vicinity of both primary bodies [61].

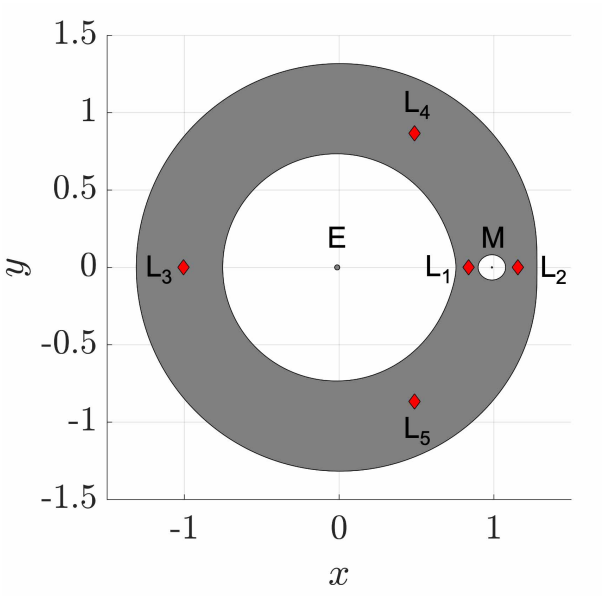

(a) $C_J = 3.2500 > C_{J_{L_1}}$

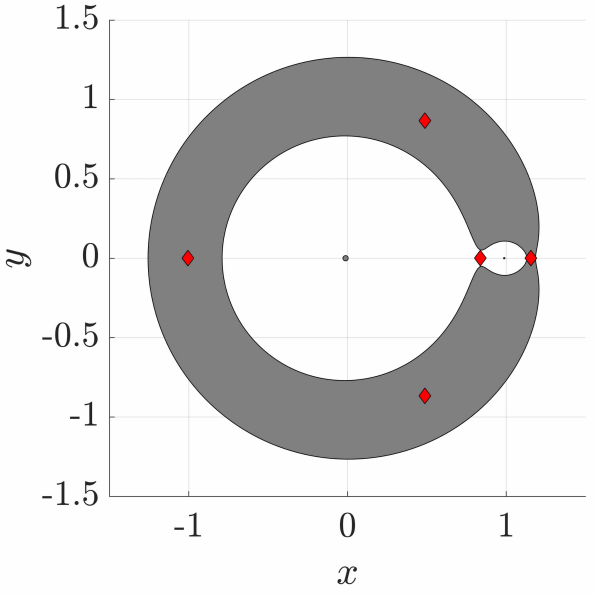

(b) $C_{J_{L_1}} > C_J = 3.1780 > C_{J_{L_2}}$

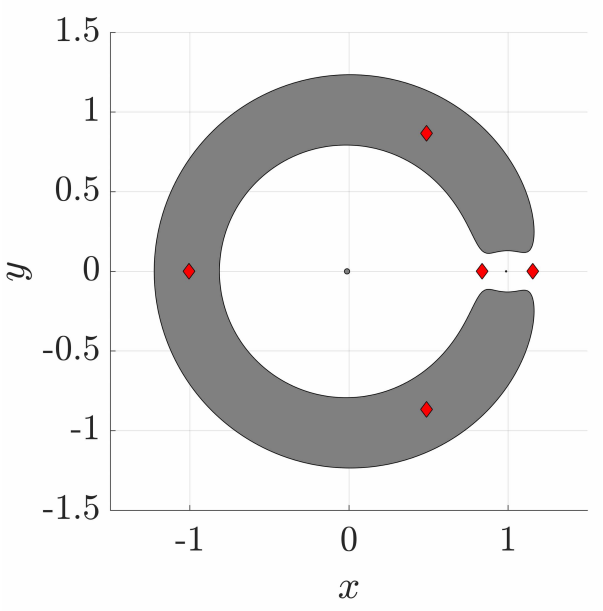

(c) $C_{J_{L_2}} > C_J = 3.1400 > C_{J_{L_3}}$

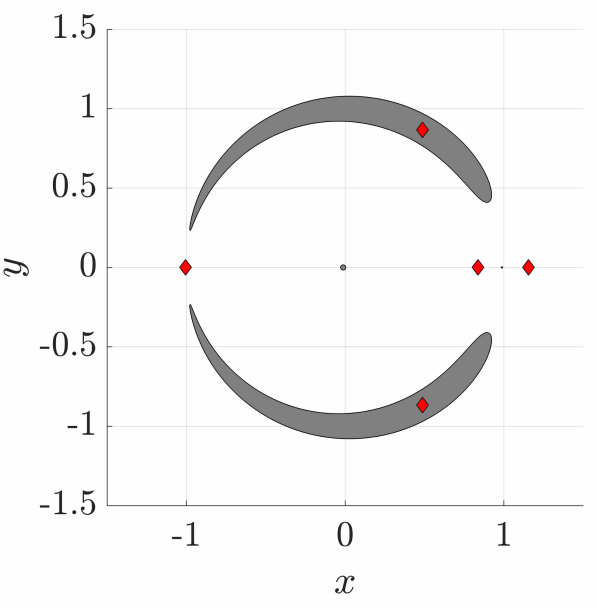

(d) $C_{J_{L_3}} > C_J = 3.0116 > C_{J_{L_{4/5}}}$

Figure 3.2: Zero velocity curves in the xy-plane of $\mathcal{R}$ computed in the Earth-Moon CR3BP at various values of C_J.

3.2.2 Stability of the Equilibrium Points

The first-order variational equations of motion presented in Section 3.1 are used to study the stability of the libration points in the CR3BP and gain insight into the behavior of the flow in the local vicinity of each point. Consider the reference solution $\boldsymbol{q}^*(t)$ to be a libration point in the CR3BP; therefore, $\boldsymbol{q}^*(t) = \boldsymbol{q}^*$ for all t because $\boldsymbol{f}(\boldsymbol{q}^*) = \boldsymbol{0}$ and the system is autonomous. Consequently, Equation 3.2 may be rewritten as

$$\dot{\boldsymbol{q}}(t) \approx [\boldsymbol{A}]\big|_{\boldsymbol{q}^*} \boldsymbol{\delta q}(t) \tag{3.11}$$

When evaluated at a libration point, $[\boldsymbol{A}]$ is constant because $\boldsymbol{q}^*$ is a stationary solution. Therefore, the local behavior of the nonlinear system near $\boldsymbol{q}^*$ may be qualitatively analyzed based on the properties of the linear time invariant system formulated about $\boldsymbol{q}^*$ in Equation 3.11 [85].

The stability of a linear time invariant system is determined by computing the eigenvalues and eigenvectors of $[\boldsymbol{A}]$ [12, 85]. Each eigenvalue possesses the form $\lambda = a + bj$ where a, b are real numbers and $j = \sqrt{-1}$; complex eigenvalues always occur in complex conjugate pairs when $[\boldsymbol{A}]$ is a real matrix [85]. Furthermore, each eigenvalue and its associated eigenvector correspond to a mode of the system where the qualitative behavior of the mode is determined by the location of the eigenvalue in the complex plane [85]. Table 3.2 summarizes the qualitative behavior of a mode in a linear time invariant system. Assuming $[\boldsymbol{A}]$ is a real matrix, stable, unstable, and center invariant subspaces are formed by the span of the eigenvectors of $[\boldsymbol{A}]$ associated with eigenvalues where $a < 0$, $a > 0$, and $a = 0$, respectively [85]. The stable, unstable, and center subspaces are denoted as E^{s}, E^{u}, and E^{c}, respectively, where the dimension of each subspace is equal to the number of eigenvectors used to define the subspace. These subspaces form a basis for the phase space of the linear system.

In the CR3BP, the in-plane and out-of-plane variations about each libration point are decoupled and therefore the in-plane and out-of-plane stability of each libration point may be evaluated independently [101, 61]. The phase space of the CR3BP is 6-dimensional; consequently, $[\boldsymbol{A}]$ is a (6×6)-dimensional real matrix that possesses a set of 6 eigenvalues and associated eigenvectors

Table 3.2: Qualitative behavior of a mode in a linear time invariant system based on the location of its associated eigenvalue in the complex plane such that the eigenvalue possesses the form $\lambda = a+bj$.

Mode Type	a	b
Stable	$a < 0$	$b = 0$
Unstable	$a > 0$	$b = 0$
Oscillatory	$a = 0$	$b \neq 0$
Stable (Spiral)	$a < 0$	$b \neq 0$
Unstable (Spiral)	$a > 0$	$b \neq 0$

and is constant when evaluated at each libration point. The eigenvalues denoted as λ_i for $i \in [1, 4]$ correspond to the in-plane modes and the eigenvalues denoted as λ_i for $i \in [5, 6]$ correspond to the out-of-plane modes. For a given value of μ, the eigenvalues of $[\boldsymbol{A}]$ evaluated at L_i are computed as

$$\begin{aligned} \lambda_{1,2} &= \pm\sqrt{\Lambda_1} \\ \lambda_{3,4} &= \pm\sqrt{\Lambda_2} \\ \lambda_{5,6} &= \pm\left(\sqrt{\left|U^*_{zz}\big|_{\boldsymbol{q}^*}\right|}\right) j \end{aligned} \tag{3.12}$$

where $|\cdot|$ denotes the absolute value of a quantity and $\Lambda_{1,2}$ are computed from the characteristic equation for the planar variational equations of motion as

$$\Lambda_{1,2} = \frac{\left(U^*_{xx}\big|_{\boldsymbol{q}^*} + U^*_{yy}\big|_{\boldsymbol{q}^*} - 4\right) \pm \sqrt{\left(4 - U^*_{xx}\big|_{\boldsymbol{q}^*} - U^*_{yy}\big|_{\boldsymbol{q}^*}\right)^2 - 4\left(U^*_{xx}\big|_{\boldsymbol{q}^*} U^*_{yy}\big|_{\boldsymbol{q}^*} - \left(U^*_{xy}\big|_{\boldsymbol{q}^*}\right)^2\right)}}{2} \tag{3.13}$$

[101, 61]. The second-order partial derivatives of U^* are defined explicitly in Section 2.1.5 and are evaluated at L_i in Equations 3.12 and 3.13. Table 3.3 summarizes the resulting linear modes associated with each libration point in the CR3BP as a function of μ.

A linear stability analysis of an equilibrium point in a nonlinear system can often provide qualitative information about the structure of solutions in its local vicinity. From the center manifold theorem, local stable, unstable, and center invariant manifolds exist tangentially to E^{s}, E^{u}, and E^{c} of the linearized system at an equilibrium point, respectively [85]. Motion along a local stable (unstable) manifold asymptotically approaches the equilibrium point in forward (reverse)

Table 3.3: Summary of the linear modes associated with each libration point in the CR3BP as a function of μ; note: $\mu_{\text{critical}} = 0.03852089650455143$.

Libration Point	μ Range	Mode Types
L_1, L_2, L_3	$(0.0, 0.5]$	Unstable In-Plane (λ_1) Stable In-Plane (λ_2) Oscillatory In-Plane (λ_3, λ_4) Oscillatory Out-of-Plane (λ_5, λ_6)
L_4, L_5	$(0.0, \mu_{\text{critical}})$	Oscillatory In-Plane (λ_1-λ_4) Oscillatory Out-of-Plane (λ_5, λ_6)
	$(\mu_{\text{critical}}, 0.5]$	Unstable Spiral In-Plane (λ_1, λ_3) Stable Spiral In-Plane (λ_2, λ_4) Oscillatory Out-of-Plane (λ_5, λ_6)

time; these manifold structures are commonly referred to as hyperbolic invariant manifolds. The corresponding global stable (unstable) manifold may then be defined by allowing states along the local stable (unstable) manifold to flow in reverse (forward) time. The stable, unstable, and center invariant manifolds associated with an equilibrium point are denoted as W^{s}, W^{u}, and W^{c} and have the same dimension as E^{s}, E^{u}, and E^{c}, respectively [85]. Furthermore, from the Hartman-Grobman theorem, hyperbolic invariant manifolds associated with an equilibrium point in an autonomous nonlinear system share the same qualitative structure as the hyperbolic invariant subspaces in the linearized system locally near the equilibrium point [85]. However, determining the structure of a center manifold associated with an equilibrium point often requires higher-order analysis and may not always be qualitatively derived from the structure of the center subspace [85, 61].

The linear modes at each libration point in the CR3BP, as summarized in Table 3.3, provide qualitative information about the structure of solutions near each libration point. From the center manifold theorem and Hartman-Grobman theorem, the presence of stable or unstable modes at a libration point in the CR3BP indicate the presence of local hyperbolic invariant manifolds that either approach or depart the libration point, respectively [85, 61]. Therefore, all three collinear libration points admit hyperbolic invariant manifolds. Additionally, as previously discussed, determining the structure of a center manifold associated with an equilibrium point often requires higher-order anal-

ysis of the equilibrium point [85, 61]. However, the CR3BP formulated with respect to a rotating observer is an autonomous Hamiltonian system. Therefore, from the Lyapunov center theorem, a one-parameter family of periodic orbits emanates from an equilibrium point for each pair of complex conjugate eigenvalues that are purely imaginary [72, 61]. Accordingly, each oscillatory mode at a libration point in the CR3BP indicates the presence of a center manifold comprised of a continuous family of periodic orbits emanating from the libration point [101, 61]. Families of periodic orbits emanate in- and out-of-plane from all five libration points. Furthermore, quasi-periodic motion may also be recovered when simultaneously exciting multiple oscillatory modes [101, 61]. Szebehely provides a detailed modal decomposition analysis in which the behavior of motion governed by the linearized and nonlinear dynamics is computed and compared in the vicinity of each libration point in the CR3BP [101]. As a result, the linear modes associated with each libration point provide substantial information about the qualitative structure of nearby motion in the CR3BP and reveal the presence of fundamental dynamical structures that may be leveraged for trajectory design.

3.3 Periodic Orbits

A periodic orbit in the CR3BP is a trajectory that precisely repeats in the rotating frame, where the minimum time interval for repetition is defined as the orbit period [101, 61]. More specifically, a periodic orbit in $\mathcal{R}$ satisfies the following condition:

$$\boldsymbol{q}(t_1) = \boldsymbol{q}(t_1 + T_{\mathrm{PO}}) \tag{3.14}$$

where $\boldsymbol{q}(t_1)$ is an initial state and T_{PO} is the period of the orbit. As discussed in Section 3.2.2, periodic orbits exist in the CR3BP within continuous one-parameter families. Periodic orbit families support identifying candidates for mission and staging orbits in the trajectory design process [101, 61].

The natural dynamics of the CR3BP provide a rich structure of continuous periodic orbit families that enable expansive exploration of a multi-body system. Periodic orbit families in the CR3BP may be classified based on a variety of properties. Orbits centered around a libration

point are referred to as libration point orbits; similarly, orbits centered around a primary body are referred to as primary-centered orbits while orbits that exhibit orbital resonance with the inertial motion of P_2 about P_1 are referred to as resonant orbits [101, 61]. Families of periodic orbits may be further classified based on the location of selected members relative to a particular primary body or libration point, bifurcations that occur along the family, the type of orbital resonance admitted by selected members, or the direction of motion of selected members. The direction of motion at a state in $\mathcal{R}$ is typically described relative to a reference location: a state that is labeled as prograde (retrograde) produces an instantaneous orbital angular momentum vector with respect to the selected reference location that possesses a positive (negative) z component. This section discusses the stability of periodic orbits and provides a detailed overview of the numerical methods used to compute a family of periodic orbits in the CR3BP.

3.3.1 Orbital Stability

The first-order variational equations of motion presented in Section 3.1 are used to study the stability of a periodic orbit in the CR3BP and gain insight into the behavior of the flow in its local vicinity. Characterizing the stability of a periodic orbit is critical in the trajectory design process because periodic orbits often serve as mission or staging orbits in a mission concept: analyzing the dynamics in the local vicinity of a periodic orbit may influence station-keeping requirements and determine whether natural dynamical structures may be leveraged to arrive onto the orbit, depart from the orbit, and/or remain bounded near the orbit [61]. Accordingly, consider the reference solution $\boldsymbol{q}^*(t)$ to be a periodic orbit with an orbit period denoted as T_{PO} in the CR3BP. The resulting Jacobian in the first-order variational equations of motion is time-varying and periodic when evaluated along $\boldsymbol{q}^*(t)$, which results in a linear time-varying system [61]. Given an initial state for the periodic orbit and a small perturbation applied to the initial state at t, the first-order evolution of the small perturbation after T_{PO} is defined as

$$\boldsymbol{\delta q}(t + T_{\mathrm{PO}}) = [\boldsymbol{\Phi}(t + T_{\mathrm{PO}}, t)]\boldsymbol{\delta q}(t) \tag{3.15}$$

where the monodromy matrix of the periodic orbit is defined as

$$[\boldsymbol{M}(t)] = [\boldsymbol{\Phi}(t + T_{\mathrm{PO}}, t)] \tag{3.16}$$

which is the STM propagated for one orbit period [85, 61].

Characterizing the properties of $[\boldsymbol{M}(t)]$ associated with a periodic orbit provides necessary insight for evaluating the local qualitative stability of the periodic orbit [61]. Consider two distinct states along a periodic orbit at t_1 and t_2, respectively. Using the properties of the STM defined in Section 3.1 as well as the periodicity of the orbit, $[\boldsymbol{M}(t_2)]$ may be defined as

$$\begin{aligned}
[\boldsymbol{M}(t_2)] &= [\boldsymbol{\Phi}(t_2 + T_{\mathrm{PO}}, t_2)] \\
&= [\boldsymbol{\Phi}(t_2 + T_{\mathrm{PO}}, t_1 + T_{\mathrm{PO}})][\boldsymbol{\Phi}(t_1 + T_{\mathrm{PO}}, t_2)] \\
&= [\boldsymbol{\Phi}(t_2 + T_{\mathrm{PO}}, t_1 + T_{\mathrm{PO}})][\boldsymbol{\Phi}(t_1 + T_{\mathrm{PO}}, t_1)][\boldsymbol{\Phi}(t_1, t_2)] \\
&= [\boldsymbol{\Phi}(t_2, t_1)][\boldsymbol{\Phi}(t_1 + T_{\mathrm{PO}}, t_1)][\boldsymbol{\Phi}(t_1, t_2)] \\
&= [\boldsymbol{\Phi}(t_1, t_2)]^{-1}[\boldsymbol{M}(t_1)][\boldsymbol{\Phi}(t_1, t_2)]
\end{aligned} \tag{3.17}$$

which demonstrates that $[\boldsymbol{M}(t_1)]$ and $[\boldsymbol{M}(t_2)]$ are similar matrices and possess the same eigenvalues [12]. Consequently, the eigenvalues of $[\boldsymbol{M}(t)]$ are constant for all t along the periodic orbit and $[\boldsymbol{M}(t)]$ may be evaluated using any reference state along the periodic orbit to determine the qualitative behavior of motion in the local vicinity of the orbit.

In the CR3BP, linearizing about a periodic orbit results in a nonautonomous linear system; however, from Floquet theory, the nonautonomous linear system can be reduced to a discrete autonomous linear system formulated about a selected state along the periodic orbit [85, 61]. The discrete system possesses a mapping interval of T_{PO} and is governed by the map $[\boldsymbol{M}(t)]$, which is constant at the selected state along the periodic orbit. Therefore, the first step in analyzing the stability of a periodic orbit in the CR3BP is to evaluate the eigenstructure of $[\boldsymbol{M}]$. In the CR3BP, $[\boldsymbol{M}]$ is a symplectic matrix due to the autonomous Hamiltonian structure of the system and the eigenvalues of a symplectic matrix always occur in reciprocal pairs [61]. Furthermore, $[\boldsymbol{M}]$ is a real matrix and therefore all complex eigenvalues occur in complex conjugate pairs [61]. Finally, $[\boldsymbol{M}]$

always admits a trivial pair of eigenvalues that are both equal to unity due to its formulation about a periodic solution and the symplectic structure of the CR3BP [61]. In the phase space of the CR3BP, one of the trivial eigenvalues corresponds to the mode associated with the periodic orbit itself while the other trivial eigenvalue corresponds to the mode associated with nearby periodic motion due to its existence in a continuous family [61].

Given the eigenstructure of $[\boldsymbol{M}]$ associated with a periodic orbit in the CR3BP, the qualitative stability of the periodic orbit may be studied. The qualitative behavior of each mode in a discrete linear time invariant system is determined by the location of the associated eigenvalue in the complex plane relative to the unit circle [12, 85]. Consequently, Table 3.4 summarizes the qualitative behavior of a mode in a discrete linear time invariant system. Assuming $[\boldsymbol{M}]$ is a real matrix, stable, unstable, and center invariant subspaces are formed by the span of the eigenvectors of $[\boldsymbol{M}]$ associated with eigenvalues where $|\lambda| < 1$, $|\lambda| > 1$, and $|\lambda| = 1$, respectively. Similar to the linear stability analysis of libration points in Section 3.2.2, the stable, unstable, and center subspaces are denoted as E^{s}, E^{u}, and E^{c}, respectively, where the dimension of each subspace is equal to the number of eigenvectors used to define the subspace [85, 61]. Recall, $[\boldsymbol{M}]$ is associated with a single state along the periodic orbit and the selection of the state is arbitrary because the eigenvalues of $[\boldsymbol{M}]$ are constant along the periodic orbit as previously demonstrated; however, the eigenvectors of $[\boldsymbol{M}]$ are not constant along the periodic orbit [85, 61]. Therefore, it is important to note that the existence and dimension of each subspace at each state along the periodic orbit is constant, but the structure of each subspace varies along the orbit due to variations in the eigenvectors of $[\boldsymbol{M}]$ evaluated at different states.

A linear stability analysis of a periodic orbit in the CR3BP provides qualitative information about the structure of solutions in the local vicinity of each state along the periodic orbit [85]. From the stable and center manifold theorems for periodic orbits, local stable, unstable, and center invariant manifolds exist tangentially to E^{s}, E^{u}, and E^{c} of the linearized system at each fixed state along the periodic orbit, respectively [85]. Furthermore, these invariant manifolds intersect each other transversally at each fixed state along the periodic orbit. The stable and unstable manifolds,

i.e., the hyperbolic invariant manifolds, share the same qualitative structure as the hyperbolic invariant subspaces in the linearized system locally near each fixed state along the periodic orbit. However, determining the structure of the center manifold typically requires higher-order analysis [85, 61]. In the CR3BP, the existence of center linear modes associated with a periodic orbit indicates the presence of quasi-periodic orbit families centered around the periodic orbit [85, 61]. As a result, the linear modes associated with a given periodic orbit provide substantial information about the qualitative structure of nearby motion in the CR3BP and reveal the presence of additional fundamental dynamical structures that may be leveraged for trajectory design.

Table 3.4: Qualitative behavior of a mode in a discrete linear time invariant system based on the location of its associated eigenvalue in the complex plane relative to the unit circle.

Mode Type	Form of λ	$\lvert\lambda\rvert$
Stable	$\lambda = a$	$\lvert\lambda\rvert < 1$
Unstable	$\lambda = a$	$\lvert\lambda\rvert > 1$
Oscillatory	$\lambda = a + bj$	$\lvert\lambda\rvert = 1$
Stable (Spiral)	$\lambda = a + bj$	$\lvert\lambda\rvert < 1$
Unstable (Spiral)	$\lambda = a + bj$	$\lvert\lambda\rvert > 1$

Stability information for a periodic orbit is often summarized using the stability indices, s_1 and s_2 [48]. Each of these indices is computed in this work as the following sum of a pair of nontrivial eigenvalues, λ and λ^{-1}, of the monodromy matrix associated with the periodic orbit:

$$s_i = \lambda + \lambda^{-1} \tag{3.18}$$

for $i \in [1, 2]$. For planar periodic orbits, s_1 is defined as the stability index associated with planar modes while s_2 corresponds to out-of-plane modes; together, their values offer useful insights into the local neighborhood of the orbit. However, the stability indices of spatial periodic orbits do not provide this clear distinction between in-plane and out-of-plane stability; in this case, the nontrivial pairs of eigenvalues corresponding to s_1 and s_2 are selected arbitrarily for a given orbit and correlated along its corresponding family. A value of the stability index between -2 and 2 indicates the existence of an oscillatory mode and, therefore, a center invariant manifold that

contains nearby quasi-periodic orbits; this is only the case when the associated eigenvalues of the stability index lie on the unit circle. An index possessing a magnitude greater than 2, however, indicates the existence of stable and unstable invariant manifolds that govern natural motion onto and away from the orbit, respectively [61]. When the order of magnitude of the stability index associated with stable and unstable modes is low, nearby trajectories exciting these modes are relatively slow to arrive onto or depart from the periodic orbit.

3.3.2 Numerical Computation via Multiple Shooting

A multiple shooting method is commonly employed in the CR3BP to compute periodic orbits; multiple shooting is a numerical method that splits a two-point boundary value problem into a series of initial value problems coupled with continuity conditions [61, 8]. Discretizing a two-point boundary value problem in this manner is particularly useful in nonlinear systems due to the sensitivity of trajectories governed by nonlinear dynamics over large time intervals. In this work, a free variable and constraint vector formulation of multiple shooting is leveraged to numerically compute periodic orbits in the CR3BP [61, 8].

The first step in computing a single periodic orbit in the CR3BP is to generate an initial guess and formulate a free variable vector. Depending on the desired type of orbit, an initial guess is constructed using either Poincaré mapping, stability analysis of a libration point, resonance analysis in the two-body problem, or bifurcation analysis of another periodic orbit family [101, 61, 43, 8]. Using one of these analysis techniques, an estimate for an initial state and period of the desired periodic orbit are obtained and denoted as $\boldsymbol{q}(t_1)$ and T_{PO}, respectively. Given these estimates, the initial guess is formed by numerically propagating $\boldsymbol{q}(t_1)$ forward in time for T_{PO} nondimensional time units. The initial guess is then discretized into a total of n_{arc} arcs with equal integration times. The state at the beginning of the i-th arc is denoted as $\boldsymbol{q}_i = \boldsymbol{q}(t_i)$ and the common integration time along each arc is defined as

$$\Delta t = \frac{T_{\mathrm{PO}}}{n_{\mathrm{arc}}} \tag{3.19}$$

The state at the beginning of each arc and the common integration time are then used to define

the free variable vector as

$$\boldsymbol{V} = \begin{bmatrix} \boldsymbol{q}_1^{\mathrm{T}} & \boldsymbol{q}_2^{\mathrm{T}} & \cdots & \boldsymbol{q}_{n_{\mathrm{arc}}}^{\mathrm{T}} & \Delta t \end{bmatrix}^{\mathrm{T}} \tag{3.20}$$

resulting in a n_{free}-dimensional vector where $n_{\mathrm{free}} = 6n_{\mathrm{arc}} + 1$. This free variable vector defines a set of parameters that may be tuned or adjusted iteratively in a differential corrections algorithm to compute a periodic orbit.

Given a free variable vector, a constraint vector is then constructed such that it is a function of the free variables and equals the zero vector when a computed trajectory is a periodic orbit. The first required constraint type is a continuity constraint applied between each neighboring pair of arcs along the orbit. The continuity constraint between the i-th and $(i+1)$-th arc along the orbit is defined as

$$\boldsymbol{F}_{\mathbf{c}_i} = \boldsymbol{q}_{i+1} - \boldsymbol{q}_{i_{\mathrm{f}}} \tag{3.21}$$

where $\boldsymbol{q}_{i_{\mathrm{f}}}$ is the final state of the i-th arc computed by propagating $\boldsymbol{q}_i$ for Δt nondimensional time units. The continuity constraints enforce continuous and smooth transitions between each neighboring pair of arcs. Similarly, the second required constraint type is a periodicity constraint applied between the initial and final arcs of the orbit. The periodicity constraint is defined as

$$\boldsymbol{F}_{\mathbf{p}} = \begin{bmatrix} \boldsymbol{q}_1\{1:4\} - \boldsymbol{q}_{n_{\mathrm{arc_f}}}\{1:4\} \\ \boldsymbol{q}_1\{6\} - \boldsymbol{q}_{n_{\mathrm{arc_f}}}\{6\} \end{bmatrix} \tag{3.22}$$

where the $\{\cdot\}$ notation denotes the rows of the associated vector (or matrix) that are included in the constraint. The periodicity constraint on $\dot{y}$ between $\boldsymbol{q}_1$ and $\boldsymbol{q}_{n_{\mathrm{arc_f}}}$ is removed because it is implicitly enforced due to the conservation of C_J along a continuous natural trajectory in the CR3BP [8]. The final constraint type included in the problem formulation is a constraint on the y-coordinate of $\boldsymbol{q}_1$, which is defined as

$$F_{\mathrm{y}} = y_1 - y_{\mathrm{des}} \tag{3.23}$$

where y_{des} is the desired y-coordinate. Fixing the y-coordinate of $\boldsymbol{q}_1$ at y_{des} helps facilitate better convergence behavior by removing the ambiguity of the initial state for a periodic orbit. The

selection of y_{des} depends on the desired type of orbit. Finally, the full constraint vector is defined as

$$\boldsymbol{F}(\boldsymbol{V}) = \begin{bmatrix} \boldsymbol{F}_{\mathbf{c}_1}^{\mathrm{T}} & \boldsymbol{F}_{\mathbf{c}_2}^{\mathrm{T}} & \cdots & \boldsymbol{F}_{\mathbf{c}_{n_{\text{arc}}-1}}^{\mathrm{T}} & \boldsymbol{F}_{\mathbf{p}}^{\mathrm{T}} & F_{\mathrm{y}} \end{bmatrix}^{\mathrm{T}} \tag{3.24}$$

resulting in a n_{con}-dimensional vector where $n_{\text{con}} = 6n_{\text{arc}}$. This constraint vector mathematically defines the constraints that must be satisfied in order for a trajectory described by $\boldsymbol{V}$ to correspond to a periodic orbit.

Given a free variable and constraint vector formulation of multiple shooting for a periodic orbit, the resulting series of initial value problems is solved using Newton's method [61, 8]. The constraint vector $\boldsymbol{F}(\boldsymbol{V})$ is comprised of equality constraints and formulates a system of equations in which each equation is satisfied when it is equal to zero. Consequently, the goal of the vector-valued Newton's method is to determine $\boldsymbol{V}$ such that $\boldsymbol{F}(\boldsymbol{V}) = \mathbf{0}$ to within a small tolerance. Consider a current free variable vector denoted as $\boldsymbol{V}$ and a desired free variable vector denoted as $\boldsymbol{V}_{\mathbf{sol}}$ that corresponds to a periodic orbit. As a result, $\boldsymbol{F}(\boldsymbol{V}_{\mathbf{sol}}) = \mathbf{0}$ and assume $\boldsymbol{V}_{\mathbf{sol}}$ is in the local vicinity of $\boldsymbol{V}$. Therefore, the first-order vector-valued Taylor series expansion of $\boldsymbol{F}(\boldsymbol{V}_{\mathbf{sol}})$ about $\boldsymbol{V}$ is defined as

$$\boldsymbol{F}(\boldsymbol{V}_{\mathbf{sol}}) = \mathbf{0} \approx \boldsymbol{F}(\boldsymbol{V}) + [\boldsymbol{DF}(\boldsymbol{V})]\,(\boldsymbol{V}_{\mathbf{sol}} - \boldsymbol{V}) \tag{3.25}$$

where

$$[\boldsymbol{DF}(\boldsymbol{V})] = \left.\frac{\partial \boldsymbol{F}(\boldsymbol{V})}{\partial \boldsymbol{V}}\right|_{\boldsymbol{V}} \tag{3.26}$$

and $[\boldsymbol{DF}(\boldsymbol{V})]$ is a $(n_{\text{con}} \times n_{\text{free}})$-dimensional matrix. To the first-order, Equation 3.25 may then be solved for the desired free variable vector to produce the following update equation at iteration i:

$$\boldsymbol{V}_{i+1} = \begin{cases} \boldsymbol{V}_i - [\boldsymbol{DF}(\boldsymbol{V}_i)]^{-1}\boldsymbol{F}(\boldsymbol{V}_i) & \text{if } n_{\text{free}} = n_{\text{con}} \\ \boldsymbol{V}_i - [\boldsymbol{DF}(\boldsymbol{V}_i)]^{\mathrm{T}}\left[[\boldsymbol{DF}(\boldsymbol{V}_i)][\boldsymbol{DF}(\boldsymbol{V}_i)]^{\mathrm{T}}\right]^{-1}\boldsymbol{F}(\boldsymbol{V}_i) & \text{if } n_{\text{free}} > n_{\text{con}} \end{cases} \tag{3.27}$$

Equation 3.27 produces the general update equation used in a vector-valued Newton's method. Given an initial guess $\boldsymbol{V} = \boldsymbol{V}_1$, Newton's method is used to iteratively update $\boldsymbol{V}$ until a terminal condition is met. Due to numerical integration errors and the use of a numerical method, the

condition $\boldsymbol{F}(\boldsymbol{V}) = \boldsymbol{0}$ may not be achieved exactly. Therefore, potential terminal conditions are $||\boldsymbol{F}(\boldsymbol{V})|| \leq \epsilon$ or a maximum number of iterations is exceeded. In this work, the value of ϵ is set as 10^{-12} and the maximum number of iterations is set at 50 for computing periodic orbits in the CR3BP. Newton's method is an efficient numerical technique for computing periodic orbits in the CR3BP; however, a good initial guess is needed for robust convergence behavior due to the linear assumptions of the methodology [106].

Implementing the vector-valued Newton's method as described relies on defining $[\boldsymbol{DF}(\boldsymbol{V})]$ and evaluating the matrix at each iteration of the algorithm for the current free variable vector. This matrix is the Jacobian of the constraints with respect to the free variables and characterizes how variations in the free variables impact the constraints [61, 8]. Numerical finite differencing algorithms are often leveraged to approximate $[\boldsymbol{DF}(\boldsymbol{V})]$; however, when possible, it is more accurate and computationally efficient to define analytical expressions for the elements of $[\boldsymbol{DF}(\boldsymbol{V})]$. Given the free variable and constraint vector formulation of multiple shooting for a periodic orbit presented in this subsection, $[\boldsymbol{DF}(\boldsymbol{V})]$ is defined analytically as

$$[\boldsymbol{DF}(\boldsymbol{V})] = \begin{bmatrix} \frac{\partial \boldsymbol{F}_{\mathbf{c}_1}}{\partial \boldsymbol{V}} \\ \frac{\partial \boldsymbol{F}_{\mathbf{c}_2}}{\partial \boldsymbol{V}} \\ \vdots \\ \frac{\partial \boldsymbol{F}_{\mathbf{c}_{n_{\text{arc}}-1}}}{\partial \boldsymbol{V}} \\ \frac{\partial \boldsymbol{F}_{\mathbf{p}}}{\partial \boldsymbol{V}} \\ \frac{\partial F_{\text{y}}}{\partial \boldsymbol{V}} \end{bmatrix} \tag{3.28}$$

where

$$\begin{aligned} \frac{\partial \boldsymbol{F}_{\mathbf{c}_i}}{\partial \boldsymbol{V}} &= \begin{bmatrix} [\boldsymbol{0}_{6\times(6(i-1))}] & -[\boldsymbol{\Phi}(t_i + \Delta t, t_i)] & [\boldsymbol{I}_{6\times 6}] & [\boldsymbol{0}_{6\times(6(n_{\text{arc}}-i)-6)}] & -\dot{\boldsymbol{q}}_{i_{\text{f}}} \end{bmatrix} \\ \frac{\partial \boldsymbol{F}_{\mathbf{p}}}{\partial \boldsymbol{V}} &= \begin{bmatrix} [\boldsymbol{I}_{6\times 6}]\{1:4\} & [\boldsymbol{0}_{4\times(6n_{\text{arc}}-12)}] & -[\boldsymbol{\Phi}(t_{n_{\text{arc}}} + \Delta t, t_{n_{\text{arc}}})]\{1:4\} & -\dot{\boldsymbol{q}}_{n_{\text{arc}_{\text{f}}}}\{1:4\} \\ [\boldsymbol{I}_{6\times 6}]\{6\} & [\boldsymbol{0}_{1\times(6n_{\text{arc}}-12)}] & -[\boldsymbol{\Phi}(t_{n_{\text{arc}}} + \Delta t, t_{n_{\text{arc}}})]\{6\} & -\dot{\boldsymbol{q}}_{n_{\text{arc}_{\text{f}}}}\{6\} \end{bmatrix} \\ \frac{\partial F_{\text{y}}}{\partial \boldsymbol{V}} &= \begin{bmatrix} 0 & 1 & [\boldsymbol{0}_{1\times(6n_{\text{arc}}-1)}] \end{bmatrix} \end{aligned} \tag{3.29}$$

Equipped with an explicit definition for $[\boldsymbol{DF}(\boldsymbol{V})]$, Newton's method is leveraged to compute periodic orbits in the CR3BP.

3.3.3 Pseudo-Arclength Continuation

Pseudo-arclength continuation is used to numerically compute a family of periodic orbits in the CR3BP [58]. As discussed throughout this section, periodic orbits exist within the CR3BP in continuous one-parameter families. Starting from an initial periodic orbit, a continuation method may be used to traverse along the parameterized family by successively computing nearby periodic orbits. Figure 3.3 depicts a conceptual example of pseudo-arclength continuation where a family of periodic orbit solutions is represented as a blue curve in the space defined by a free variable vector $\boldsymbol{V}$ and a parameter p. Given a current periodic orbit at p_i, a nearby periodic orbit along the solution curve is desired as depicted in Figure 3.3. First, a unit vector that is tangent to the solution curve at p_i is computed and scaled by δs. Then, an initial guess for the nearby periodic orbit is generated by perturbing the current orbit solution along the tangent vector. Finally, a new periodic orbit at p_{i+1} along the solution curve is recovered from the initial guess. This process may then be repeated to compute additional members along the family. There are a variety of numerical techniques that may be used for continuation; however, pseudo-arclength continuation is specifically leveraged because it does not require a priori knowledge of the solution curve and is more robust than simpler methods, such as natural parameter continuation [58, 8].

The free variable and constraint vectors defined in Section 3.3.2 for computing periodic orbits in the CR3BP are formulated such that the null space of $[\boldsymbol{DF}(\boldsymbol{V})]$ is 1-dimensional and there are an infinite number of solutions to $\boldsymbol{F}(\boldsymbol{V}) = \boldsymbol{0}$. Consider a current periodic orbit denoted as $\boldsymbol{V}_{\mathbf{curr}}$ that is computed using Newton's method as described in Section 3.3.2. The unit vector that is tangent to the solution curve of the corresponding family at the current periodic orbit is computed as the null space of $[\boldsymbol{DF}(\boldsymbol{V}_{\mathbf{curr}})]$ and denoted as $\hat{\boldsymbol{n}}_{\mathbf{curr}}$ [58, 8]. An initial guess for a new periodic orbit along the family is then computed as

$$\boldsymbol{V}_{\mathbf{new}} = \boldsymbol{V}_{\mathbf{curr}} + \delta s \hat{\boldsymbol{n}}_{\mathbf{curr}} \tag{3.30}$$

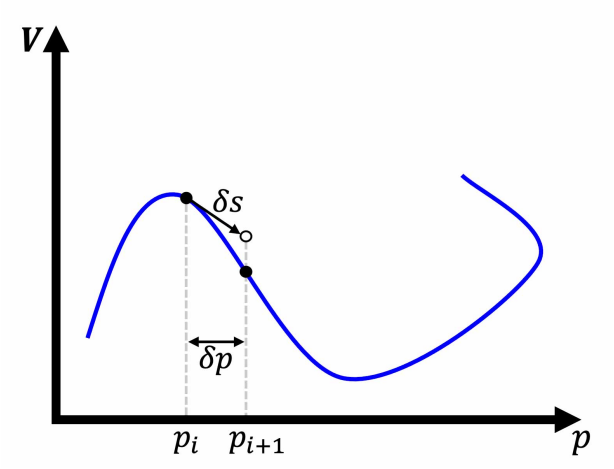

Figure 3.3: Conceptual example of pseudo-arclength continuation (derived from [8]).

where δs is specified by a human analyst. Finally, Newton's method is used to recover a new periodic orbit along the family given the initial guess $\boldsymbol{V} = \boldsymbol{V}_{\mathbf{new}}$. However, the constraint vector is modified to ensure the new periodic orbit is recovered at a step size of δs from $\boldsymbol{V}_{\mathbf{curr}}$ along $\hat{\boldsymbol{n}}_{\mathbf{curr}}$. The modified constraint vector is defined as

$$\boldsymbol{H}(\boldsymbol{V}) = \begin{bmatrix} \boldsymbol{F}(\boldsymbol{V}) \\ (\boldsymbol{V} - \boldsymbol{V}_{\mathbf{curr}})^{\mathrm{T}} \hat{\boldsymbol{n}}_{\mathbf{curr}} - \delta s \end{bmatrix} \tag{3.31}$$

and the modified Jacobian of the constraints with respect to the free variables is defined as

$$[\boldsymbol{DH}(\boldsymbol{V})] = \begin{bmatrix} [\boldsymbol{DF}(\boldsymbol{V})] \\ \hat{\boldsymbol{n}}_{\mathbf{curr}}^{\mathrm{T}} \end{bmatrix} \tag{3.32}$$

Using this modified system of equations within Newton's method, a new periodic orbit is recovered and the process may be repeated to successively step along the desired family of periodic orbits. In this work, the continuation process terminates when a desired number of orbits is computed or Newton's method fails to converge. As an example, Figure 3.4 displays segments of the L_1, L_2, and L_3 Lyapunov orbit families as well as segments of the L_1, L_2, and L_3 northern halo orbit families computed in the Earth-Moon CR3BP using Newton's method and pseudo-arclength continuation.

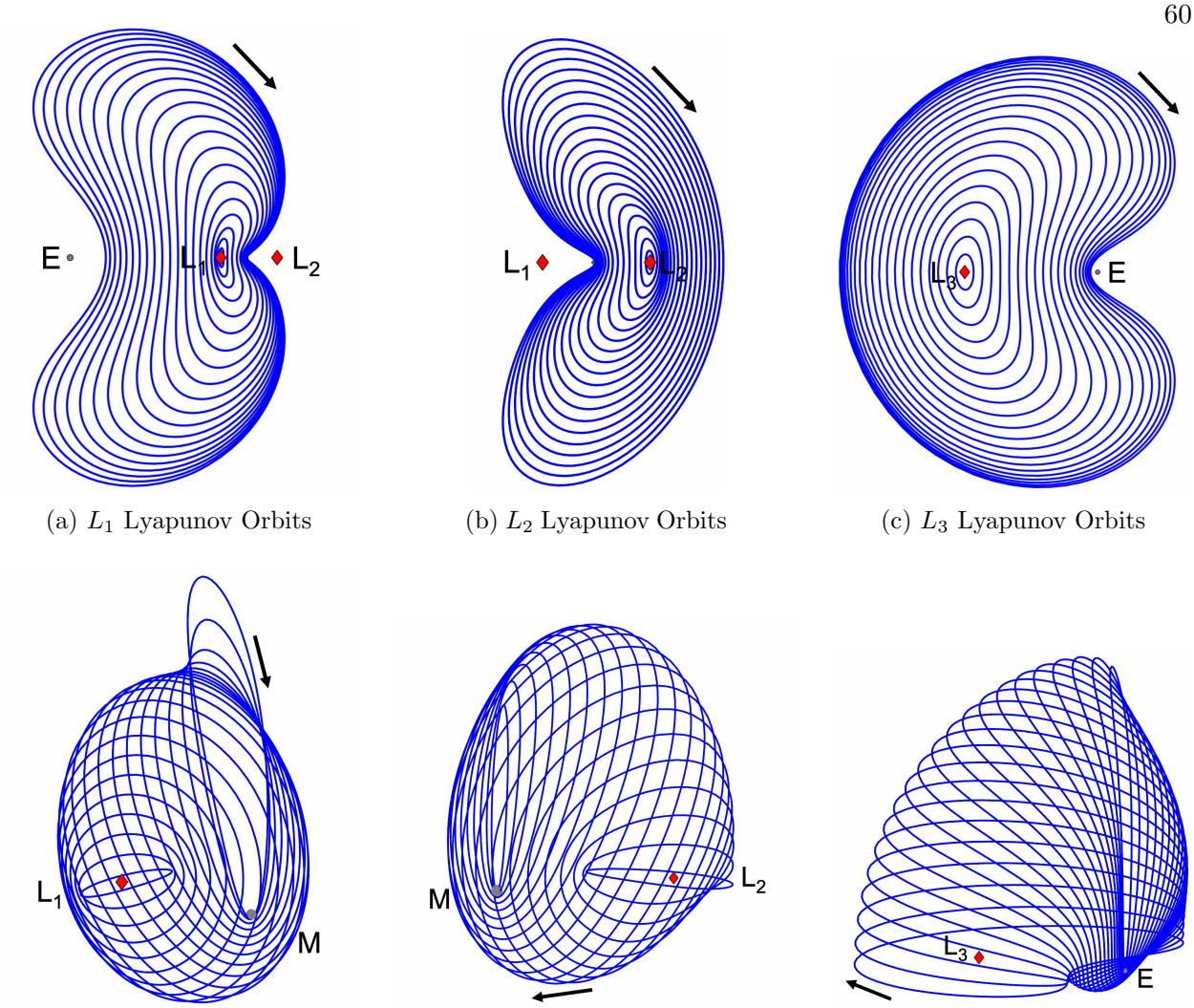

(a) L_1 Lyapunov Orbits (b) L_2 Lyapunov Orbits (c) L_3 Lyapunov Orbits

(d) L_1 Northern Halo Orbits (e) L_2 Northern Halo Orbits (f) L_3 Northern Halo Orbits

Figure 3.4: Segments of the L_1, L_2, and L_3 Lyapunov orbit families as well as segments of the L_1, L_2, and L_3 northern halo orbit families computed in the Earth-Moon CR3BP.

3.4 Hyperbolic Invariant Manifolds

Hyperbolic invariant manifolds may approximate natural transport mechanisms throughout a multi-body system [61, 32, 50]. In the CR3BP, the existence of stable and unstable linear modes associated with a state along a periodic orbit indicate the presence of hyperbolic invariant manifolds that naturally approach and depart a periodic orbit, respectively [101, 61]. Due to the eigenstructure of the monodromy matrix associated with a periodic orbit in the CR3BP, the existence of a stable

manifold guarantees the existence of an associated unstable manifold. The stable and unstable manifolds associated with a periodic orbit may be denoted as $W^{\mathrm{s}}_{\mathrm{PO}}$ and $W^{\mathrm{u}}_{\mathrm{PO}}$, respectively. A trajectory along $W^{\mathrm{s}}_{\mathrm{PO}}$ asymptotically approaches the periodic orbit as $t \to \infty$ and a trajectory along $W^{\mathrm{u}}_{\mathrm{PO}}$ asymptotically approaches the periodic orbit as $t \to -\infty$ [61]. When the magnitude of the eigenvalues associated with the stable and unstable modes are close to unity, trajectories along the stable and unstable manifolds are relatively slow to arrive onto and depart from the periodic orbit, respectively.

In the absence of generalized analytical descriptions, an approximation of a stable or unstable manifold in the CR3BP is typically computed numerically. First, an unstable periodic orbit is discretized into a set of states. At a selected state along the periodic orbit, $\boldsymbol{q}_{\mathbf{PO}}$, a perturbation of magnitude d is applied in the direction of either a stable eigenvector, $\boldsymbol{v}_{\mathbf{s}}$, or an unstable eigenvector, $\boldsymbol{v}_{\mathbf{u}}$, of $[\boldsymbol{M}]$ computed at $\boldsymbol{q}_{\mathbf{PO}}$. The resulting perturbed state depends on the desired manifold structure and is defined as

$$\begin{cases} \boldsymbol{q}^{\mathbf{s}}_{\mathbf{PO}} = \boldsymbol{q}_{\mathbf{PO}} \pm d\left(\frac{\boldsymbol{v}_{\mathbf{s}}}{||\boldsymbol{v}_{\mathbf{s}}\{1{:}3\}||}\right) & \text{for the stable manifold} \\ \boldsymbol{q}^{\mathbf{u}}_{\mathbf{PO}} = \boldsymbol{q}_{\mathbf{PO}} \pm d\left(\frac{\boldsymbol{v}_{\mathbf{u}}}{||\boldsymbol{v}_{\mathbf{u}}\{1{:}3\}||}\right) & \text{for the unstable manifold} \end{cases} \tag{3.33}$$

where $\boldsymbol{v}_{\mathbf{s/u}}$ is normalized by the magnitude of its position components [61]. The perturbed state approximately lies along the desired local manifold because the corresponding linear subspace is tangent to the manifold at the selected state along the periodic orbit as discussed in Section 3.3.1. Depending on the desired manifold, the perturbed state is propagated backward (forward) in time to produce a trajectory along the global stable (unstable) half-manifold. This numerical process is then repeated for multiple states along the periodic orbit to produce a discrete approximation of the global half-manifold over a time interval of interest. Termination criteria within the time interval of interest may include reaching a maximum number of apses with respect to a reference location, crossing a specified boundary in the configuration space, or impacting a primary body [61]. As an example, Figure 3.5 displays trajectories computed along the stable and unstable half-manifolds associated with an L_1 Lyapunov orbit at $C_J \approx 3.1802$ in the Earth-Moon CR3BP.

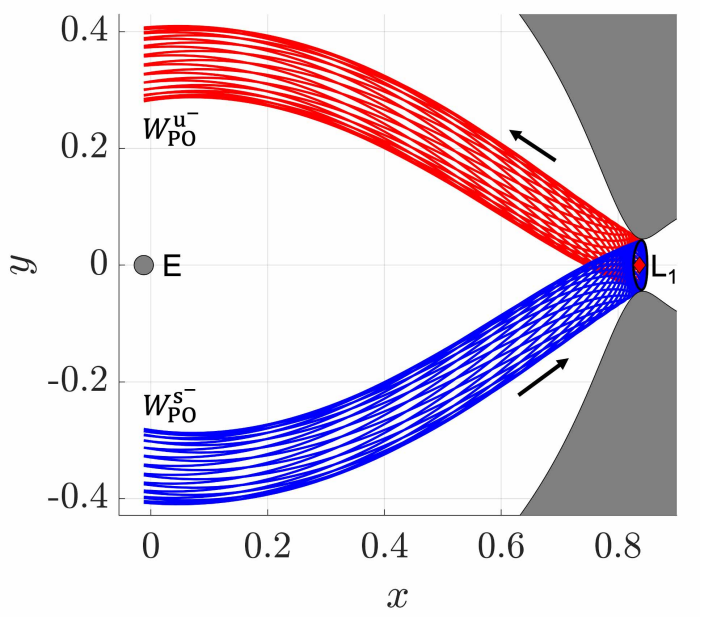

(a) Stable and unstable half-manifolds directed towards the Earth.

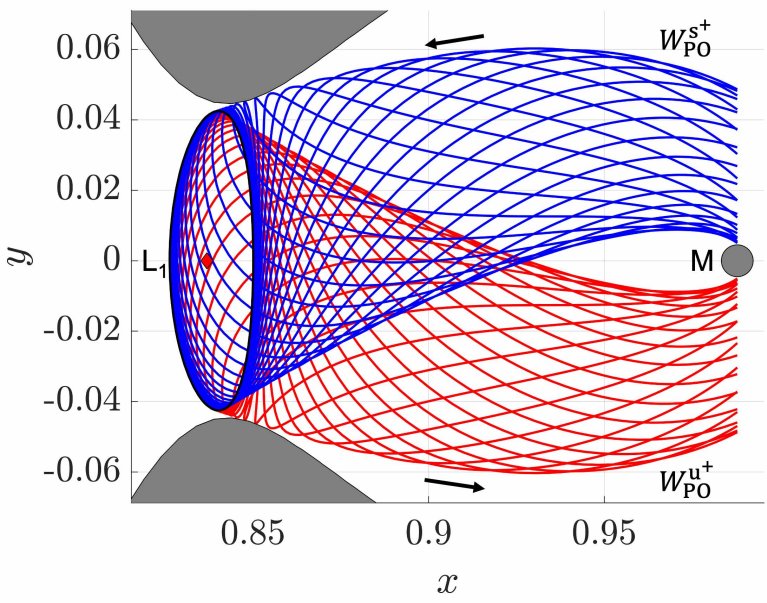

(b) Stable and unstable half-manifolds directed towards the Moon.

Figure 3.5: Trajectories computed along the stable (blue) and unstable (red) half-manifolds associated with an L_1 Lyapunov orbit at $C_J \approx 3.1802$ in the Earth-Moon CR3BP.

Chapter 4

Numerically Correcting Trajectories via Collocation

In a multi-body system, a spacecraft trajectory is typically computed by solving a two-point boundary value problem using multiple shooting or collocation methods [17, 6]. Collocation is used in this work for numerically correcting transfers because it is often more robust with respect to the quality of an initial guess compared to multiple shooting [17]. Collocation is a numerical method used to implicitly integrate the differential equations of a dynamical system [17, 6, 103]. Using collocation, a solution to a dynamical system is recovered by approximating the solution as sets of piecewise polynomials that satisfy the system dynamics at collocation nodes. This chapter presents a detailed overview of a free variable and constraint vector formulation of collocation used to transform the trajectory design problem into a parameter design problem and robustly compute continuous solutions from primitive-based initial guesses. The formulation summarized in this chapter is based upon the generalized odd-degree collocation scheme with hybrid mesh refinement presented by Grebow and Pavlak [35]. Note: An earlier version of the discussion in Section 4.1 appeared in a conference paper by Smith and Bosanac [98].

4.1 Correcting Trajectories in the CR3BP

4.1.1 Trajectory Discretization

Consider an initial guess for a trajectory that is comprised of a sequence of discontinuous segments. Given an initial guess for a trajectory containing n_{seg} segments in the CR3BP, the first step of the corrections process is to define a discrete mesh of nodes along the trajectory. The i-th segment is discretized into m_i arcs and a total of $m_i + 1$ nodes at their boundaries. The method used to discretize each segment depends on the design application and may be tailored by the trajectory designer. The nodes generated in this discretization process are referred to as boundary nodes, where each node is described by its state and time along the trajectory. The state and time associated with a given node are defined as $\boldsymbol{q}^i_{j,k}$ and $t^i_{j,k}$, respectively, where i refers to the segment index along the trajectory, j refers to the arc index along the i-th segment, and k refers to the node index along the j-th arc in the i-th segment. Across the n_{seg} segments, this discretization produces a total of m arcs and the mesh is defined as the following set:

$$\Pi = \{\boldsymbol{q}^i_{j,k} \mid \boldsymbol{q}^i_{j,k} \in \mathbb{R}^{n_{\text{state}}},\ t^i_{j,k} \in \{t^i_{1,1}, t^i_{2,1}, ..., t^i_{m_i,1}, t^i_{m_i,n}\}\ \forall\ i \in [1, n_{\text{seg}}]\} \tag{4.1}$$

where $n_{\text{state}} = 6$ is the dimension of each instance of $\boldsymbol{q}$; n is the number of nodes along each arc; each pair of consecutive arcs within a segment share a common boundary node; and it is assumed that $t^i_{m_i,n}$ is equal to $t^{i+1}_{1,1}$ for each pair of consecutive segments despite not sharing a common boundary node. Accordingly, the resulting mesh Π is comprised of all the boundary nodes placed along the trajectory.

After Π is defined for the given trajectory, collocation nodes are placed along each arc in the mesh using an implicit integration method and node spacing strategy. The implicit integration method is selected first because it determines the number of nodes placed along each arc. Higher-order polynomials have successfully been used for implicit integration in nonlinear dynamical systems due to the complexity of the dynamics [17, 103, 59]. Lower-order polynomials may also be used; however, to achieve a similar level of accuracy, a fine mesh with many small arcs is needed

when using lower-order polynomials compared to a coarser mesh with less arcs when using higher-order polynomials. Based on previous successful applications of collocation for trajectory design in multi-body systems and the Mission Analysis, Operations, and Navigation Toolkit Environment (MONTE) Collocation tool, the degree of the polynomials is assumed to be odd and 7-th order polynomials are used in this work [78, 35, 87]. Therefore, $n = 7$ collocation nodes are placed along each of the m_i arcs within each of the n_{seg} segments of the trajectory such that the placement of the nodes is determined by a selected node spacing strategy.

In collocation, a node spacing strategy is used to determine the location of the collocation nodes placed along each arc of the trajectory. First, each arc is parameterized by a normalized time quantity, τ, spanning from -1 to 1. The transformation from the time t to the normalized time τ at a state along the j-th arc in the i-th segment is defined as

$$\tau = 2\left(\frac{t - t^i_{j,1}}{\Delta t^i_j}\right) - 1 \tag{4.2}$$

where $\Delta t^i_j = t^i_{j,n} - t^i_{j,1}$ is the total integration time along the j-th arc in the i-th segment. Using this normalized time parameterization, a node spacing strategy is selected to place the collocation nodes along each arc. A common node spacing strategy that has successfully been used by a variety of researchers in spacecraft trajectory design is Legendre-Gauss-Lobatto (LGL) node spacing [17, 116, 35]. In this method, collocation nodes are placed at the boundary nodes of each arc and at the normalized times τ equal to the roots of the derivative of the $(n-1)$-th order Legendre polynomial, ranging from -1 to 1. In addition, an LGL weighting term, w, is computed for each node. Table 4.1 lists the computed values of τ_k and w_k for the collocation nodes placed along an arc using LGL node spacing where $n = 7$ [45]. Leveraging LGL node spacing is advantageous because it simplifies the corrections problem by considering boundary nodes as collocation nodes [35].

Along each arc, the odd-numbered collocation nodes are classified as free nodes and the even-numbered collocation nodes are classified as defect nodes. The free nodes are used to construct the approximating polynomials along each arc, whereas the defect nodes are used to evaluate how well the system dynamics are approximated by the polynomials along each arc. The polynomials of the

Table 4.1: Computed values of τ_k and w_k for the collocation nodes placed along an arc using 7-th order LGL node spacing.

Node Index (k)	τ_k	w_k
1	-1.0	0.04761904761904762
2	-0.8302238962785670	0.2768260473615659
3	-0.4688487934707142	0.4317453812098626
4	0.0	0.4876190476190476
5	0.4688487934707142	0.4317453812098626
6	0.8302238962785670	0.2768260473615659
7	1.0	0.04761904761904762

j-th arc in the i-th segment are denoted as $\boldsymbol{p}_j^i(\tau)$; the explicit definition of the polynomials along each arc is discussed in Section 4.1.2. Figure 4.1 depicts a conceptual example of the trajectory discretization with each arc containing a set of 7 nodes, including 4 free nodes (blue) and 3 defect nodes (red), as determined by the 7-th order implicit integration method; these nodes are spaced along each arc using LGL node spacing. Furthermore, the boundary nodes (outlined in black) are considered collocation nodes and are classified as free nodes. As depicted in Figure 4.1, consecutive arcs within a segment share a common free boundary node. However, the final free boundary node along segment i is distinct from the initial free boundary node along segment $i+1$ despite the assumption that $t_{m_i,n}^i = t_{1,1}^{i+1}$ holds for each pair of consecutive segments. This discretization process provides the foundation for the collocation scheme and differential corrections strategy discussed throughout the remainder of this section.

4.1.2 Collocation Scheme

The implicit integration method and node spacing strategy selected for trajectory discretization govern the collocation scheme utilized in the differential corrections process. Given a mesh Π for a trajectory, collocation nodes are placed along each arc in the mesh based on the selected implicit integration method and node spacing strategy. The placement of the free nodes then dictates the structure of the polynomial sets computed along each arc. Each state variable along the j-th

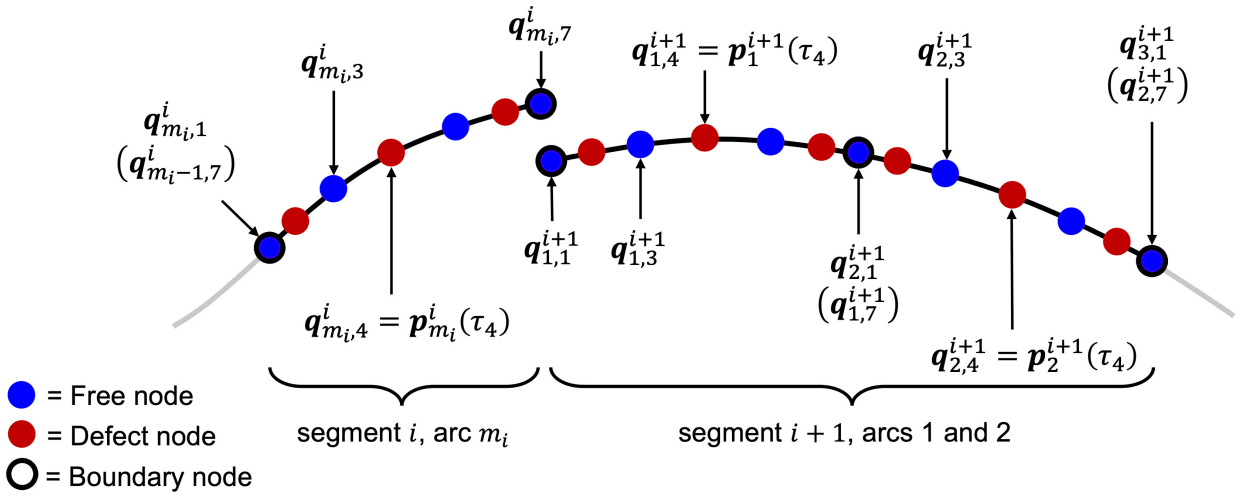

Figure 4.1: Conceptual example of collocation nodes placed along multiple arcs of segment i and $i+1$ using 7-th order LGL node spacing.

arc in the i-th segment of the trajectory is approximated with a distinct n-th order polynomial parameterized by τ. Therefore, the state vector at τ along the j-th arc in the i-th segment is approximated as

$$\boldsymbol{p}^i_j(\tau) = \left[\boldsymbol{C}_{\mathbf{coll}}{}^i_j\right]\boldsymbol{\tau} \tag{4.3}$$

where $\left[\boldsymbol{C}_{\mathbf{coll}}{}^i_j\right]$ is a $(n_{\text{state}} \times (n+1))$-dimensional matrix and

$$\boldsymbol{\tau} = \begin{bmatrix} 1 & \tau & \tau^2 & \cdots & \tau^{n-1} & \tau^n \end{bmatrix}^{\mathrm{T}} \tag{4.4}$$

The matrix $\left[\boldsymbol{C}_{\mathbf{coll}}{}^i_j\right]$ defines the coefficients for a set of n_{state} polynomials, i.e., a distinct polynomial for each dimension of the state, where each row of the matrix provides the coefficients for each distinct polynomial. The vector $\boldsymbol{\tau}$ may then be used to evaluate these polynomials and compute an approximated state along the corresponding arc at a desired value of τ. Furthermore, the normalized time derivative of $\boldsymbol{p}^i_j(\tau)$ is defined as

$$\dot{\boldsymbol{p}}^i_j(\tau) = \left[\boldsymbol{C}_{\mathbf{coll}}{}^i_j\right]\dot{\boldsymbol{\tau}} \tag{4.5}$$

where

$$\dot{\boldsymbol{\tau}} = \begin{bmatrix} 0 & 1 & 2\tau & \cdots & (n-1)\tau^{n-2} & n\tau^{n-1} \end{bmatrix}^{\mathrm{T}} \tag{4.6}$$

Although $n = 7$ is used in this work, n is a design parameter in this collocation scheme and may be selected as any odd integer where $n \geq 3$.

The free nodes are used to construct the approximating polynomials along each arc of the trajectory. Therefore, the polynomial coefficient matrix along the j-th arc in the i-th segment is computed as

$$\left[\boldsymbol{C}_{\mathbf{coll}}{}_j^i\right] = \left[\boldsymbol{U}_{\mathbf{coll}}{}_j^i\right][\boldsymbol{A}_{\mathbf{coll}}]^{-1} \tag{4.7}$$

where

$$\left[\boldsymbol{U}_{\mathbf{coll}}{}_j^i\right] = \begin{bmatrix} \boldsymbol{q}_{j,1}^i & \boldsymbol{q}_{j,3}^i & \cdots & \boldsymbol{q}_{j,n}^i & | & \dot{\boldsymbol{q}}_{j,1}^i & \dot{\boldsymbol{q}}_{j,3}^i & \cdots & \dot{\boldsymbol{q}}_{j,n}^i \end{bmatrix} \tag{4.8}$$

and

$$[\boldsymbol{A}_{\mathbf{coll}}] = \begin{bmatrix} \boldsymbol{\tau}_1 & \boldsymbol{\tau}_3 & \cdots & \boldsymbol{\tau}_n & | & \dot{\boldsymbol{\tau}}_1 & \dot{\boldsymbol{\tau}}_3 & \cdots & \dot{\boldsymbol{\tau}}_n \end{bmatrix} \tag{4.9}$$

The matrix $\left[\boldsymbol{U}_{\mathbf{coll}}{}_j^i\right]$ is comprised of the states at the free nodes along the j-th arc in the i-th segment as well as their corresponding normalized time derivatives. The normalized time derivative of $\boldsymbol{q}_{j,k}^i$ is defined as

$$\dot{\boldsymbol{q}}_{j,k}^i = \frac{\Delta t_j^i}{2} \boldsymbol{f}(\boldsymbol{q}_{j,k}^i) \tag{4.10}$$

using the equations of motion for the CR3BP defined in Equation 2.21. Finally, the states and corresponding normalized time derivatives of the defect nodes are approximated by the constructed polynomials along each arc of the trajectory. The states at the defect nodes along the j-th arc in the i-th segment are computed using the polynomials as

$$\left[\boldsymbol{P}_{\mathbf{coll}}{}_j^i\right] = \left[\boldsymbol{C}_{\mathbf{coll}}{}_j^i\right][\boldsymbol{B}_{\mathbf{coll}}] \tag{4.11}$$

where

$$\left[\boldsymbol{P}_{\mathbf{coll}}{}_j^i\right] = \begin{bmatrix} \boldsymbol{p}_j^i(\tau_2) & \boldsymbol{p}_j^i(\tau_4) & \cdots & \boldsymbol{p}_j^i(\tau_{n-1}) \end{bmatrix} \tag{4.12}$$

and

$$[\boldsymbol{B}_{\mathbf{coll}}] = \begin{bmatrix} \boldsymbol{\tau}_2 & \boldsymbol{\tau}_4 & \cdots & \boldsymbol{\tau}_{n-1} \end{bmatrix} \tag{4.13}$$

Similarly, the normalized time derivatives of the defect nodes along the j-th arc in the i-th segment are approximated by the polynomials as

$$\left[\dot{\boldsymbol{P}}_{\mathbf{coll}}{}^{i}_{j}\right] = \left[\boldsymbol{C}_{\mathbf{coll}}{}^{i}_{j}\right][\boldsymbol{D}_{\mathbf{coll}}] \tag{4.14}$$

where

$$\left[\dot{\boldsymbol{P}}_{\mathbf{coll}}{}^{i}_{j}\right] = \begin{bmatrix} \dot{\boldsymbol{p}}^{i}_{j}(\tau_2) & \dot{\boldsymbol{p}}^{i}_{j}(\tau_4) & \cdots & \dot{\boldsymbol{p}}^{i}_{j}(\tau_{n-1}) \end{bmatrix} \tag{4.15}$$

and

$$[\boldsymbol{D}_{\mathbf{coll}}] = \begin{bmatrix} \dot{\boldsymbol{\tau}}_2 & \dot{\boldsymbol{\tau}}_4 & \cdots & \dot{\boldsymbol{\tau}}_{n-1} \end{bmatrix} \tag{4.16}$$

The matrices $[\boldsymbol{A}_{\mathbf{coll}}]^{-1}$, $[\boldsymbol{B}_{\mathbf{coll}}]$, and $[\boldsymbol{D}_{\mathbf{coll}}]$ are all constant matrices that only need to be computed once based on the selected implicit integration method and node spacing strategy. Using this collocation scheme, a free variable and constraint vector are formulated to transform the trajectory design problem into a parameter design problem.

4.1.3 Trajectory Corrections

To formulate a corrections problem that uses collocation, a free variable vector is defined using the state at each free node and the time elapsed along each of the m arcs of a trajectory. Mathematically, the free variable vector $\boldsymbol{V}^i$ for the i-th segment, composed of m_i arcs, is defined as

$$\boldsymbol{V}^i = \begin{bmatrix} \begin{bmatrix} \boldsymbol{q}^i_{1,1} \\ \boldsymbol{q}^i_{1,3} \\ \vdots \\ \boldsymbol{q}^i_{1,n-2} \end{bmatrix}^{\mathrm{T}} & \begin{bmatrix} \boldsymbol{q}^i_{2,1} \\ \boldsymbol{q}^i_{2,3} \\ \vdots \\ \boldsymbol{q}^i_{2,n-2} \end{bmatrix}^{\mathrm{T}} & \cdots & \begin{bmatrix} \boldsymbol{q}^i_{m_i-1,1} \\ \boldsymbol{q}^i_{m_i-1,3} \\ \vdots \\ \boldsymbol{q}^i_{m_i-1,n-2} \end{bmatrix}^{\mathrm{T}} & \begin{bmatrix} \boldsymbol{q}^i_{m_i,1} \\ \boldsymbol{q}^i_{m_i,3} \\ \vdots \\ \boldsymbol{q}^i_{m_i,n} \end{bmatrix}^{\mathrm{T}} & \begin{bmatrix} \Delta t^i_1 \\ \Delta t^i_2 \\ \vdots \\ \Delta t^i_{m_i} \end{bmatrix}^{\mathrm{T}} \end{bmatrix} \tag{4.17}$$

where $n = 7$. The free variable vector for the entire trajectory is then defined as

$$\boldsymbol{V} = \begin{bmatrix} \boldsymbol{V}^1 & \boldsymbol{V}^2 & \cdots & \boldsymbol{V}^{n_{\mathrm{seg}}} \end{bmatrix}^{\mathrm{T}} \tag{4.18}$$

to produce a n_{free}-dimensional vector for n_{seg} segments where $n_{\mathrm{free}} = (3n-2)m + 6n_{\mathrm{seg}}$.

To compute a continuous trajectory described by $\boldsymbol{V}$, a set of continuity constraints must be satisfied. Continuity is automatically enforced between arcs within a segment due to the use of LGL nodes because each pair of consecutive arcs shares a common free boundary node [35]. However, continuity is not automatically enforced between consecutive segments, as depicted conceptually in Figure 4.1 between nodes $\boldsymbol{q}^i_{m_i,n}$ and $\boldsymbol{q}^{i+1}_{1,1}$. Therefore, the continuity constraint is defined between each pair of consecutive segments as

$$\boldsymbol{F}^i_{\mathbf{c}} = \begin{cases} \boldsymbol{q}^{i+1}_{1,1} - \boldsymbol{q}^i_{m_i,n} & \text{if natural motion} \\ \boldsymbol{r}^{i+1}_{1,1} - \boldsymbol{r}^i_{m_i,n} & \text{if impulsive maneuver applied} \end{cases} \tag{4.19}$$

where $\boldsymbol{r}$ contains only the position components of $\boldsymbol{q}$ if an impulsive maneuver is applied prior to the beginning of the $(i+1)$-th segment.

Defect constraints must also be satisfied along each arc of the entire trajectory to enforce the system dynamics at each defect node. The state of each defect node is computed directly from the constructed polynomials along the corresponding arc. Then, each defect constraint evaluates the difference between the approximated dynamics, computed using the normalized time derivatives of the polynomials, and the actual dynamics, computed at each defect node using Equation 4.10. The defect constraint vector for the j-th arc in the i-th segment is defined as

$$\boldsymbol{F}^i_{\mathbf{d}_j} = \begin{bmatrix} \boldsymbol{\Delta}^i_{j,2} \\ \boldsymbol{\Delta}^i_{j,4} \\ \vdots \\ \boldsymbol{\Delta}^i_{j,n-1} \end{bmatrix} = \begin{bmatrix} (\dot{\boldsymbol{p}}^i_j(\tau_2) - \dot{\boldsymbol{q}}^i_{j,2})w_2 \\ (\dot{\boldsymbol{p}}^i_j(\tau_4) - \dot{\boldsymbol{q}}^i_{j,4})w_4 \\ \vdots \\ (\dot{\boldsymbol{p}}^i_j(\tau_{n-1}) - \dot{\boldsymbol{q}}^i_{j,n-1})w_{n-1} \end{bmatrix} \tag{4.20}$$

where $n = 7$ and each w_k term is the LGL weight associated with the k-th collocation node. Then, the defect constraint vector for the i-th segment is defined as $\boldsymbol{F}^i_{\mathbf{d}} = \begin{bmatrix} \boldsymbol{F}^{i^{\mathrm{T}}}_{\mathbf{d}_1} & \boldsymbol{F}^{i^{\mathrm{T}}}_{\mathbf{d}_2} & \cdots & \boldsymbol{F}^{i^{\mathrm{T}}}_{\mathbf{d}_{m_i}} \end{bmatrix}$.

A constraint vector for the entire trajectory captures both the continuity and defect constraints. This constraint vector is defined as

$$\boldsymbol{F}(\boldsymbol{V}) = \begin{bmatrix} \boldsymbol{F}^{1^{\mathrm{T}}}_{\mathbf{c}} & \boldsymbol{F}^{2^{\mathrm{T}}}_{\mathbf{c}} & \cdots & \boldsymbol{F}^{n_{\mathrm{seg}}-1^{\mathrm{T}}}_{\mathbf{c}} & \boldsymbol{F}^1_{\mathbf{d}} & \boldsymbol{F}^2_{\mathbf{d}} & \cdots & \boldsymbol{F}^{n_{\mathrm{seg}}}_{\mathbf{d}} \end{bmatrix}^{\mathrm{T}} \tag{4.21}$$

to produce a n_{con}-dimensional vector, where $n_{\text{con}} = (3n-3)m + 6(n_{\text{seg}}-1) - 3n_{\text{man}}$ and n_{man} is the number of impulsive maneuvers applied along the trajectory. Using a corrections algorithm, the free variable vector may be iteratively updated from an initial guess to compute a trajectory that satisfies these constraints to within a tolerance of 10^{-12} in the CR3BP.

The free variable and constraint vectors defined in Equations 4.18 and 4.21, respectively, may be modified in a straightforward manner to also include impulsive maneuvers between consecutive arcs within a given segment. For example, consider the general case of an impulsive maneuver applied between arcs j and $j+1$ along the i-th segment. In this case, $\boldsymbol{q}^i_{j,n}$ is included in Equation 4.18 and considered distinct from $\boldsymbol{q}^i_{j+1,1}$; therefore, a position continuity constraint defined as $\boldsymbol{F}^i_{\mathbf{c}_j} = \boldsymbol{r}^i_{j+1,1} - \boldsymbol{r}^i_{j,n}$ must be included in Equation 4.21 to account for the desired maneuver. Accordingly, the free variable and constraint vector formulation of collocation presented in this subsection defines the constraints that must be satisfied in order for a trajectory described by $\boldsymbol{V}$ to numerically correspond to a continuous solution that may include impulsive maneuvers. Additional path and boundary constraints may also be incorporated in Equation 4.21 depending on the design scenario.

The Jacobian matrix of the constraints with respect to the free variables characterizes how variations in the free variables impact the constraints in a corrections problem. The nonzero elements of $[\boldsymbol{DF}(\boldsymbol{V})]$ for the free variable and constraint vector formulation presented in this subsection are computed analytically as:

Nonzero Elements of $[\boldsymbol{DF}(\boldsymbol{V})]$ for the Continuity Constraints in the CR3BP

$$\begin{aligned}
\frac{\partial \boldsymbol{F}^i_{\mathbf{c}}}{\partial \boldsymbol{q}^{i+1}_{1,1}} &= \begin{cases} [\boldsymbol{I}_{6\times 6}] & \text{if natural motion} \\ \begin{bmatrix} [\boldsymbol{I}_{3\times 3}] & [\boldsymbol{0}_{3\times 3}] \end{bmatrix} & \text{if impulsive maneuver applied} \end{cases} \\
\frac{\partial \boldsymbol{F}^i_{\mathbf{c}}}{\partial \boldsymbol{q}^{i}_{m_i,n}} &= \begin{cases} -[\boldsymbol{I}_{6\times 6}] & \text{if natural motion} \\ \begin{bmatrix} -[\boldsymbol{I}_{3\times 3}] & [\boldsymbol{0}_{3\times 3}] \end{bmatrix} & \text{if impulsive maneuver applied} \end{cases} \\
\frac{\partial \boldsymbol{F}^i_{\mathbf{c}_j}}{\partial \boldsymbol{q}^{i}_{j+1,1}} &= \begin{bmatrix} [\boldsymbol{I}_{3\times 3}] & [\boldsymbol{0}_{3\times 3}] \end{bmatrix} \\
\frac{\partial \boldsymbol{F}^i_{\mathbf{c}_j}}{\partial \boldsymbol{q}^{i}_{j,n}} &= \begin{bmatrix} -[\boldsymbol{I}_{3\times 3}] & [\boldsymbol{0}_{3\times 3}] \end{bmatrix}
\end{aligned} \tag{4.22}$$

Nonzero Elements of $[\boldsymbol{DF}(\boldsymbol{V})]$ for the Defect Constraints in the CR3BP

Defect constraints along the j-th arc in the i-th segment:

$$[\boldsymbol{\Delta}^i_j] = \begin{bmatrix} \boldsymbol{\Delta}^i_{j,2} & \boldsymbol{\Delta}^i_{j,4} & \cdots & \boldsymbol{\Delta}^i_{j,n-1} \end{bmatrix} = \left[\boldsymbol{U}_{\mathbf{coll}}{}^i_j\right][\boldsymbol{G}_{\mathbf{coll}}] - \left[\boldsymbol{V}_{\mathbf{coll}}{}^i_j\right][\boldsymbol{W}_{\mathbf{coll}}] \tag{4.23}$$

where

$$\begin{aligned}
\left[\boldsymbol{V}_{\mathbf{coll}}{}^i_j\right] &= \frac{\Delta t^i_j}{2}\begin{bmatrix} \boldsymbol{f}(\boldsymbol{p}^i_j(\tau_2)) & \boldsymbol{f}(\boldsymbol{p}^i_j(\tau_4)) & \cdots & \boldsymbol{f}(\boldsymbol{p}^i_j(\tau_{n-1})) \end{bmatrix} \\
[\boldsymbol{G}_{\mathbf{coll}}] &= [\boldsymbol{A}_{\mathbf{coll}}]^{-1}[\boldsymbol{D}_{\mathbf{coll}}][\boldsymbol{W}_{\mathbf{coll}}] \in \mathbb{R}^{(n+1)\times((n-1)/2)} \\
[\boldsymbol{H}_{\mathbf{coll}}] &= [\boldsymbol{A}_{\mathbf{coll}}]^{-1}[\boldsymbol{B}_{\mathbf{coll}}] \in \mathbb{R}^{(n+1)\times((n-1)/2)} \\
[\boldsymbol{W}_{\mathbf{coll}}] &= \begin{bmatrix} w_2 & 0 & \cdots & 0 \\ 0 & w_4 & \cdots & 0 \\ \vdots & \vdots & \ddots & \vdots \\ 0 & 0 & \cdots & w_{n-1} \end{bmatrix}
\end{aligned} \tag{4.24}$$

Definitions required for computing the nonzero elements of $[\boldsymbol{DF}(\boldsymbol{V})]$ for the defect constraints:

$$\begin{aligned}
&[\boldsymbol{A}] = \text{ Jacobian matrix of CR3BP dynamics defined in Equation 2.29} \\
&k \in \{1,2,3,...,n\} \quad \rightarrow \quad k_{\mathrm{o}} \in \{1,3,...,n\} \quad , \quad k_{\mathrm{e}} \in \{2,4,...,n-1\} \\
&\% \text{ is the modulo operator}
\end{aligned} \tag{4.25}$$

Partial derivative of $\boldsymbol{\Delta}^i_{j,k_\mathrm{e}}$ with respect to $\boldsymbol{q}^i_{j,k_\mathrm{o}}$:

$$\frac{\partial \boldsymbol{\Delta}^i_{j,k_\mathrm{e}}}{\partial \boldsymbol{q}^i_{j,k_\mathrm{o}}} = w_{k_\mathrm{e}} \frac{\partial \dot{\boldsymbol{p}}^i_j(\tau_{k_\mathrm{e}})}{\partial \boldsymbol{q}^i_{j,k_\mathrm{o}}} - w_{k_\mathrm{e}} \frac{\Delta t^i_j}{2} \frac{\partial \boldsymbol{f}(\boldsymbol{p}^i_j(\tau_{k_\mathrm{e}}))}{\partial \boldsymbol{p}^i_j(\tau_{k_\mathrm{e}})} \frac{\partial \boldsymbol{p}^i_j(\tau_{k_\mathrm{e}})}{\partial \boldsymbol{q}^i_{j,k_\mathrm{o}}} \tag{4.26}$$

where

$$\begin{aligned}
w_{k_\mathrm{e}} \frac{\partial \dot{\boldsymbol{p}}^i_j(\tau_{k_\mathrm{e}})}{\partial \boldsymbol{q}^i_{j,k_\mathrm{o}}} &= \left[\boldsymbol{G}_{\mathbf{coll}}\right] \left\{ \frac{k_\mathrm{o}+1}{2}, \frac{k_\mathrm{e}}{2} \right\} [\boldsymbol{I}_{6\times 6}] + \left[\boldsymbol{G}_{\mathbf{coll}}\right] \left\{ \frac{k_\mathrm{o}+9}{2}, \frac{k_\mathrm{e}}{2} \right\} \frac{\Delta t^i_j}{2} [\boldsymbol{A}]\big|_{\boldsymbol{q}^i_{j,k_\mathrm{o}}} \\
\frac{\partial \boldsymbol{f}(\boldsymbol{p}^i_j(\tau_{k_\mathrm{e}}))}{\partial \boldsymbol{p}^i_j(\tau_{k_\mathrm{e}})} &= [\boldsymbol{A}]\big|_{\boldsymbol{p}^i_j(\tau_{k_\mathrm{e}})} \\
\frac{\partial \boldsymbol{p}^i_j(\tau_{k_\mathrm{e}})}{\partial \boldsymbol{q}^i_{j,k_\mathrm{o}}} &= \left[\boldsymbol{H}_{\mathbf{coll}}\right] \left\{ \frac{k_\mathrm{o}+1}{2}, \frac{k_\mathrm{e}}{2} \right\} [\boldsymbol{I}_{6\times 6}] + \left[\boldsymbol{H}_{\mathbf{coll}}\right] \left\{ \frac{k_\mathrm{o}+9}{2}, \frac{k_\mathrm{e}}{2} \right\} \frac{\Delta t^i_j}{2} [\boldsymbol{A}]\big|_{\boldsymbol{q}^i_{j,k_\mathrm{o}}}
\end{aligned} \tag{4.27}$$

Partial derivative of $\boldsymbol{\Delta}^i_{j,k_\mathrm{e}}$ with respect to Δt^i_j:

$$\frac{\partial \boldsymbol{\Delta}^i_{j,k_\mathrm{e}}}{\partial \Delta t^i_j} = w_{k_\mathrm{e}} \frac{\partial \dot{\boldsymbol{p}}^i_j(\tau_{k_\mathrm{e}})}{\partial \Delta t^i_j} - w_{k_\mathrm{e}} \frac{\partial}{\partial \Delta t^i_j} \left(\frac{\Delta t^i_j}{2} \boldsymbol{f}(\boldsymbol{p}^i_j(\tau_{k_\mathrm{e}})) \right) \tag{4.28}$$

where

$$\begin{aligned}
w_{k_\mathrm{e}} \frac{\partial \dot{\boldsymbol{p}}^i_j(\tau_{k_\mathrm{e}})}{\partial \Delta t^i_j} &= \frac{1}{2} \left(\sum_{\substack{k_\mathrm{o}=1, \\ k_\mathrm{o}\%2=1}}^{n} [\boldsymbol{G}_{\mathbf{coll}}] \left\{ \frac{k_\mathrm{o}+9}{2}, \frac{k_\mathrm{e}}{2} \right\} \boldsymbol{f}\left(\boldsymbol{q}^i_{j,k_\mathrm{o}}\right) \right) \\
\frac{\partial}{\partial \Delta t^i_j} \left(\frac{\Delta t^i_j}{2} \boldsymbol{f}(\boldsymbol{p}^i_j(\tau_{k_\mathrm{e}})) \right) &= \frac{1}{2} \boldsymbol{f}(\boldsymbol{p}^i_j(\tau_{k_\mathrm{e}})) + \frac{\Delta t^i_j}{2} [\boldsymbol{A}]\big|_{\boldsymbol{p}^i_j(\tau_{k_\mathrm{e}})} \frac{\partial \boldsymbol{p}^i_j(\tau_{k_\mathrm{e}})}{\partial \Delta t^i_j} \\
\frac{\partial \boldsymbol{p}^i_j(\tau_{k_\mathrm{e}})}{\partial \Delta t^i_j} &= \frac{1}{2} \left(\sum_{\substack{k_\mathrm{o}=1, \\ k_\mathrm{o}\%2=1}}^{n} [\boldsymbol{H}_{\mathbf{coll}}] \left\{ \frac{k_\mathrm{o}+9}{2}, \frac{k_\mathrm{e}}{2} \right\} \boldsymbol{f}\left(\boldsymbol{q}^i_{j,k_\mathrm{o}}\right) \right)
\end{aligned} \tag{4.29}$$

4.1.4 Mesh Refinement

The numerical accuracy of a trajectory computed using collocation depends on its mesh of boundary nodes, Π, as well as the collocation scheme used to place nodes along each arc in Π. Despite the defect constraints being satisfied along each arc in Π, a solution may not accurately approximate the system dynamics between collocation nodes, particularly in sensitive regions of the dynamical system [87]. Therefore, a mesh refinement procedure is coupled with collocation to improve the accuracy of the solution. In this work, a hybrid mesh refinement algorithm is employed that closely follows the procedure presented by Grebow and Pavlak, which uses both analytical and numerical analysis to control the error along a trajectory computed using collocation [35, 87].

Once a solution is computed via corrections, Π is iteratively refined to ensure the resulting solution constructed using sets of piecewise polynomials is numerically accurate. The trajectory discretization process presented in Section 4.1.1 produces a total of m arcs along a trajectory and Π is comprised of the resulting boundary nodes. To facilitate a clear discussion of the mesh refinement process an alternative index notation is first introduced. The index notation introduced in Section 4.1.1 to differentiate between segments of the trajectory, arcs along each segment, and nodes along each arc is critical for defining the corrections problem because a primitive-based initial guess is comprised of a set of discontinuous trajectory segments. However, the mesh refinement procedure is primarily concerned with the state and time of each boundary node as well as the integration time along each arc, i.e., Δt_j^i. Therefore, to simplify notation for discussing the mesh refinement process, the index a is used to denote the index of a given arc along the entire trajectory such that $a \in [1, m]$. Consequently, for the purpose of mesh refinement, the state and time associated with the k-th collocation node along the a-th arc of the trajectory are denoted as $\boldsymbol{q}_{a,k}$ and $t_{a,k}$, respectively, where $k \in [1, n]$. The boundary nodes of the a-th arc correspond to $k = 1$ and $k = n$. Furthermore, the integration time along the a-th arc is alternatively denoted as $\Delta t_a = t_{a,n} - t_{a,1}$. Using this alternative index notation, an overview of the mesh refinement procedure is presented in this subsection.

Given an initial corrected trajectory, the first step of the mesh refinement procedure is to use Carl de Boor's method to iteratively distribute error equally between the arcs along the current solution [21, 92, 35]. During this process, the number of arcs in the mesh and the total flight time for the trajectory are constant, whereas the integration time along each arc varies. At each iteration of de Boor's method, the error along the a-th arc is calculated as

$$e_a = K(\Delta t_a)^{n+1}\xi_a \tag{4.30}$$

where K is a constant that depends on the selected polynomial degree and type and ξ_a is a scalar approximation of the $(n+1)$-th unnormalized time derivative of $\boldsymbol{p}_a(\tau)$. A detailed overview of the method for computing K is provided by Russell and Christiansen: $K = 2.935793951418951 \times 10^{-9}$

for polynomials constructed using 7-th order LGL node spacing [92]. Furthermore, ξ_a is defined as

$$\xi_a = \begin{cases} 2\max\left(\frac{\left|\boldsymbol{p}_{a+1}(\tau)^{(n)} - \boldsymbol{p}_a(\tau)^{(n)}\right|}{\Delta t_a + \Delta t_{a+1}}\right) & \text{if } a = 1 \\ \max\left(\frac{\left|\boldsymbol{p}_a(\tau)^{(n)} - \boldsymbol{p}_{a-1}(\tau)^{(n)}\right|}{\Delta t_{a-1} + \Delta t_a}\right) + \max\left(\frac{\left|\boldsymbol{p}_{a+1}(\tau)^{(n)} - \boldsymbol{p}_a(\tau)^{(n)}\right|}{\Delta t_a + \Delta t_{a+1}}\right) & \text{if } 1 < a < m \\ 2\max\left(\frac{\left|\boldsymbol{p}_a(\tau)^{(n)} - \boldsymbol{p}_{a-1}(\tau)^{(n)}\right|}{\Delta t_{a-1} + \Delta t_a}\right) & \text{if } a = m \end{cases} \tag{4.31}$$

where

$$\boldsymbol{p}_a(\tau)^{(n)} = \frac{2^n}{(\Delta t_a)^n}\left[\boldsymbol{C}_{\mathbf{coll}}{}^i_j\right]\boldsymbol{\tau}^{(n)} \tag{4.32}$$

such that

$$\boldsymbol{\tau}^{(n)} = \begin{bmatrix}[\mathbf{0}_{1\times n}] & n!\end{bmatrix}^{\mathrm{T}} \tag{4.33}$$

[21, 92, 35]. Equation 4.32 defines the n-th unnormalized time derivative of $\boldsymbol{p}_a(\tau)$. Using these equations, an estimate of the error due to the use of a polynomial approximation may be computed for each arc along the current trajectory.

Once the error for each arc along the current trajectory is computed, the mesh is updated to equally distribute the current total error between the arcs along the trajectory. The time at the first boundary node of the a-th arc is updated such that $t_{a,1} = t_{\text{bnd}}$ where t_{bnd} satisfies the following equation:

$$I(t_{\text{bnd}}) = \frac{(a-1)}{m} I(t_{m,n}) \quad \text{s.t.} \quad I(t) = \int_{t_{1,1}}^{t} \xi(s)^{\frac{1}{n+1}}\, ds \tag{4.34}$$

where $\xi(s)$ is a piecewise constant function equal to ξ_a when $s \in [t_{a,1}, t_{a,n}]$ [21, 92, 35]. These updated times form a new time distribution of boundary nodes and supply a foundation for updating the collocation nodes to equally distribute error along the trajectory. Given a new time distribution of boundary nodes, the polynomials of the previous mesh are used to compute the updated state at each boundary node along the trajectory. The free LGL nodes for each arc are then recomputed using the polynomials of the previous mesh between the updated boundary nodes. This process equally distributes the approximated error along the entire solution between all arcs in the mesh.

Once the mesh is updated, the differential corrections process outlined in Section 4.1.3 is used to compute a refined continuous trajectory with the updated mesh as an initial guess. This error

distribution process repeats until one of the following terminal conditions is met: the maximum error difference along the current solution between any two arcs is $\leq 10^{-5}$; the maximum error difference along the current solution changed by $\leq 10\%$ from the previous iteration; or a maximum number of iterations, selected in this work as 5, is exceeded. The values for these termination criteria are selected empirically based on the convergence behavior of the transfers constructed in this work. The equal error distribution process is summarized as follows using de Boor's method:

Equal Error Distribution Refinement for a Natural Trajectory

Given: A mesh Π for a corrected trajectory with no impulsive maneuvers between $t_{1,1}$ and $t_{m,n}$. Note: Impulsive maneuvers may occur at $t_{1,1}$ and $t_{m,n}$ but the trajectory is natural between $t_{1,1}$ and $t_{m,n}$.

(1) Using Equation 4.30, compute the error e_a for each arc along the current trajectory defined by Π.

(2) Compute the maximum error difference, $\Delta e_{\max}$, between any two given arcs along Π. The error difference between two arcs, a_1 and a_2, along Π is computed as $\Delta e = |e_{a_1} - e_{a_2}|$.

(3) Terminate the equal error distribution procedure if $\Delta e_{\max} \leq 10^{-5}$, $\Delta e_{\max}$ changed by $\leq 10\%$ from the previous iteration, or the maximum number of iterations is reached. Otherwise, execute Steps 4-7 of the procedure.

(4) Using Equation 4.34 and the assumption that $\xi(s)$ is a piecewise constant function along each arc, compute the boundary nodes for a new mesh Π_{new}:

   (a) Define $\boldsymbol{q}_{1,1}$ and $t_{1,1}$ in Π_{new} based on Π. The initial boundary node in Π_{new} and Π are equivalent.

   (b) Define $\boldsymbol{q}_{m,n}$ and $t_{m,n}$ in Π_{new} based on Π. The final boundary node in Π_{new} and Π are equivalent.

   (c) Compute $I(t_{m,n}) = \sum_{a=1}^{m} \xi_a^{\frac{1}{n+1}} \Delta t_a$ based on Π.

   (d) For $a \in [2, m]$:

(i) Compute $I(t_{\text{bnd}}) = \frac{(a-1)}{m} I(t_{m,n})$ based on Π.

(ii) Locate the arc index, a^*, along Π such that $I(t_{a^*,1}) < I(t_{\text{bnd}}) \leq I(t_{a^*,n})$.

(iii) Solve for t_{bnd} such that $(I(t_{\text{bnd}}) - I(t_{a^*,1})) = \xi_{a^*}^{\frac{1}{n+1}} (t_{\text{bnd}} - t_{a^*,1})$.

(iv) Compute $\tau_{\text{bnd}} = 2\left(\frac{t_{\text{bnd}} - t_{a^*,1}}{\Delta t_{a^*}}\right) - 1$.

(v) Define $\boldsymbol{q}_{a,1}$ and $t_{a,1}$ in Π_{new} such that $\boldsymbol{q}_{a,1} = \boldsymbol{p}_{a^*}(\tau_{\text{bnd}})$ and $t_{a,1} = t_{\text{bnd}}$, where $\boldsymbol{p}_{a^*}(\tau_{\text{bnd}})$ is computed from the polynomials constructed along the arc a^* in Π.

(vi) If arcs $a-1$ and a do not share a common free boundary node in Π, then define $\boldsymbol{q}_{a-1,n}$ and $t_{a-1,n}$ in Π_{new} such that $\boldsymbol{q}_{a-1,n} = \boldsymbol{p}_{a^*}(\tau_{\text{bnd}})$ and $t_{a-1,n} = t_{\text{bnd}}$. Note: Arcs $a-1$ and a do not share a common free boundary node if arc a is the start of a new segment.

(5) Compute the free nodes along each arc in Π_{new}. Using an odd-degree LGL node spacing strategy, the boundary nodes are considered collocation nodes and are classified as free nodes. Therefore, only the internal free nodes along each arc must be computed in this step. For each τ_k along the a-th arc:

(a) Compute $t_{a,k} = \left(\frac{\tau_k + 1}{2}\right) \Delta t_a + t_{a,1}$ where $t_{a,1}$ and Δt_a are obtained from Π_{new}.

(b) Locate the arc index, a^*, along Π such that $t_{a,k}$ occurs within the arc.

(c) Compute $\tau_{k^*} = 2\left(\frac{t_{a,k} - t_{a^*,1}}{\Delta t_{a^*}}\right) - 1$.

(d) Compute $\boldsymbol{q}_{a,k} = \boldsymbol{p}_{a^*}(\tau_{k^*})$, where $\boldsymbol{p}_{a^*}(\tau_{k^*})$ is computed from the polynomials constructed along the arc a^* in Π.

(6) Compute the new sets of polynomials along each arc in Π_{new} using the updated collocation nodes computed in the previous steps.

(7) Construct an initial guess from Π_{new} and use the differential corrections process outlined in Section 4.1.3 to compute a refined continuous trajectory. Then, return to Step 1 where the mesh of the refined continuous trajectory is defined as Π.

This procedure outlines the process of using de Boor's method to equally distribute error between arcs defined along a natural trajectory.

In this work, a trajectory may contain impulsive maneuvers between $t_{1,1}$ and $t_{m,n}$. Therefore, a slightly modified error distribution approach may be used to equally distribute error between arcs defined along a maneuver-enabled trajectory. The first modification occurs in Step 2: the maximum error difference between any two given arcs is computed between each pair of consecutive maneuvers and then $\Delta e_{\max}$ is defined for the current trajectory as the maximum value of these error differences. The second and final modification of the procedure occurs in Step 4: during each iteration of the procedure, Step 4 is applied separately to the sequence of arcs between each pair of consecutive impulsive maneuvers. For example, consider a pair of consecutive impulsive maneuvers where the first maneuver occurs at the beginning of arc $a_{\Delta v_i}$ and the second maneuver occurs at the end of arc $a_{\Delta v_{i+1}}$. In this case, the boundary nodes are adjusted between $t_{a_{\Delta v_i},1}$ and $t_{a_{\Delta v_{i+1}},n}$ instead of between $t_{1,1}$ and $t_{m,n}$. Therefore, the modified procedure equally distributes the cumulative error between each pair of consecutive maneuvers rather than along the entire solution. Given these modifications, de Boor's method may be used to effectively distribute error between arcs defined along either a natural or a maneuver-enabled trajectory.

When the equal error distribution step is terminated, the next step of the mesh refinement procedure is to use Control with Explicit Propagation (CEP) to iteratively merge arcs along the mesh in order to reduce the size of the sparse corrections problem [35, 87]. This step of mesh refinement numerically computes the error at the end of each pair of consecutive arcs in the mesh, except when an impulsive maneuver occurs between them. For example, the state at the initial boundary node of the first arc is propagated until the time associated with the final boundary node of the second arc. Then, the state error is computed between the final propagated state and the state associated with the final boundary node of the second arc. If the magnitude of the error vector is below a tolerance of 10^{-13}, then the two arcs are merged into a single arc. In this case, the initial boundary node of the first arc and the final boundary node of the second arc serve as the initial and final boundary nodes, respectively, of the merged arc. Then, the free LGL nodes are

recomputed between the updated boundary nodes using the polynomials of the previously converged mesh and the procedure is repeated for the next two consecutive arcs in the mesh. If any arcs are merged along the entire trajectory, then the updated mesh is used to compute a refined continuous trajectory by reapplying the differential corrections process outlined in Section 4.1.3. The merging process is repeated until no arcs are merged along the solution or a maximum number of iterations is exceeded. In this work, the maximum number of merging iterations is selected empirically as 10 based on the convergence behavior of the transfers computed in this investigation.

After completing the merging process, CEP is also used to iteratively split arcs along the mesh by numerically computing the error at the end of each arc. For example, the state at the initial boundary node of an arc is propagated until the time associated with the final boundary node of the arc. Then, the state error is computed between the final propagated state and the state at the final boundary node of the arc. If the magnitude of the error vector is above a tolerance of 10^{-12}, then the arc is split into two separate arcs at its midpoint in terms of time. The polynomials from the previously converged mesh are used to compute the state and time at the midpoint of the arc and then the free LGL nodes are recomputed for each of the resulting arcs as previously described. If any arcs are split along the entire trajectory, then the updated mesh is used to compute a refined continuous trajectory by reapplying the differential corrections process outlined in Section 4.1.3. This process is repeated until no arcs are split along the solution. Similar to the merging loop, the splitting process is also terminated if a maximum of 10 iterations is exceeded.

The goal of the hybrid mesh refinement process presented in this subsection is to ensure a trajectory computed using collocation is numerically accurate. Therefore, the mesh refinement process is terminated early if a trajectory fails to converge when computing a refined continuous trajectory from an updated mesh. Furthermore, a trajectory that successfully completes the mesh refinement process may not achieve the desired level of accuracy due to the maximum iteration limits set within each step. Consequently, a final evaluation of the resulting trajectory is required. Using CEP, the state error is computed at the end of each arc and if the magnitude of the error vector is above a tolerance of 10^{-12} along any arc then the trajectory is considered unconverged.

In this case, the maximum iteration limits may be adjusted and the mesh refinement procedure may be reapplied. However, the tolerances and termination criteria defined for de Boor's method and CEP are considered design parameters and are selected in this work empirically based on the convergence behavior of the transfers constructed in this investigation.

4.2 Correcting Trajectories in an Ephemeris Model

4.2.1 Initial Guess Generation from the CR3BP

A continuous trajectory computed in the CR3BP may be used as an initial guess to attempt to recover a similar solution in a point mass ephemeris model [61, 106]. However, as discussed in Section 2.2, a point mass ephemeris model is a higher fidelity approximation of a multi-body system that is nonautonomous. Therefore, transitioning a trajectory from the CR3BP into a point mass ephemeris model depends on the initial epoch. In some cases, the geometry of a trajectory is well-preserved between the CR3BP and the selected ephemeris model. However, in other cases, the initial guess from the CR3BP may not lead to successful convergence or the trajectory recovered in the ephemeris model may no longer resemble the initial guess. In this subsection, a procedure for transitioning a trajectory from the CR3BP into an ephemeris model to form an initial guess is discussed.

The first step of transitioning a trajectory from the CR3BP into a point mass ephemeris model is to specify a desired reference epoch, $\tilde{t}_{\mathrm{E}_{\mathrm{ref}}}$, and select a list of primary bodies (P_1, P_2, ..., P_N). As discussed in Section 2.2.2, the reference epoch is specified as a Gregorian calendar date in UTC and then converted into ephemeris time using SPICE [106, 76]. Furthermore, as discussed in Section 2.3.3, the primary bodies in the reference CR3BP system are denoted as P_{A} and P_{B}. If $\tilde{M}_1 \geq \tilde{M}_2$, P_1 corresponds to P_{A} in the reference CR3BP system; otherwise, P_1 corresponds to P_{B}. Given these specifications, a continuous trajectory computed in the CR3BP may be transformed from $\mathcal{R}$ into $\mathcal{E}$.

The continuous trajectory computed in the CR3BP is a nondimensional trajectory in $\mathcal{R}$

defined relative to the origin of $\mathcal{R}$ from an initial time, t_1, to a final time, t_2. Using Equation 2.42, the nondimensional times, t_1 and t_2, are converted into the corresponding epochs, $\tilde{t}_{\mathrm{E}_1}$ and $\tilde{t}_{\mathrm{E}_2}$, based on $\tilde{t}_{\mathrm{E}_{\mathrm{ref}}}$. The procedure presented in Section 2.3.3 to transform a trajectory from the rotating frame to a primary-centered inertial frame that uses the axes of the ICRF is then applied to the trajectory. The state at each free node along the continuous trajectory is transformed from $\mathcal{R}$ into $\mathcal{E}$. The corresponding trajectory is no longer continuous when transformed into $\mathcal{E}$; however, this process provides an initial guess of free nodes in $\mathcal{E}$ defined relative to the origin of $\mathcal{E}$ from t_1 to t_2 with a reference epoch $\tilde{t}_{\mathrm{E}_{\mathrm{ref}}}$. Given the initial guess, a continuous trajectory may be computed in the specified point mass ephemeris model using the same collocation scheme and a similar differential corrections strategy as presented for the CR3BP in Section 4.1.

4.2.2 Trajectory Corrections

To formulate a corrections problem that uses collocation in a point mass ephemeris model, a free variable vector is defined using the state at each free node and the initial time of each of the m arcs of a trajectory. Mathematically, the free variable vector $\boldsymbol{V}^i$ for the i-th segment, composed of m_i arcs, is defined as

$$\boldsymbol{V}^i = \left[\begin{bmatrix} \boldsymbol{q\varepsilon}^i_{1,1} \\ \boldsymbol{q\varepsilon}^i_{1,3} \\ \vdots \\ \boldsymbol{q\varepsilon}^i_{1,n-2} \end{bmatrix}^{\mathrm{T}} \begin{bmatrix} \boldsymbol{q\varepsilon}^i_{2,1} \\ \boldsymbol{q\varepsilon}^i_{2,3} \\ \vdots \\ \boldsymbol{q\varepsilon}^i_{2,n-2} \end{bmatrix}^{\mathrm{T}} \cdots \begin{bmatrix} \boldsymbol{q\varepsilon}^i_{m_i-1,1} \\ \boldsymbol{q\varepsilon}^i_{m_i-1,3} \\ \vdots \\ \boldsymbol{q\varepsilon}^i_{m_i-1,n-2} \end{bmatrix}^{\mathrm{T}} \begin{bmatrix} \boldsymbol{q\varepsilon}^i_{m_i,1} \\ \boldsymbol{q\varepsilon}^i_{m_i,3} \\ \vdots \\ \boldsymbol{q\varepsilon}^i_{m_i,n} \end{bmatrix}^{\mathrm{T}} \begin{bmatrix} t^i_{1,1} \\ t^i_{2,1} \\ \vdots \\ t^i_{m_i,1} \end{bmatrix}^{\mathrm{T}} \right] \tag{4.35}$$

where $n = 7$. The free variable vector for the entire trajectory is then defined as

$$\boldsymbol{V} = \begin{bmatrix} \boldsymbol{V}^1 & \boldsymbol{V}^2 & \cdots & \boldsymbol{V}^{n_{\mathrm{seg}}} & t^{n_{\mathrm{seg}}}_{m,n} \end{bmatrix}^{\mathrm{T}} \tag{4.36}$$

to produce a n_{free}-dimensional vector for n_{seg} segments where $n_{\mathrm{free}} = (3n-2)m + 6n_{\mathrm{seg}} + 1$.

To compute a continuous trajectory described by $\boldsymbol{V}$, a set of continuity constraints must be satisfied. As discussed in Section 4.1.3, continuity is automatically enforced between arcs within a segment due to the use of LGL nodes because each pair of consecutive arcs shares a common

free boundary node [35]. However, continuity is not automatically enforced between consecutive segments. Therefore, the continuity constraint is defined between each pair of consecutive segments as

$$\boldsymbol{F}_{\mathbf{c}}^{i} = \begin{cases} \boldsymbol{q}_{\boldsymbol{\mathcal{E}}}{}_{1,1}^{i+1} - \boldsymbol{q}_{\boldsymbol{\mathcal{E}}}{}_{m_i,n}^{i} & \text{if natural motion} \\ \boldsymbol{r}_{\boldsymbol{\mathcal{E}}}{}_{1,1}^{i+1} - \boldsymbol{r}_{\boldsymbol{\mathcal{E}}}{}_{m_i,n}^{i} & \text{if impulsive maneuver applied} \end{cases} \tag{4.37}$$

where $\boldsymbol{r}_{\boldsymbol{\mathcal{E}}}$ contains only the position components of $\boldsymbol{q}_{\boldsymbol{\mathcal{E}}}$ if an impulsive maneuver is applied prior to the beginning of the $(i+1)$-th segment.

Defect constraints must also be satisfied along each arc of the entire trajectory to enforce the system dynamics at each defect node. The defect constraints are defined in the same manner as presented for the CR3BP in Section 4.1.3. However, it is important to note that the differential corrections scheme is formulated in $\mathcal{E}$ for a point mass ephemeris model. Therefore, the time derivatives are denoted using the $(\cdot)'$ notation instead of the $\dot{(\cdot)}$ notation introduced in Chapter 2. The defect constraint vector for the j-th arc in the i-th segment is defined as

$$\boldsymbol{F}_{\mathbf{d}_j}^{i} = \begin{bmatrix} \boldsymbol{\Delta}_{j,2}^{i} \\ \boldsymbol{\Delta}_{j,4}^{i} \\ \vdots \\ \boldsymbol{\Delta}_{j,n-1}^{i} \end{bmatrix} = \begin{bmatrix} \left(\boldsymbol{p}_{\boldsymbol{\mathcal{E}}}{}_{j}^{\prime\, i}(\tau_2) - \boldsymbol{q}_{\boldsymbol{\mathcal{E}}}{}_{j,2}^{\prime\, i}\right) w_2 \\ \left(\boldsymbol{p}_{\boldsymbol{\mathcal{E}}}{}_{j}^{\prime\, i}(\tau_4) - \boldsymbol{q}_{\boldsymbol{\mathcal{E}}}{}_{j,4}^{\prime\, i}\right) w_4 \\ \vdots \\ \left(\boldsymbol{p}_{\boldsymbol{\mathcal{E}}}{}_{j}^{\prime\, i}(\tau_{n-1}) - \boldsymbol{q}_{\boldsymbol{\mathcal{E}}}{}_{j,n-1}^{\prime\, i}\right) w_{n-1} \end{bmatrix} \tag{4.38}$$

where $n = 7$ and each w_k term is the LGL weight associated with the k-th collocation node. Then, the defect constraint vector for the i-th segment is defined as $\boldsymbol{F}_{\mathbf{d}}^{i} = \begin{bmatrix} \boldsymbol{F}_{\mathbf{d}_1}^{i^{\mathrm{T}}} & \boldsymbol{F}_{\mathbf{d}_2}^{i^{\mathrm{T}}} & \cdots & \boldsymbol{F}_{\mathbf{d}_{m_i}}^{i^{\mathrm{T}}} \end{bmatrix}$.

A constraint vector for the entire trajectory captures both the continuity and defect constraints. This constraint vector is defined as

$$\boldsymbol{F}(\boldsymbol{V}) = \begin{bmatrix} \boldsymbol{F}_{\mathbf{c}}^{1^{\mathrm{T}}} & \boldsymbol{F}_{\mathbf{c}}^{2^{\mathrm{T}}} & \cdots & \boldsymbol{F}_{\mathbf{c}}^{n_{\mathrm{seg}}-1^{\mathrm{T}}} & \boldsymbol{F}_{\mathbf{d}}^{1} & \boldsymbol{F}_{\mathbf{d}}^{2} & \cdots & \boldsymbol{F}_{\mathbf{d}}^{n_{\mathrm{seg}}} \end{bmatrix}^{\mathrm{T}} \tag{4.39}$$

to produce a n_{con}-dimensional vector, where $n_{\mathrm{con}} = (3n-3)m + 6(n_{\mathrm{seg}}-1) - 3n_{\mathrm{man}}$ and n_{man} is the number of impulsive maneuvers applied along the trajectory. As discussed in Section 4.1.3, impulsive maneuvers may also be included between consecutive arcs within a given segment. Given an impulsive maneuver applied between arcs j and $j+1$ along the i-th segment, a position continuity

constraint is defined as $\boldsymbol{F}^i_{\mathbf{c}_j} = \boldsymbol{r\varepsilon}^i_{j+1,1} - \boldsymbol{r\varepsilon}^i_{j,n}$. To account for the desired maneuver in the corrections problem formulation, $\boldsymbol{q\varepsilon}^i_{j,n}$ is included in Equation 4.36 and considered distinct from $\boldsymbol{q\varepsilon}^i_{j+1,1}$; furthermore, $\boldsymbol{F}^i_{\mathbf{c}_j}$ is included in Equation 4.39. Using a corrections algorithm, the free variable vector may be iteratively updated from an initial guess to compute a trajectory that satisfies these constraints to within a tolerance of 10^{-8} in a point mass ephemeris model.

The free variable and constraint vector formulation presented in this subsection for correcting a trajectory in a point mass ephemeris model is very similar to the formulation presented for the CR3BP; however, there are a few differences. Due to the nonautonomous structure of a point mass ephemeris model, the times associated with the boundary nodes are included in the free variable vector rather than the integration times along the corresponding arcs. Furthermore, as previously discussed and indicated with the use of the $(\cdot)'$ notation, all time derivatives are computed with respect to an inertial observer fixed in $\mathcal{E}$ rather than with respect to a rotating observer fixed in $\mathcal{R}$. In addition, a larger constraint tolerance of 10^{-8} is used due to an increase in numerical sensitivity when transitioning from the CR3BP into a point mass ephemeris model. Finally, the mesh refinement procedure presented in Section 4.1.4 may be applied in the same manner for either dynamical model. The only differences occur in the selection of the tolerances for removing and adding arcs to the mesh. In a point mass ephemeris model, tolerances of 10^{-9} and 10^{-8} are specified for merging and splitting arcs, respectively, during the CEP refinement procedure. However, as previously discussed, the selection of numerical tolerances and termination criteria for the differential corrections process are considered design parameters that may be adjusted based on the design scenario.

Leveraging collocation for differential corrections results in a sparse corrections problem because the Jacobian matrix of the constraints with respect to the free variables is primarily comprised of elements that are equal to zero. The nonzero elements of $[\boldsymbol{DF}(\boldsymbol{V})]$ for the free variable and constraint vector formulation presented in this subsection are computed analytically as:

Nonzero Elements of $[\boldsymbol{DF}(\boldsymbol{V})]$ for the Continuity Constraints in a Point Mass Ephemeris Model

$$\begin{aligned}
\frac{\partial \boldsymbol{F}^i_{\mathbf{c}}}{\partial \boldsymbol{q\varepsilon}^{i+1}_{1,1}} &= \begin{cases} [\boldsymbol{I}_{6\times 6}] & \text{if natural motion} \\ \begin{bmatrix} [\boldsymbol{I}_{3\times 3}] & [\boldsymbol{0}_{3\times 3}] \end{bmatrix} & \text{if impulsive maneuver applied} \end{cases} \\
\frac{\partial \boldsymbol{F}^i_{\mathbf{c}}}{\partial \boldsymbol{q\varepsilon}^{i}_{m_i,n}} &= \begin{cases} -[\boldsymbol{I}_{6\times 6}] & \text{if natural motion} \\ \begin{bmatrix} -[\boldsymbol{I}_{3\times 3}] & [\boldsymbol{0}_{3\times 3}] \end{bmatrix} & \text{if impulsive maneuver applied} \end{cases} \\
\frac{\partial \boldsymbol{F}^i_{\mathbf{c}_j}}{\partial \boldsymbol{q\varepsilon}^{i}_{j+1,1}} &= \begin{bmatrix} [\boldsymbol{I}_{3\times 3}] & [\boldsymbol{0}_{3\times 3}] \end{bmatrix} \\
\frac{\partial \boldsymbol{F}^i_{\mathbf{c}_j}}{\partial \boldsymbol{q\varepsilon}^{i}_{j,n}} &= \begin{bmatrix} -[\boldsymbol{I}_{3\times 3}] & [\boldsymbol{0}_{3\times 3}] \end{bmatrix}
\end{aligned} \tag{4.40}$$

Nonzero Elements of $[\boldsymbol{DF}(\boldsymbol{V})]$ for the Defect Constraints in a Point Mass Ephemeris Model

Defect constraints along the j-th arc in the i-th segment:

$$[\boldsymbol{\Delta}^i_j] = \begin{bmatrix} \boldsymbol{\Delta}^i_{j,2} & \boldsymbol{\Delta}^i_{j,4} & \cdots & \boldsymbol{\Delta}^i_{j,n-1} \end{bmatrix} = \left[\boldsymbol{U}_{\mathbf{coll}}{}^i_j\right][\boldsymbol{G}_{\mathbf{coll}}] - \left[\boldsymbol{V}_{\mathbf{coll}}{}^i_j\right][\boldsymbol{W}_{\mathbf{coll}}] \tag{4.41}$$

where

$$\begin{aligned}
\left[\boldsymbol{V}_{\mathbf{coll}}{}^i_j\right] &= \frac{\Delta t^i_j}{2}\begin{bmatrix} \boldsymbol{f}(\boldsymbol{p\varepsilon}^i_j(\tau_2), t^i_{j,2}) & \boldsymbol{f}(\boldsymbol{p\varepsilon}^i_j(\tau_4), t^i_{j,4}) & \cdots & \boldsymbol{f}(\boldsymbol{p\varepsilon}^i_j(\tau_{n-1}), t^i_{j,n-1}) \end{bmatrix} \\
[\boldsymbol{G}_{\mathbf{coll}}] &= [\boldsymbol{A}_{\mathbf{coll}}]^{-1}[\boldsymbol{D}_{\mathbf{coll}}][\boldsymbol{W}_{\mathbf{coll}}] \in \mathbb{R}^{(n+1)\times((n-1)/2)} \\
[\boldsymbol{H}_{\mathbf{coll}}] &= [\boldsymbol{A}_{\mathbf{coll}}]^{-1}[\boldsymbol{B}_{\mathbf{coll}}] \in \mathbb{R}^{(n+1)\times((n-1)/2)} \\
[\boldsymbol{W}_{\mathbf{coll}}] &= \begin{bmatrix} w_2 & 0 & \cdots & 0 \\ 0 & w_4 & \cdots & 0 \\ \vdots & \vdots & \ddots & \vdots \\ 0 & 0 & \cdots & w_{n-1} \end{bmatrix}
\end{aligned} \tag{4.42}$$

Definitions required for computing the nonzero elements of $[\boldsymbol{DF}(\boldsymbol{V})]$ for the defect constraints:

$$
\begin{aligned}
&[\boldsymbol{A}(t)] = \text{ Jacobian matrix of point mass ephemeris dynamics defined in Equation 2.43} \\
&[\boldsymbol{A_t}(t)] = \begin{bmatrix} 0 & 0 & 0 & \frac{\partial X''}{\partial t} & \frac{\partial Y''}{\partial t} & \frac{\partial Z''}{\partial t} \end{bmatrix}^{\mathrm{T}} \text{ defined from Equation 2.45} \\
&\frac{\partial t^i_{j,k}}{\partial t^i_{j,1}} = \frac{-\tau_k + 1}{2} \quad , \quad \frac{\partial t^i_{j,k}}{\partial t^i_{j,n}} = \frac{\tau_k + 1}{2} \\
&k \in \{1, 2, 3, ..., n\} \quad \rightarrow \quad k_{\mathrm{o}} \in \{1, 3, ..., n\} \quad , \quad k_{\mathrm{e}} \in \{2, 4, ..., n-1\} \\
&\% \text{ is the modulo operator}
\end{aligned}
\tag{4.43}
$$

Partial derivative of $\boldsymbol{\Delta}^i_{j,k_{\mathrm{e}}}$ with respect to $\boldsymbol{q\varepsilon}^i_{j,k_{\mathrm{o}}}$:

$$
\frac{\partial \boldsymbol{\Delta}^i_{j,k_{\mathrm{e}}}}{\partial \boldsymbol{q\varepsilon}^i_{j,k_{\mathrm{o}}}} = w_{k_{\mathrm{e}}} \frac{\partial \boldsymbol{p'\varepsilon}^{\,i}_{j}(\tau_{k_{\mathrm{e}}})}{\partial \boldsymbol{q\varepsilon}^i_{j,k_{\mathrm{o}}}} - w_{k_{\mathrm{e}}} \frac{\Delta t^i_j}{2} \frac{\partial \boldsymbol{f}\left(\boldsymbol{p\varepsilon}^i_j(\tau_{k_{\mathrm{e}}}), t^i_{j,k_{\mathrm{e}}}\right)}{\partial \boldsymbol{p\varepsilon}^i_j(\tau_{k_{\mathrm{e}}})} \frac{\partial \boldsymbol{p\varepsilon}^i_j(\tau_{k_{\mathrm{e}}})}{\partial \boldsymbol{q\varepsilon}^i_{j,k_{\mathrm{o}}}} \tag{4.44}
$$

where

$$
\begin{aligned}
w_{k_{\mathrm{e}}} \frac{\partial \boldsymbol{p'\varepsilon}^{\,i}_{j}(\tau_{k_{\mathrm{e}}})}{\partial \boldsymbol{q\varepsilon}^i_{j,k_{\mathrm{o}}}} &= \left[\boldsymbol{G_{\mathbf{coll}}}\right] \left\{ \frac{k_{\mathrm{o}}+1}{2}, \frac{k_{\mathrm{e}}}{2} \right\} [\boldsymbol{I}_{6\times 6}] + \left[\boldsymbol{G_{\mathbf{coll}}}\right] \left\{ \frac{k_{\mathrm{o}}+9}{2}, \frac{k_{\mathrm{e}}}{2} \right\} \frac{\Delta t^i_j}{2} [\boldsymbol{A}(t)]\big|_{\boldsymbol{q\varepsilon}^i_{j,k_{\mathrm{o}}}, t^i_{j,k_{\mathrm{o}}}} \\
\frac{\partial \boldsymbol{f}\left(\boldsymbol{p\varepsilon}^i_j(\tau_{k_{\mathrm{e}}}), t^i_{j,k_{\mathrm{e}}}\right)}{\partial \boldsymbol{p\varepsilon}^i_j(\tau_{k_{\mathrm{e}}})} &= [\boldsymbol{A}(t)]\big|_{\boldsymbol{p\varepsilon}^i_j(\tau_{k_{\mathrm{e}}}), t^i_{j,k_{\mathrm{e}}}} \\
\frac{\partial \boldsymbol{p\varepsilon}^i_j(\tau_{k_{\mathrm{e}}})}{\partial \boldsymbol{q\varepsilon}^i_{j,k_{\mathrm{o}}}} &= \left[\boldsymbol{H_{\mathbf{coll}}}\right] \left\{ \frac{k_{\mathrm{o}}+1}{2}, \frac{k_{\mathrm{e}}}{2} \right\} [\boldsymbol{I}_{6\times 6}] + \left[\boldsymbol{H_{\mathbf{coll}}}\right] \left\{ \frac{k_{\mathrm{o}}+9}{2}, \frac{k_{\mathrm{e}}}{2} \right\} \frac{\Delta t^i_j}{2} [\boldsymbol{A}(t)]\big|_{\boldsymbol{q\varepsilon}^i_{j,k_{\mathrm{o}}}, t^i_{j,k_{\mathrm{o}}}}
\end{aligned}
\tag{4.45}
$$

Partial derivative of $\boldsymbol{\Delta}^i_{j,k_{\mathrm{e}}}$ with respect to $t^i_{j,1}$:

$$
\frac{\partial \boldsymbol{\Delta}^i_{j,k_{\mathrm{e}}}}{\partial t^i_{j,1}} = w_{k_{\mathrm{e}}} \frac{\partial \boldsymbol{p'\varepsilon}^{\,i}_{j}(\tau_{k_{\mathrm{e}}})}{\partial t^i_{j,1}} - w_{k_{\mathrm{e}}} \frac{\partial}{\partial t^i_{j,1}} \left(\frac{\Delta t^i_j}{2} \boldsymbol{f}\left(\boldsymbol{p\varepsilon}^i_j(\tau_{k_{\mathrm{e}}}), t^i_{j,k_{\mathrm{e}}}\right) \right) \tag{4.46}
$$

where

$$
\begin{aligned}
w_{k_{\mathrm{e}}} \frac{\partial \boldsymbol{p'\varepsilon}^{\,i}_{j}(\tau_{k_{\mathrm{e}}})}{\partial t^i_{j,1}} &= \sum_{\substack{k_{\mathrm{o}}=1, \\ k_{\mathrm{o}}\%2=1}}^{n} \left[\boldsymbol{G_{\mathbf{coll}}}\right] \left\{ \frac{k_{\mathrm{o}}+9}{2}, \frac{k_{\mathrm{e}}}{2} \right\} \left(\frac{-1}{2} \boldsymbol{f}\left(\boldsymbol{q\varepsilon}^i_{j,k_{\mathrm{o}}}, t^i_{j,k_{\mathrm{o}}}\right) + \frac{\Delta t^i_j}{2} \frac{\partial \boldsymbol{f}(\boldsymbol{q\varepsilon}^i_{j,k_{\mathrm{o}}}, t^i_{j,k_{\mathrm{o}}})}{\partial t^i_{j,1}} \right) \\
\frac{\partial \boldsymbol{f}(\boldsymbol{q\varepsilon}^i_{j,k_{\mathrm{o}}}, t^i_{j,k_{\mathrm{o}}})}{\partial t^i_{j,1}} &= [\boldsymbol{A_t}(t)]\big|_{\boldsymbol{q\varepsilon}^i_{j,k_{\mathrm{o}}}, t^i_{j,k_{\mathrm{o}}}} \frac{\partial t^i_{j,k_{\mathrm{o}}}}{\partial t^i_{j,1}} \\
\frac{\partial}{\partial t^i_{j,1}} \left(\frac{\Delta t^i_j}{2} \boldsymbol{f}\left(\boldsymbol{p\varepsilon}^i_j(\tau_{k_{\mathrm{e}}}), t^i_{j,k_{\mathrm{e}}}\right) \right) &= \frac{-1}{2} \boldsymbol{f}\left(\boldsymbol{p\varepsilon}^i_j(\tau_{k_{\mathrm{e}}}), t^i_{j,k_{\mathrm{e}}}\right) + \frac{\Delta t^i_j}{2} \frac{\partial \boldsymbol{f}\left(\boldsymbol{p\varepsilon}^i_j(\tau_{k_{\mathrm{e}}}), t^i_{j,k_{\mathrm{e}}}\right)}{\partial t^i_{j,1}}
\end{aligned}
\tag{4.47}
$$

such that

$$\begin{aligned}
\frac{\partial \boldsymbol{f}\left(\boldsymbol{p\varepsilon}_j^i(\tau_{k_\mathrm{e}}), t_{j,k_\mathrm{e}}^i\right)}{\partial t_{j,1}^i} &= [\boldsymbol{A}_\mathbf{t}(t)]\big|_{\boldsymbol{p\varepsilon}_j^i(\tau_{k_\mathrm{e}}), t_{j,k_\mathrm{e}}^i} \frac{\partial t_{j,k_\mathrm{e}}^i}{\partial t_{j,1}^i} + [\boldsymbol{A}(t)]\big|_{\boldsymbol{p\varepsilon}_j^i(\tau_{k_\mathrm{e}}), t_{j,k_\mathrm{e}}^i} \frac{\partial \boldsymbol{p\varepsilon}_j^i(\tau_{k_\mathrm{e}})}{\partial t_{j,1}^i} \\
\frac{\partial \boldsymbol{p\varepsilon}_j^i(\tau_{k_\mathrm{e}})}{\partial t_{j,1}^i} &= \sum_{\substack{k_\mathrm{o}=1,\\ k_\mathrm{o}\%2=1}}^{n} [\boldsymbol{H}_\mathbf{coll}]\left\{\frac{k_\mathrm{o}+9}{2}, \frac{k_\mathrm{e}}{2}\right\}\left(\frac{-1}{2}\boldsymbol{f}\left(\boldsymbol{q\varepsilon}_{j,k_\mathrm{o}}^i, t_{j,k_\mathrm{o}}^i\right) + \frac{\Delta t_j^i}{2}\frac{\partial \boldsymbol{f}(\boldsymbol{q\varepsilon}_{j,k_\mathrm{o}}^i, t_{j,k_\mathrm{o}}^i)}{\partial t_{j,1}^i}\right)
\end{aligned} \tag{4.48}$$

Partial derivative of $\boldsymbol{\Delta}_{j,k_\mathrm{e}}^i$ with respect to $t_{j,n}^i$:

$$\frac{\partial \boldsymbol{\Delta}_{j,k_\mathrm{e}}^i}{\partial t_{j,n}^i} = w_{k_\mathrm{e}}\frac{\partial \boldsymbol{p'\varepsilon}_j^{\,i}(\tau_{k_\mathrm{e}})}{\partial t_{j,n}^i} - w_{k_\mathrm{e}}\frac{\partial}{\partial t_{j,n}^i}\left(\frac{\Delta t_j^i}{2}\boldsymbol{f}\left(\boldsymbol{p\varepsilon}_j^i(\tau_{k_\mathrm{e}}), t_{j,k_\mathrm{e}}^i\right)\right) \tag{4.49}$$

where

$$\begin{aligned}
w_{k_\mathrm{e}}\frac{\partial \boldsymbol{p'\varepsilon}_j^{\,i}(\tau_{k_\mathrm{e}})}{\partial t_{j,n}^i} &= \sum_{\substack{k_\mathrm{o}=1,\\ k_\mathrm{o}\%2=1}}^{n} [\boldsymbol{G}_\mathbf{coll}]\left\{\frac{k_\mathrm{o}+9}{2}, \frac{k_\mathrm{e}}{2}\right\}\left(\frac{1}{2}\boldsymbol{f}\left(\boldsymbol{q\varepsilon}_{j,k_\mathrm{o}}^i, t_{j,k_\mathrm{o}}^i\right) + \frac{\Delta t_j^i}{2}\frac{\partial \boldsymbol{f}(\boldsymbol{q\varepsilon}_{j,k_\mathrm{o}}^i, t_{j,k_\mathrm{o}}^i)}{\partial t_{j,n}^i}\right) \\
\frac{\partial \boldsymbol{f}(\boldsymbol{q\varepsilon}_{j,k_\mathrm{o}}^i, t_{j,k_\mathrm{o}}^i)}{\partial t_{j,n}^i} &= [\boldsymbol{A}_\mathbf{t}(t)]\big|_{\boldsymbol{q\varepsilon}_{j,k_\mathrm{o}}^i, t_{j,k_\mathrm{o}}^i}\frac{\partial t_{j,k_\mathrm{o}}^i}{\partial t_{j,n}^i} \\
\frac{\partial}{\partial t_{j,n}^i}\left(\frac{\Delta t_j^i}{2}\boldsymbol{f}\left(\boldsymbol{p\varepsilon}_j^i(\tau_{k_\mathrm{e}}), t_{j,k_\mathrm{e}}^i\right)\right) &= \frac{1}{2}\boldsymbol{f}\left(\boldsymbol{p\varepsilon}_j^i(\tau_{k_\mathrm{e}}), t_{j,k_\mathrm{e}}^i\right) + \frac{\Delta t_j^i}{2}\frac{\partial \boldsymbol{f}\left(\boldsymbol{p\varepsilon}_j^i(\tau_{k_\mathrm{e}}), t_{j,k_\mathrm{e}}^i\right)}{\partial t_{j,n}^i}
\end{aligned} \tag{4.50}$$

such that

$$\begin{aligned}
\frac{\partial \boldsymbol{f}\left(\boldsymbol{p\varepsilon}_j^i(\tau_{k_\mathrm{e}}), t_{j,k_\mathrm{e}}^i\right)}{\partial t_{j,n}^i} &= [\boldsymbol{A}_\mathbf{t}(t)]\big|_{\boldsymbol{p\varepsilon}_j^i(\tau_{k_\mathrm{e}}), t_{j,k_\mathrm{e}}^i} \frac{\partial t_{j,k_\mathrm{e}}^i}{\partial t_{j,n}^i} + [\boldsymbol{A}(t)]\big|_{\boldsymbol{p\varepsilon}_j^i(\tau_{k_\mathrm{e}}), t_{j,k_\mathrm{e}}^i} \frac{\partial \boldsymbol{p\varepsilon}_j^i(\tau_{k_\mathrm{e}})}{\partial t_{j,n}^i} \\
\frac{\partial \boldsymbol{p\varepsilon}_j^i(\tau_{k_\mathrm{e}})}{\partial t_{j,n}^i} &= \sum_{\substack{k_\mathrm{o}=1,\\ k_\mathrm{o}\%2=1}}^{n} [\boldsymbol{H}_\mathbf{coll}]\left\{\frac{k_\mathrm{o}+9}{2}, \frac{k_\mathrm{e}}{2}\right\}\left(\frac{1}{2}\boldsymbol{f}\left(\boldsymbol{q\varepsilon}_{j,k_\mathrm{o}}^i, t_{j,k_\mathrm{o}}^i\right) + \frac{\Delta t_j^i}{2}\frac{\partial \boldsymbol{f}(\boldsymbol{q\varepsilon}_{j,k_\mathrm{o}}^i, t_{j,k_\mathrm{o}}^i)}{\partial t_{j,n}^i}\right)
\end{aligned} \tag{4.51}$$

Chapter 5

Clustering Techniques

Generalizable and exact analytical criteria for grouping solutions along a set of trajectories in a multi-body system according to both qualitative and quantitative characteristics do not currently exist. Thus, clustering techniques are employed in this investigation to group similar trajectory solutions and construct summarizing sets of motion primitives. Clustering is an unsupervised learning method for separating the members of a dataset into a finite number of groups based on a defined set of features [46]. Data in the same cluster possess similar properties while data in different clusters possess dissimilar properties in the prescribed feature space. Manually processing and analyzing a large and complex dataset in a rapid and effective manner may not be feasible for a human analyst. Therefore, a clustering approach may be used to numerically discover and summarize fundamental patterns within a dataset while limiting the burden on a human analyst [46]. This chapter presents an overview of the clustering techniques leveraged in this work to generate sets of motion primitives that summarize families of fundamental trajectories in the CR3BP. Note: The discussion presented in this chapter was first published in an article by Smith and Bosanac in Celestial Mechanics and Dynamical Astronomy Vol. 134 No. 7 (2022) by Springer Nature [99].

5.1 Clustering Algorithms

A clustering algorithm divides a dataset into separate groupings, or clusters, such that data in the same cluster are similar and data in different clusters are dissimilar [46]. Consider a general dataset composed of n_d members where each member is described by an m_f-dimensional feature vector denoted as $\boldsymbol{f}$. A clustering algorithm may then be applied to the $(n_\mathrm{d} \times m_\mathrm{f})$-dimensional dataset to construct groupings of the members. The resulting clusters are influenced by various factors including: the dataset supplied to the clustering algorithm, the selected feature space description, the type of clustering method and associated algorithm used to perform the clustering, and the input parameters governing the selected algorithm [3]. Constructing the data source and defining an appropriate feature space is determined by a human analyst and may impact the utility of the clustering results. The features that may be incorporated in $\boldsymbol{f}$ depend on the type of objects in the dataset and should be selected based on the primary features of interest for a desired application. Furthermore, it is often challenging to select an appropriate algorithm for a desired application because the structure of the dataset is typically not known a priori. Each clustering algorithm also typically requires the selection of one or more input parameters that can produce fundamentally different clustering results for the same dataset. Despite these challenges, clustering is a powerful data mining method that may be used to efficiently analyze and summarize complex datasets while reducing the burden on a human analyst [3].

In this investigation, a consensus clustering approach is employed to construct motion primitives from families of fundamental solutions in the CR3BP. Consensus clustering uses an ensemble of individual clustering results to form a single clustering solution [3, 31]. Furthermore, consensus clustering may mitigate the challenges of algorithm and input parameter selection in the clustering process. Weighted Evidence Accumulation Clustering (WEAC) is leveraged to perform consensus clustering due to its capacity to produce clusters of arbitrary shapes, sizes, and densities [31, 52]. As an input to the WEAC algorithm, individual clustering results are constructed using k-means, a partition-based method, and agglomerative clustering, a hierarchical method, each governed by

a variety of input parameters. The k-means algorithm is used due to its iterative nature and computational efficiency, while agglomerative clustering is used due to its deterministic nature and the useful insights gained from the resulting dendrogram [46]. Furthermore, both of these clustering algorithms have successfully been used in shape-based time-series clustering applications [3]. This section supplies an overview of these clustering algorithms. All clustering results produced throughout this work are generated in Python using the Scikit-Learn v1.0.2 module and a custom implementation of the WEAC algorithm [84, 52].

5.1.1 *K*-Means

The k-means algorithm is a partition-based clustering method that groups members of a dataset according to their distance from k centroids. The centroid of a cluster is defined as the mean feature vector of the members assigned to the cluster [46]. The algorithm requires the number of clusters, k, as an input; then, the centroids are initialized by randomly selecting k members of the dataset [46]. Clusters are then formed by associating each member of the dataset to the closest centroid using the l^2-norm as a distance metric. After assigning each member to a cluster, the centroid of each cluster is recomputed and the members are reassigned to their new closest centroids to form new clusters. This process is repeated iteratively with the goal of minimizing the sum of the squared Euclidean distances between the centroid of each cluster and its associated members, which tends to produce evenly-sized and globular clusters. These steps are depicted conceptually in Figure 5.1 for a 2-dimensional dataset where $k = 3$. The algorithm terminates either when the clusters remain unchanged from one iteration to the next or a maximum number of iterations is exceeded. If k-means clustering converges on a clustering result prior to reaching the specified maximum number of iterations, the algorithm recovers a local minimum that depends on the selection of the initial centroids [84]. Furthermore, the primary limitation of k-means is selecting the desired number of clusters when the structure of the dataset is not known or understood a priori. However, using k-means within the consensus clustering process offers one approach to selecting an appropriate value of k without a priori knowledge of the dataset or significant reliance on a

human-in-the-loop when applied to a variety of distinct datasets.

To increase the stability and robustness of using k-means clustering, the algorithm is often applied multiple times to the same dataset but with different initial centroids [84, 46]. Then, the clustering result with the lowest inertia, E, is selected; minimizing the inertia indicates the computation of more compact clusters that minimize the sum of the squared Euclidean distances between the centroid of each cluster and its associated members. The inertia is a metric that is defined as

$$E = \sum_{i=1}^{k} \sum_{\boldsymbol{f} \in C_i} ||\boldsymbol{f} - \boldsymbol{c}_i||^2 \tag{5.1}$$

where C_i is the i-th cluster, $\boldsymbol{f}$ is the feature vector of a member in the i-th cluster, and $\boldsymbol{c}_i$ is the centroid of the i-th cluster [84, 46]. By selecting the clustering result with the lowest inertia, the algorithm becomes more stable and less dependent on the selection of the initial centroids.

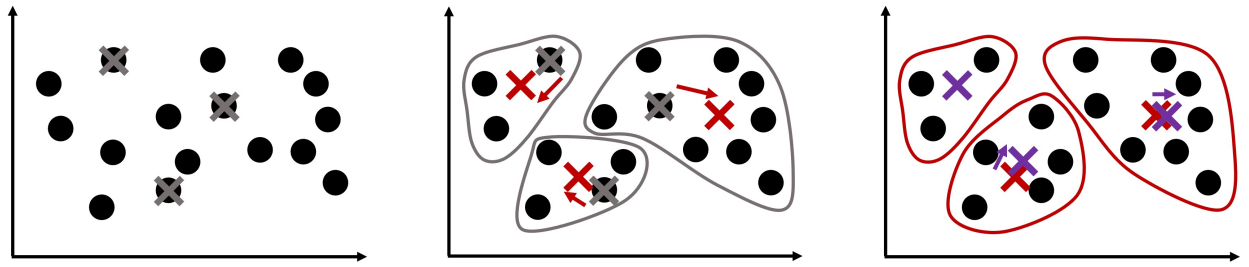

(a) Randomly assign k centroids.

(b) Assign each point to a cluster and compute new centroids.

(c) Reassign each point to a cluster and compute new centroids.

Figure 5.1: Example of k-means performed on a 2-dimensional dataset where $k = 3$.

5.1.2 Agglomerative Clustering

Agglomerative clustering uses a bottom-up approach to hierarchically represent a dataset as a tree with each node corresponding to a cluster. For a dataset composed of n_d members, the tree has n_d leaves, each initially corresponding to a separate cluster [46]. At each step of the algorithm, the distances between all of the current clusters are computed and the pair of clusters with the smallest inter-cluster distance is combined. This process continues until all members are

grouped into a single cluster. The resulting tree of clusters is often summarized by a dendrogram that reflects the structure of the dataset at various inter-cluster distances [46]. The dendrogram also captures the lifetime of a specified number of clusters, defined as the range of inter-cluster distances at which those clusters are present and constant [31]; long lifetimes in the dendrogram often indicate natural groupings of the dataset. Figure 5.2 provides a conceptual example of the agglomerative clustering process on a 2-dimensional dataset. In Figure 5.2, all of the data points are initially allocated to separate clusters (gray) and combine into new clusters at various inter-cluster distances (red, light orange, purple, and dark orange) until all of the clusters are merged together (black). To generate the final clustering result, the dendrogram is cut at a specified inter-cluster distance and the corresponding clusters in the hierarchy are obtained. A suitable value of the inter-cluster distance may be selected either: manually, automatically as the midpoint of the inter-cluster distance range with the longest lifetime, or automatically as the midpoint of the inter-cluster distance range corresponding to a desired number of clusters.

The method used to compute the inter-cluster distance, known as the linkage type, fundamentally influences the underlying tree structure produced by agglomerative clustering. Common linkage types include single, complete, average, and Ward linkage [3, 46]. Single linkage measures

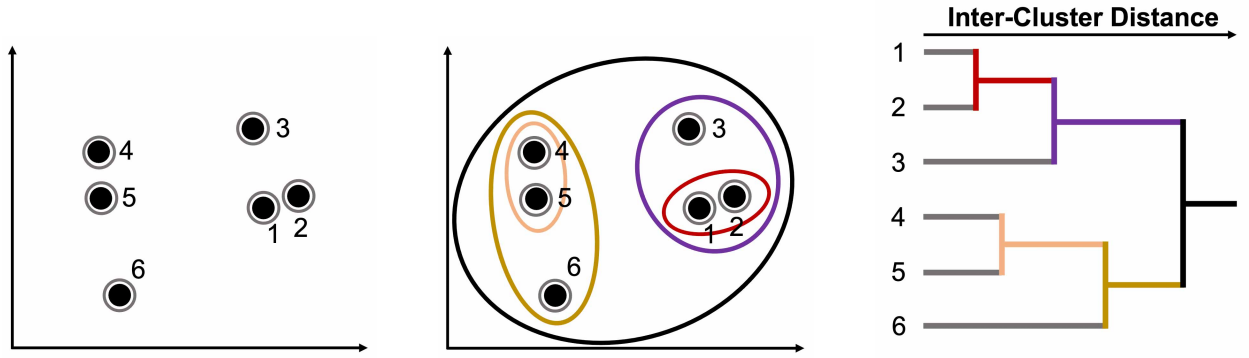

(a) Initialize each data point as a separate cluster.

(b) Consecutively form clusters based on increasing inter-cluster distance.

(c) Generate a hierarchy tree, i.e., a dendrogram, based on increasing inter-cluster distance.

Figure 5.2: Example of agglomerative clustering performed on a 2-dimensional dataset.

the inter-cluster distance between two clusters as the distance between the closest two members in the two clusters whereas complete linkage uses the farthest two members. Average linkage measures the inter-cluster distance as the average of the distances between all of the members of the two clusters. Ward linkage, however, captures the increase in the sum of squared distances between each member of two clusters and its associated centroid due to merging the clusters. Mathematically, Ward linkage defines the inter-cluster distance between clusters C_i and C_j as

$$d(C_i, C_j) = \sqrt{\frac{2|C_i||C_j|}{|C_i| + |C_j|}} ||\boldsymbol{c}_i - \boldsymbol{c}_j|| \tag{5.2}$$

where $|C_i|$ and $|C_j|$ are the number of members in the i-th and j-th clusters, respectively; and $\boldsymbol{c}_i$ and $\boldsymbol{c}_j$ are the centroids of the i-th and j-th clusters, respectively [57]. Using Equation 5.2, Ward linkage tends to produce compact and well-separated clusters while considering the overall structure of each cluster. Average linkage is also useful for considering the overall structure of clusters throughout the merging process. However, single and complete linkage only focus on the local and global structure of clusters, respectively, during the merging process and are more sensitive to noise and outliers in a dataset [3]. Distinctly different tree structures and, subsequently, clustering results may be produced using different definitions of inter-cluster distance.

5.1.3 Weighted Evidence Accumulation Clustering

WEAC generates a consensus clustering result from an ensemble of base clustering results. A significant benefit of using consensus clustering is the capacity to produce better quality and more robust results than a single clustering solution for a variety of datasets, while also supporting automated input parameter selection [3, 31, 52]. The WEAC algorithm requires an ensemble of N_c base clustering results as an input, defined as the set $\mathbb{P}$. Each base clustering result, $\boldsymbol{P}_i$ for $i \in [1, N_\mathrm{c}]$, is the set of cluster labels assigned to the members of a dataset. These base clustering results may be generated in any manner. For example, the ensemble may be generated by a single algorithm with varying input parameters and/or a variety of clustering algorithms [31, 52]. In this work, both k-means and agglomerative clustering with Ward linkage are used to generate an

ensemble of base clustering solutions, each for several distinct values of k within a specified range. Each base clustering solution is considered a piece of independent evidence for the natural groupings within the dataset that is used in generating a consensus result from the ensemble of accumulated evidence in $\mathbb{P}$.

Given an ensemble of base clustering results, WEAC assumes two members of a dataset naturally belong to the same cluster if they are consistently co-located in the base clustering results. This characteristic is quantified by a weighted ensemble co-association matrix. First, a co-association matrix, $[\boldsymbol{S}_i]$, is computed for each base clustering result. Each matrix is a $(n_\mathrm{d} \times n_\mathrm{d})$-dimensional similarity matrix in which $[\boldsymbol{S}_i]\{a, b\} = 1$ if members a and b are grouped in the same cluster and $[\boldsymbol{S}_i]\{a, b\} = 0$ if members a and b are grouped in different clusters within a single base clustering result. Then, a weight, w_i, is computed for each base clustering result using its normalized crowd agreement index (NCAI) [52]. To compute each weight, the crowd agreement index (CAI) for each base clustering result is defined as

$$\mathrm{CAI}(\boldsymbol{P}_i) = \frac{1}{N_\mathrm{c} - 1} \sum_{j=1, j\neq i}^{N_\mathrm{c}} \mathrm{Sim}(\boldsymbol{P}_i, \boldsymbol{P}_j) \tag{5.3}$$

where $\mathrm{Sim}(\boldsymbol{P}_i, \boldsymbol{P}_j)$ measures the similarity between two base clustering results as the maximal normalized mutual information shared between the two solutions as defined by Strehl and Ghosh [100]. Therefore, $\mathrm{CAI}(\boldsymbol{P}_i)$ quantifies the average amount of information that $\boldsymbol{P}_i$ shares with the ensemble and is normalized as

$$\mathrm{NCAI}(\boldsymbol{P}_i) = \frac{\mathrm{CAI}(\boldsymbol{P}_i)}{\mathrm{argmax}_{\boldsymbol{P}_j \in \mathbb{P}} \mathrm{CAI}(\boldsymbol{P}_j)} \tag{5.4}$$

The NCAI of each base clustering result ranges from 0 to 1 and is used to calculate the weight, w_i, for the co-association matrix of each clustering result $\boldsymbol{P}_i$ as

$$w_i = \frac{I_\mathrm{NCAI}(\boldsymbol{P}_i)}{\sum_{j=1}^{N_\mathrm{c}} I_\mathrm{NCAI}(\boldsymbol{P}_j)} \tag{5.5}$$

where $I_\mathrm{NCAI}(\boldsymbol{P}_i) = (\mathrm{NCAI}(\boldsymbol{P}_i))^\beta$ and β is selected to adjust the influence of the NCAI weighting. Based on the parameter analysis conducted by Huang et al. [52] on a variety of datasets, a value

of $\beta = 2$ is used in this work. Finally, the weighted ensemble co-association matrix, $[\boldsymbol{A}_{\mathbf{coa}}]$, is computed as

$$[\boldsymbol{A}_{\mathbf{coa}}] = \sum_{i=1}^{N_c} w_i [\boldsymbol{S}_i] \tag{5.6}$$

This weighted ensemble co-association matrix describes the similarity between the members of a dataset based on how consistently the members are co-located in the same cluster throughout the ensemble of base clustering results.

The final clustering solution is produced in WEAC based on the weighted ensemble co-association matrix. Agglomerative clustering with average linkage is applied to the dataset using $[\boldsymbol{A}_{\mathbf{coa}}]$ as a precomputed similarity matrix to generate a consensus clustering result; average linkage is selected for the linkage type due to its capacity to support a general similarity measure and capture the average characteristics of entire clusters. Each element of $[\boldsymbol{A}_{\mathbf{coa}}]$ is a measure of the similarity between two members of the dataset and approximately reflects the percentage of results in which the members are co-located in the same cluster throughout the clustering ensemble. Consequently, the distance between two members of the dataset, a and b, is equal to $1-[\boldsymbol{A}_{\mathbf{coa}}]\{a, b\}$. The final number of clusters is then selected by sampling the resulting dendrogram at the midpoint of the inter-cluster distance range with the longest lifetime above a specified threshold [31, 52]. By formulating an alternative measure of similarity between members of a dataset, WEAC leverages the evidence accumulated by a large ensemble of clustering solutions to generate a single consensus result. As a result, WEAC reduces the sensitivity and complexity of algorithm and input parameter selection during the clustering process.

5.2 Clustering Refinement

A clustering algorithm attempts to identify the natural groupings of the members within a dataset based on a prescribed feature space. However, in some cases, additional cluster refinement is useful due to the potential sparsity of a dataset or the relative weighting between components of the feature vector incorrectly grouping members of the dataset that are similar yet distinct; such issues

may occur in high-dimensional feature spaces due to the curse of dimensionality [3]. Incorporating a post-clustering refinement step into a clustering approach may also make the process more robust with respect to algorithm and input parameter selections. Inspired by a previous use of graph theory for more complex cluster refinement in hierarchical clustering, a k-nearest neighbor (k-NN) graph is a simple and powerful tool that may be used to determine if a cluster should be further split into smaller groups [56, 46].

To construct a k-NN graph for a dataset, each member of the dataset is considered a node in the graph and is connected to its k_{nn} nearest neighbors via directed edges [46]. The k_{nn} nearest neighbors for each member of the dataset are computed based on a desired distance measure, such as the l^2-norm. Depending on the use case of the k-NN graph, additional conditions may be placed on the graph construction process. When using a k-NN graph for cluster refinement, a graph may be constructed for each cluster using the feature vectors of its members. The number of connected components in a graph for a given cluster is then used to decide whether the associated cluster should be further split into separate additional clusters.

A compact cluster will likely only contain one connected component in a k-NN graph, whereas a cluster consisting of several smaller and separated subclusters may contain multiple connected components depending on the selected value of k_{nn}. When $k_{\text{nn}} = 1$, a sparse graph is produced and may contain a large number of connected components that each possess only two members, resulting in an excessive fragmentation of an original cluster. However, $k_{\text{nn}} \geq 2$ generates a more connected graph that may avoid this issue and preserve the structure of compact clusters. A larger value of k_{nn} naturally results in a more connected graph because k_{nn} dictates the number of nearest neighbors each member is connected to in the graph [46]. Therefore, k_{nn} may be selected based on the desired scale of cluster refinement. Figure 5.3 depicts a conceptual example of a k-NN graph constructed for a cluster of objects that admits three connected components when $k_{\text{nn}} = 2$. In this case, the cluster would be split into three separate clusters based on the connected components in the graph. Leveraging a k-NN graph for cluster refinement limits the burden on a human analyst when additional refinement is deemed appropriate.

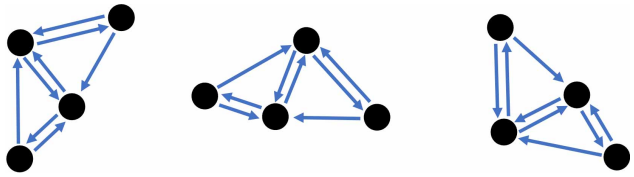

Figure 5.3: Conceptual example of a k-NN graph constructed for a cluster of objects that admits three connected components when $k_{\text{nn}} = 2$.

5.3 Motion Primitive Definition and Extraction

Motion primitives have been used in various disciplines to construct a reduced basis set of path segments, actions, configurations, or behaviors that reflects the characteristics of a solution space; however, the exact definition of a motion primitive depends on the field of application [29, 54, 79, 90, 112]. Frazzoli defines trajectory primitives in the context of autonomous vehicle motion planning as a set of path segments that capture the characteristics of the solution space, support complex path construction, and support extraction of key state description parameters [29]. Similarly, a motion primitive set is defined in this investigation as a set of arcs that capture the characteristics of a larger set of trajectories and support assembly of an initial guess for a more complex path in a multi-body system. Although motion primitives may be extracted analytically or by a human analyst in simple environments, their extraction is significantly more challenging and time-consuming in complex and higher-dimensional dynamical systems [29, 54, 112].

In complex dynamical environments, data is often sampled or observed from the environment and then data mining techniques such as feature selection, dimensionality reduction, and clustering are employed to uncover the fundamental primitives in the system. Due to the complexity of the solution space in a multi-body system, clustering is leveraged in this work to group solutions that possess a similar set of characteristics; these characteristics of interest are defined using domain knowledge. A representative member from each cluster is then designated as the motion primitive [9, 55, 46]. Together, the reduced set of trajectories that form a motion primitive set summarize a larger set of trajectories that exist in a multi-body system.

A motion primitive is extracted as the most representative member of a cluster of similar trajectories. In the data-driven approach employed in this work, the medoid of a cluster is the member of the cluster that is most similar to all other members in the cluster within the prescribed feature space; as a guaranteed member of the cluster, this definition is particularly advantageous for arbitrarily-shaped clusters [46]. Using the definition of a medoid, the motion primitive associated with the i-th cluster is identified as

$$\boldsymbol{f}_{\mathbf{MP}_i} = \underset{\boldsymbol{f} \in C_i}{\operatorname{argmin}} \sum_{j=1}^{|C_i|} ||\boldsymbol{f} - \boldsymbol{f}_j|| \tag{5.7}$$

where $\boldsymbol{f}_{\mathbf{MP}_i}$ is the feature vector of the motion primitive of the i-th cluster, C_i; $|C_i|$ is the number of members in the i-th cluster; and $\boldsymbol{f}_j$ is the feature vector of the j-th member in the i-th cluster [107]. Figure 5.4 depicts a conceptual example of motion primitives identified from a set of clusters where the primitive of each cluster is denoted in the associated color. Each motion primitive may be used to represent and summarize the members within its cluster. Despite the simplicity of this example, it demonstrates the concept and value of identifying a representative member from a cluster as a motion primitive.

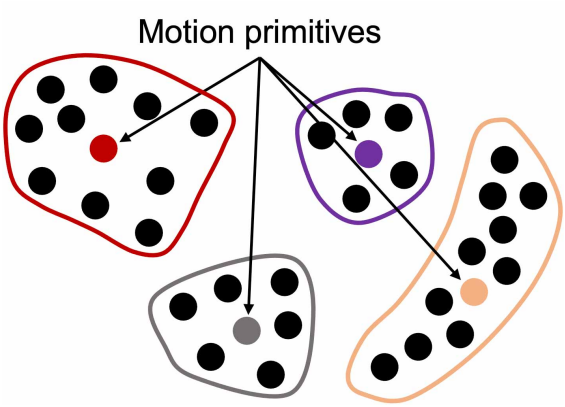

Figure 5.4: Conceptual example of motion primitives identified from a set of clusters.

Chapter 6

Motion Primitive Construction in a Multi-Body System

Rapid trajectory design in multi-body systems often leverages individual arcs along natural dynamical structures that exist in an approximate dynamical model, such as the CR3BP. To reduce the complexity of this analysis in a chaotic gravitational environment, motion primitive sets are constructed to represent the finite geometric, stability, and/or energetic characteristics exhibited by sets of trajectories. The summarizing sets of motion primitives may then support the construction of initial guesses for complex trajectories. In the absence of generalizable analytical criteria for extracting these representative solutions, a data-driven procedure is formulated. Specifically, k-means and agglomerative clustering are used in conjunction with WEAC, a form of consensus clustering, to construct sets of motion primitives in an unsupervised manner. This data-driven procedure is used to construct motion primitive sets that summarize a variety of periodic orbit families and natural trajectories along hyperbolic invariant manifolds in the CR3BP. This chapter presents and demonstrates the motion primitive construction process developed to summarize fundamental dynamical structures in the CR3BP. Note: The approach and examples presented in this chapter were first published in an article by Smith and Bosanac in Celestial Mechanics and Dynamical Astronomy Vol. 134 No. 7 (2022) by Springer Nature [99].

6.1 Translating Trajectory Characteristics into a Feature Vector

The results of a clustering approach depend on the feature space encoding that translates domain knowledge into a quantitative description of the dataset [3]. Selecting a feature vector is member-specific because the available features depend on the type of members in the dataset, but it is also application-specific because the features should be selected to recover a useful summary of the dataset for the desired application. During the early stages of trajectory design and the study of natural motion in complex gravitational environments, human analysts tend to examine the geometry, stability, and energy of fundamental dynamical structures [61, 38, 40]. This section outlines the feature vectors formulated to reflect one approach to encoding these characteristics for periodic orbits and nonperiodic trajectories that lie along stable or unstable manifolds in the CR3BP. The definitions of the feature vectors support the motion primitive extraction process presented in this work.

6.1.1 Describing Trajectory Geometry

The geometry of a trajectory in the CR3BP is quantitatively described by discretizing the solution into a sequence of states [120]. Sampling a trajectory at equally spaced times may capture small geometric variations along the path. However, selecting a single time distribution or number of states that sufficiently represent a general set of trajectories in a chaotic dynamical system is challenging. Rather, this work uses a generalizable and curve-based approach to produce a lower-dimensional description: sampling a trajectory at apses relative to a specified stationary reference point, such as a primary body or libration point [9, 120]. Each apsis corresponds to either a local minimum or maximum distance from the reference point along the trajectory; furthermore, the state at each apsis along the trajectory is denoted as $\boldsymbol{q}_i^{\text{refPt}}$, where refPt indicates the specified reference point for the apsis and i is the index of the apsis along the trajectory.

The state information at each apsis along a trajectory is scaled to prevent unintended feature biases during clustering [46]. First, the state at each apsis is translated relative to a stationary

center point, i.e., cenPt, which is specified for the corresponding set of trajectories; by default, the selected center point is the same as the reference point used to compute the apses along each trajectory in the dataset. However, these two points may be different because in some cases it may be desirable to compute apses with respect to one location and then define the resulting states relative to a distinctly different location. Then, the relative state at each apsis is decomposed into its position and velocity components. The relative position vector at each apsis is defined as $\boldsymbol{r}_{\text{cenPt},i} = \boldsymbol{r}_i^{\text{refPt}} - \boldsymbol{r}_{\mathbf{cenPt}}$ and the relative velocity vector at each apsis is defined as $\dot{\boldsymbol{r}}_{\text{cenPt},i} = \dot{\boldsymbol{r}}_i^{\text{refPt}}$, where $\boldsymbol{r}_{\mathbf{cenPt}}$ is the position of the selected center point with respect to the origin of $\mathcal{R}$. Using these definitions, the relative position components at the i-th apsis along a trajectory are normalized between -1 and 1 as

$$\check{\boldsymbol{r}}_{\text{cenPt},i} = \frac{\boldsymbol{r}_{\text{cenPt},i}}{r_{\max}} \tag{6.1}$$

where the $\check{(\cdot)}$ notation denotes a normalized quantity and $r_{\max}$ is the global maximum distance of an apsis from cenPt along all members of the corresponding set of trajectories. Furthermore, the relative velocity at the i-th apsis along a trajectory is normalized as

$$\dot{\check{\boldsymbol{r}}}_{\text{cenPt},i} = \frac{\dot{\boldsymbol{r}}_{\text{cenPt},i}}{||\dot{\boldsymbol{r}}_{\text{cenPt},i}||} \tag{6.2}$$

which reflects the velocity unit vector at each apsis with components possessing values between -1 and 1. Equations 6.1 and 6.2 may be used to define a feature vector that describes the geometry of a trajectory.

Consider a trajectory that admits s apses computed with respect to a specified stationary reference point in the CR3BP. The geometric component of a feature vector, $\boldsymbol{f}_{\mathbf{g}}$, describing the trajectory is defined in this work as

$$\boldsymbol{f}_{\mathbf{g}} = \left[\check{\boldsymbol{r}}_{\text{cenPt},1}^{\text{T}} \quad \dot{\check{\boldsymbol{r}}}_{\text{cenPt},1}^{\text{T}} \quad \cdots \quad \check{\boldsymbol{r}}_{\text{cenPt},s}^{\text{T}} \quad \dot{\check{\boldsymbol{r}}}_{\text{cenPt},s}^{\text{T}} \quad [\mathbf{0}_{1\times(6(s_{\max}-s))}]\right] \tag{6.3}$$

where all features are in the range $[-1, 1]$. This geometric component of a feature vector possesses a dimension of $1 \times 6s_{\max}$ where $s_{\max}$ is the maximum number of apses that occur along any member of the corresponding set of trajectories. The clustering algorithms leveraged in this work require

the feature vectors to have the same length. Therefore, if the number of apses is not constant across all members of a set of trajectories, then a placeholder zero vector is included in the remaining elements of $\boldsymbol{f}_{\mathbf{g}}$ as indicated in Equation 6.3 [9]. Setting the placeholder features to zero ensures that the placeholder states are distinct from the states describing actual apses. Using these definitions, this component of the feature vector supplies a straightforward geometric description of a trajectory that is computationally efficient to construct, limits unintended feature bias, may be generalized across various trajectories, and, when applied to the trajectory sets examined in this investigation, does not produce an excessively high-dimensional description.

6.1.2 Describing Orbital Stability

A function is defined to incorporate stability indices into the feature vector for a periodic orbit. This function is designed to: reduce unintended feature bias when the maximum value along the family possesses a large order of magnitude, offer a continuous stability description to avoid a loss of information, and mitigate excessive compression between the critical values of -2 and 2. To appropriately characterize the stability properties along a periodic orbit family, it may be desirable to capture complex variations of the stability indices within the oscillatory mode regime, differentiate between a pair of oscillatory or stable and unstable modes, and avoid an artificial separation between strictly oscillatory modes and the pairs of eigenvalues that possess magnitudes that are close to unity. Furthermore, it may not be essential to distinguish between stability indices with large magnitudes. To achieve these goals in characterizing a periodic orbit in the CR3BP, the stability component of a feature vector, $\boldsymbol{f}_{\mathbf{s}}$, is defined using a hyperbolic tangent function, which retains continuity and produces values between -1 and 1. Mathematically, the stability component of the feature vector is defined in this work as

$$\boldsymbol{f}_{\mathbf{s}} = \begin{bmatrix} \tanh\left(\frac{s_1}{2}\right) & \tanh\left(\frac{s_2}{2}\right) \end{bmatrix} \tag{6.4}$$

For a planar periodic orbit, s_1 and s_2 are calculated using the in-plane and out-of-plane modes, respectively. However, for a spatial periodic orbit, s_1 and s_2 each reflect the evolution of a single

pair of eigenvalues along the family, ensuring continuity in the stability indices as discussed in Section 3.3.1. Through the definition in Equation 6.4, stability indices within the range $[-2, 2]$ produce a feature vector component within the approximate range $[-0.7616, 0.7616]$ to maintain significant resolution in the stability component of the feature vector. Due to continuity in the hyperbolic tangent function, there is also no artificial separation between a stability index with a magnitude that is strictly below 2 and one that is only slightly above. In addition, the asymptotes of the hyperbolic tangent function limit the differentiation between stability indices with large magnitudes.

6.1.3 Describing Orbital Energy

Orbital energy is often used to supply preliminary insight into accessible regions of motion and heuristics for maneuver planning. In the CR3BP, the Jacobi constant, as defined in Equation 2.26, is inversely proportional to the total energy of P_3 in $\mathcal{R}$ [61]. Therefore, the energy component of a feature vector, f_e, for a natural trajectory in the CR3BP is defined as

$$f_\mathrm{e} = \check{C}_J \tag{6.5}$$

where $\check{C}_J$ is the Jacobi constant normalized to within the range $[-1, 1]$ using the minimum and maximum values of C_J along the corresponding set of trajectories. This component of the feature vector supplies a single parameter to describe the energetic properties of each member of a set of trajectories in the CR3BP.

6.1.4 Defining Feature Vectors

Leveraging the geometric, stability, and energetic properties of a trajectory in the CR3BP, feature vector definitions are formulated separately for periodic orbits and trajectories along a stable or unstable manifold. The feature vector $\boldsymbol{f}_\mathbf{PO}$ is constructed to describe a periodic orbit and simultaneously capture a variety of considerations of interest to a trajectory designer during initial

guess construction. This parametric feature vector is defined as

$$\boldsymbol{f}_{\mathbf{PO}} = \begin{bmatrix} \boldsymbol{f}_{\mathbf{g}} & \boldsymbol{f}_{\mathbf{s}} & f_{\mathrm{e}} \end{bmatrix} \tag{6.6}$$

and possesses a length of $m_{\mathrm{f}} = 6s_{\max} + 3$. For a planar periodic orbit, the out-of-plane position and velocity features are omitted, resulting in a feature vector with a length of $m_{\mathrm{f}} = 4s_{\max} + 3$. Similarly, the feature vector $\boldsymbol{f}_{\mathbf{Mani}}$ is constructed to describe the geometry of a trajectory along either a stable or unstable manifold associated with an unstable periodic orbit. This feature vector is defined as

$$\boldsymbol{f}_{\mathbf{Mani}} = \begin{bmatrix} \boldsymbol{f}_{\mathbf{g}} & \Delta\check{t}_1 & \cdots & \Delta\check{t}_{s-1} & [\mathbf{0}_{1\times(s_{\max}-s)}] \end{bmatrix} \tag{6.7}$$

where $\Delta\check{t}_i$ is the nondimensional time between two consecutive apses, normalized by the total integration time of the trajectory. Note, the terminal state of the trajectory is included in $\boldsymbol{f}_{\mathbf{g}}$, which may or may not correspond to a desired apsis. The additional normalized time features are included in $\boldsymbol{f}_{\mathbf{Mani}}$ to capture the variations in transit time along a nonperiodic trajectory. Similar to the use of placeholder states in $\boldsymbol{f}_{\mathbf{g}}$, values of zero are used for the remaining normalized time features in $\boldsymbol{f}_{\mathbf{Mani}}$ when $s < s_{\max}$ for a trajectory. Furthermore, f_{e} is not included in the feature vector because in this work all of the manifold trajectories in a given dataset are associated with one periodic orbit and, therefore, possess the same value of the Jacobi constant. Therefore, $\boldsymbol{f}_{\mathbf{Mani}}$ possesses a length of $m_{\mathrm{f}} = 7s_{\max} - 1$ for a spatial manifold, or $m_{\mathrm{f}} = 5s_{\max} - 1$ in the planar case, and quantitatively summarizes the geometry of a trajectory along a stable or unstable manifold. Both feature vector definitions supply a finite, quantitative description of trajectories along a family to create an $(n_{\mathrm{d}} \times m_{\mathrm{f}})$-dimensional dataset that is input to a clustering algorithm for motion primitive extraction.

6.2 Summarizing Periodic Orbit Families

The motion primitive construction process is defined for periodic orbits in the CR3BP and demonstrated in detail via application to the planar distant prograde orbit (DPO) and spatial L_1 northern halo orbit families in the Earth-Moon CR3BP. Each of these periodic orbit families

exhibits several changes in geometry, stability, and energy along the family. Some of these changes may be identified through analytical separation criteria capturing a change in the number of apses or locating when a critical value or turning point occurs for a parameter calculated along the family. These analytically identifiable changes supply a straightforward verification of some of the groupings within the clustering results. However, the clustering process should be able to produce additional differentiation between periodic orbits that a human may be able to visually identify but may not be described by an associated set of generalizable and clear analytical criteria formulated as a function of the feature space description. Thus, both of these families of periodic orbits serve as a suitable example for demonstrating the procedure for extracting motion primitives that summarize the finite set of geometric, stability, and energetic characteristics admitted by its members. Following a detailed demonstration in the context of these two families, the motion primitive extraction process is applied to a wider variety of periodic orbit families in the Earth-Moon and Sun-Earth CR3BP systems.

6.2.1 Motion Primitive Construction Process for Periodic Orbits

For a family of periodic orbits, the motion primitive construction procedure consists of the following steps:

Motion Primitive Construction Process for Periodic Orbits in the CR3BP

Given: A family of periodic orbits computed in a desired system in the CR3BP, composed of n_d members with refPt and cenPt specified for the family.

(1) For each orbit along the periodic orbit family: compute the apses that occur along the orbit with respect to refPt, the stability indices, and the Jacobi constant.

(2) Construct an $(n_\mathrm{d} \times m_\mathrm{f})$-dimensional dataset containing the m_f-dimensional feature vector $\boldsymbol{f}_{\mathbf{PO}}$ of each orbit, as defined in Equation 6.6, to describe the geometry, stability, and energy of each periodic orbit.

(3) Generate an ensemble of N_c base clustering results by applying k-means and agglomerative

clustering with Ward linkage to the dataset, each for $N_c/2$ values of k in a specified range.

(4) Specify an inter-cluster distance threshold, $d_{\min}$, ranging from 0 to 1 and apply WEAC to the ensemble of base clustering results computed in Step 3. The clustering result selected using WEAC possesses a number of clusters with the largest lifetime above $d_{\min}$.

(5) Extract a set of motion primitives as the medoids of the clusters in the final consensus clustering result to summarize the periodic orbit family.

Once the desired set of trajectories is computed, this procedure only requires a human analyst to select the range of values of k to form the base clustering results and the value of $d_{\min}$ used within WEAC. In applying this procedure to the DPO and L_1 northern halo orbit families in the Earth-Moon CR3BP, the following values are selected: $k \in [3, 18]$ to produce $N_c = 2 \times 16 = 32$ base clustering results that are input to WEAC, and $d_{\min} = 0.4$. The range of selected k values is a wide range that encompasses a reasonable number of expected distinct characteristics along each family; however, the range may be adjusted based on the given family. The threshold value of $d_{\min} = 0.4$ (i.e., a similarity value of 0.6) is selected because it ensures that clusters with members that are co-located more than approximately 60% of the time on average remain clustered together in the final consensus-derived result. The final "cut" of the dendrogram is above $d_{\min} = 0.4$ and therefore WEAC identifies a natural cluster boundary where the additional merging of two smaller clusters no longer results in a cluster with members that are frequently co-located. The computation time for this clustering procedure to generate motion primitives summarizing a periodic orbit family is on the order of 10^0 seconds for each example in this section using an iMac with a 3GHz 6-Core Intel Core i5 processor.

6.2.2 Summarizing the Earth-Moon Distant Prograde Orbit Family

The DPO family is composed of members that exhibit multiple distinct geometric and stability properties while encircling the Moon [13, 62]. Figure 6.1 displays a subset of the DPO family, computed in the Earth-Moon CR3BP using multiple shooting for corrections and pseudo-arclength

continuation. Each orbit in the computed segment of the family is plotted in $\mathcal{R}$ with the black arrows indicating direction of motion. The libration points are displayed using red diamonds while the Moon is plotted to scale using a gray circle. Additionally, the in-plane (s_1) and out-of-plane (s_2) stability indices along this segment of the DPO family are displayed in Figure 6.2 as a function of the Jacobi constant. Note that the stability indices are scaled in Figure 6.2 using the function $2\sinh^{-1}(s_i)/\sinh^{-1}(2)$ to improve visualization. A stability index associated with oscillatory modes produces a value of this function within the range $[-2, 2]$ while a stability index associated with a stable and unstable mode pair produces a function value that is greater than 2 in magnitude; note that the sign of the stability index is preserved through this normalization. In addition, four orbits, each denoted with a distinct color, are highlighted in Figure 6.1 and their associated parameters are plotted in Figure 6.2 to facilitate a clear description of the family. These two figures reveal

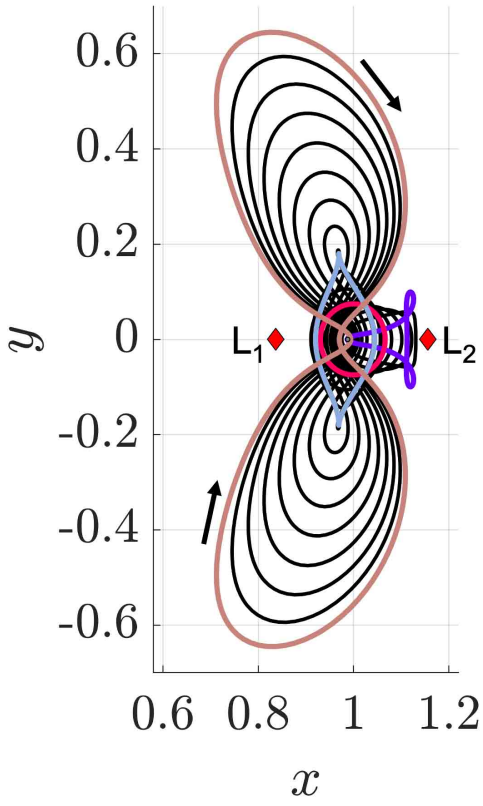

Figure 6.1: Computed segment of the DPO family displayed in $\mathcal{R}$ in the Earth-Moon CR3BP [99].

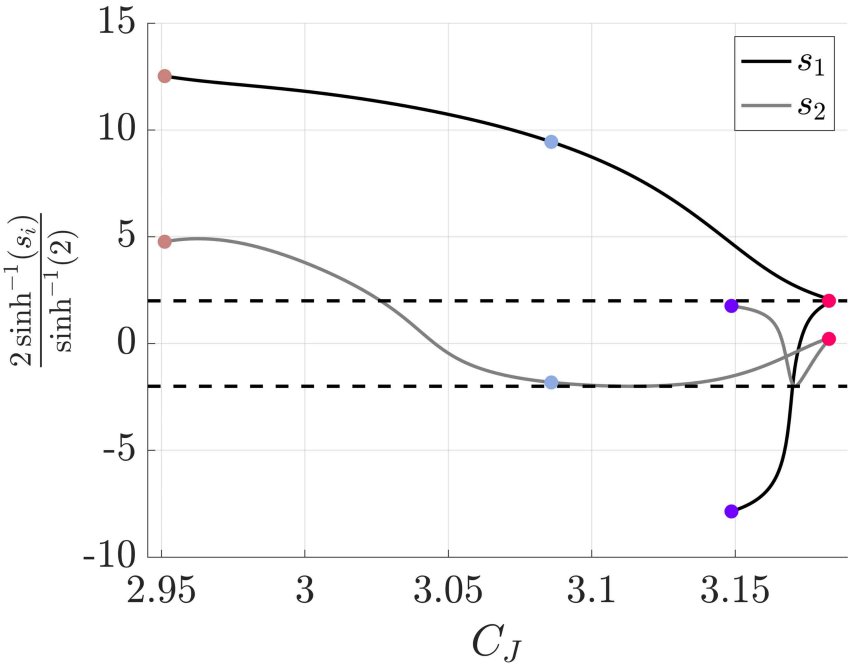

Figure 6.2: Stability indices, s_1 and s_2, along the computed segment of the DPO family in the Earth-Moon CR3BP [99].

distinct changes in geometry, stability, and energy along the DPO family: some changes may be described via quantitative separation criteria, whereas other changes are challenging to define in an analytical and generalizable manner. These complex variations render the planar DPO family a useful first scenario for demonstrating the motion primitive construction process.

To support verification of the recovered motion primitives, the geometry and stability of members of the DPO family are characterized. At one end of the computed segment of the family near $C_J \approx 3.1487$, denoted in purple in Figures 6.1 and 6.2, the orbits possess stable and unstable in-plane modes and oscillatory out-of-plane modes. In addition, motion along these orbits is generally prograde in the rotating frame: there are two prograde perilunes, with one occurring close to the Moon and one located close to L_2, and two retrograde apolunes that occur near L_2 and symmetrically about the x-axis. As the Jacobi constant increases, the magnitude of the velocity vector at the two apolunes decreases. After reaching a magnitude of zero in the rotating frame, the

velocity vector changes direction and the associated orbit possesses two prograde apolunes. These prograde apolunes approach the x-axis as the Jacobi constant continues to increase. Eventually, the orbits evolve to possess only one perilune and one apolune; both apses relative to the Moon are prograde and located on the x-axis. This evolution of the geometry is accompanied by a change in the in-plane stability such that these members of the DPO family do not possess any stable or unstable modes. As the Jacobi constant increases further, the perilune distance increases and the apolune distance decreases until the orbit resembles an oval. Eventually, the orbits possess two prograde perilunes on the x-axis and two prograde apolunes symmetrically located about the x-axis. As the Jacobi constant reaches a maximum, denoted in red in Figures 6.1 and 6.2, another change in the stability occurs and the associated members of the DPO family possess stable and unstable in-plane modes. With a decreasing Jacobi constant, the apolunes occur at increasing values of y and decreasing values of x, with a speed that decreases. After the velocity magnitude passes through zero, denoted in light blue in Figures 6.1 and 6.2, and at low values of the Jacobi constant, orbits along the DPO family possess low prograde perilunes and high retrograde apolunes. The out-of-plane stability also changes, resulting in these members of the DPO family possessing only stable and unstable modes through the end of the computed segment of the family, as indicated in light brown in Figures 6.1 and 6.2.

The observed distinct changes in geometry and stability are summarized to facilitate verification of the clustering results. Table 6.1 lists these changes using labels beginning with "G" to indicate a change in the geometry, assessed via the number and direction of motion at each apsis, and a prefix "S" indicating a qualitative change in stability; the numbers in each label are assigned to changes that occur as the family is traversed from a Jacobi constant starting at $C_J \approx 3.1487$, reaching a maximum at $C_J \approx 3.1827$, and ending at $C_J \approx 2.9511$. A horizontal bar in Table 6.1 indicates that a change did not occur in a specific property. These distinct changes in the geometry and stability support verifying some of the cluster-based differentiation between orbits during the motion primitive construction process. Specifically, the final clustering result should at least separate solutions of distinct geometries, as listed in Table 6.1, while also admitting additional

Table 6.1: Dominant geometric and stability changes along the computed segment of the DPO family; prograde is abbreviated as "pro." and retrograde is abbreviated as "retro." to describe direction of motion [99].

Label	Before Change		After Change		Approx. C_J
	Apses	Stability	Apses	Stability	
$G1$	2 retro. apolune	$s_1 < -2$	2 pro. apolune	—	3.1610
	2 pro. perilune	$-2 < s_2 < 2$	—	—	
$G2/S1$	2 pro. apolune	$s_1 < -2$	1 pro. apolune	$-2 < s_1 < 2$	3.1698 ($G2$)
	2 pro. perilune	$-2 < s_2 < 2$	1 pro. perilune	—	3.1700 ($S1$)
$G3/S2$	1 pro. apolune	$-2 < s_1 < 2$	2 pro. apolune	$s_1 > 2$	3.1822 ($G3$)
	1 pro. perilune	$-2 < s_2 < 2$	2 pro. perilune	—	3.1827 ($S2$)
$G4$	2 pro. apolune	$s_1 > 2$	2 retro. apolune	—	3.0859
	2 pro. perilune	$-2 < s_2 < 2$	—	—	
$S3$	2 retro. apolune	$s_1 > 2$	—	—	3.0264
	2 pro. perilune	$-2 < s_2 < 2$	—	$s_2 > 2$	

differentiation for geometric changes that are challenging to describe in an analytical and generalizable manner. Due to the form of the stability component of the feature vector for a periodic orbit, the stability changes listed in Table 6.1 may potentially, but not necessarily, lie close to the boundaries of some clusters.

Consensus clustering is used to differentiate periodic orbits within the DPO family. First, the parametric feature vector defined in Equation 6.6 is used to represent the geometric, stability, and energetic properties of 400 members of the family, computed using multiple shooting for corrections and pseudo-arclength continuation. The geometry of each orbit is represented as a sequence of apses computed with respect to the Moon, where both refPt and cenPt are specified as P_2. Furthermore, the out-of-plane position and velocity features of each apsis are omitted because all members of the DPO family lie in the plane of the primaries. The feature vectors of the selected members of this family are used to form a (400×19)-dimensional dataset where $s_{\max} = 4$. Then, k-means and agglomerative clustering with Ward linkage are applied to the dataset, each for 16 values of k ranging from 3 to 18, to produce 32 base clustering results. The resulting dendrogram formed when WEAC is applied to this ensemble of clustering results is displayed in Figure 6.3. Each

vertical blue line represents a cluster and each horizontal blue line represents the merging of two clusters at various values of the inter-cluster distance, displayed on the vertical axis. Values on the horizontal axis are not labeled because they indicate the cluster identification numbers, which are arbitrarily set by the algorithm as new clusters are formed with new values of inter-cluster distance. Furthermore, the solid black line indicates the specified inter-cluster distance threshold of $d_{\min} = 0.4$. Analyzing the dendrogram, the number of clusters with the largest lifetime above this threshold is $k = 9$, as indicated by the bounding dashed red lines. Other potential natural cluster boundaries in the dataset occur for $k = 6$ and $k = 7$ as evident in the dendrogram based on the size of each cluster lifetime. However, $k = 9$ is selected consistent with possessing the largest lifetime above the threshold. Motion primitives are extracted from this clustering result as the medoid of each cluster.

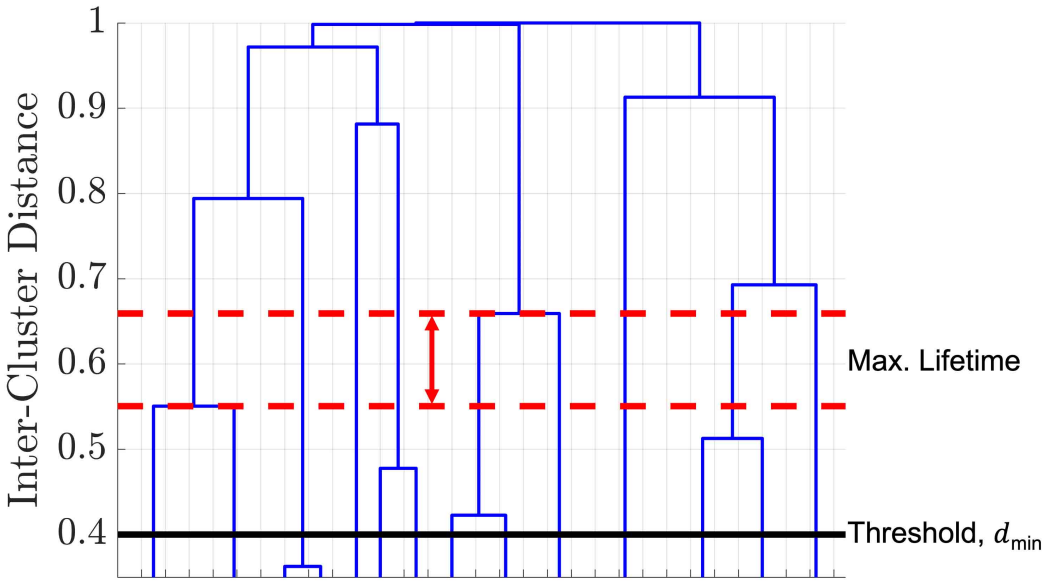

Figure 6.3: Dendrogram constructed via WEAC to determine clusters of periodic orbits in the DPO family [99].

The motion primitives and associated clusters are depicted in the configuration space and as a function of Jacobi constant to support further analysis. First, the 9 clusters of periodic orbits are displayed in Figure 6.4 in $\mathcal{R}$ using unique colors, with the black arrows indicating direction

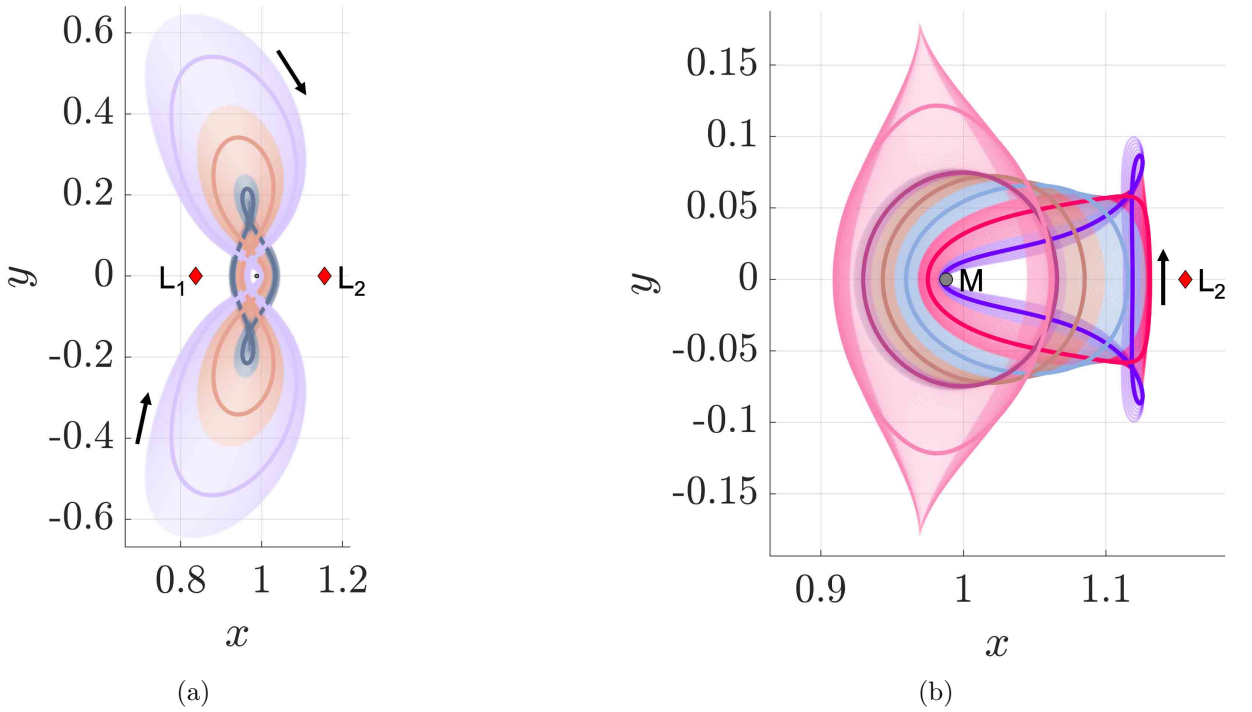

Figure 6.4: Motion primitives constructed for the DPO family in the Earth-Moon CR3BP, displayed with respect to the corresponding clusters in $\mathcal{R}$; clusters and motion primitives are split across two subfigures for visual clarity [99].

of motion relative to the Moon. Within each cluster, the periodic orbit selected as the motion primitive is highlighted in bold while additional members lie within the region of the same color. To support further analyzing these results, these clusters and motion primitives are also displayed on the left of Figure 6.5 as a function of C_J. DPOs at various values of C_J are displayed on the right of Figure 6.5 for reference; the selected orbits correspond to those highlighted in Figure 6.1. Each cluster in Figure 6.5 is colored consistent with Figure 6.4 and each motion primitive is located by a black diamond. Furthermore, the four dominant geometry changes ($G1$, $G2$, $G3$, $G4$) and the three dominant stability changes ($S1$, $S2$, $S3$) summarized in Table 6.1 are denoted with dashed black and gray lines, respectively.

Analysis of the clustering results in Figures 6.4 and 6.5 reveals that the motion primitive set successfully captures variations in geometry and stability of members along the DPO family:

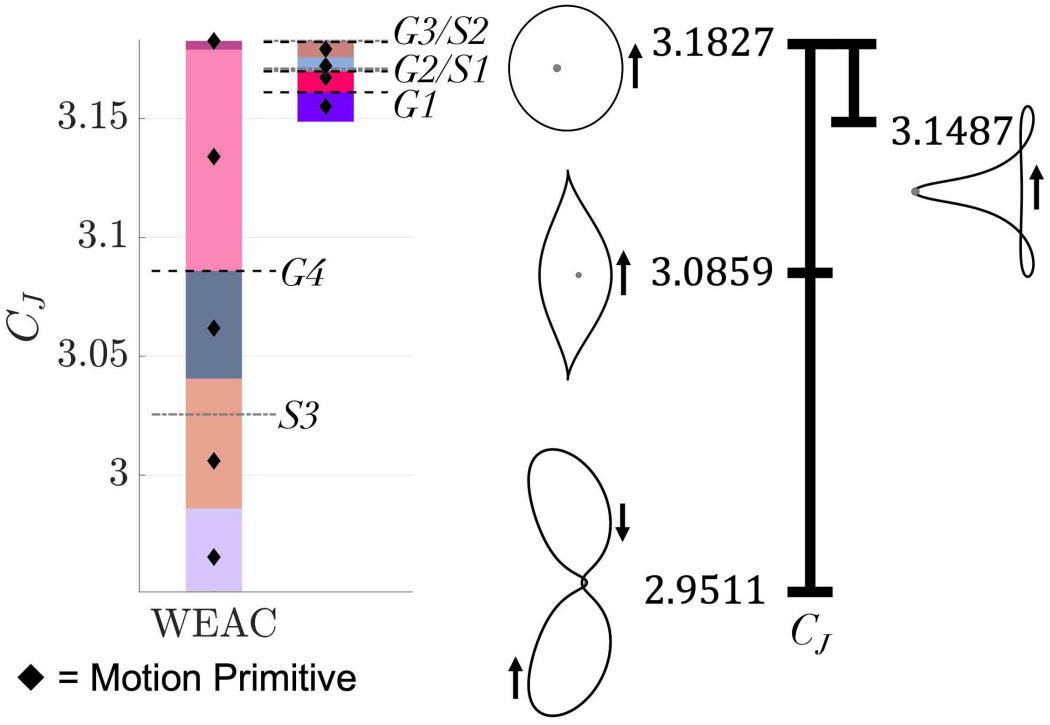

Figure 6.5: Clustering result and motion primitives for the DPO family in the Earth-Moon CR3BP as a function of C_J; dominant changes in geometry and stability are labeled on left of figure [99].

including those identified in Table 6.1 and more subtle changes that are challenging to describe in an analytical and generalizable manner. The presented procedure successfully identifies, at a minimum, all four distinct changes in geometry via changes in the number of and direction of motion at the apses. Additional clusters capture more subtle changes in Jacobi constant, stability, and geometry. For example, as C_J decreases after the change in geometry at $G4$, WEAC identifies three different clusters of orbits with two high retrograde apolunes and two low prograde perilunes due to the variations in C_J and stability. In fact, the third stability change, $S3$, is identified by the clustering approach but not exactly at the boundary due to the continuous feature description used to capture orbital stability. The distinct geometric differences between each of these clusters is visible in Figure 6.4a: although members of these clusters admit a similar general shape, regions along each orbit with a different direction of motion possess a distinctly different relative size in the configuration space. Another example of successful geometric differentiation is visible in Figure 6.4b: the pink

cluster possessing members with the largest y-amplitudes admit a significantly different geometry and evolution of the location of apses compared with members in the neighboring cluster that possess smaller y-amplitudes. This example demonstrates the capacity to use clustering to extract a small set of motion primitives representing a family of planar periodic orbits.

6.2.3 Summarizing the Earth-Moon L_1 Northern Halo Orbit Family

The L_1 halo orbits comprise a spatial family that emerges from a bifurcation along the L_1 Lyapunov orbit family [11, 118]. Figure 6.6 displays a subset of the L_1 northern halo family computed in the Earth-Moon CR3BP with selected members highlighted in distinct colors; note, only the northern orbits are analyzed due to their symmetry with the southern halo orbits about the plane of the primaries. At one end of the computed segment of the L_1 northern halo family, denoted in light brown in Figure 6.6, members intersect the L_1 planar Lyapunov orbit family and revolve in a clockwise manner about L_1. At the other end of the computed segment of the family, denoted in purple in Figure 6.6, members possess large z-amplitudes above the plane of the primaries and a low perilune. Analysis of Figure 6.6 reveals a variation in the shape and three-dimensional geometry along this spatial family. However, unlike the previous example with the DPO family, these geometric changes cannot be straightforwardly identified or analytically separated because the number of apses and the direction of motion at each apsis relative to the Moon are constant along the family. There are some changes in the number of apses relative to L_1, but the direction of motion at these apses also remains constant along the family. With geometry changes that are visually identifiable but challenging to locate analytically, the L_1 northern halo orbit family offers a suitable second demonstration case for the motion primitive construction process.

The stability indices of the computed segment of the L_1 northern halo orbit family also admit multiple qualitative changes. Figure 6.7 displays the stability indices, s_1 and s_2, scaled using the same normalization function as Figure 6.2 and plotted as a function of the Jacobi constant; the parameters associated with the highlighted orbits in Figure 6.6 are indicated in Figure 6.7 using the same color scheme. In addition, the qualitative changes in the orbital stability along the family

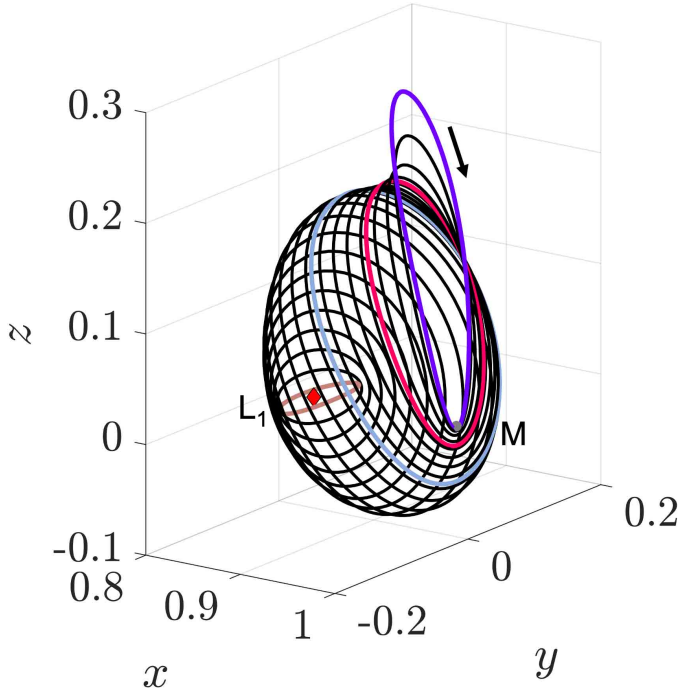

Figure 6.6: Computed segment of the L_1 northern halo orbit family displayed in $\mathcal{R}$ in the Earth-Moon CR3BP [99].

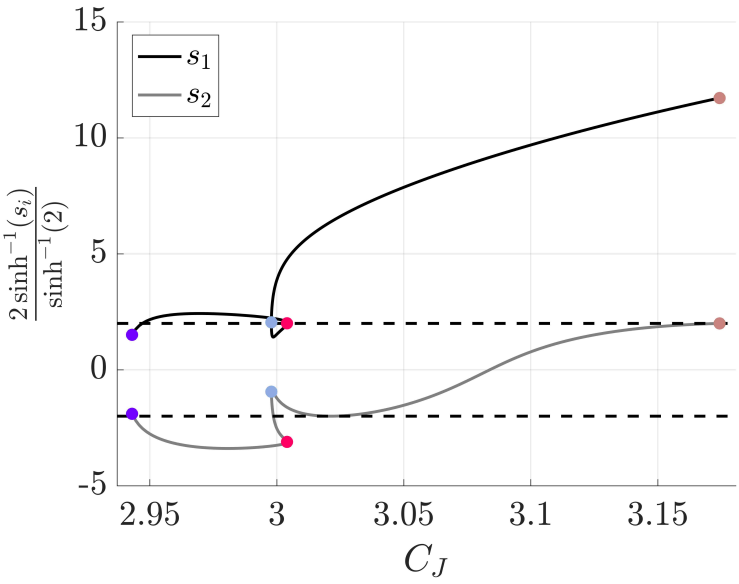

Figure 6.7: Stability indices, s_1 and s_2, along the computed segment of the L_1 northern halo orbit family in the Earth-Moon CR3BP [99].

Table 6.2: Dominant stability changes along the computed segment of the L_1 northern halo orbit family [99].

Label	Before Change	After Change	Approx. C_J
$S1$	$-2 < s_1 < 2$ $-2 < s_2 < 2$	— $s_2 < -2$	2.9435
$S2$	$-2 < s_1 < 2$ $s_2 < -2$	$s_1 > 2$ —	2.9470
$S3$	$s_1 > 2$ $s_2 < -2$	$-2 < s_1 < 2$ —	3.0040
$S4$	$-2 < s_1 < 2$ $s_2 < -2$	— $-2 < s_2 < 2$	2.9986
$S5$	$-2 < s_1 < 2$ $-2 < s_2 < 2$	$s_1 > 2$ —	2.9978

are summarized in Table 6.2 using the same configuration as Table 6.1. There are five primary changes in stability along the computed segment of the family. The s_1 index exhibits three changes in stability that occur in regions of the family where the halo orbits possess a large inclination and low perilune. For members of the family that approach the L_1 libration point with a Jacobi constant that is above $C_J = 3.0$, s_1 possesses a large positive value that indicates the existence of stable and unstable modes governing fast arrival onto or departure from the periodic orbit. Finally, s_2 exhibits two changes in stability: the value of s_2 passes through the critical value of -2 near Jacobi constants of $C_J \approx 2.9435$ and $C_J \approx 2.9986$. For members of the L_1 northern halo orbit family that possess a high inclination, low perilune, and values of the Jacobi constant that are less than $C_J = 3.0$, the magnitudes of s_1 and s_2 are on the order of 10^0. Consequently, the orbits in this region of the family that possess stable and unstable modes admit relatively slow natural arrival and departure motion along the associated hyperbolic invariant manifolds.

Using the geometric, stability, and energetic properties of members along the L_1 northern halo orbit family, an associated set of motion primitives is constructed. Similar to the DPO example, multiple shooting and pseudo-arclength continuation are used to compute 498 orbits along the L_1 northern halo orbit family. Then, the feature space encoding is constructed using Equation 6.6,

where both refPt and cenPt are specified as P_2 which is consistent with the evolution of this family towards the Moon. Together, these orbits and feature vectors produce a (498×15)-dimensional dataset where $s_{\max} = 2$. Next, k-means and agglomerative clustering with Ward linkage are applied to the dataset, each for 16 values of k ranging from 3 to 18, to generate the ensemble of base clustering results. WEAC is then applied to this ensemble with an inter-cluster distance threshold of $d_{\min} = 0.4$. Figure 6.8 displays the dendrogram produced by WEAC for this family of halo orbits. As denoted in Figure 6.8 with dashed red lines, the clusters produced using $k = 11$ possess the largest lifetime. The associated clusters, denoted by unique colors, and the motion primitives, denoted with black diamonds, are displayed in Figure 6.9a as a function of the discretized orbit number along the family; although this quantity does not possess a physical significance, it enables a clear and unique initial visualization of the results. Furthermore, the five dominant stability changes ($S1$, $S2$, $S3$, $S4$, $S5$) summarized in Table 6.2 are denoted with dashed gray lines. Figures 6.9b and 6.9c display two different views of the members of each cluster in $\mathcal{R}$; the motion primitives are highlighted in bold and the corresponding clusters capture the regions of the family that possess similar properties to each motion primitive.

Despite the absence of distinct or hard boundaries between members within the 15-dimensional feature space, the motion primitive set successfully captures the variety of geometric and stability characteristics exhibited by the L_1 northern halo orbit family. Figure 6.9a reveals that members are differentiated into separate clusters in the vicinity of, but not exactly at the location of, each qualitative change in orbital stability; such a result is not unexpected due to the definition of the stability component of the feature vector as a continuous function. $S1$, $S2$, $S3$, and $S4$ each describe stability changes where the two nontrivial pairs of eigenvalues of the monodromy matrix remain close to the unit circle in the complex plane and, therefore, the values of the stability component of the feature vector are similar on either side of each soft boundary. On the other hand, $S5$ is more closely captured by the clustering approach because it marks a more distinct change in stability as the magnitude of s_1 increases significantly away from the critical value of 2. The remaining clusters along the family above the dashed line for $S5$ in Figure 6.9a primarily reflect changes in geometry.

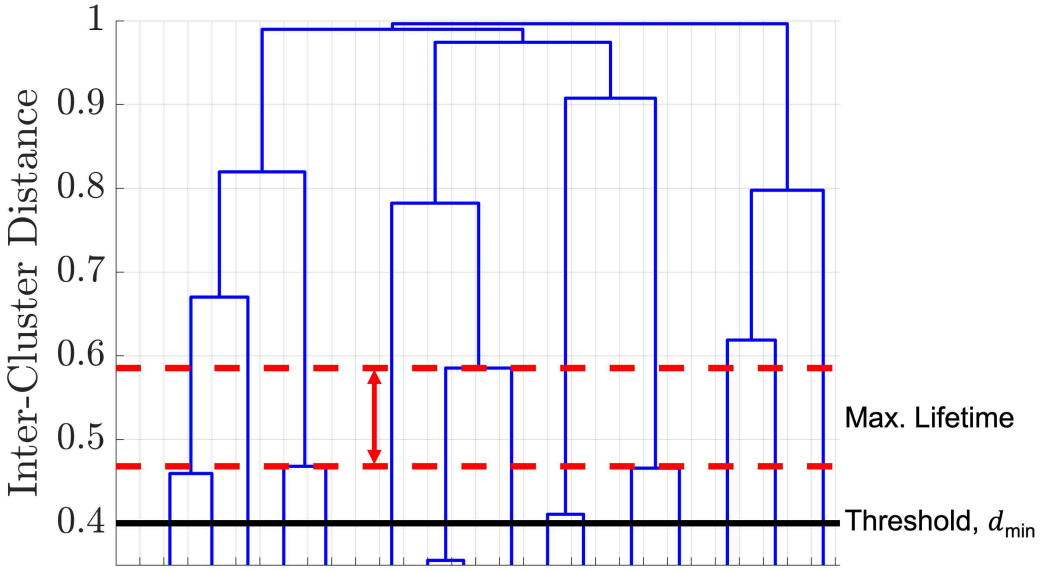

Figure 6.8: Dendrogram constructed via WEAC to determine clusters of periodic orbits in the L_1 northern halo orbit family [99].

In fact, analysis of Figures 6.9b and 6.9c reveals that these clusters capture the evolution of the eccentricity, inclination, shape, and location of members along this family as they evolve towards the plane of the primaries near L_1 and away from the Moon. The reduced set of motion primitives effectively captures the characteristics of the computed members of the L_1 northern halo orbit family, thereby supplying a simplified representation of the continuous family of spatial periodic orbits for use in rapid and informed trajectory design strategies.

6.2.4 Summarizing Periodic Orbit Families throughout a Multi-Body System

To further demonstrate the utility of summarizing a subset of the solution space of a multi-body system, the motion primitive construction process is applied to a variety of planar and spatial periodic orbit families throughout the Earth-Moon CR3BP. In addition, the motion primitive construction process is also applied to a couple of periodic orbit families in the Sun-Earth CR3BP to demonstrate the general applicability of the approach in any system. Each family of orbits is summarized based on its geometric, stability, and energetic properties following the procedure outlined

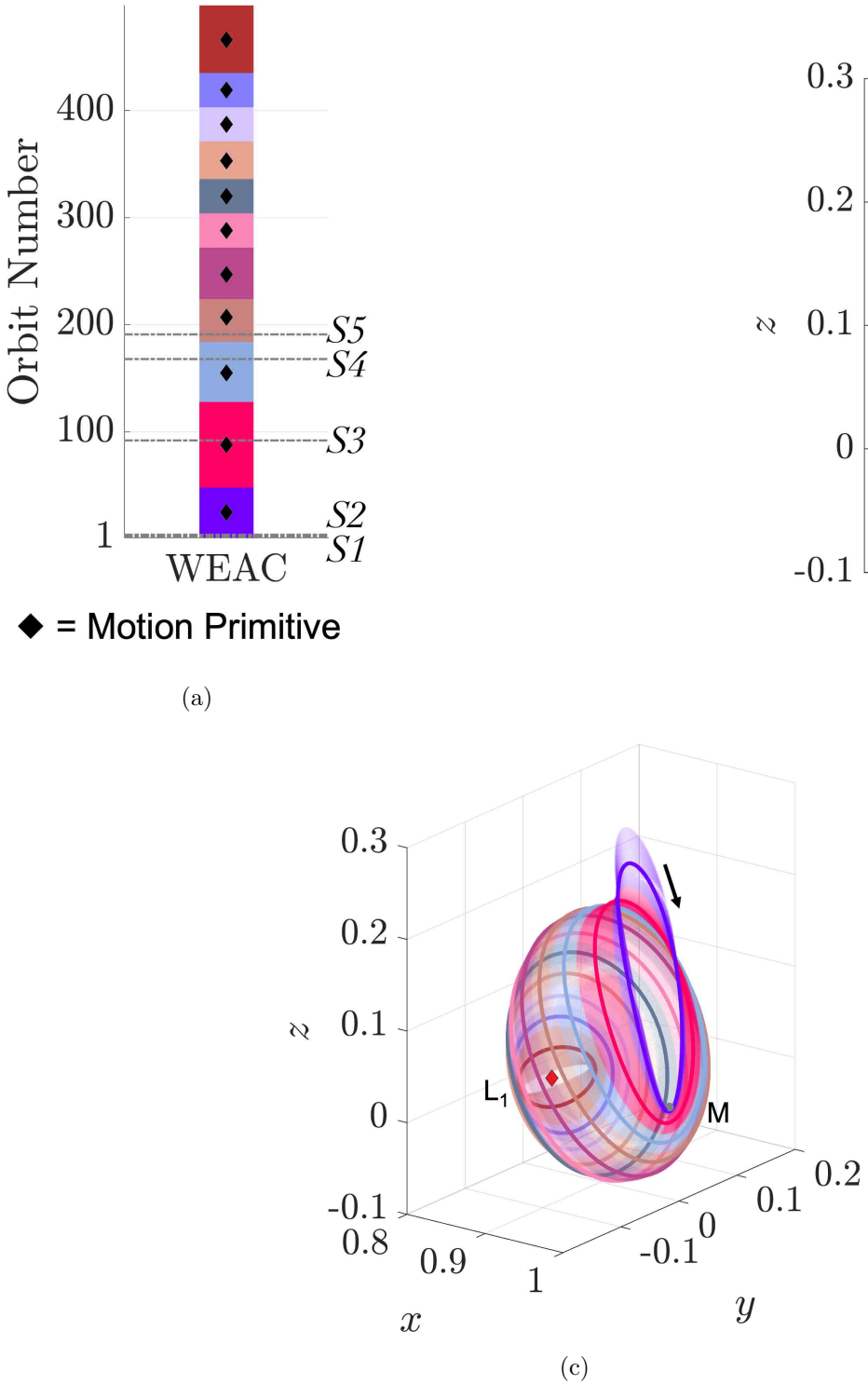

Figure 6.9: Clustering result and motion primitives for the L_1 northern halo orbits in the Earth-Moon CR3BP [99].

in Section 6.2.1. Figures 6.10-6.13 display the set of motion primitives constructed to summarize a variety of planar periodic orbit families in the Earth-Moon CR3BP including: the low prograde orbits (LoPOs); distant retrograde orbits (DROs); L_1, L_2, and L_3 Lyapunov orbits; L_5 short and long period orbits; and 3:1 resonant orbits. The black arrows indicate direction of motion, while each color indicates a distinct cluster and the associated motion primitive is highlighted in bold. The corresponding cluster for each motion primitive also reflects the region of existence of the primitive in the configuration space. Note that although colors are frequently repeated across distinct families for visual clarity, each cluster is localized to a single family of periodic orbits.

Using a similar configuration as Figures 6.10-6.13, Figures 6.14-6.16 display the motion primitives generated to summarize the northern L_2 and L_3 halo orbits; the L_1, L_2, and L_3 axial orbits; and the L_1, L_2, and L_3 vertical orbits. These orbit families are diverse in terms of their geometric, stability, and energetic properties as well as their locations in the configuration space of the Earth-Moon system. Finally, Figure 6.17 displays the motion primitives generated to summarize the L_2 Lyapunov orbits and the L_2 northern halo orbits computed in the Sun-Earth CR3BP. Despite the diversity and complexity exhibited by each family of periodic orbits, the general motion primitive construction process presented in Section 6.2.1 is applied to each family in the same manner with identical input parameters. This automated, unsupervised approach successfully constructs groupings that capture the fundamental characteristics of members along each family. As a result, these examples indicate the capacity for a data-driven procedure to extract smaller sets of motion primitives that summarize the wide variety of periodic orbits that influence the solution space within a multi-body system. This simpler representation of periodic orbit families may be used in reducing the complexity of constructing an initial guess for a complex trajectory.

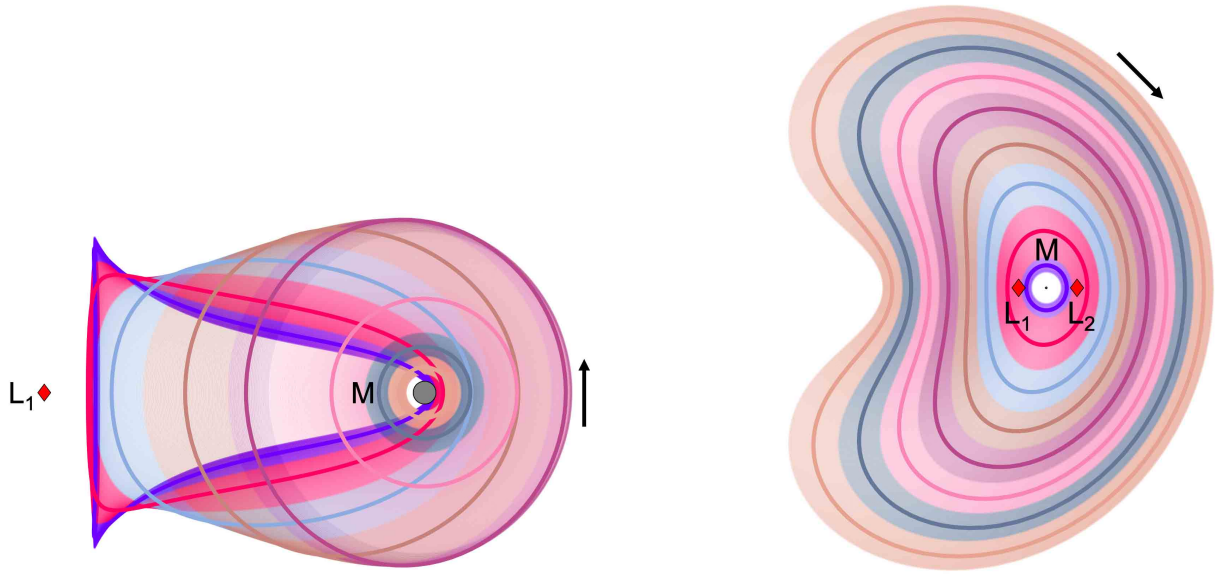

(a) LoPO (b) DRO

Figure 6.10: Motion primitives summarizing segments of the low prograde orbit (LoPO) and distant retrograde orbit (DRO) families in the Earth-Moon CR3BP, displayed with respect to the corresponding clusters in $\mathcal{R}$ [99].

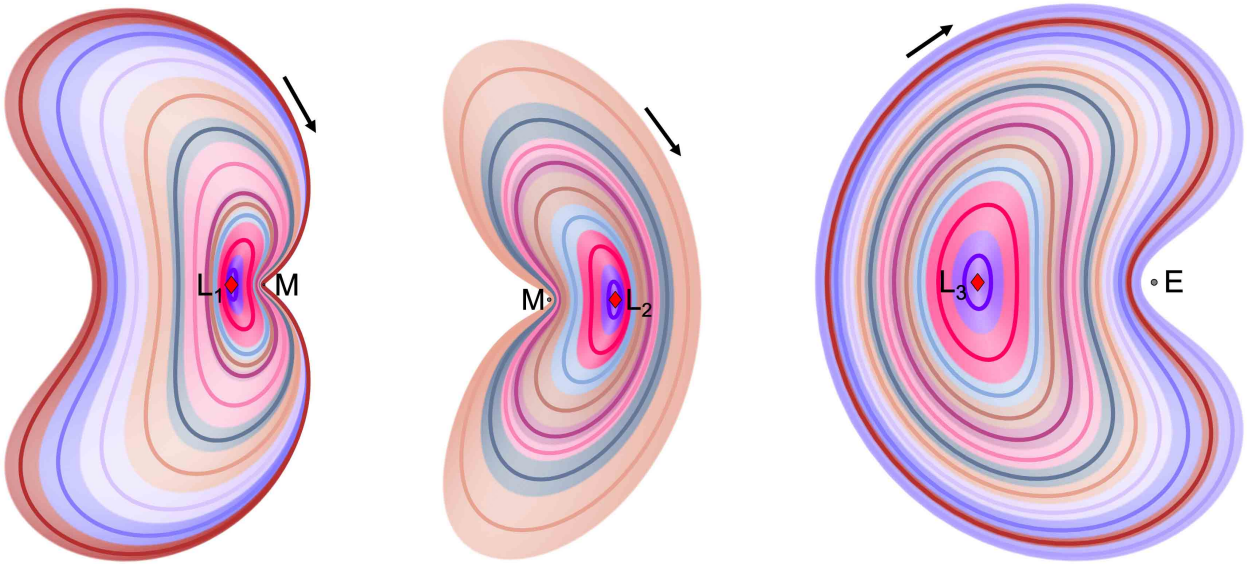

(a) L_1 Lyapunov Orbits (b) L_2 Lyapunov Orbits (c) L_3 Lyapunov Orbits

Figure 6.11: Motion primitives summarizing segments of the Lyapunov orbit families in the Earth-Moon CR3BP, displayed with respect to the corresponding clusters in $\mathcal{R}$ [99].

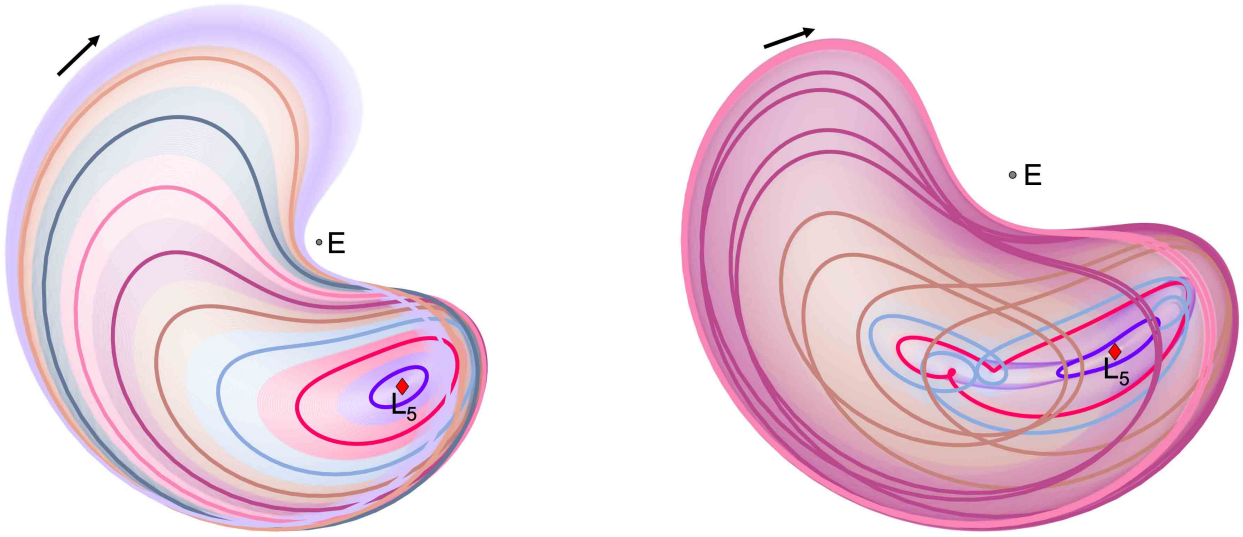

(a) L_5 SPO (b) L_5 LPO

Figure 6.12: Motion primitives summarizing segments of the L_5 short period orbit (SPO) and long period orbit (LPO) families in the Earth-Moon CR3BP, displayed with respect to the corresponding clusters in $\mathcal{R}$ [99].

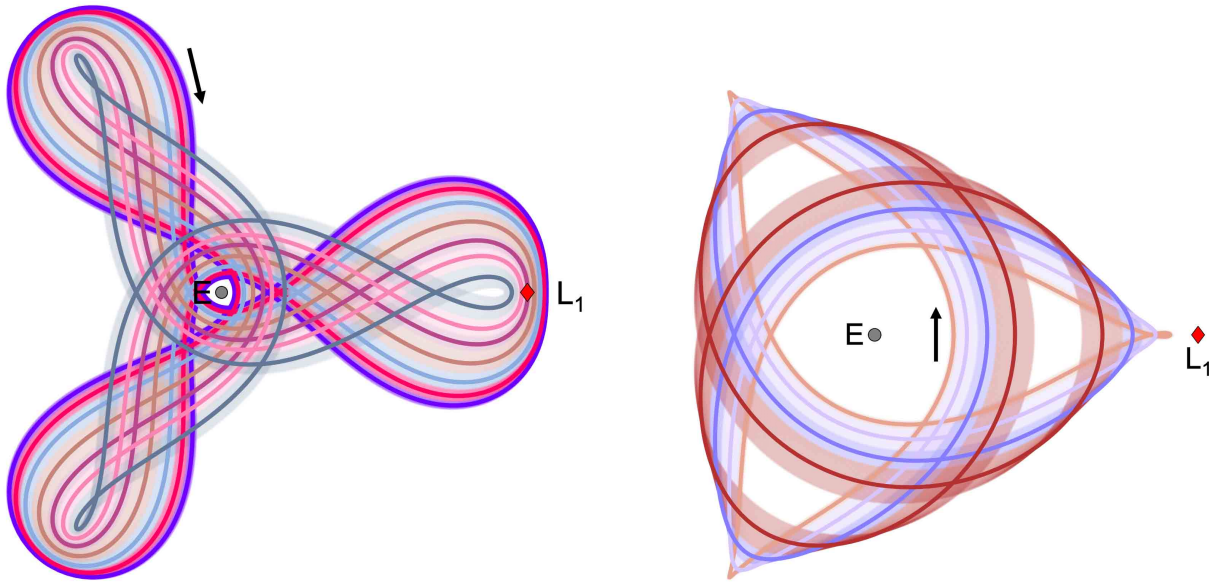

(a) (b)

Figure 6.13: Motion primitives summarizing a segment of the 3:1 resonant orbit family in the Earth-Moon CR3BP, displayed with respect to the corresponding clusters in $\mathcal{R}$; clusters and motion primitives are split across two subfigures for visual clarity [99].

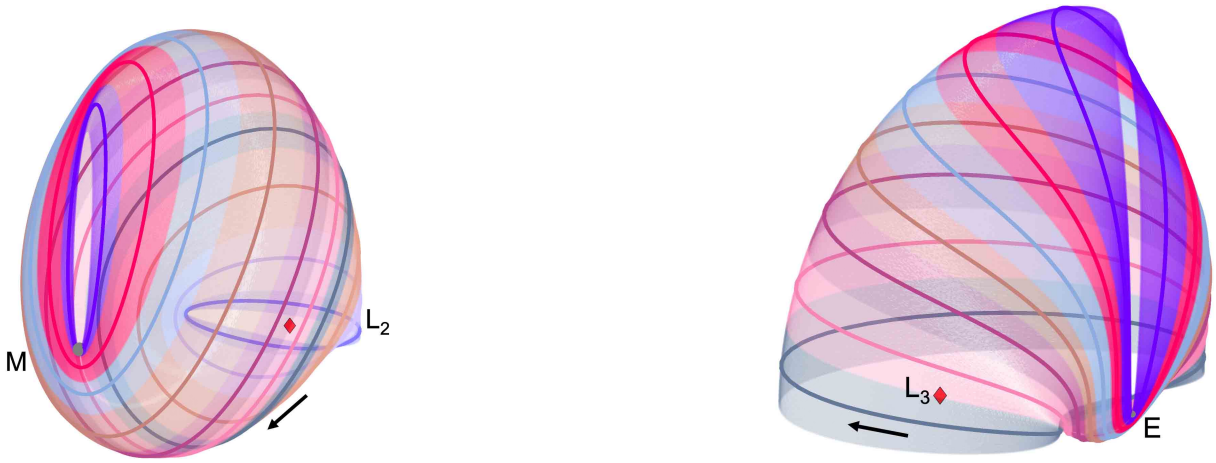

(a) L_2 Northern Halo Orbits (b) L_3 Northern Halo Orbits

Figure 6.14: Motion primitives summarizing segments of the northern halo orbit families in the Earth-Moon CR3BP, displayed with respect to the corresponding clusters in $\mathcal{R}$ [99].

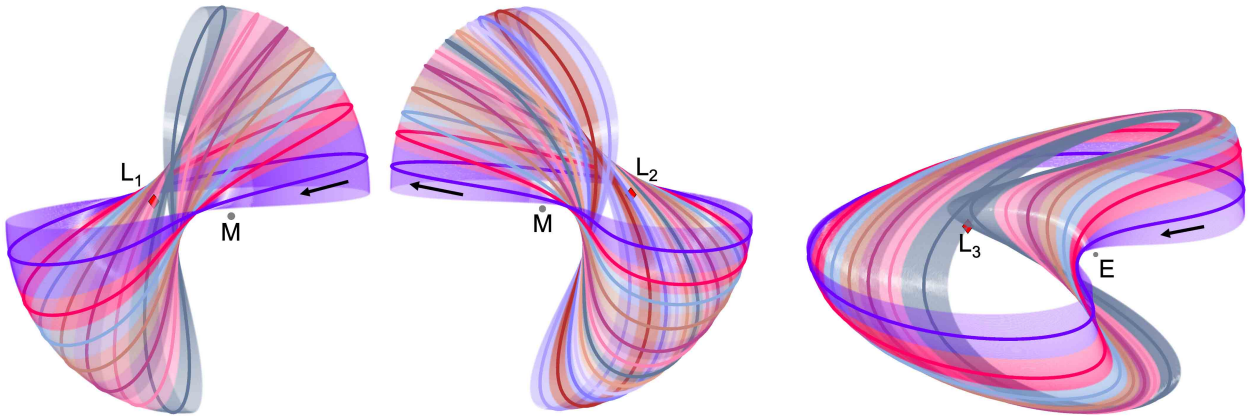

(a) L_1 Axial Orbits (b) L_2 Axial Orbits (c) L_3 Axial Orbits

Figure 6.15: Motion primitives summarizing segments of the axial orbit families in the Earth-Moon CR3BP, displayed with respect to the corresponding clusters in $\mathcal{R}$ [99].

6.3 Summarizing Hyperbolic Invariant Manifolds

The role of hyperbolic invariant manifolds in governing natural transport throughout a multi-body system has resulted in trajectory designers analyzing the geometry of arcs of finite duration along stable and unstable manifolds and assembling them to construct initial guesses for complex

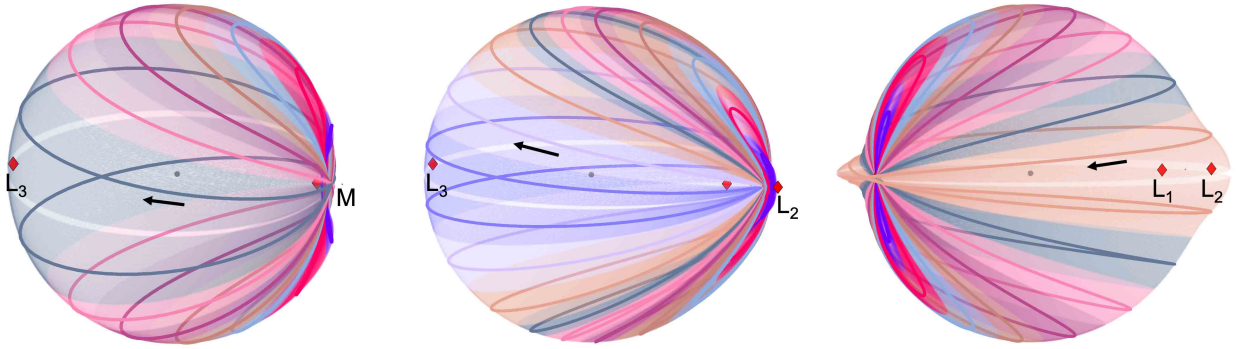

(a) L_1 Vertical Orbits (b) L_2 Vertical Orbits (c) L_3 Vertical Orbits

Figure 6.16: Motion primitives summarizing segments of the vertical orbit families in the Earth-Moon CR3BP, displayed with respect to the corresponding clusters in $\mathcal{R}$ [99].

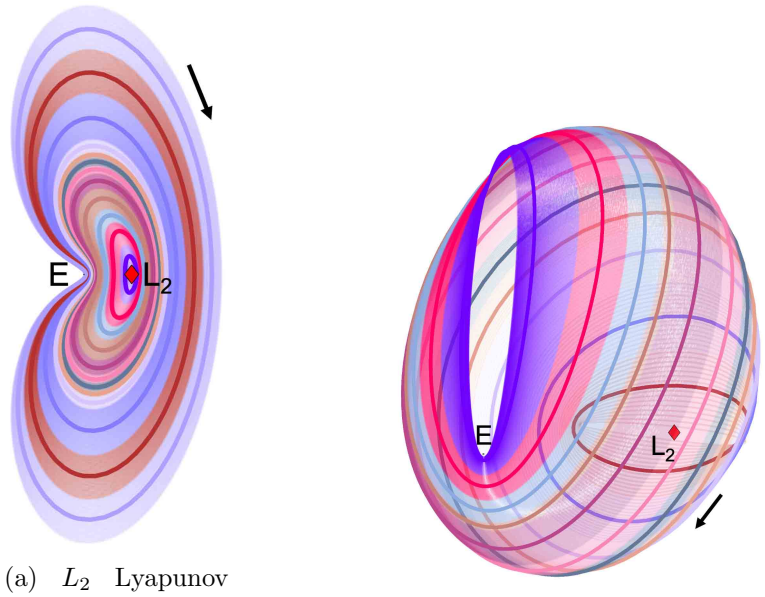

(a) L_2 Lyapunov Orbits (b) L_2 Northern Halo Orbits

Figure 6.17: Motion primitives summarizing segments of the L_2 Lyapunov and L_2 northern halo orbit families in the Sun-Earth CR3BP, displayed with respect to the corresponding clusters in $\mathcal{R}$.

transfers [61]. In this section, the motion primitive construction process is defined for summarizing a set of arcs computed along a stable or unstable manifold associated with a periodic orbit in the CR3BP. The process is demonstrated by summarizing arcs along an unstable half-manifold associated with a single L_1 Lyapunov orbit in the Earth-Moon CR3BP. This procedure is similar to

the process presented in Section 6.2.1 for periodic orbit families with some modifications, primarily in the computation and description of the nonperiodic trajectories comprising the dataset and the incorporation of additional cluster refinement.

6.3.1 Generating a Set of Arcs along a Hyperbolic Invariant Manifold

In the absence of generalized analytical descriptions, an approximation of a stable or unstable manifold is typically computed numerically as discussed in Section 3.4. First, an unstable periodic orbit is selected and discretized into a set of N_{PO} states equally spaced in time or arclength. Then, each state along the periodic orbit is perturbed such that it approximately lies along the desired local half-manifold. Finally, each state is propagated backward (forward) in time to produce a trajectory along the desired global stable (unstable) half-manifold over a time interval of interest with a set of termination criteria. The termination criteria depend on the desired manifold and therefore must be specified by a human analyst when generating the manifold structure. Depending on the termination criteria, the resulting trajectories along the desired half-manifold may be propagated for long time intervals and exhibit complex variations in geometry, particularly near a primary body. Consequently, each of the N_{PO} trajectories is discretized into multiple shorter arcs.

Given a set of N_{PO} trajectories computed along a desired half-manifold, each trajectory is first discretized into a sequence of nodes, where each node corresponds to either an apsis computed relative to a specified refPt or the terminal state of the trajectory. Each trajectory is then discretized into multiple shorter arcs based on a node window and shift size. The node window size, n_{window}, determines the length of each arc while the node shift size, n_{shift}, determines the manner in which the arcs are generated along each trajectory. Figure 6.18 provides a conceptual example of discretizing a trajectory composed of 8 nodes into multiple shorter arcs where $n_{\mathrm{window}} = 4$ and $n_{\mathrm{shift}} = 1$. The first arc is defined from the first node of the trajectory to the fourth node, the second arc is defined from the second node to the fifth node, and so forth until the final computed arc terminates at the final recorded node of the trajectory. Based on this selection of $n_{\mathrm{window}} = 4$ and $n_{\mathrm{shift}} = 1$, the conceptual trajectory segment depicted in Figure 6.18 is split into a total of 5 shorter overlapping

arcs. In some cases, the final shift along the trajectory may cause the node window to extend past the final node of the trajectory. In this case, the final computed arc terminates at the final recorded node of the trajectory and contains fewer nodes than n_{window}. Similarly, if n_{window} is larger than the total number of nodes computed along a given trajectory, then the trajectory is considered a single arc. Using this discretization process, each trajectory along a desired half-manifold may be split into multiple shorter arcs that capture the complex variations in geometry over shorter time intervals along the manifold structure. The resulting set of arcs may then be used to construct a summarizing set of motion primitives.

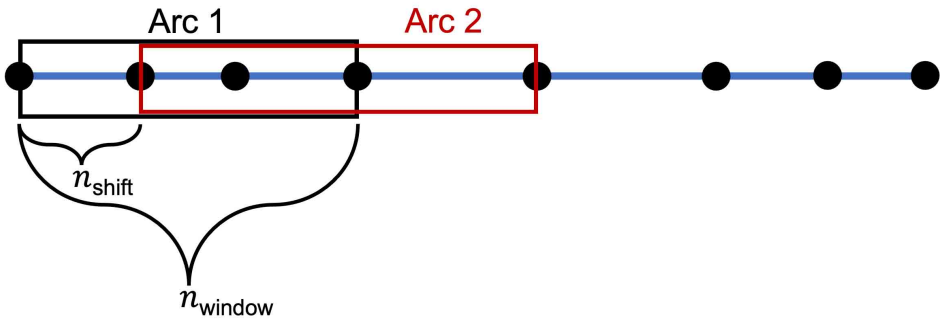

Figure 6.18: Conceptual example of discretizing a trajectory into multiple shorter arcs where $n_{\text{window}} = 4$ and $n_{\text{shift}} = 1$.

6.3.2 Motion Primitive Construction Process for Hyperbolic Invariant Manifolds

To construct a set of motion primitives summarizing arcs along a hyperbolic invariant manifold, the clustering procedure is defined as follows:

Motion Primitive Construction Process for Hyperbolic Invariant Manifolds in the CR3BP

Given: A set of arcs computed along a stable or unstable half-manifold associated with an unstable periodic orbit in a desired system in the CR3BP, composed of n_{d} members with with refPt and cenPt specified for the set of arcs.

(1) For each arc along the desired half-manifold: compute the apses that occur along the arc with respect to refPt, the terminal state of the arc if it does not coincide with the last

apsis, and the time between each pair of consecutive apses (including the terminal state).

(2) Construct an $(n_{\mathrm{d}} \times m_{\mathrm{f}})$-dimensional dataset containing the m_{f}-dimensional feature vector $\boldsymbol{f}_{\mathbf{Mani}}$ of each arc, as defined in Equation 6.7, to describe the geometry of each arc.

(3) Generate an ensemble of N_{c} base clustering results by applying k-means and agglomerative clustering with Ward linkage to the dataset, each for $N_{\mathrm{c}}/2$ values of k in a specified range.

(4) Specify an inter-cluster distance threshold, $d_{\min}$, ranging from 0 to 1 and apply WEAC to the ensemble of base clustering results computed in Step 3. The clustering result selected using WEAC possesses a number of clusters with the largest lifetime above $d_{\min}$.

(5) If applicable, refine the clusters produced by WEAC using the following refinement procedure:

   (a) Specify values for l_{csize}, l_{sim}, and k_{nn}. Each of these parameters is used in the refinement procedure: l_{csize} is a cluster size limit, l_{sim} is a similarity value limit, and k_{nn} is used for constructing a k-NN graph.

   (b) For each cluster C_i produced by WEAC:

      (i) Compute the number of members in C_i, i.e. $|C_i|$.

      (ii) If $|C_i| > l_{\mathrm{csize}}$, construct a k-NN graph from the members of C_i using the specified value of k_{nn}. To construct the k-NN graph, each member of C_i is defined by its position features contained in $\boldsymbol{f}_{\mathbf{Mani}}$ and the l^2-norm is used to compute the distance between two members in C_i. If there is more than one connected component in the resulting graph, then C_i is split into distinct subclusters that each correspond to one connected component in the graph. Note: A subcluster that is comprised of only one or two members cannot be identified using a k-NN graph when $k_{\mathrm{nn}} \geq 2$; these types of subclusters may be considered as outliers. To address these edge cases and include outlier detection, two rules are formulated during the graph construction process:

(ii.a) Consider the case where member a in C_i is not a nearest neighbor of any other members in C_i. If the average similarity of member a with its nearest neighbors in C_i (evaluated using $[\boldsymbol{A}_{\mathbf{coa}}]$) is $\geq l_{\text{sim}}$, then connect member a to only its closest nearest neighbor; otherwise, do not connect member a to any of its nearest neighbors.

(ii.b) Consider the case where member a in C_i is only a nearest neighbor of member b in C_i. If member a also considers member b to be a nearest neighbor, then connect member a to member b; otherwise, do not connect member a to any of its nearest neighbors.

(iii) If $|C_i| \leq l_{\text{csize}}$, use the similarity values from $[\boldsymbol{A}_{\mathbf{coa}}]$ computed in WEAC to refine C_i. Two members in C_i are grouped together in the same subcluster if they have a similarity value $\geq l_{\text{sim}}$. If this grouping process produces more than one subcluster, then C_i is split into its distinct subclusters. Note: For small clusters, a k-NN graph is well-connected for even small values of k_{nn} due to its size. Therefore, the similarity values computed in WEAC are leveraged to refine small clusters and ensure members in each resulting subcluster have a high degree of similarity.

(6) Extract a set of motion primitives as the medoids of the clusters in the final clustering result to summarize the set of arcs computed along the desired stable or unstable half-manifold.

Once the set of arcs are computed along the desired stable or unstable half-manifold, this procedure only requires a human analyst to select the range of values of k to form the base clustering results, the value of d_{min} used within WEAC, and, if applicable, l_{csize}, l_{sim}, and k_{nn} used for cluster refinement.

In applying this process to an unstable half-manifold associated with an L_1 Lyapunov orbit in the Earth-Moon CR3BP, the inter-cluster distance threshold is set at $d_{\text{min}} = 0.4$. Furthermore, the range of k values used to generate the cluster ensemble is selected based on the size of the dataset

as $k \in [10, 75]$ [31, 52]. This range is selected to ensure the evidence supplied to WEAC in the form of base clustering results encompasses both a small number of clusters, which tends to raise the average similarity values between members in $[\boldsymbol{A}_{\mathbf{coa}}]$, and a large number of clusters, which tends to lower the average similarity values in $[\boldsymbol{A}_{\mathbf{coa}}]$; as a result, a wide range of k values tends to balance out these effects to more clearly reflect the natural structure of a complex dataset [31, 52]. The computation time for this clustering procedure to generate motion primitives summarizing the arcs along a hyperbolic invariant manifold is on the order of 10^1 seconds for the example in this section using an iMac with a 3GHz 6-Core Intel Core i5 processor.

An additional step for cluster refinement is included in the motion primitive construction procedure due to the potential sparsity of arcs computed along a hyperbolic invariant manifold and for cases when related, yet visually distinct arcs are incorrectly clustered together; such issues may occur in high-dimensional feature spaces due to the curse of dimensionality [3]. The cluster refinement procedure requires three input parameters to be specified by a human analyst: l_{csize}, l_{sim}, and k_{nn}. The value of l_{csize} is used to differentiate between large and small clusters. As outlined in Step 5 of the motion primitive construction procedure, large clusters are refined using a k-NN graph and small clusters are refined using the similarity values from $[\boldsymbol{A}_{\mathbf{coa}}]$ computed in WEAC. This distinction is needed because a k-NN graph for a small cluster may be well-connected for even small values of k_{nn} due to its size. Consequently, using the similarity values from $[\boldsymbol{A}_{\mathbf{coa}}]$ provides an effective method for ensuring members within each small cluster have a high degree of similarity, as determined by the selected value of $l_{\text{sim}} \in [0, 1]$. A larger value of l_{sim} results in more differentiation while a smaller value of l_{sim} results in less differentiation within small clusters. Finally, the value of k_{nn} determines the degree of connectivity in the k-NN graph constructed for each large cluster. A larger value of k_{nn} naturally results in a more connected graph because k_{nn} dictates the number of nearest neighbors each member is connected to in the graph [46]. Consequently, l_{csize}, l_{sim}, and k_{nn} may be intuitively selected based on the desired scale of cluster refinement. Similar to the input parameters for the clustering process, these input parameters for the cluster refinement procedure may be selected and then adjusted in an iterative fashion by inspecting the resulting

clusters. Despite the need to select input parameters, the unsupervised refinement process limits the burden on a human analyst when additional cluster refinement is deemed appropriate.

6.3.3 Summarizing an Unstable Half-Manifold of an Earth-Moon L_1 Lyapunov Orbit

A set of motion primitives is constructed to summarize segments of a global unstable half-manifold associated with an L_1 Lyapunov orbit in the Earth-Moon CR3BP. The global unstable half-manifold is generated for a motion primitive extracted from the L_1 Lyapunov orbit family; specifically, the L_1 Lyapunov orbit primitive is an unstable orbit that exists at $C_J \approx 3.1670$. The trajectories that lie along this unstable manifold exhibit many close approaches and revolutions around the Moon, while some trajectories impact the Moon or leave the vicinity of the Moon through the L_1 or L_2 gateways. Figure 6.19a displays short segments of trajectories, denoted in red, computed along the unstable half-manifold departing the selected L_1 Lyapunov orbit, denoted in black, towards the Moon. In Figure 6.19, the Moon is plotted to scale and the gray regions correspond to the forbidden regions of motion bounded by ZVCs.

The selected L_1 Lyapunov orbit is discretized into a set of $N_{\text{PO}} = 500$ states equally spaced in time. Then, 500 trajectories are propagated along the desired unstable half-manifold of the L_1 Lyapunov orbit. Each trajectory is propagated until either 15 subsequent apses occur relative to the Moon, an impact with the Moon occurs (assuming a spherical approximation of the Moon), or the trajectory departs the lunar vicinity through either the L_1 or L_2 gateways. Figure 6.19b displays the resulting Poincaré map with an apsis surface of section recording up to 15 apses with respect to the Moon. In addition, the terminal state of each trajectory that impacts the Moon or departs the lunar vicinity in also included in Figure 6.19b even if it does not correspond to an apsis event. Next, each trajectory is discretized into multiple shorter arcs using the method outlined in Section 6.3.1 where $n_{\text{window}} = 4$ and $n_{\text{shift}} = 1$. This discretization process produces up to 12 smaller overlapping arcs along each trajectory, where each arc possesses up to 4 apses with respect to the Moon. These arcs are then used to form the dataset that describes the unstable

half-manifold of the selected L_1 Lyapunov orbit.

The motion primitive construction process for a general hyperbolic invariant manifold outlined in Section 6.3.2 is applied to the set of arcs generated from the unstable half-manifold of the selected L_1 Lyapunov orbit. Using the feature vector $\boldsymbol{f}_{\mathbf{Mani}}$ defined in Equation 6.7, the resulting dataset is a (1196×19)-dimensional dataset. Given the expected diverse and complex geometric variations along manifold structures as well as the size of the dataset, $k \in [10, 75]$ is selected to encompass a reasonable number of distinct characteristics in the dataset. WEAC is then applied to the resulting 132 base clustering results; in addition, the cluster refinement procedure is also leveraged with the following input parameter selections: $l_{\text{csize}} = 5$, $l_{\text{sim}} = 0.9$, and $k_{\text{nn}} = 2$. As a result of this process, 69 clusters and their associated motion primitives are generated to summarize the manifold structure.

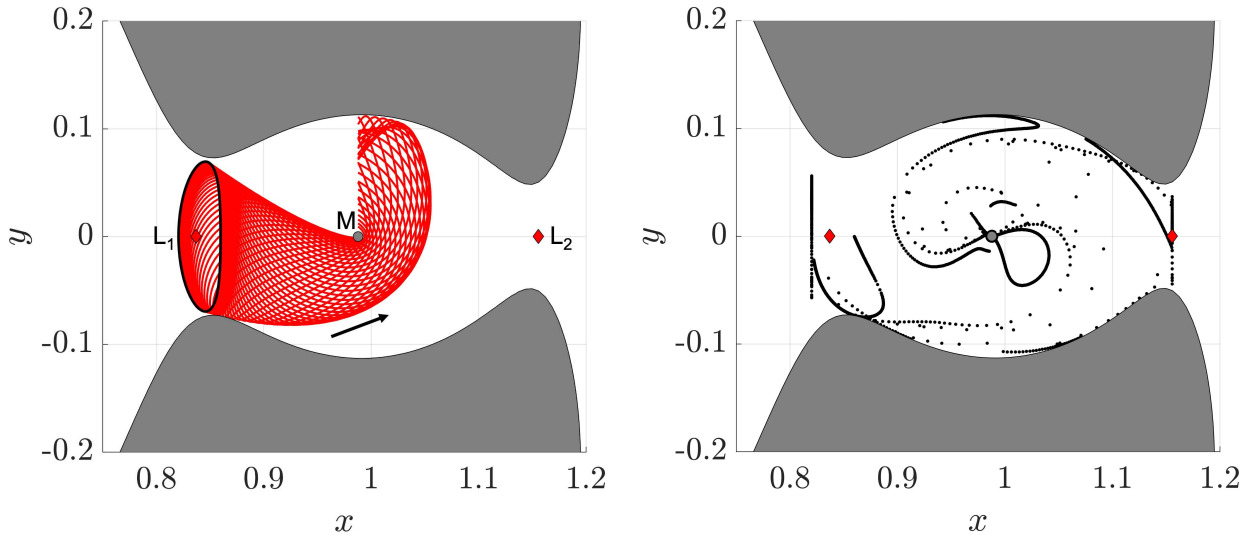

(a) Unstable half-manifold of the selected L_1 Lyapunov orbit generated towards the Moon for up to two returns to an $x = 1 - \mu$ surface of section.

(b) Poincaré map with an apsis surface of section recording up to 15 apses with respect to the Moon for 500 trajectories that lie along an unstable half-manifold of the selected L_1 Lyapunov orbit. In addition, the terminal state of each trajectory that impacts the Moon or departs the lunar vicinity is also included on the map.

Figure 6.19: Unstable half-manifold of an L_1 Lyapunov orbit at $C_J \approx 3.1670$ generated towards the Moon with up to 500 trajectories [99].

Trajectory arcs lying along the unstable half-manifold of an L_1 Lyapunov orbit at $C_J \approx 3.1670$ exhibit a variety of distinct geometries in the lunar vicinity. Following application of the presented procedure to this dataset, the resulting 69 clusters and motion primitives are displayed in Figures 6.20 and 6.21. Each cluster and its corresponding motion primitive is labeled with the prefix "U" followed by a number to facilitate discussion of the results. In these figures, the corresponding trajectories for each cluster are plotted in $\mathcal{R}$ with the motion primitives denoted in bold and unique colors assigned to distinct clusters. Clusters that contain only two members, such as U37, depict both members of the cluster with one member arbitrarily selected as the motion primitive because either arc is suitable to summarize the motion in the cluster. Analysis of these figures reveals that the motion primitives extracted from clusters U2, U3, U7, U14, U16, U26, and U66 effectively capture several distinct geometries admitted by arcs that impact the Moon after departing the vicinity of the L_1 Lyapunov orbit. Furthermore, a variety of motion primitives summarize different types of motion that depart the lunar vicinity through the L_1 gateway (U1, U17, U18, U30, U35, U59, U60, U63, U64, U67, U68) as well as the L_2 gateway (U19-21, U24, U46). In addition, multiple fundamental departure geometries from the initial L_1 Lyapunov orbit are uncovered via clusters U4, U5, U9, U45, and U65-U69. The remaining motion primitives effectively summarize the geometries admitted by subsequent arcs along the selected unstable half-manifold in the lunar vicinity: a variety of arcs revolving around the Moon with varying close approaches are recovered as well as the flow of trajectories towards the L_2 gateway. Some of the arcs revolving around the Moon possess segments that resemble known periodic orbits. For example, clusters U33, U34, U38-U44, U47-U50, and U53-U57 contain segments with similar geometries to members of the DPO family at $C_J \approx 3.1670$. This set of motion primitives supplies a succinct summary of the trajectories along an unstable half-manifold that may be useful when designing a transfer in cislunar space.

Due to the feature space definition and the potential sparsity of trajectories discretized along a hyperbolic invariant manifold, the original WEAC results may sometimes produce clusters that appear to contain distinct smaller subclusters. Before refining the clusters, the initial WEAC result for the arcs computed along the unstable half-manifold associated with the L_1 Lyapunov orbit at

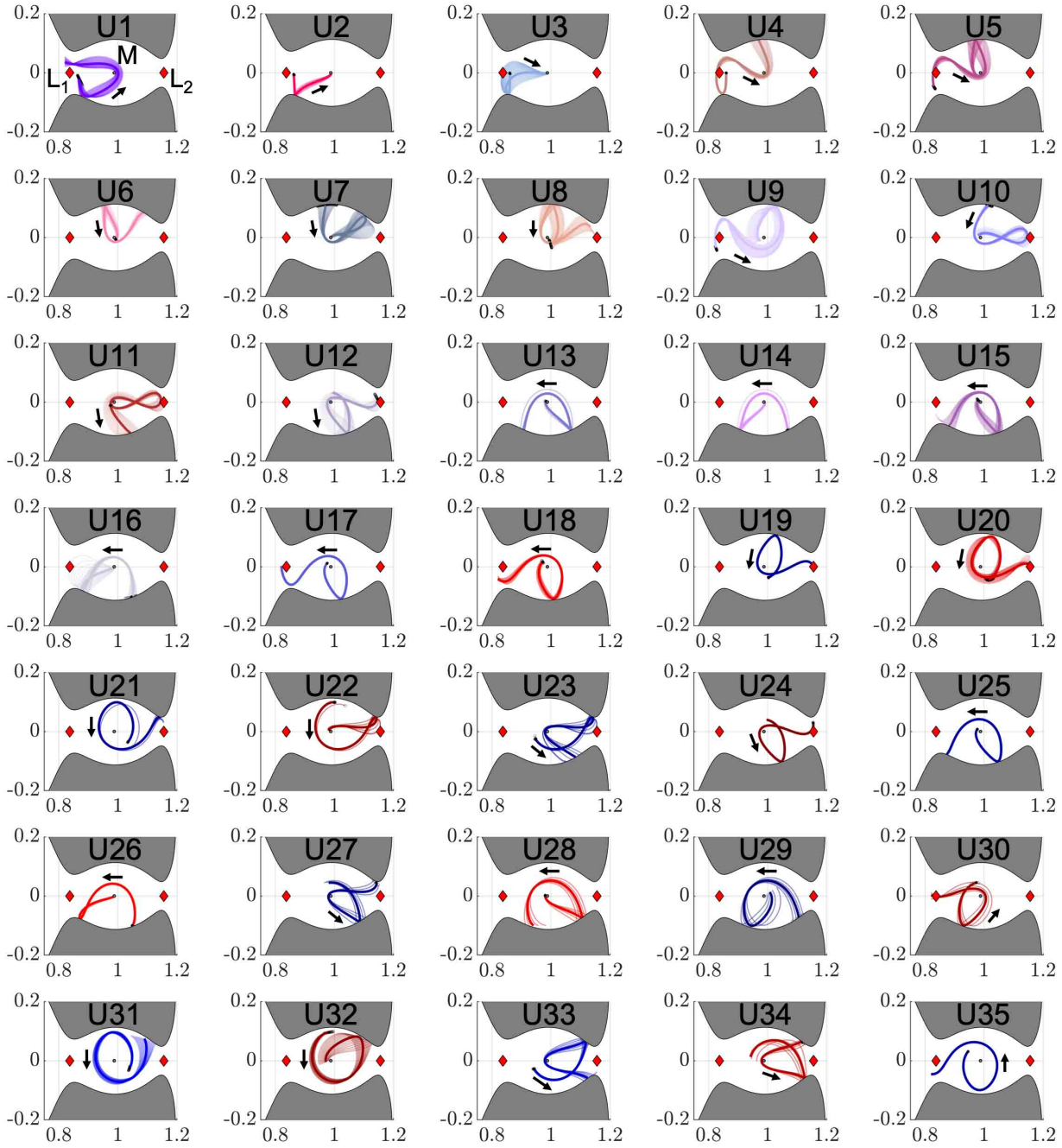

Figure 6.20: Trajectory clusters U1-U35 computed along the unstable half-manifold directed towards the Moon for an L_1 Lyapunov orbit at $C_J \approx 3.1670$; motion primitives are denoted in bold.

$C_J \approx 3.1670$ identifies 33 distinct clusters; 20 of these clusters are refined. A majority of these clusters consist of one dense subcluster and one or more smaller sparse subclusters containing only

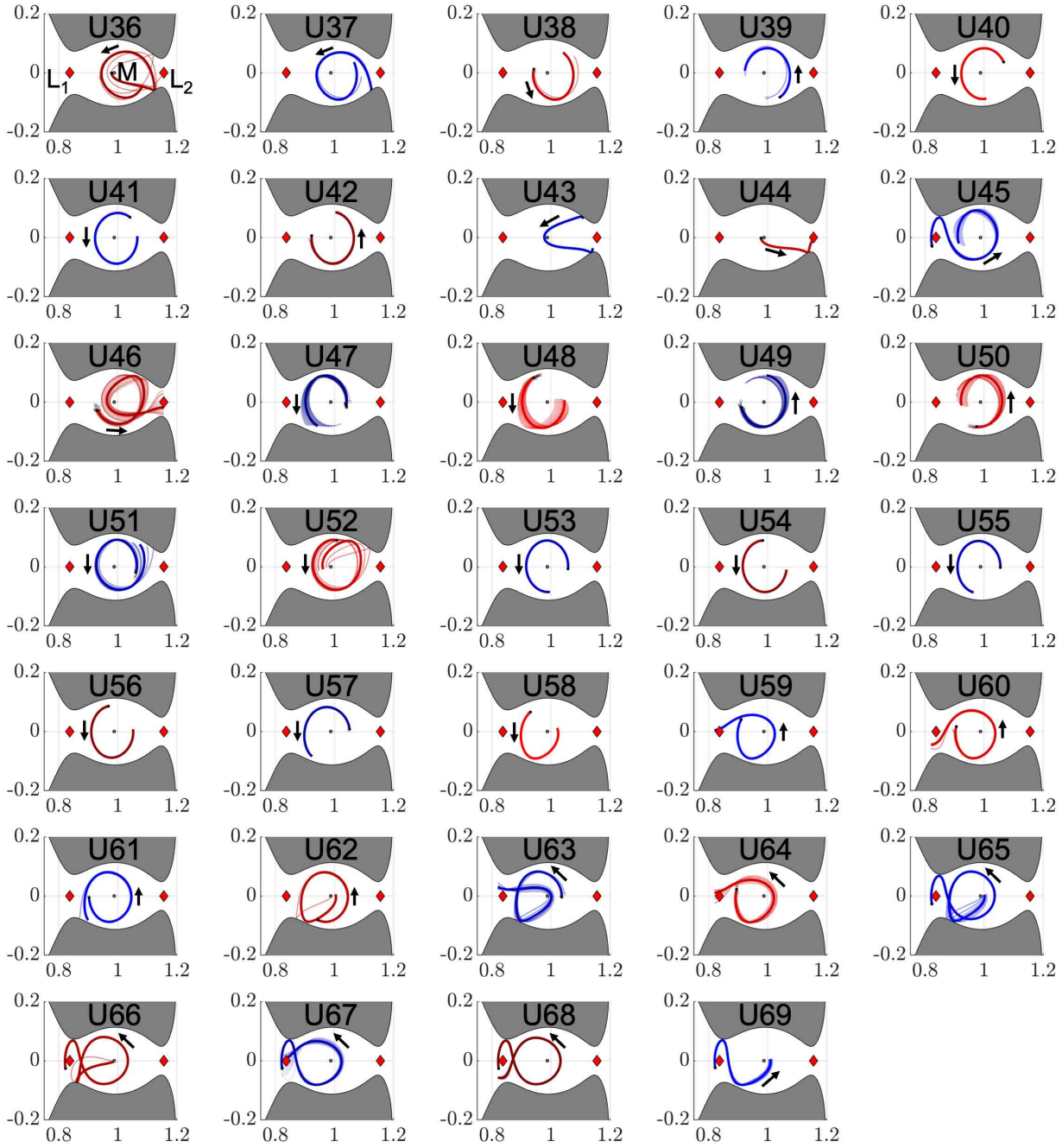

Figure 6.21: Trajectory clusters U36-U69 computed along the unstable half-manifold directed towards the Moon for an L_1 Lyapunov orbit at $C_J \approx 3.1670$; motion primitives are denoted in bold.

a few members, typically ranging from 1 to 7 members. A total of 36 outlier arcs are identified (approximately 3.01% of the total members of the dataset) such that 23 of the final 69 clusters

contain only one or two members.

To demonstrate the utility of the cluster refinement procedure, consider clusters U11 and U23 in Figure 6.20. The WEAC approach originally produced the cluster displayed in Figure 6.22a that appears to contain one dense subcluster (U11) and one smaller sparse subcluster consisting of 6 members (U23); these subclusters are distinct despite sharing some similarities in their general geometries. As a result, the cluster is automatically refined using the process outlined in Step 5 of the motion primitive construction procedure for hyperbolic invariant manifolds. A k-NN graph is constructed from the original cluster and is used to separate it into two distinct clusters, U11 and U23, as displayed in Figure 6.22b. To provide additional context, a representation of the k-NN graph used to separate U11 and U23 into distinctly separate clusters is displayed in Figure 6.22c. As previously discussed, due to the sparsity of the dataset there may be clusters with only a few members that are incorrectly grouped with trajectories that are most similar to them in the prescribed feature space. In these cases, the presented refinement approach is able to successfully identify and form smaller subclusters to improve the final clustering result for the dataset while limiting the burden on a human analyst. However, the refinement procedure may sometimes lead to excessive fragmentation of the original clustering results; furthermore, a clustering approach is not expected to be 100% accurate [3]. Consequently, selecting input parameters for both the clustering procedure and the cluster refinement approach are considered design choices that may be iteratively updated by a human analyst until the clustering result and set of motion primitives is considered sufficient for the desired application; this process of tuning input parameters is simplified by using a consensus clustering approach and is significantly less difficult and time-consuming than manually inspecting datasets containing thousands of trajectories.

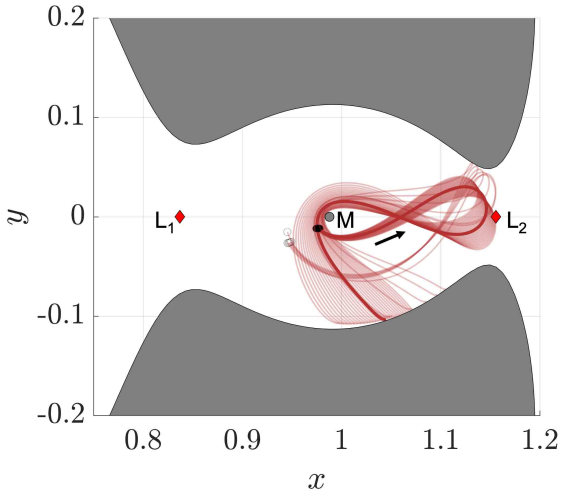

(a) An original cluster produced by WEAC appearing to contain one dense subcluster and one smaller sparse subcluster.

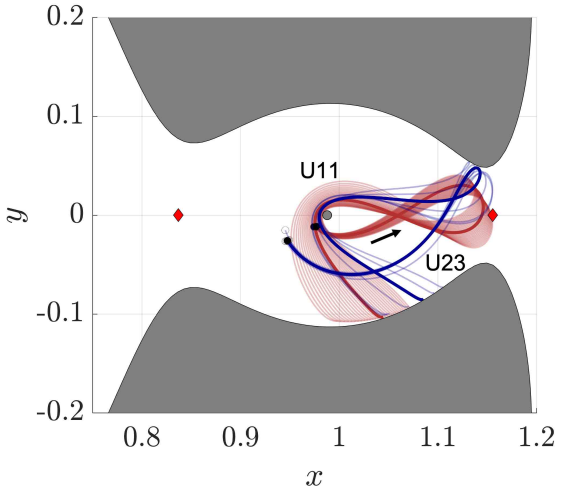

(b) Refined pair of clusters generated from the original cluster produced by WEAC.

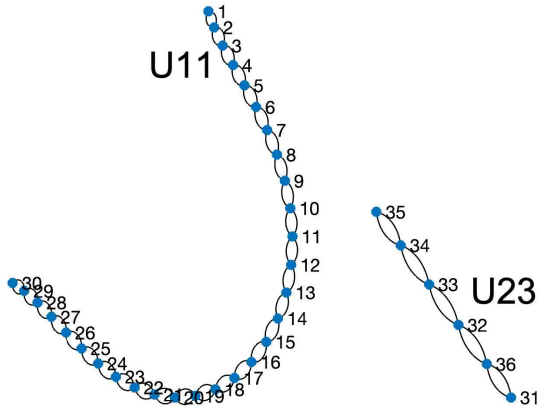

(c) Representation of the k-NN graph used to refine the cluster displayed in Figure 6.22a.

Figure 6.22: Refinement of a single cluster produced by WEAC into two distinct clusters during the motion primitive construction process for the unstable half-manifold of an L_1 Lyapunov orbit at $C_J \approx 3.1670$ [99].

Chapter 7

Motion Primitive Approach to Trajectory Design in a Multi-Body System

The increasing number and variety of spacecraft that are expected to operate within cislunar space and other multi-body gravitational environments throughout the solar system necessitates the continued development of strategies for rapid trajectory design and design space exploration. In the field of robotics, similar needs have been addressed using motion primitives that capture the fundamental building blocks of motion and are used to rapidly construct complex paths. Inspired by this concept, this work leverages motion primitives to construct a framework for rapid and informed spacecraft trajectory design in a multi-body gravitational system. First, motion primitives of fundamental solutions, e.g., selected periodic orbits and their stable and unstable manifolds, are generated via clustering to form a discrete summary of segments of the phase space. Graphs of motion primitives are then constructed and searched to produce primitive sequences that form candidate initial guesses for transfers of distinct geometries. Continuous transfers are computed from each initial guess using multi-objective constrained optimization and collocation. In this chapter, the primitive-based trajectory design framework is presented and demonstrated by evaluating a planar transfer design scenario from an L_1 Lyapunov orbit to an L_2 Lyapunov orbit in the Earth-Moon CR3BP with impulsive maneuvers. Note: An earlier version of the approach presented in this chapter appeared in a conference paper by Smith and Bosanac [98].

7.1 Primitive-Based Trajectory Design Process

In this chapter, a primitive-based initial guess construction framework is formulated to rapidly generate trajectories in the CR3BP. This procedure consists of the following steps:

(1) Construct a motion primitive library that summarizes the characteristics of arcs that exist within segments of the solution space.

(2) Construct a motion primitive graph that discretely approximates a subset of the continuous solution space.

(3) Search the graph for motion primitive sequences that serve as candidates for initial guesses for trajectories.

(4) Construct an initial guess for each trajectory by refining each motion primitive sequence.

(5) Correct each initial guess to produce a continuous trajectory with impulsive maneuvers using direct collocation and optimization.

(6) Compute additional transfers spanning segments of the design space, where appropriate.

This chapter summarizes and demonstrates each step of the initial guess construction process using the example of a planar transfer from an L_1 Lyapunov orbit to an L_2 Lyapunov orbit in the Earth-Moon CR3BP with impulsive maneuvers.

7.2 Step 1: Construct a Motion Primitive Library

The first step in the initial guess construction framework is to construct a library of motion primitives along with information approximating the regions of the phase space spanned by arcs with similar properties. In existing applications, motion primitives have been extracted using a variety of methods such as manual labeling, analytical approximations via basis functions, or clustering [29, 79, 112, 90]. Then, an initial guess for a trajectory may be coarsely constructed from an ordered sequence of motion primitives within the library [117, 63, 29]. In the absence of

general analytical expressions to describe the solution space and due to the significant burden of manual labeling, data mining techniques are used to construct sets of motion primitives, as outlined in Chapter 6, that are leveraged as the fundamental building blocks for initial guess construction.

Consider a set of motion primitives and their corresponding clusters generated from a larger set of trajectories. The region within the phase space spanned by trajectories resembling a specific motion primitive supplies information that is valuable in constructing a motion primitive graph that is searched to form an initial guess for a trajectory. In robotics, a motion primitive is commonly defined as a type of control input or fundamental type of action a robot may take to move anywhere within its environment unless hindered by a hardware or operational constraint [29, 79, 112]. However, trajectories in the chaotic environment of the CR3BP that resemble a specific motion primitive, given the specific definition used in this work, only exist within a particular region of the phase space. Furthermore, it may be challenging or computationally expensive to analytically or numerically describe the volumes of the phase space spanned by each cluster of similar trajectories. Thus, in the proof of concept presented in this investigation, a small set of representative members from the cluster associated with each motion primitive is also stored in the motion primitive library. This set is defined as $R_{\mathrm{e}} = \{\boldsymbol{q}_{\mathbf{R}}(t) \in C\}$, where $\boldsymbol{q}_{\mathbf{R}}(t)$ is one of a small number of representative trajectories that exist across cluster C corresponding to a specific motion primitive.

To select the representative trajectories that form the set R_{e} for a given primitive without requiring manual labeling or a prespecified sampling scheme, a straightforward clustering approach is used. First, the cluster C associated with a given motion primitive is partitioned into k subclusters using the k-means algorithm, which is computationally efficient and tends to produce evenly-sized clusters [46]. A representative trajectory is then computed as the medoid from each subcluster [99]. Appended to this set of k trajectories is a set of trajectories that lie at the extrema of the values of the following quantities calculated across each cluster: for periodic orbit families, the Jacobi constant; and for hyperbolic invariant manifolds, the total propagation time along an arc. Finally, if C contains fewer than k members, then all of the trajectories in C are labeled as representative trajectories. Although this approach used within this proof of concept admits a low complexity,

a parametric approximation that directly describes the region of the phase space spanned by arcs with similar characteristics to the motion primitive is an interesting avenue for future work.

To demonstrate this step of the design process, fundamental solutions are generated to support the construction of a planar transfer from an L_1 Lyapunov orbit to an L_2 Lyapunov orbit in the Earth-Moon CR3BP. The selected L_1 Lyapunov orbit exists at $C_J \approx 3.1670$ whereas the selected L_2 Lyapunov orbit exists at $C_J \approx 3.1666$. Both of these orbits are primitives of their associated periodic orbit families, as computed in Chapter 6 and displayed in Figure 6.11, and are unstable. Next, the planar stable and unstable half-manifolds of these L_1 and L_2 Lyapunov orbits are generated towards the Moon. Trajectories within each half-manifold are propagated until either completing up to 15 apses relative to the Moon in backward and forward time, respectively; departing through the L_1 or L_2 gateways; or impacting the Moon. These trajectories that lie along the stable or unstable manifolds of the selected periodic orbits are then sampled to produce a larger set of arcs, each spanning a shorter time interval. Each arc begins at a perilune or apolune and is propagated for up to 3 additional apses relative to the Moon, unless meeting the specified termination conditions [99].

Motion primitives of the arcs along the stable and unstable half-manifolds of the selected L_1 and L_2 Lyapunov orbits are extracted using the procedure summarized in Chapter 6. Table 7.1 lists the number of primitives calculated within each set. Furthermore, Figure 7.1 displays the initial L_1 Lyapunov orbit primitive, the target L_2 Lyapunov orbit primitive, and a small subset of motion primitives from their stable and unstable half-manifolds. Each primitive is denoted in bold and the region of the configuration space spanned by the associated small set of representative trajectories is depicted as a transparent surface. The entire set of primitives generated for these stable and unstable manifolds appear in Appendix A. Although the planar stable and unstable manifolds of a Lyapunov orbit are symmetric about the x-axis in the CR3BP, Table 7.1 reveals that they are not summarized by an equivalent number of motion primitives. The small difference is likely attributable to the nondeterministic nature of k-means clustering, which is used to generate part of the ensemble of clustering results. Specifically, k-means clustering is observed to sometimes produce

slightly different clusters of arcs in sparsely-covered regions of the higher-dimensional feature space that is used to describe the arcs along each of the stable and unstable manifolds. Nevertheless, these motion primitives supply a summary of the distinct geometries of arcs along each stable or unstable half-manifold. Together, they form a condensed primitive library for the example design scenario used to demonstrate the technical approach in this chapter.

Table 7.1: Motion primitives in the library for the planar transfer design scenario from an L_1 to L_2 Lyapunov orbit.

Fundamental Solution	Number of Primitives	Approx. C_J
L_1 Lyapunov orbit	1	3.1670
L_1 Lyapunov orbit unstable manifold	69	3.1670
L_1 Lyapunov orbit stable manifold	68	3.1670
L_2 Lyapunov orbit	1	3.1666
L_2 Lyapunov orbit unstable manifold	88	3.1666
L_2 Lyapunov orbit stable manifold	89	3.1666

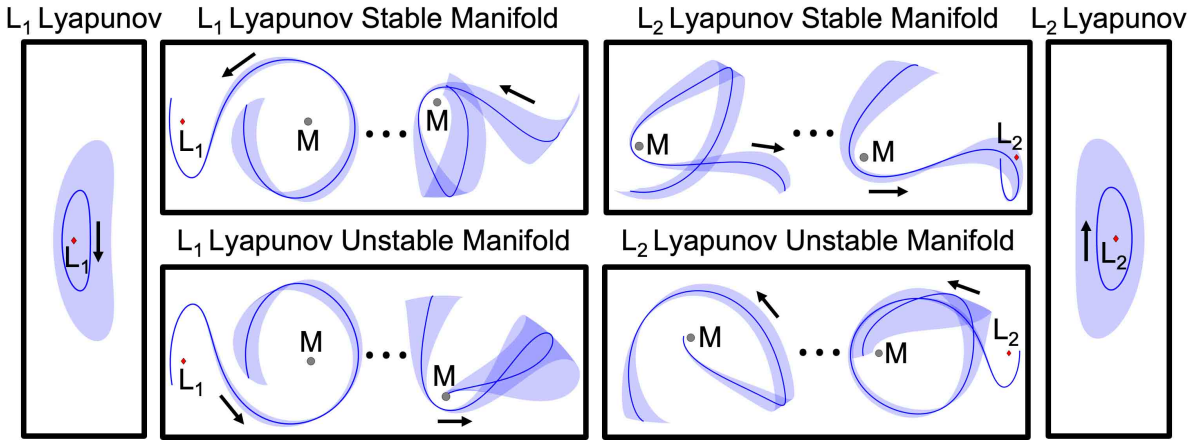

Figure 7.1: Summary of information stored in the motion primitive library for the planar L_1 to L_2 Lyapunov orbit transfer design scenario in the Earth-Moon CR3BP: selected motion primitives (bold) and regions spanned by the representative trajectories of each cluster (transparent).

7.3 Step 2: Construct a Motion Primitive Graph

A motion primitive graph is constructed to discretely represent a region of the continuous solution space in a multi-body system. In general, a graph is a discrete data structure composed

of a set of nodes and edges that is often used to model the properties and internal relationships of a network of objects [63, 46]. When applied to motion primitive and funnel libraries, Frazzoli and Majumdar and Tedrake defined the nodes of a graph as primitives or funnels and added directed edges between only those nodes that may be composed in a sequence [29, 68]. Similar to this formulation, this work defines each node in the graph as a motion primitive and its associated representative trajectory set. Then, weighted, directed edges reflect the potential for selected pairs of primitives to be composed in a sequence to produce a nearby continuous trajectory with similar geometric properties. Using this application of graph theory, the trajectory design problem is reframed as a discrete graph search problem. However, to incorporate designer expertise and reduce computational complexity, the graph construction process is composed of two steps: (1) constructing subgraphs reflecting the potential connectivity between motion primitives associated with a single type of dynamical structure and (2) constructing a modular, high-level itinerary graph to connect these subgraphs.

Formulating a motion primitive graph begins with determining the sequential composability of an ordered pair of primitives; a property that is described by Majumdar and Tedrake as their potential to produce a nearby trajectory [68]. In funnel libraries, this property is straightforwardly calculated by identifying overlapping funnels [68]. However, to avoid overfitting to an incomplete approximation of the region of the phase space spanned by trajectories with similar properties to each primitive, the potential for sequential composability of two motion primitives $\boldsymbol{q}_{\mathbf{MP}_i}(t)$ and $\boldsymbol{q}_{\mathbf{MP}_j}(t)$ and, potentially, their associated sets of representative trajectories R_{e_i} and R_{e_j} is estimated using the following measure:

$$\Delta q = \alpha_{\mathrm{pos}} \Delta r + \alpha_{\mathrm{vel}} \Delta v \tag{7.1}$$

where $\Delta r, \Delta v$ are the magnitudes of the position and velocity difference, respectively, between two primitives and, potentially, their associated sets of representative trajectories. In addition, α_{pos} and α_{vel} are selected to scale the position and velocity differences, respectively. Selecting $\alpha_{\mathrm{vel}} \neq 0$ is useful when maneuver requirements are a high design priority. With this definition, a lower value

of Δq corresponds to a higher potential for two sequentially composed motion primitives to produce a nearby continuous path when corrected with impulsive maneuvers.

To evaluate the potential for sequential composability of two motion primitives, the state difference between two trajectories is calculated. First, each trajectory is discretized into a sequence of states: in the Lyapunov design example, each periodic orbit primitive is discretized into 50 states equally spaced in arclength and each manifold arc primitive is discretized into apses with respect to the Moon as well as its boundary states. Then, the state difference between two trajectories is calculated using one of the following four measures:

(1) the difference between the final state of the first trajectory and the initial state of the second trajectory

(2) the minimum difference between any state along the first trajectory and the initial state of the second trajectory

(3) the minimum difference between the final state of the first trajectory and any state along the second trajectory

(4) the minimum difference between any state along the first trajectory and any state along the second trajectory

Figure 7.2 supplies a conceptual depiction of each of these state difference definitions; note that the last three definitions enable identification of two trajectories with closely located segments that could produce a nearby, continuous path. To evaluate Equation 7.1, the state difference may be calculated using only the primitives or both the primitives and the associated representative trajectory sets. If these representative trajectories are used, the state difference is calculated as the minimum state difference between any representative trajectory (including the primitive) from the first set and any representative trajectory (including the primitive) from the second set.

Using the potential for sequential composability, a subgraph of each motion primitive set is independently formed. With a motion primitive at each node of a subgraph, weighted and directed

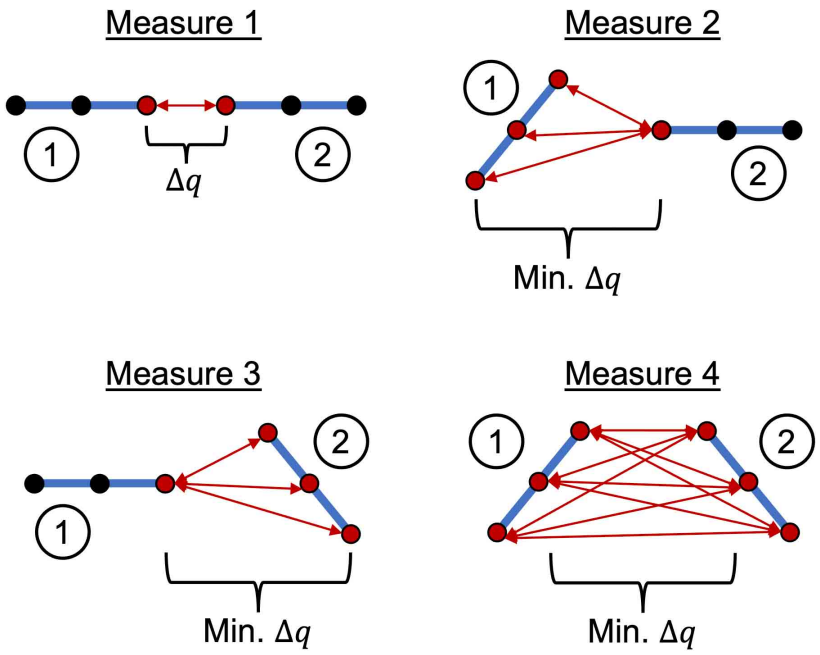

Figure 7.2: Conceptual depiction of Measures 1-4 used to compute the state difference between an ordered pair of trajectories that are each summarized by a sequence of states.

edges are added to the k_{nn} nearest neighbors of each node where $k_{\text{nn}} \geq 0$ is a parameter selected by the trajectory designer. If $k_{\text{nn}} = 0$, the subgraph has no internal edges and therefore motion primitives within the subgraph may not be sequentially composed. However, for $k_{\text{nn}} > 0$, the neighbors for each primitive are identified using the k_{nn} lowest values of Δq for each possible ordered primitive pair, calculated using Measure 1 between the primitives and, if desired, their associated representative trajectories. Measure 1 is used to prioritize reducing overlapping segments between pairs of primitives derived from the same dynamical structure. However, this is a choice that may be modified by the trajectory designer as appropriate. The edge weights are then assigned as the sequential composability, Δq, for each connected pair of primitives. A conceptual representation of a subgraph is depicted in Figure 7.3a where each black circle is a node in the graph and is connected to its three nearest neighbors in the set ($k_{\text{nn}} = 3$). As a result, the subgraph reflects the potential for an ordered sequence of two motion primitives summarizing arcs along the same dynamical structure to be useful in the initial guess construction process.

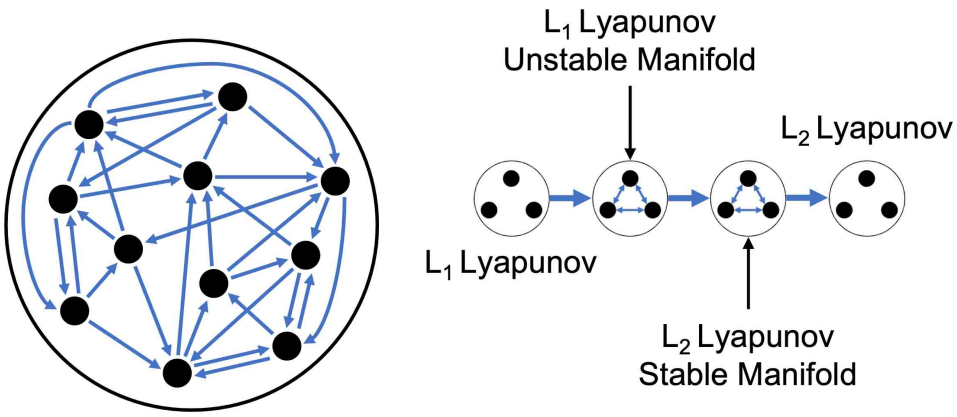

(a) (b)

Figure 7.3: (a) Conceptual representation of a subgraph and (b) a high-level itinerary graph for the planar L_1 to L_2 Lyapunov orbit transfer design scenario in the Earth-Moon CR3BP.

The subgraphs are then connected according to a modular high-level itinerary graph that is constructed by the trajectory designer. In particular, the designer specifies any external connections, i.e., directed edges, between the subgraphs that each capture members of a primitive set associated with a single dynamical structure. This step enables the designer to incorporate their expertise, or even lack thereof, in a scenario into the structure of the graph. To construct the external connections between subgraphs, each individual primitive in the source subgraph is connected to its k_{nn} nearest neighbors in the target subgraph via directed edges. However, there is one exception: if the target subgraph only contains a single primitive then only the edges between the single target primitive and its k_{nn} nearest neighbors in the source subgraph are created. Similar to the subgraph construction process, the external edge weights are assigned as the potential sequential composability between each connected pair of primitives: Measure 2 is used to compute Δq if the source primitive is a periodic orbit and the target primitive is a manifold arc but otherwise Measure 3 is used. Measure 3 prioritizes connecting the source primitive to target primitives that are closely located with its terminal state while also allowing overlapping segments between connected pairs of primitives from different subgraphs. These measures used to calculate the edge weights may also be modified by the trajectory designer as appropriate. In the resulting complete motion primitive

graph, the selected value of k_{nn} determines the degree of connectivity while also influencing the computational complexity of storing and searching the graph.

To demonstrate the presented approach, consider a high-level itinerary graph constructed using selected primitive sets from the library in Table 7.1 for the planar L_1 to L_2 Lyapunov orbit transfer example. A conceptual representation of this graph appears in Figure 7.3b. In this figure, the arrows within the icon associated with an unstable manifold of the initial L_1 Lyapunov orbit indicate that the nodes of the subgraph are connected by internal edges, thereby allowing multiple primitives from the unstable manifold set to be sequentially composed in an initial guess. In contrast, the icon for the L_1 Lyapunov orbit denotes a subgraph with no internal edges, indicating that two primitives from this set may not be sequentially composed. The unidirectional arrows between subgraphs then indicate a desired order for composing primitives from each set. This high-level itinerary graph indicates that in this example an initial guess may only be composed of the following primitives in the specified order: one primitive from the L_1 Lyapunov orbit family set, one or more primitives from the unstable half-manifold of the selected L_1 Lyapunov orbit, one or more primitives from the stable half-manifold of the selected L_2 Lyapunov orbit, and one primitive from the L_2 Lyapunov orbit family set. If these arrows were bidirectional, then primitives from each subgraph could be composed in any order, consistent with the designer either having less insight into the transfer geometry or considering a wider variety of solution itineraries.

For the planar L_1 to L_2 Lyapunov orbit transfer example, a motion primitive graph is constructed using the high-level itinerary graph in Figure 7.3b and the corresponding primitive sets from the library in Table 7.1. The primitives within and between each subgraph are connected with their $k_{\text{nn}} = 15$ nearest neighbors using $\alpha_{\text{pos}} = 10$ and $\alpha_{\text{vel}} = 1$, which are selected empirically to capture both position and velocity differences between motion primitives but emphasize position differences. Additionally, the set of representative trajectories associated with each motion primitive, excluding the selected initial and target orbit primitives, is incorporated into the edge weight computations. In this case, the sets of representative trajectories associated with the selected initial and target orbit primitives are not considered because the exact orbits are desired. However, this

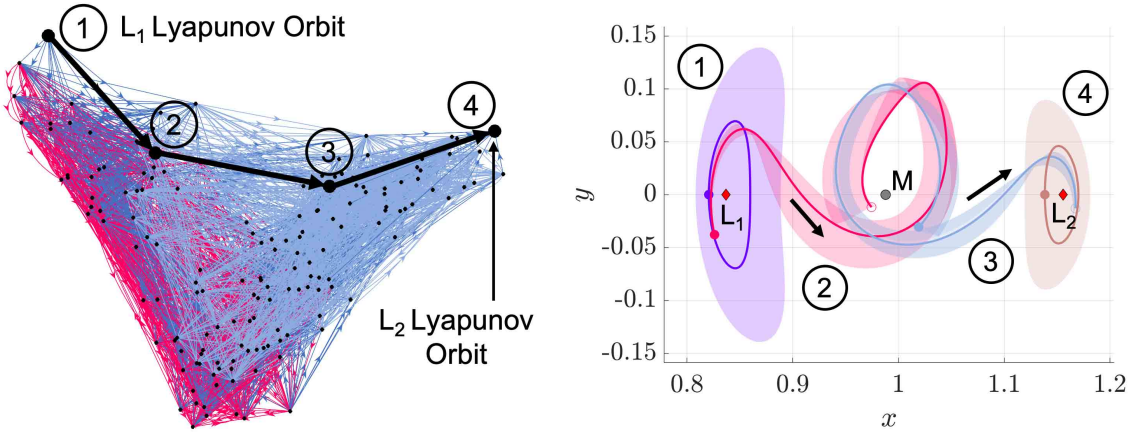

(a) (b)

Figure 7.4: A motion primitive sequence for a planar transfer from an L_1 to L_2 Lyapunov orbit in the Earth-Moon CR3BP displayed in (a) the constructed motion primitive graph and (b) the configuration space in $\mathcal{R}$.

may not always be the case and a human analyst may decide when it is applicable to incorporate the representative trajectory sets for the initial and target orbit primitives; incorporating these sets may be applicable when the designer is more generally interested in transfers between orbits that simply resemble the selected initial and target orbit primitives. The resulting motion primitive graph is displayed in Figure 7.4a: each node in the graph is depicted as a black dot, the internal edges within the L_1 Lyapunov unstable manifold subgraph are denoted in red, the internal edges within the L_2 Lyapunov stable manifold subgraph are denoted in light blue, and all external edges between nodes in different subgraphs are depicted with dark blue arrows. Although challenging for a designer to visualize, this motion primitive graph is searched to construct coarse, primitive-based initial guesses for trajectories of distinct geometries.

7.4 Step 3: Identify Candidate Motion Primitive Sequences

A motion primitive graph is searched to produce primitive sequences that support coarsely constructing initial guesses for trajectories. There are many different graph search techniques that may be used. In this proof of concept, the common brute-force search algorithm, depth-first search

(DFS), is used to enumerate all potential paths in a motion primitive graph from an initial node to a target node with a desired length [63]; the use of alternative and potentially more efficient search algorithms is an avenue of future work. The sequence length is defined as the number of primitives assembled in a single sequence. The quality of each candidate primitive sequence in predicting a nearby continuous trajectory is then captured by the average edge weight along the path. These candidate sequences are then ranked based on their quality and the trajectory designer may consider a desired subset for refinement and corrections in subsequent steps.

Given a ranked list of candidate primitive sequences generated from a motion primitive graph, a designer may explore the design space by either examining all possible sequences or querying the list of candidates. In this work, a straightforward filtering approach is used for rapid exploration: only the top Q sequences that each begin with a unique motion primitive after the initial node are examined. Of course, some transfers with unique geometries may be generated from two sequences of equal length that share a common motion primitive after the initial node. However, this approach enables a trajectory designer to systematically sift through a smaller ranked list as opposed to potentially thousands or millions of primitive sequences. Furthermore, this approach biases the filtered subset of primitive sequences towards exhibiting sufficiently distinct geometries to support a proof of concept. An interesting avenue of future work involves examining alternative and, potentially, automated approaches to querying the unfiltered list to produce the best unique primitive sequences connecting the initial and target nodes.

To demonstrate this step of the framework in the context of the planar L_1 to L_2 Lyapunov orbit transfer example in the Earth-Moon CR3BP, the top-ranked sequence of four primitives with the lowest average edge weight is generated from the motion primitive graph displayed in Figure 7.4a. This primitive sequence is plotted in the Earth-Moon rotating frame in Figure 7.4b: each primitive is denoted in bold using a distinct color along with a transparent region generated from the associated representative trajectories. Furthermore, the initial (final) state of each primitive is denoted with a filled (empty) circle. This candidate sequence is not guaranteed to predict a nearby continuous trajectory with similar geometric properties. However, a trajectory designer

may examine the primitive sequence and average value of Δq to determine whether to perform further analysis and refinement. Although this example presents only the top-ranked sequence of four motion primitives, it supports demonstrating the coarse construction of an initial guess for a transfer using motion primitives. Additional primitive sequences for this design scenario are presented in Chapter 8.

In this step of the primitive-based trajectory design process, a path may not exist between the selected initial node and the selected target node in the constructed motion primitive graph. The existence of a path, or multiple paths, between the initial and target nodes depends on the structure and connectivity of the motion primitive graph. If a path between the initial and target nodes does not exist, a human analyst needs to revert back to Step 2 and construct a modified motion primitive graph. The human analyst may adjust the structure of the high-level itinerary graph, select different measures for evaluating the sequential composability of primitives within each subgraph and between subgraphs, and/or adjust the value of k_{nn} used to create the edges in the motion primitive graph. It is also important to note that the existence of a path between the initial and target nodes may depend on the selected path length. Therefore, an avenue of future work is to characterize the properties of a motion primitive graph in order to inform and assist a human analyst in either (1) selecting a range of suitable path lengths to evaluate or (2) reverting back to Step 2 to refine the structure and connectivity of the motion primitive graph.

7.5 Step 4: Construct an Initial Guess from a Primitive Sequence

A candidate motion primitive sequence is refined to improve the quality of a coarsely-constructed initial guess and facilitate a successful numerical corrections process. The primitive sequence displayed in Figure 7.4b possesses state discontinuities between each consecutive pair of primitives and exhibits a significant overlap between the second and third primitives in the sequence. The first refinement step is to morph the primitives to further reduce the state discontinuities along the initial guess. Recall that a finite set of representative trajectories with similar properties to each motion primitive are also stored within the library; using a combination of these

representative trajectories may produce a better initial guess than using the primitives. Thus, all possible candidate initial guesses with similar geometry to the original motion primitive sequence are constructed by using either each motion primitive or one of the associated representative trajectories. As discussed in Section 7.3, the representative trajectory sets for the initial and target orbit primitives may be excluded depending on the design scenario. The average value of the potential sequential composability (defined in Section 7.3 as the quantity Δq) along each candidate sequence of trajectory segments is then computed using the corresponding state difference measures from the motion primitive graph for each consecutive pair of primitives. The sequence of segments with the smallest average value of Δq produces the morphed initial guess.

Generating the morphed initial guess may suffer from combinatorial explosion depending on the length of the original primitive sequence as well as the number of representative trajectories associated with each primitive. Figure 7.5 provides a conceptual example of the potential combinations of trajectory segments for a four-primitive sequence where each primitive, denoted using the same color scheme as Figure 7.4b, has three associated representative trajectories. In this conceptual example, there are 256 potential sequences and the sequence with the smallest average of Δq produces the morphed initial guess. However, the number of potential sequences during the morphing process may become intractable as longer primitive sequences and larger sets of representative trajectories associated with each motion primitive are considered. To mitigate this challenge, the morphing process may be split into a series of smaller combinatorial problems. For example, consider a sequence of 10 primitives that is split into three subsequences where the subsequences consist of primitives 1-4, 5-8, and 9-10, respectively. The morphing process is then applied to each subsequence individually and a desired number of the top-ranked candidates are retained for each subsequence. Finally, the candidate subsequences are successively merged such that only the desired number of top-ranked candidates are retained after each merging step until the final merger where the top-ranked sequence serves as the morphed initial guess. This alternative morphing process is only applied in this work for motion primitive sequences comprised of more than six primitives. In this process, the human designer specifies the maximum number of

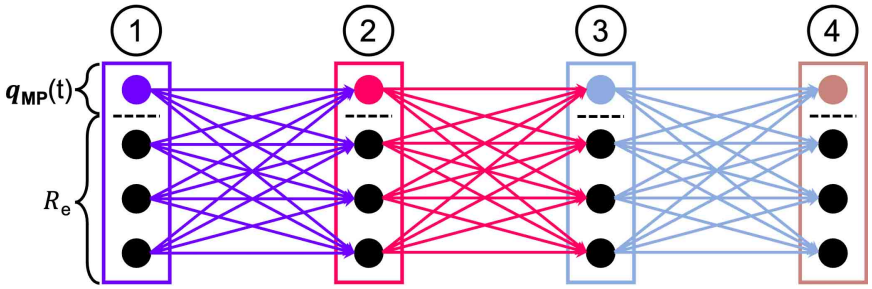

Figure 7.5: Conceptual depiction of the potential combinations of trajectory segments during the morphing process for a four-primitive sequence where each primitive, denoted using the same color scheme as Figure 7.4b, has three associated representative trajectories.

primitives to include in each subsequence and selects the desired number of top-ranked candidates to retain for each morphing subproblem.

The second refinement step is to trim each segment in the morphed initial guess to remove any overlapping portions. The trimming process is applied only to the internal segments between the initial and final periodic orbits and is completed automatically using one of three different methods: forward, backward, or joint sequential trimming. Figure 7.6 depicts a conceptual example of each trimming method. The forward method trims each segment to start at its closest state in the phase space relative to the final state of the previous segment in the sequence. Conversely, the backward method trims each segment to end at its closest state in the phase space relative to the initial state of the next segment in the sequence. Finally, the joint method trims each pair of segments to begin or end at their closest states in the phase space. In each case, the difference between two individual states is evaluated using Δq as defined in Section 7.3.

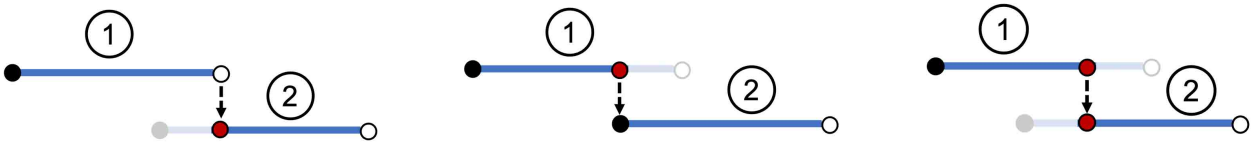

(a) (b) (c)

Figure 7.6: Conceptual depiction of the (a) forward, (b) backward, and (c) joint sequential trimming methods that may be used to refine an ordered sequence of primitives.

A single trimming method is not generally applicable to all candidate initial guesses; therefore, the trimming process that produces the best refined initial guess is selected. First, the morphed initial guess is trimmed using each of the three possible trimming methods. Then, the average value of the potential sequential composability along each trimmed sequence of segments is computed using the following measures: Measure 2 is used to measure the state difference between the initial periodic orbit and the second segment in the sequence; Measure 1 is used to measure the state difference between each pair of interior segments because the interior segments have been trimmed; and Measure 3 is used to measure the state difference between the second to last segment in the sequence and the final periodic orbit. Note that Measures 2 and 3 are used here to supply flexibility in the departure or arrival locations along a periodic orbit. Similar to the morphing process, the trimming method that produces an initial guess with the lowest average value of Δq is selected to produce the refined initial guess. Finally, there is a possibility that a segment may be trimmed such that it possesses a brief integration time and does not impact the geometry of the initial guess, but may cause numerical issues during corrections. Therefore, segments that do not exceed a specified minimum integration time are removed from the initial guess; in this work, this threshold is selected empirically as 0.01 nondimensional time units and may be adjusted as applicable based on the design scenario.

Using the outlined refinement process, the primitive sequence depicted in Figure 7.4b is morphed and trimmed. Figure 7.7 displays the original primitive sequence in dashed gray and the resulting refined initial guess in blue. The overlap between the second and third arcs, as evident in Figure 7.4b, is removed using backward sequential trimming. Morphing the initial guess and then trimming the resulting segments significantly improves the quality of the initial guess in the sensitive region of the phase space near the Moon.

7.6 Step 5: Recover a Continuous, Optimal Trajectory

The final step of the initial guess construction framework is to compute a continuous trajectory that resembles a primitive-based initial guess. To implement this step, the goal is to correct

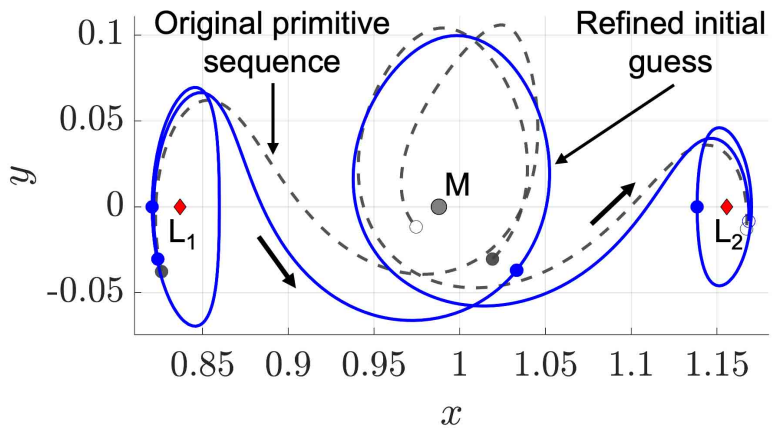

Figure 7.7: Refined primitive-based initial guess for a planar transfer from an L_1 to L_2 Lyapunov orbit in the Earth-Moon CR3BP.

the trajectory while also minimizing the dissimilarities between the final continuous trajectory and the initial guess in the configuration space. In robotic motion planning as well as periodic orbit computation in multi-body systems, constrained optimization methods have previously been used to compute trajectories with similar geometries as a reference path [47, 8]. However, computing a geometrically similar solution to an initial guess may not be the only design objective for a mission scenario. Maneuver magnitudes are also often a common concern. Thus, a multi-objective constrained optimization problem is formulated using a free variable and constraint vector formulation of collocation applied to a transfer between two periodic orbits with impulsive maneuvers.

First, for transfers between two periodic orbits in the CR3BP, the periodic orbits are removed from the initial guess and the corrections scheme is formulated such that the transfer is constrained to depart from the desired initial orbit and arrive onto the desired target orbit. Each segment of the initial guess is then discretized into a set of arcs. For the planar L_1 to L_2 Lyapunov orbit transfer example, each segment is discretized into arcs based on apses with respect to the Moon and then each resulting arc is further discretized into an additional set of 5 arcs with equal arclength to produce an initial mesh. The number of arcs with equal arclength between each apsis is a design parameter that may be adjusted by the trajectory designer. However, if the time elapsed along

the j-th arc in the i-th segment, Δt_j^i, produced during the discretization step is below a specified threshold then it is not further discretized into smaller arcs. In this work, the threshold on the minimum value of Δt_j^i is 0.10 nondimensional time units; this quantity is selected empirically and may be altered by the trajectory designer. Adjusting the discretization of each segment in this manner attempts to avoid placing too many nodes in a short span of time and is observed to facilitate better convergence behavior in the corrections process.

Given a discretized initial guess and using the collocation approach outlined in Chapter 4, 7-th order polynomials and LGL nodes are used to place collocation nodes along each arc and formulate both the continuity and defect constraints for the constrained optimization problem. The free nodes and Δt_j^i along each arc of the initial guess are included in the free variable vector, as defined in Equation 4.18. The bounds on each Δt_j^i variable are set as $[10^{-5}, 1.0]$ where the upper limit is greater than the time along any arc in the initial guess and may be adjusted accordingly. Two additional free variables, Δt_{depart} and $\Delta t_{\text{arrival}}$, are defined as the time measured from specified states along the initial and final periodic orbits. The quantities are included in the free variable vector to allow the departure and arrival locations along each periodic orbit to vary. The bounds on Δt_{depart} are set as $[-T_{\text{i}}, T_{\text{i}}]$ and the bounds on $\Delta t_{\text{arrival}}$ are set as $[-T_{\text{f}}, T_{\text{f}}]$, where T_{i} and T_{f} are the period of the initial and target orbit, respectively. Furthermore, Δt_{depart} is initialized in the range $[-T_{\text{i}}/2, T_{\text{i}}/2]$ and $\Delta t_{\text{arrival}}$ is initialized in the range $[-T_{\text{f}}/2, T_{\text{f}}/2]$ based on the closest departure and arrival states for the initial guess.

A set of boundary constraints is required to ensure the transfer departs from the desired initial orbit and arrives onto the desired target orbit. The free variable Δt_{depart} determines the departure location along the initial orbit and $\Delta t_{\text{arrival}}$ determines the arrival location along the target orbit. Figure 7.8 depicts a conceptual example of Δt_{depart} and $\Delta t_{\text{arrival}}$ where the resulting state at departure is denoted as $\boldsymbol{q}_{\mathbf{depart}}$ and the resulting state at arrival is denoted as $\boldsymbol{q}_{\mathbf{arrival}}$. Assuming impulsive maneuvers are used to depart from the initial orbit and arrive onto the target

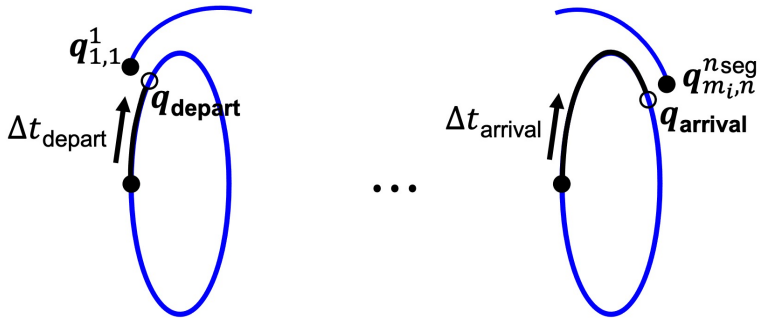

Figure 7.8: Conceptual depiction of the boundary conditions for a transfer between two periodic orbits in the CR3BP.

orbit, the boundary constraints are defined as

$$\begin{aligned} \boldsymbol{F}_{\textbf{depart}} &= \boldsymbol{r}^1_{1,1} - \boldsymbol{r}_{\textbf{depart}} \\ \boldsymbol{F}_{\textbf{arrival}} &= \boldsymbol{r}^{n_{\text{seg}}}_{m_i,n} - \boldsymbol{r}_{\textbf{arrival}} \end{aligned} \tag{7.2}$$

and the nonzero elements of the Jacobian matrix for differential corrections are defined as

$$\begin{aligned} \frac{\partial \boldsymbol{F}_{\textbf{depart}}}{\partial \boldsymbol{q}^1_{1,1}} &= \Big[[\boldsymbol{I}_{3\times 3}] \quad [\boldsymbol{0}_{3\times 3}] \Big] \\ \frac{\partial \boldsymbol{F}_{\textbf{depart}}}{\partial \Delta t_{\text{depart}}} &= -\dot{\boldsymbol{r}}_{\textbf{depart}} \\ \frac{\partial \boldsymbol{F}_{\textbf{arrival}}}{\partial \boldsymbol{q}^{n_{\text{seg}}}_{m_i,n}} &= \Big[[\boldsymbol{I}_{3\times 3}] \quad [\boldsymbol{0}_{3\times 3}] \Big] \\ \frac{\partial \boldsymbol{F}_{\textbf{depart}}}{\partial \Delta t_{\text{arrival}}} &= -\dot{\boldsymbol{r}}_{\textbf{arrival}} \end{aligned} \tag{7.3}$$

These boundary constraints provide flexibility in the departure and arrival conditions of the transfer and are incorporated in the corrections process for computing maneuver-enabled transfers between the initial and target orbit.

Impulsive maneuvers are placed along the transfer at locations that are specified by a trajectory designer. In this investigation, maneuvers are applied at the beginning and end of the initial guess to depart from the initial orbit and arrive onto the target orbit. Impulsive maneuvers are also placed between each neighboring pair of trimmed primitives and/or at apses with respect to a specified reference point. While mission requirements for specific applications may constrain the placement of these maneuvers at alternative locations, this maneuver placement approach supports

the proof of concept in this work. However, if two consecutive maneuvers are placed too close together in configuration space then one maneuver is removed: the departure and arrival maneuvers are always retained and the maneuvers placed between consecutive trimmed primitives are prioritized above maneuvers at apses. In this work, a maneuver is removed when two consecutive maneuvers are within 0.03 nondimensional distance units; a threshold that is selected empirically but may be adjusted as needed.

Using these definitions, a constrained optimization problem is formulated to compute a trajectory that balances geometrically resembling a primitive-based initial guess with reducing the maneuver requirements. A summary of the corrections procedure is depicted in Figure 7.9. First, the free variable vector is defined as $\boldsymbol{V}_{\mathbf{trans}} = [\boldsymbol{V}^{\mathrm{T}}, \Delta t_{\mathrm{depart}}, \Delta t_{\mathrm{arrival}}]^{\mathrm{T}}$ and the constraint vector is defined as $\boldsymbol{F}_{\mathbf{trans}}(\boldsymbol{V}_{\mathbf{trans}}) = [\boldsymbol{F}(\boldsymbol{V})^{\mathrm{T}}, \boldsymbol{F}_{\mathbf{depart}}^{\mathrm{T}}, \boldsymbol{F}_{\mathbf{arrival}}^{\mathrm{T}}]^{\mathrm{T}}$, where $\boldsymbol{V}$ and $\boldsymbol{F}(\boldsymbol{V})$ are defined in Equations 4.18 and 4.21, respectively. Then, an objective function is formulated as a linear combination of the difference in geometry between two trajectories and the cumulative maneuver requirements. This objective function is defined as

$$J(\boldsymbol{V}_{\mathbf{trans}}) = w_{\mathrm{geo}}((\boldsymbol{V}_{\mathbf{pos}} - \boldsymbol{V}_{\mathbf{IG_{pos}}})^{\mathrm{T}}(\boldsymbol{V}_{\mathbf{pos}} - \boldsymbol{V}_{\mathbf{IG_{pos}}})) + w_{\mathrm{man}} \left(\sum_{i=1}^{n_{\mathrm{man}}} \Delta v_i^2 \right) \tag{7.4}$$

where $\boldsymbol{V}_{\mathbf{pos}}$ and $\boldsymbol{V}_{\mathbf{IG_{pos}}}$ reflect only the position components of the free variable vector at the current iteration and the free variable vector of the initial guess, respectively; $\boldsymbol{w}_{\mathbf{opt}} = [w_{\mathrm{geo}}, w_{\mathrm{man}}]$ are the relative weights of the geometric difference and maneuver requirement terms, respectively; Δv_i is the magnitude of the i-th impulsive maneuver; and n_{man} is the total number of maneuvers. Given an initial guess, the open source Interior Point OPTimizer (IPOPT) software library equipped with the MA97 linear solver from the Harwell Subroutine Library (HSL) is used to solve the trajectory corrections problem while minimizing this objective function with the selected values of w_{geo} and w_{man} for up to 1000 iterations [111, 51].

The mesh associated with the solution to the constrained optimization problem is then refined to ensure the trajectory approximated by a sequence of polynomials meets a desired level of accuracy. As depicted in Figure 7.9, the mesh refinement process involves sequentially distributing error

along the solution, removing any unnecessary arcs to reduce the size of the parameter optimization problem, and finally adding arcs to the mesh to ensure the solution is numerically accurate. These mesh refinement steps are implemented using the approach outlined in Chapter 4 while holding the time-of-flight (TOF) of the trajectory constant. After each refinement step, the updated mesh supplies an initial guess for the trajectory that is corrected via optimization as indicated with a gold triangle in Figure 7.9. This optimization step during the merging and splitting phases of refinement uses $w_{\text{geo}} = 1.0$ and $w_{\text{man}} = 0.0$ as indicated in Figure 7.9 to prioritize preserving the geometry of the refined solution. Each refinement step continues until the terminal conditions outlined in Chapter 4. Following this mesh refinement process, the final output is a continuous trajectory that meets a desired accuracy threshold while also balancing minimizing maneuver requirements and retaining the geometry of the initial guess.

The numerical corrections procedure summarized in Figure 7.9 is applied to the initial guess displayed in Figure 7.7 for the L_1 to L_2 Lyapunov orbit transfer example. The objective function weights in Equation 7.4 are selected as $\boldsymbol{w}_{\mathbf{opt}} = [0.9, 0.1]$ to prioritize maintaining the transfer geometry of the initial guess while computing a more maneuver-efficient solution. Of course, these

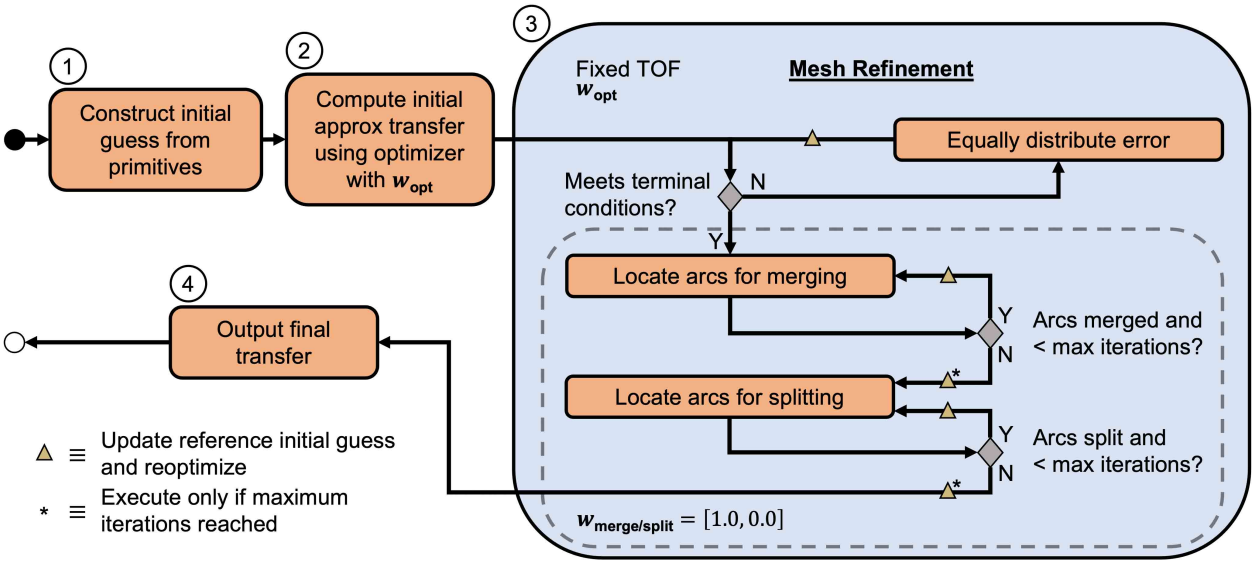

Figure 7.9: Conceptual overview of the corrections algorithm used to compute a trajectory that balances resembling a primitive-based initial guess with reducing maneuver requirements.

weights may be adjusted to prioritize a different balance of these two objectives. Following optimization, the resulting continuous trajectory is displayed in Figure 7.10 with the refined initial guess displayed in dashed gray, the initial and target periodic orbits displayed in solid gray, and the final continuous solution displayed in solid blue. The corrected transfer includes a departure maneuver of 2.71 m/s, an arrival maneuver of 6.47 m/s, a total Δv of 9.18 m/s, and a TOF between the initial and final periodic orbits that is equal to 22.34 days. This trajectory closely resembles the refined initial guess due to the objective function formulation, the selected values of the coefficients w_{geo} and w_{man}, and the quality of the initial guess. Despite the foundational nature of this example, it demonstrates the procedure for using motion primitives to coarsely construct an initial guess with a desired transfer geometry and generate a nearby continuous trajectory.

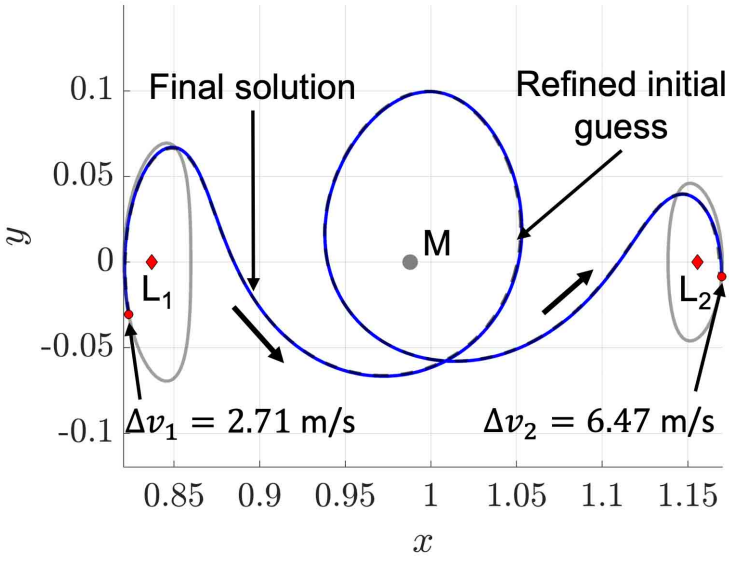

Figure 7.10: Continuous 22.34 day planar transfer from an L_1 Lyapunov orbit to an L_2 Lyapunov orbit in the Earth-Moon CR3BP, computed from a primitive-based initial guess.

Recall from Section 7.4, a primitive-based initial guess is not guaranteed to predict a nearby continuous trajectory with similar geometric properties. As a result, the refinement process outlined in Section 7.5 is used to improve the quality of a primitive-based initial guess. However, this refinement process still does not guarantee the existence of a continuous solution that is geomet-

rically similar to the initial guess. Therefore, the corrections algorithm presented in this section may fail to converge in some cases. If the corrections algorithm fails to converge, a human analyst may adjust a variety of design parameters and rerun the algorithm to attempt to achieve successful convergence. For example, alternative discretization and maneuver placement approaches may be used, higher-order polynomials may be used in the collocation scheme, additional path constraints may be incorporated in the constraint vector, the selected values of $\boldsymbol{w_{opt}}$ may be adjusted, and so forth. Adjusting one or more of these design parameters may produce a continuous solution. However, the corrections algorithm may still fail to converge depending on the quality of the initial guess and the existence of a nearby solution to the dynamical system. If needed, a human analyst may then revert back to Steps 3-4 of the design framework to identify an alternative primitive-based initial guess if one exists.

7.7 Step 6: Explore the Transfer Design Space

The primitive-based trajectory design process presented in this chapter supports efficient exploration of a transfer design space via rapid construction of transfers of various geometries, flight times, and maneuver requirements. First, a set of individual transfers are generated by correcting multiple initial guesses formed using unique sequences of motion primitives. Because motion primitives are extracted in this work to represent the finite array of geometries of arcs along individual orbit families and their stable or unstable manifolds, distinct sequences of motion primitives support the recovery of point solutions with distinct geometries. Next, each of these point solutions is used as a foundation for exploring the design space in its local neighborhood. Through natural parameter continuation, additional transfers are computed by varying the weights, w_{geo} and w_{man}, used in the multi-objective optimization process outlined in Section 7.6. As w_{geo} is decreased and w_{man} is increased, the resulting transfers place more emphasis on minimizing the cumulative maneuver requirements and less emphasis on closely resembling the initial guess. Accordingly, for each unique primitive sequence, this numerical continuation process tends to produce a set of trajectories with gradually varying geometries, flight times, and maneuver requirements. This

section supplies a description of the technical approach for each component of the design space exploration as well as selected examples for demonstration purposes; however, a wider array of results appear in Chapter 8.

A motion primitive graph that has been constructed for a specific transfer scenario is searched to produce a variety of motion primitive sequences that could lead to transfers of distinct geometries. Using the search methodology outlined in Section 7.4, these sequences may possess either distinct lengths or correspond to the top Q ranked motion primitive sequences of the same length; recall that the value of Q is selected by the trajectory designer and may be bounded based on the connectivity of the graph. Then, each unique sequence of motion primitives produced during this search is used to construct an initial guess that is corrected using the procedure outlined in Section 7.6. Figure 7.11 displays an example of two additional planar and maneuver-enabled transfers with distinct geometries computed for the L_1 to L_2 Lyapunov orbit transfer design scenario explored throughout this chapter. The transfer displayed in Figure 7.11a is constructed from a four-primitive sequence. Although this transfer completes a single revolution around the Moon, it exhibits a distinct geometry compared to the transfer presented in Figure 7.10. On the other hand, the transfer displayed in Figure 7.11b is constructed from a six-primitive sequence, exhibiting a more complex geometry with multiple revolutions around the Moon while also possessing some segments that resemble arcs along the simpler transfer presented in Figure 7.10. Repeating this procedure for each unique sequence of motion primitives produces a set of continuous transfers with various geometries.

Natural parameter continuation is used to compute additional trajectories with a similar geometry to each corrected transfer but with varying flight times and maneuver requirements. These transfers are generated by varying the relative values of the weights w_{geo} and w_{man} used in the multi-objective optimization process described in Section 7.6. In this work, these weights are linearly varied from $\boldsymbol{w_{\text{opt}}} = \boldsymbol{w_1} = [0.9, 0.1]$ to $\boldsymbol{w_{\text{opt}}} = \boldsymbol{w_2} = [0.1, 0.9]$; w_{geo} is decremented by 0.05 and w_{man} is incremented by 0.05 during each iteration. This continuation process begins with a corrected transfer (computed using $\boldsymbol{w_{\text{opt}}} = \boldsymbol{w_1}$) that already possesses a mesh of nodes

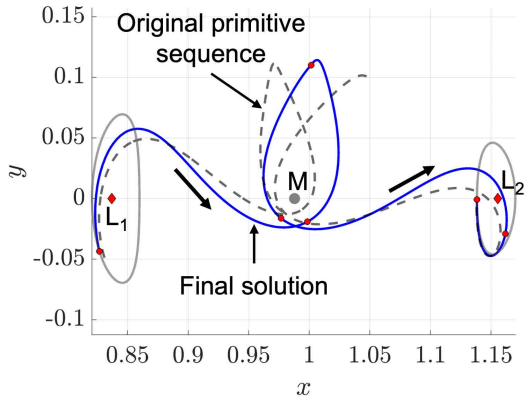

(a) Planar transfer constructed from a four-primitive sequence.

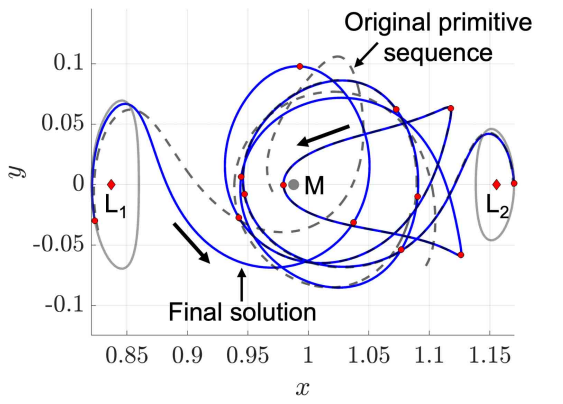

(b) Planar transfer constructed from a six-primitive sequence.

Figure 7.11: Examples of planar transfers with distinct geometries from an L_1 Lyapunov orbit to an L_2 Lyapunov orbit in the Earth-Moon CR3BP, computed from primitive-based initial guesses.

with a suitable error distribution, i.e., the output of Block 4 in Figure 7.9. Each iteration of the continuation procedure then repeats the corrections process depicted in Figure 7.9 by updating $\boldsymbol{w}_{\mathbf{opt}}$, starting in Block 2, and then skipping the error distribution loop during mesh refinement by moving directly to the gray dashed box in Block 3. As these weights are varied, the corrected solution from the previous iteration serves as the initial guess for the current iteration. However, to prevent the optimizer from producing solutions with significantly longer flight times, e.g., by adding revolutions near the initial or final orbits, as w_{geo} is decreased and w_{man} is increased, the transfer TOF is constrained at each step of the continuation process to not exceed an increase of 5% from the last computed solution; this threshold may be adjusted as desired. This constraint is only applied in Block 2 because the TOF is fixed during the mesh refinement process. Finally, the continuation process is terminated early if the optimizer does not converge on a solution during a given iteration. The output of the natural parameter continuation procedure is a set of transfers with gradually varying geometries, flight times, and maneuver requirements.

The process for using natural parameter continuation to produce transfers with varying maneuver requirements and flight times is applied to the transfer displayed in Figure 7.11a. The center

of Figure 7.12 presents a summary of the flight time and total Δv of each transfer computed with distinct values of the weights w_{geo} and w_{man}. For clarity, the characteristics of each transfer are indicated by a marker that varies from black when $\boldsymbol{w_{\text{opt}} = w_1}$ to copper when $\boldsymbol{w_{\text{opt}} = w_2}$. For selected values of these weights, annotated and numbered in the center of Figure 7.12, the associated transfers are plotted at the boundaries of the figure. The four solutions displayed in Figure 7.12 demonstrate the gradual evolution of geometry, TOF, and maneuver requirements across transfers in the local vicinity of the first solution displayed in Figure 7.11a.

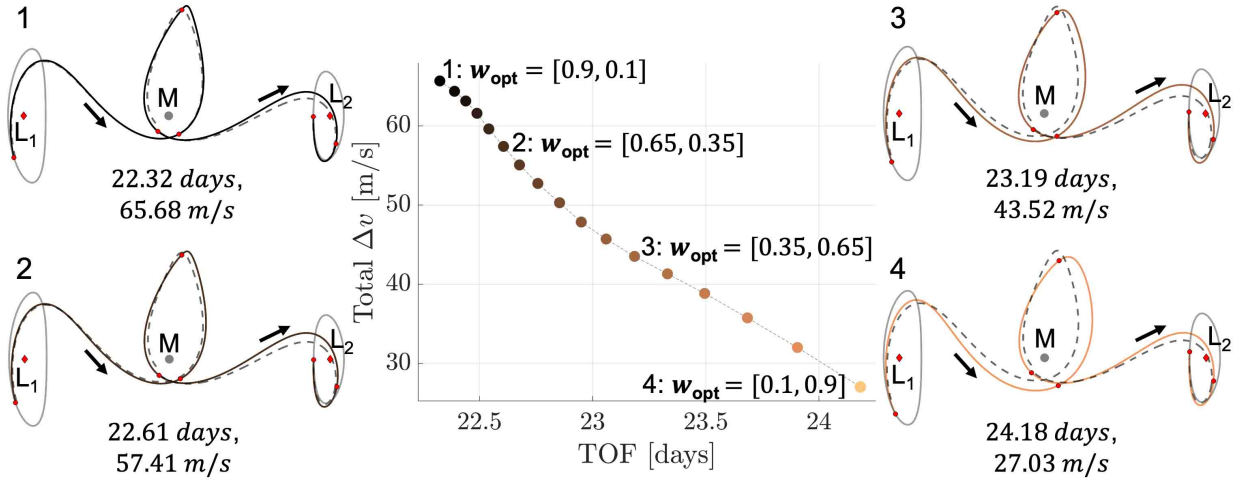

Figure 7.12: Evolution of the geometry, TOF, and maneuver requirements across transfers in the local vicinity of the point solution displayed in Figure 7.11a, computed using the continuation procedure that varies the weights of the multi-objective optimization problem.

In some cases, distinct primitive sequences may produce geometrically similar solutions after either refinement or the application of natural parameter continuation. Accordingly, the complete set of transfers that are generated during the design space exploration are grouped by their geometry using a k-NN graph. The geometric difference between two transfers, A and B, is assessed using a modified Hausdorff distance, $d_H(A, B)$, that is calculated as

$$d_H(A,B) = \max\left(\frac{\sum_{i=1}^{N_A} \min_{j=1,\ldots,N_B} \|\boldsymbol{r}_{\boldsymbol{A}_i} - \boldsymbol{r}_{\boldsymbol{B}_j}\|}{N_A}, \frac{\sum_{i=1}^{N_B} \min_{j=1,\ldots,N_A} \|\boldsymbol{r}_{\boldsymbol{B}_i} - \boldsymbol{r}_{\boldsymbol{A}_j}\|}{N_B} \right) \tag{7.5}$$

where N_A (N_B) is the number of states sampled along trajectory A (B) and $\boldsymbol{r}_{\boldsymbol{A}_i}$ ($\boldsymbol{r}_{\boldsymbol{B}_i}$) is the i-th

position vector sampled along trajectory A (B) and measured relative to a specified reference point [23]. Each transfer is discretized by sampling the initial state of each arc of its mesh generated during corrections as well as the final state of the entire transfer. By using a modified Hausdorff distance to evaluate the difference between two transfers in the configuration space, each transfer may be sampled with a distinct number of nodes.

A k-NN graph is constructed by connecting each transfer to its k_{nn} nearest neighbors via edges, assessed using $d_H(A, B)$. However, if two transfers do not mutually consider each other a nearest neighbor, their edge is removed; this step assists with identifying a single transfer with a unique geometry. In addition, a TOF difference limit denoted as $l_{\Delta\text{TOF}}$ is also used to determine if an edge should be removed between two transfers due to differences in TOF. The parameter $l_{\Delta\text{TOF}}$ may be specified as either a percentage value or a time quantity. If $l_{\Delta\text{TOF}}$ is specified as a percentage value, then the edge between two transfers, A and B, is removed if $|(\text{TOF}_B - \text{TOF}_A)|/\text{TOF}_A > l_{\Delta\text{TOF}}$; otherwise, if $l_{\Delta\text{TOF}}$ is specified as a time quantity, then the edge between transfers A and B is removed if $|\text{TOF}_B - \text{TOF}_A| > l_{\Delta\text{TOF}}$. The parameters TOF_A and TOF_B are the flight times of transfers A and B, respectively. Each group of geometrically similar transfers is then identified as each connected component in the k-NN graph; this approach is similar to the process used for cluster refinement. Finally, manual inspection is performed to further separate any transfers that admit similar yet distinct geometries. Leveraging the primitive-based trajectory design process presented in this chapter enables this rapid exploration of a transfer design space and the ability to efficiently identify solutions with distinct geometries.

Chapter 8

Primitive-Based Trajectory Design Space Exploration

The primitive-based initial guess construction framework presented in Chapter 7 enables rapid generation of trajectories with distinct geometries in a multi-body system. In this chapter, a variety of transfer design scenarios are explored to demonstrate the utility of this approach. Each transfer design scenario considered in this work is evaluated within the Earth-Moon system; however, the design framework may be generally applied within any multi-body system. First, a more expansive exploration of the planar transfer design scenario from an L_1 Lyapunov orbit to an L_2 Lyapunov orbit with impulsive maneuvers is conducted. Then, a spatial transfer design scenario from an L_1 northern halo orbit to an L_2 northern halo orbit with impulsive maneuvers is explored. Finally, a subset of the transfer design space between an L_2 southern NRHO and selected DROs is explored due to the recent interest in the use of NRHOs for cislunar exploration. Each of these transfer design scenarios showcases different capabilities of the presented framework: the Lyapunov and northern halo orbit transfers demonstrate the ability to design both planar and spatial transfers, respectively; whereas, the L_2 southern NRHO to DRO transfer scenario demonstrates the ability to design transfers between mission orbits with large energy and geometric differences. The primitive-based trajectory design process supports efficient exploration of each transfer design space via rapid construction of transfers of various geometries, flight times, and impulsive maneuver requirements. Note: An earlier version of the results and discussion presented in Sections 8.1 and 8.2 appeared in a conference paper by Smith and Bosanac [98].

8.1 Planar Transfers from an L_1 to L_2 Lyapunov Orbit in the Earth-Moon System

8.1.1 Constructing Transfers with Distinct Geometries

Planar transfers are constructed from an L_1 Lyapunov orbit at $C_J \approx 3.1670$ to an L_2 Lyapunov orbit at $C_J \approx 3.1666$ in the Earth-Moon CR3BP with impulsive maneuvers. Figure 8.1 displays the selected Lyapunov orbits in the Eath-Moon rotating frame and Table 8.1 lists the properties of each orbit. The transfers constructed between these orbits are computed using a motion primitive graph that includes primitives extracted from both the stable and unstable manifolds of the initial and final orbits, as listed in Table 7.1 and displayed in Appendix A. The associated high-level itinerary graph is depicted in Figure 8.2, allowing motion primitives that summarize arcs along each manifold to be composed in any order. Accordingly, this graph expands both the array of primitives and their potential sequences compared to the graph in Figure 7.3b previously used for demonstration purposes in Chapter 7. The graph used in this section may, for example, reflect that the trajectory designer possesses limited insight into a desired itinerary or may be interested in exploring a wider region of the solution space. To construct the motion primitive graph, the following configuration parameters are used: $k_{\text{nn}} = 15$, $\alpha_{\text{pos}} = 10$, and $\alpha_{\text{vel}} = 1$. Additionally, the set of representative trajectories associated with each motion primitive, excluding the selected initial and target orbit primitives, is incorporated into the edge weight computations and the average edge weight is used to evaluate the quality of each primitive sequence. The computation time for constructing the motion primitive graph in this scenario is on the order of 10^0 minutes using an iMac with a 3GHz 6-Core Intel Core i5 processor.

A variety of initial guesses are constructed by searching the motion primitive graph in Figure 8.2 to produce unique sequences of four, five, and six motion primitives. There are a total of 665, 45,202, and 2,681,481 primitive sequences from the initial node to the target node in the graph consisting of four, five, and six primitives, respectively; of course, not all primitives sequences necessarily predict the existence of a nearby continuous and maneuver-enabled trajectory. However,

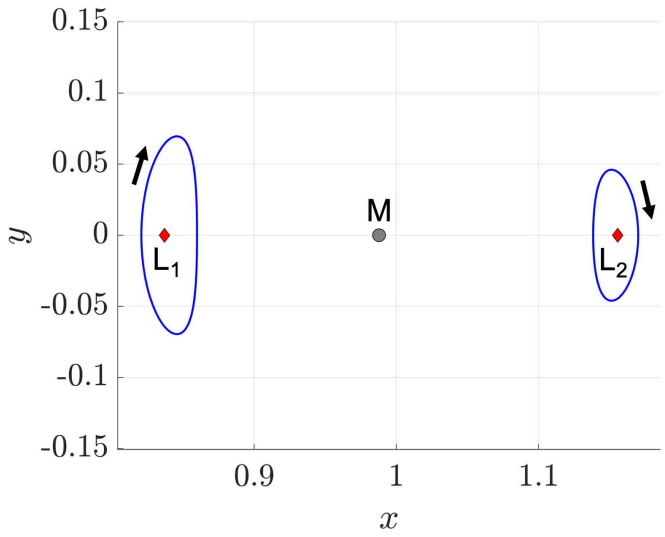

Figure 8.1: Configuration of the initial L_1 Lyapunov orbit at $C_J \approx 3.1670$ and the target L_2 Lyapunov orbit at $C_J \approx 3.1666$ in $\mathcal{R}$ for the Lyapunov orbit transfer design scenario in the Earth-Moon CR3BP.

Table 8.1: Properties of the initial L_1 Lyapunov orbit and the target L_2 Lyapunov orbit for the Lyapunov orbit transfer design scenario in the Earth-Moon CR3BP.

	Initial Orbit	Target Orbit
Orbit Type	L_1 Lyapunov	L_2 Lyapunov
C_J	3.167002726384443	3.166629662653735
T_{PO}	2.771947883503871 ($\approx$ 12.04 days)	3.384017960434504 ($\approx$ 14.70 days)
s_1	2206.96970174085	1383.83755114156
s_2	2.01702391788686	1.95156115640437

using the filtering process presented in Section 7.4, the $Q = 15$ top-ranked sequences that begin with a unique primitive are examined for each path length. The result is 45 primitive sequences that are each refined to produce an initial guess for a transfer. The computation time required to search for and construct these 45 primitive-based initial guesses is on the order of 10^0 minutes using an iMac with a 3GHz 6-Core Intel Core i5 processor; a majority of the computation time is associated with computing the sequences of six motion primitives. The time complexity of searching the motion primitive graph and refining each top-ranked motion primitive sequence increases significantly as the path length increases due to the combinatorial challenges of using DFS. As discussed in Chapter

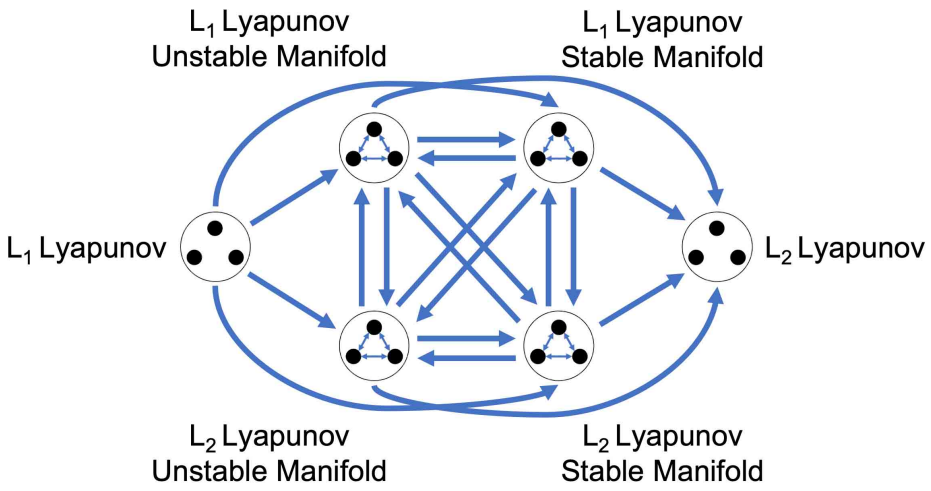

Figure 8.2: High-level itinerary graph for a planar L_1 to L_2 Lyapunov orbit transfer design scenario in the Earth-Moon CR3BP.

7, the use of alternative and more efficient search algorithms is an avenue of future work. Finally, a similar computation time is also observed for constructing the initial guesses in the transfer design scenarios presented in Sections 8.2 and 8.3.

Each initial guess is corrected with several unconstrained impulsive maneuvers. Specifically, each initial guess incorporates a departure maneuver from the initial orbit, an arrival maneuver onto the target orbit, a maneuver between each neighboring pair of segments, and a maneuver at each apse with respect to the Moon. However, as discussed in Section 7.6, a maneuver is removed if two consecutive maneuvers are placed too close together in configuration space. Of course, maneuver placement schemes may vary across applications and be subject to constraints, potentially impacting the corrected trajectories. However, with this maneuver placement scheme, all 45 initial guesses are successfully corrected using $\boldsymbol{w}_{\mathbf{opt}} = [0.9, 0.1]$ to produce nearby continuous, maneuver-enabled, and planar transfers from the desired initial L_1 Lyapunov orbit to the target L_2 Lyapunov orbit.

An initial summary of the transfers that solve the multi-objective optimization problem with $\boldsymbol{w}_{\mathbf{opt}} = [0.9, 0.1]$ is presented using the cumulative maneuver requirements for each transfer and

the sequential composability of the associated refined initial guesses. In Figure 8.3a, the total Δv of each transfer is displayed on the vertical axis using a $\log_{10}$ scale and the horizontal axis displays the normalized average potential for sequential composability, $\Delta\check{q}_{\text{avg}}$, of the refined initial guess for each transfer; a min-max normalization scheme is used to normalize Δq_{avg} between 0 and 1 for each path length. In Figure 8.3a, the properties of corrected transfers that do not impact a spherical approximation of the Moon are indicated with blue markers, whereas gray markers correspond to continuous transfers that impact the Moon. Although there is no explicit altitude constraint during corrections, only three of the corrected transfers impact the Moon. Furthermore, red markers, where applicable, correspond to discontinuous trajectories that are not successfully corrected; their values of total Δv are estimated using the free variable vector at the final iteration of the optimization algorithm. Finally, as denoted in Figure 8.3, the shape of each marker indicates the number of sequentially composed motion primitives used to compute the associated transfer. Across the set of 45 transfers, Figure 8.3a reveals a gradual increase in total Δv requirements, from 9.96 m/s to 1150.83 m/s, with increasing values of $\Delta\check{q}_{\text{avg}}$. A wide range of Δv requirements is expected given the variability in the quality of each initial guess, the emphasis placed on recovering transfers that resemble their respective initial guesses, and the use of unconstrained impulsive maneuvers.

Continuation is used to compute additional transfers that prioritize minimizing maneuver requirements more heavily than resembling the initial guess. Specifically, each of the 45 corrected transfers displayed in Figure 8.3a forms an initial guess for the natural parameter continuation process discussed in Section 7.7. The relative optimization weights are gradually varied from $\boldsymbol{w_1} = [0.9, 0.1]$ to $\boldsymbol{w_2} = [0.1, 0.9]$ and only 42 transfers are successfully corrected to solve the optimization problem with $\boldsymbol{w_2}$; three transfers could not be computed using these scalar weights, likely due to numerical sensitivities near the Moon. In Figure 8.3b, these transfers are summarized using the same configuration as Figure 8.3a. Using this continuation-based approach, the corrected transfers possess cumulative maneuver requirements between 6.81 m/s and 67.18 m/s, which are significantly lower than the original transfers summarized in Figure 8.3a.

To effectively examine a set of transfers that exist within a subset of the design space, the

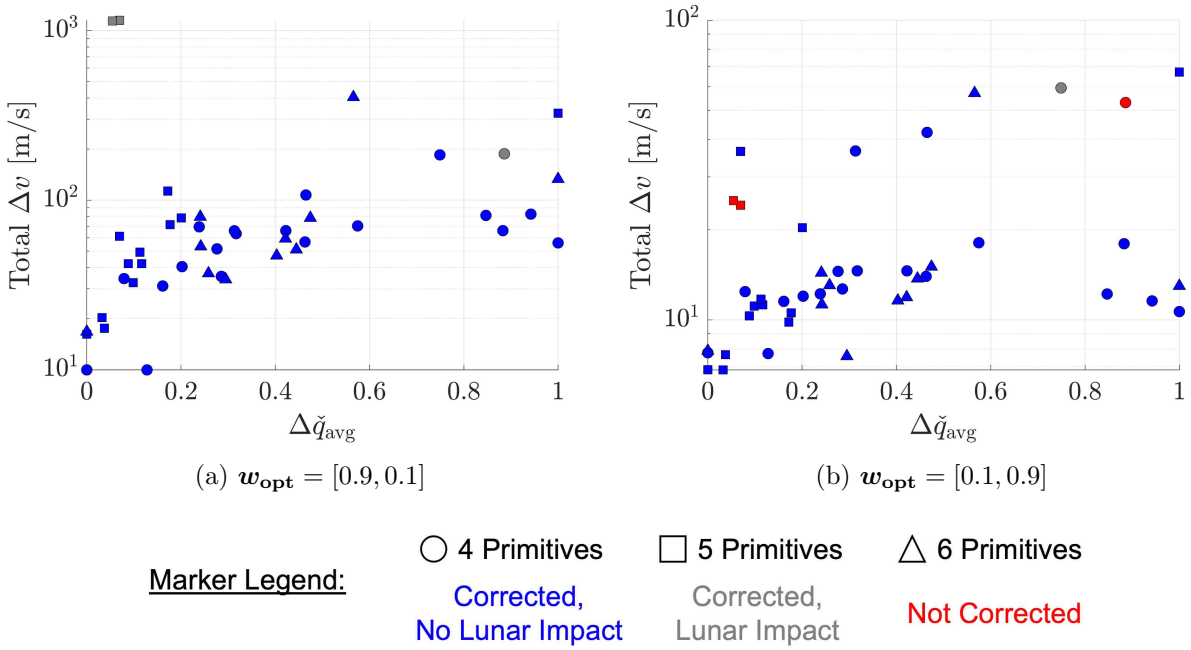

Figure 8.3: Total Δv of planar transfers computed from an L_1 Lyapunov orbit to an L_2 Lyapunov orbit in the Earth-Moon CR3BP as a function of $\Delta\check{q}_{\text{avg}}$.

transfers summarized in Figure 8.3b are grouped by their geometry using the process described in Section 7.7. In this example, the parameters $k_{\text{nn}} = 4$ and $l_{\Delta\text{TOF}} = 10\%$ are selected empirically to construct the k-NN graph; as described in Section 7.7, k_{nn} determines the degree of connectivity for the k-NN graph and $l_{\Delta\text{TOF}}$ is a TOF difference limit. Figure 8.4a displays the resulting total Δv of each transfer with respect to its TOF, with each group of geometrically similar transfers indicated by distinctly colored markers. The transfer with the minimum Δv cost from each group is highlighted with a black circle and numbered. A total of 16 distinct types of transfers are extracted from the set of 42 planar, maneuver-enabled transfers that are corrected using $\boldsymbol{w_2}$ to connect the selected L_1 Lyapunov orbit to the target L_2 Lyapunov orbit in the Earth-Moon CR3BP. As displayed in Figure 8.4a, the corrected transfers possess flight times ranging from 20.90 days to 53.28 days and maneuver requirements from 6.81 m/s to 67.18 m/s.

The continuation process for each transfer generally results in significant reductions in total

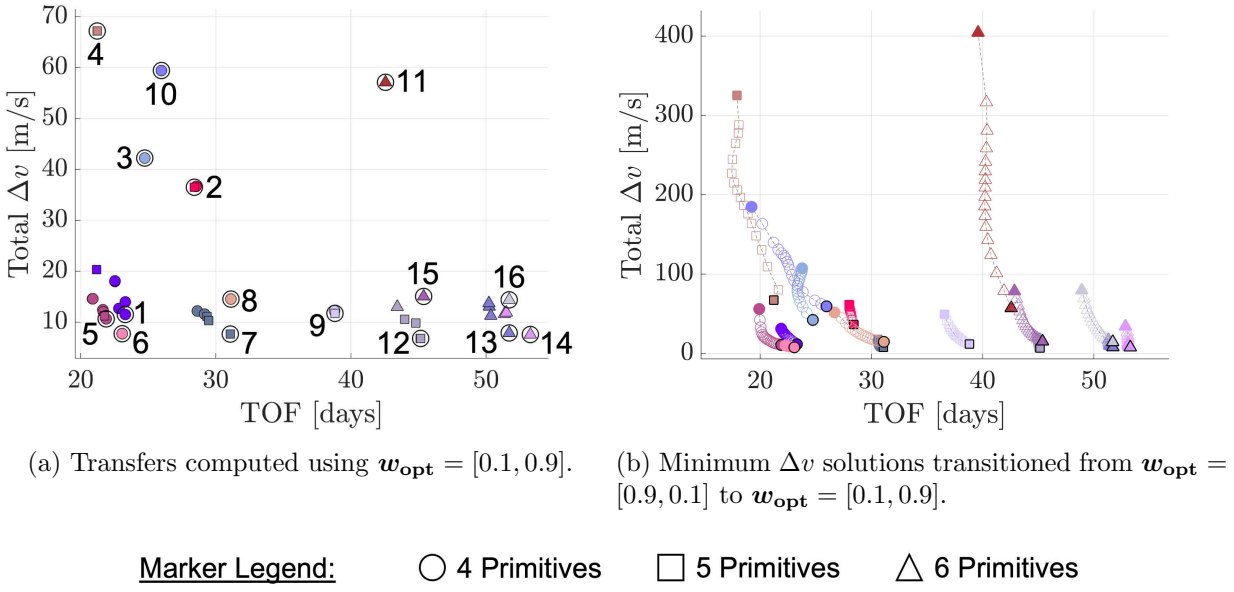

(a) Transfers computed using $\boldsymbol{w}_{\mathbf{opt}} = [0.1, 0.9]$.

(b) Minimum Δv solutions transitioned from $\boldsymbol{w}_{\mathbf{opt}} = [0.9, 0.1]$ to $\boldsymbol{w}_{\mathbf{opt}} = [0.1, 0.9]$.

Figure 8.4: Total Δv and TOF of planar transfers computed from an L_1 Lyapunov orbit to an L_2 Lyapunov orbit in the Earth-Moon CR3BP, where geometrically similar transfers are denoted in the same color and the minimum Δv solution for each transfer geometry is highlighted.

maneuver cost coupled with increases in TOF. This information is evident in Figure 8.4b, which displays the evolution of the characteristics of the minimum Δv solution from each group during the continuation process. In this figure, the solutions computed using $\boldsymbol{w_2}$ are indicated by a filled marker with a black edge while the associated solutions computed using $\boldsymbol{w_1}$ are indicated by only a filled marker with no edge color. These results indicate that motion primitives support the coarse design of a set of initial guesses for trajectories with distinct geometries that may also be refined to possess various flight times and maneuver requirements.

To visualize the geometric variations across the recovered set of transfers, the minimum Δv transfer from each of the 16 groups is plotted in the configuration space. These transfers are displayed in Figure 8.5 in the xy-plane of the Earth-Moon rotating frame using the same colors and numbering scheme as in Figure 8.4a. In each subfigure, the Moon is displayed as a gray circle plotted to scale while L_1 and L_2 are depicted with red diamonds. The refined primitive-based

initial guess for each transfer is displayed in dashed gray, the initial and target orbits are displayed in solid gray, each impulsive maneuver is located with a red circle, and black arrows indicate the direction of motion. Below each transfer is the associated flight time and total Δv. These transfers recovered using the presented motion primitive approach to trajectory design exhibit a variety of geometries.

Most of the minimum Δv transfers that solve the multi-objective optimization problem us-

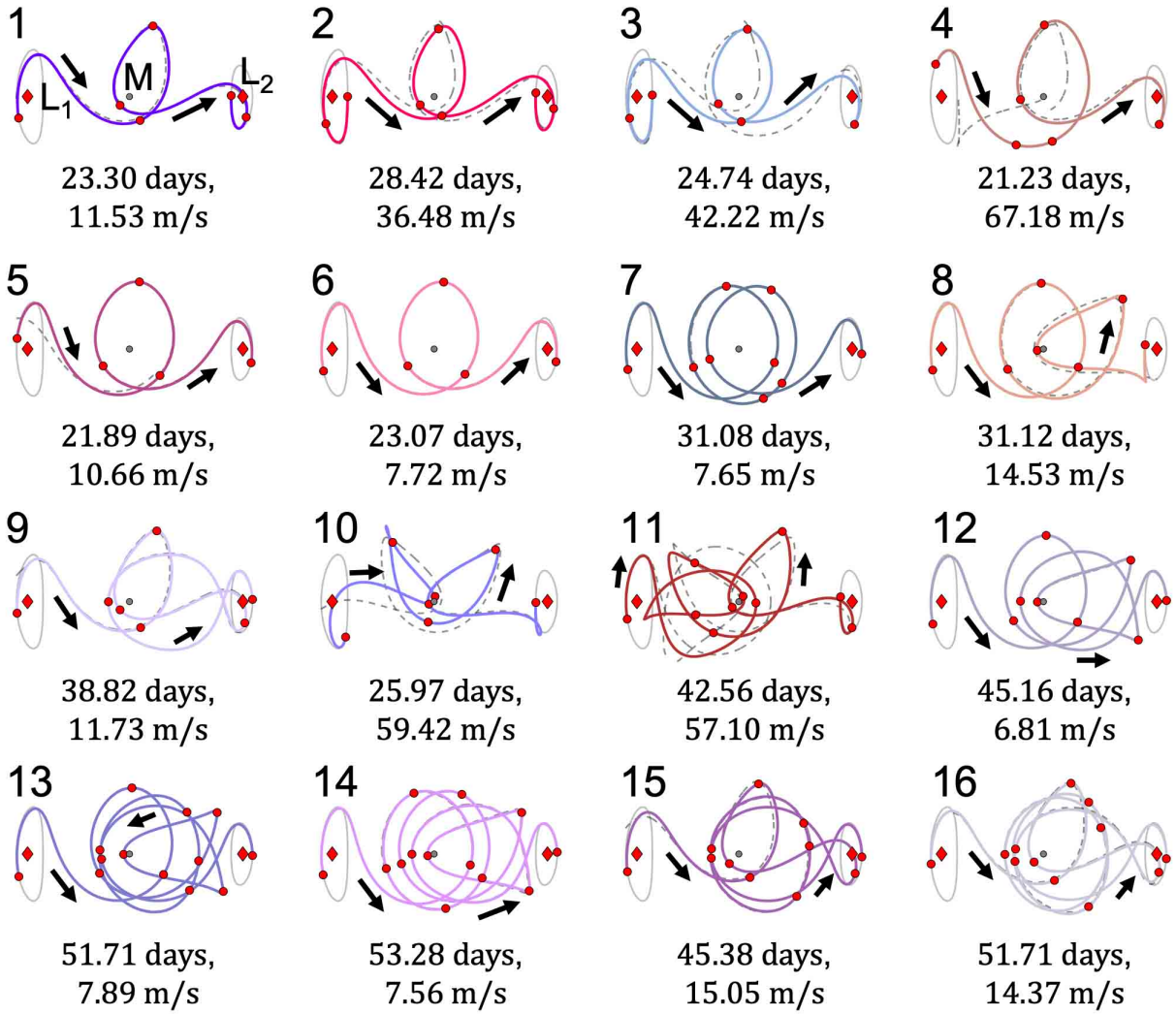

Figure 8.5: Planar transfers with distinct geometries computed from primitive-based initial guesses between an L_1 and L_2 Lyapunov orbit in the Earth-Moon CR3BP, displayed in the xy-plane of $\mathcal{R}$.

ing $\boldsymbol{w_2}$ closely resemble their refined primitive-based initial guess. In Figure 8.5, the initial guess (dashed gray) lies close to the continuous transfer (solid color) in most cases, indicating the utility of coarsely designing transfers with specific geometries using motion primitives when Δq_{avg} is sufficiently low. Noticeable deviations between the corrected transfer and initial guess are, however, evident in Transfers 4, 10, and 11, which are derived from motion primitive sequences with larger discontinuities, i.e., larger values of Δq_{avg}. Prioritizing maneuver requirements more heavily than resembling the initial guess can lead to more significant changes in geometry during the continuation process when the original primitive-based initial guess possesses larger discontinuities. Finally, Transfer 6 uses the same primitives as the example presented in Chapter 7. This result demonstrates the capacity to recover similar, straightforward solutions when limited a priori knowledge is incorporated into the graph construction process.

The k-NN graph approach for grouping transfers based on their geometry may separate transfers that could potentially belong to the same group or place transfers in a single group that could be separated. In some cases, transfer groups that are identified as possessing distinct geometries only vary in their departure or arrival locations along the initial or target orbits. For instance, Transfers 5 and 6 are constructed from unique primitive sequences and have slightly different departure locations along the initial orbit but share a similar geometry, flight time, and total Δv. These transfers could potentially be considered to belong within the same transfer group but are located in distinct components of the k-NN graph. Alternative values for k_{nn} and $l_{\Delta\text{TOF}}$, incorporation of the transfers constructed during natural parameter continuation, or modification of the grouping process may lead to these transfers being placed in the same group. However, differentiating between transfers with different departure or arrival locations along the initial or target orbits may also be desirable to identify transfers with similar overall geometries yet distinct characteristics near the boundary orbits.

The solutions presented in Figure 8.5 reveal that transfers constructed from sequences of additional primitives generally exhibit complex geometries but often contain some common elements with the transfers constructed from fewer primitives. For example, Transfers 15 and 16 initially

exhibit a similar geometry to Transfer 9 but perform additional revolutions around the Moon before approaching the target L_2 Lyapunov orbit. These transfers possess similarly low maneuver requirements and flight times that differ by 6-7 days with each additional revolution as evident in Figure 8.4a. The separation of these similar, yet distinct transfer geometries demonstrates the value of incorporating $l_{\Delta\text{TOF}}$ into the transfer grouping process discussed in Section 7.7. The modified Hausdorff distance used to construct the k-NN graph (defined in Equation 7.5) assesses the geometric similarity between transfers described by a distinct number of nodes but does not consider temporal variations in the transfers. The selected value of $l_{\Delta\text{TOF}} = 10\%$ prevents some transfers from being grouped together due to their TOF differences despite their geometric similarities. Leveraging this graph-based grouping procedure reduces the burden on a human analyst during the design space exploration process by eliminating the need to manually identify each group of geometrically similar transfers.

8.1.2 Examining the Local Neighborhood of Transfers

The minimum Δv transfers identified in Figure 8.5 provide a summary of solutions with distinct geometries that may be considered during the trajectory design process for a mission concept. However, the design of a trajectory for a mission concept is often heavily constrained based on spacecraft hardware properties and operational requirements. Therefore, it is often important to assess the flexibility of a trajectory based on geometry, flight time, and maneuver requirements with respect to mission constraints. A more flexible solution is desirable to accommodate evolving design requirements throughout the mission design process and it may present a more robust nominal trajectory profile with respect to operational contingency scenarios, such as inefficient engine performance. The primitive-based trajectory design space exploration process presented in this work may support this type of analysis during preliminary mission concept development. Each point solution identified in Figure 8.4a may correspond to an associated group of similar geometric solutions and is derived from a series of transfers with evolving properties computed using natural parameter continuation.

Transfer 1 displayed in Figure 8.5 is examined in more detail to study the associated set of transfers in its local vicinity. Figure 8.6 displays the group of transfers associated with Transfer 1 in the xy-plane of $\mathcal{R}$ in the Earth-Moon CR3BP where Transfer 1 is denoted in bold. Using this figure, a human analyst may visually identify variations in geometry and maneuver placement across the group of similar solutions. These solutions are also depicted in the TOF-Δv trade space in Figure 8.4a in the same color: the group of transfers possess flight times ranging from 21.18 days to 23.31 days and maneuver requirements from 11.53 m/s to 20.33 m/s. Analyzing a group of similar transfers in this manner provides insight into the potential flexibility of the overall geometry with respect to changes in TOF and total Δv.

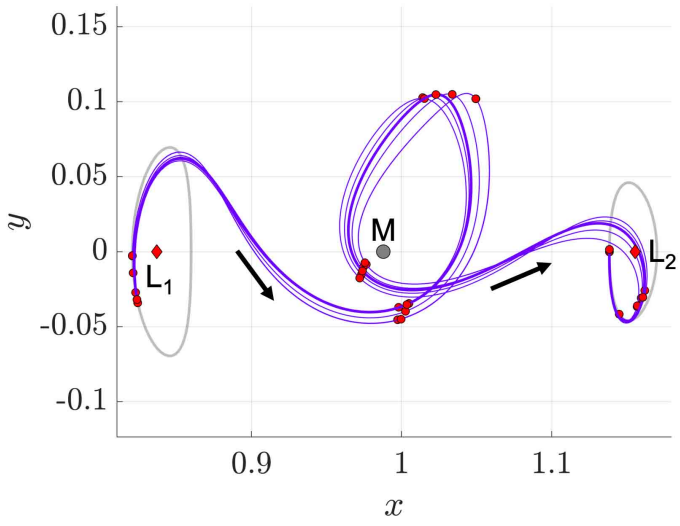

Figure 8.6: Group of planar transfers associated with Transfer 1 from Figure 8.5 between an L_1 and L_2 Lyapunov orbit in the Earth-Moon CR3BP.

Each transfer displayed in Figure 8.4a is derived from a set of transfers computed using natural parameter continuation starting with a primitive-based initial guess. This set of associated transfers may expand the applicable region of the TOF-Δv trade space for the given transfer geometry. Figures 8.7-8.9 display the evolution of Transfer 1 during the natural parameter continuation process. Figure 8.7 displays the continuous transfer (blue) computed from the primitive-based initial guess (dashed gray) using $\boldsymbol{w_{opt}} = [0.9, 0.1]$: Figure 8.7a displays the transfer in $\mathcal{R}$ with the

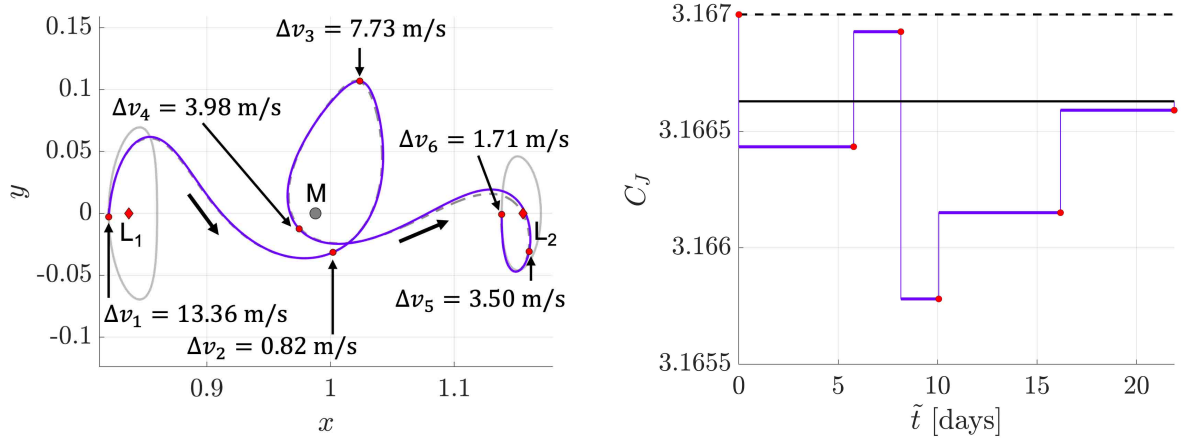

(a) Transfer displayed in the xy-plane of $\mathcal{R}$.

(b) Evolution of C_J along the transfer.

Figure 8.7: Continuous 21.90 day planar transfer from an L_1 Lyapunov orbit to an L_2 Lyapunov orbit in the Earth-Moon CR3BP, computed from a primitive-based initial guess using $\boldsymbol{w}_{\mathbf{opt}} = [0.9, 0.1]$.

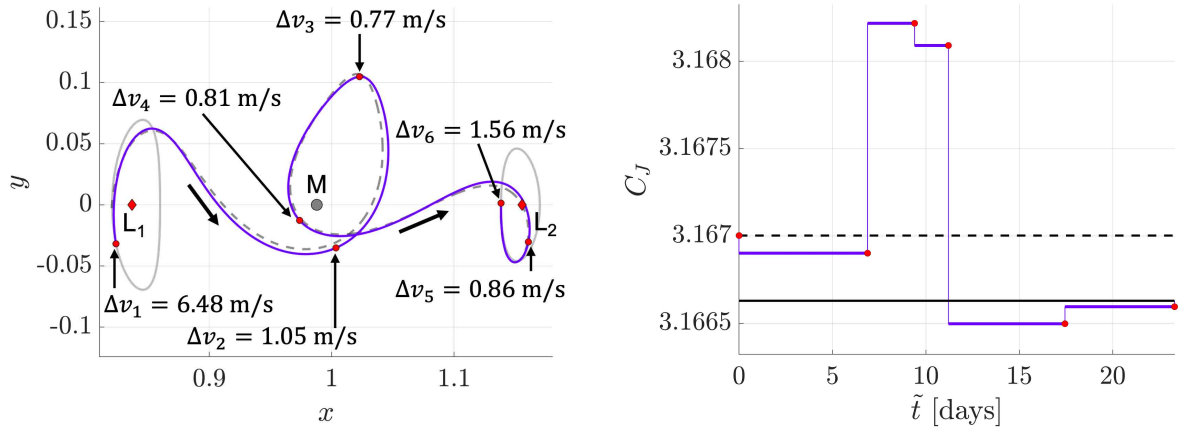

(a) Transfer displayed in the xy-plane of $\mathcal{R}$.

(b) Evolution of C_J along the transfer.

Figure 8.8: Continuous 23.30 day planar transfer from an L_1 Lyapunov orbit to an L_2 Lyapunov orbit in the Earth-Moon CR3BP, computed at $\boldsymbol{w}_{\mathbf{opt}} = [0.1, 0.9]$ using the continuation procedure that varies the weights of the multi-objective optimization problem starting from the transfer displayed in Figure 8.7.

magnitude of each impulsive maneuver provided and Figure 8.7b displays the evolution of C_J along the transfer as a function of time. The Jacobi constant of the initial orbit is indicated with a dashed

black line and the Jacobi constant of the target orbit is indicated with a solid black line in Figure 8.7b. Given the quality of the initial guess, the recovered continuous solution closely matches the initial guess with a flight time of 21.90 days and a total Δv requirement of 31.10 m/s. Using the same visualization method as Figure 8.7, Figure 8.8 displays the continuous transfer computed using $\boldsymbol{w_{opt}} = [0.1, 0.9]$ at the end of the continuation process with a flight time of 23.30 days and a total Δv requirement of 11.53 m/s. Comparing the transfers in Figures 8.7 and 8.8, the impulsive maneuver magnitudes are significantly reduced as a result of the continuation process while still preserving the overall geometry of the transfer. However, as evident in Figure 8.8, the solution computed using $\boldsymbol{w_{opt}} = [0.1, 0.9]$ deviates more significantly from the primitive-based initial guess but exhibits fewer large changes in C_J along the transfer. Finally, Figure 8.9 displays all of the intermediate transfers computed during the natural parameter continuation process using the same black to copper color scheme as Figure 7.12. As more emphasis is placed on the maneuver requirements, the total Δv of the transfers decreases while the TOF increases. Yet, the overall transfer geometry is well preserved. The most significant change in geometry corresponds to a change in the departure location along the initial orbit as evident in Figure 8.9.

An additional interesting transfer to examine in more detail is Transfer 11 displayed in Figure 8.5. Transfer 11 appears to contain some similar geometric elements as Transfer 10 but exhibits a significantly longer TOF due to an additional revolution around the Moon; furthermore, this transfer is not grouped with any of the other transfers computed using $\boldsymbol{w_{opt}} = [0.1, 0.9]$. Using the same format as Figures 8.7-8.9 for Transfer 1, Figures 8.10-8.12 display the evolution of Transfer 11 throughout the natural parameter continuation process. As depicted in Figure 8.10, the transfer computed using $\boldsymbol{w_{opt}} = [0.9, 0.1]$ closely resembles the primitive-based initial guess but the total Δv requirement for this transfer is 404.32 m/s, which is significantly larger than most of the other computed transfers. As a result of the continuation process, the total Δv requirement is reduced to 57.10 m/s and the flight time increases by 2.96 days; however, this reduction in total Δv is achieved primarily through altering the geometric structure of the transfer. The transfer computed using $\boldsymbol{w_{opt}} = [0.1, 0.9]$ is displayed in Figure 8.11 and its evolution throughout the continuation

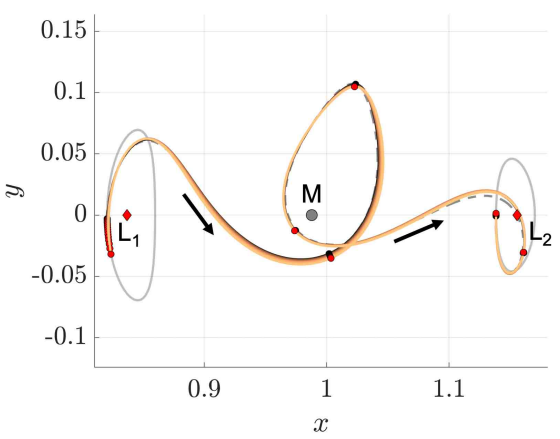

(a) Transfers displayed in the xy-plane of $\mathcal{R}$.

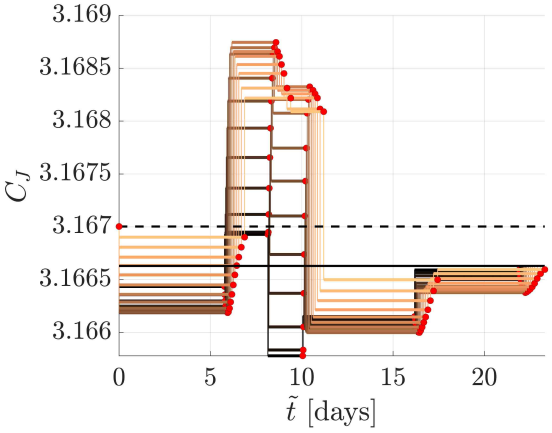

(b) Evolution of C_J along each transfer.

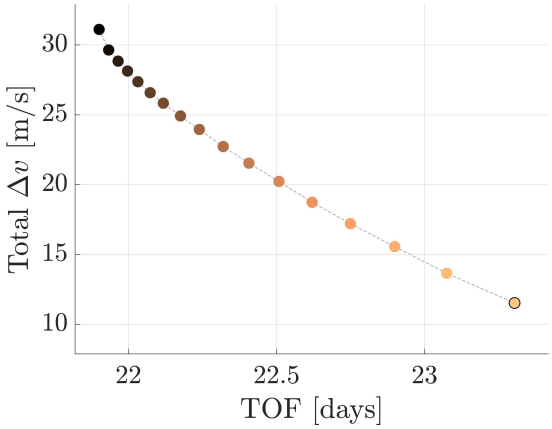

(c) Evolution of the TOF and total Δv for the set of transfers due to changes in $\boldsymbol{w}_{\mathbf{opt}}$.

Figure 8.9: Evolution of the geometry, TOF, and maneuver requirements across transfers in the local vicinity of Transfer 1 from Figure 8.5, computed using the continuation procedure that varies the weights of the multi-objective optimization problem.

process is displayed in Figure 8.12. As evident in Figure 8.12, the most significant change in geometry occurs throughout the first revolution of the transfer around the Moon with a noticeable apsidal rotation. Despite these changes in geometry, the transfer computed using $\boldsymbol{w}_{\mathbf{opt}} = [0.1, 0.9]$ still loosely resembles the original primitive-based initial guess. The geometric evolution of each transfer during the continuation procedure is often dependent on the quality and structure of the initial guess. In some cases, the geometry of a transfer is tightly preserved and primarily exhibits

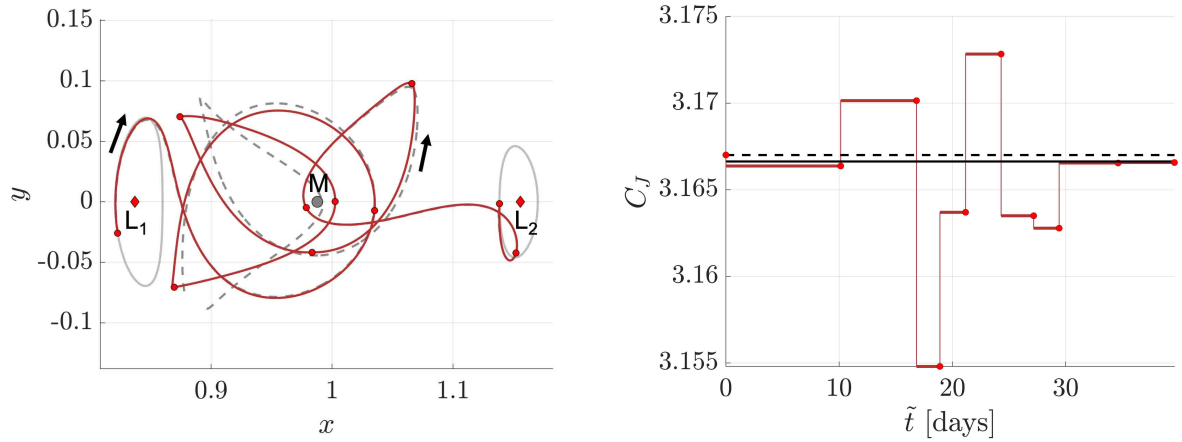

(a) Transfer displayed in the xy-plane of $\mathcal{R}$.

(b) Evolution of C_J along the transfer.

Figure 8.10: Continuous 39.60 day planar transfer from an L_1 Lyapunov orbit to an L_2 Lyapunov orbit in the Earth-Moon CR3BP, computed from a primitive-based initial guess using $\boldsymbol{w_{opt}} = [0.9, 0.1]$.

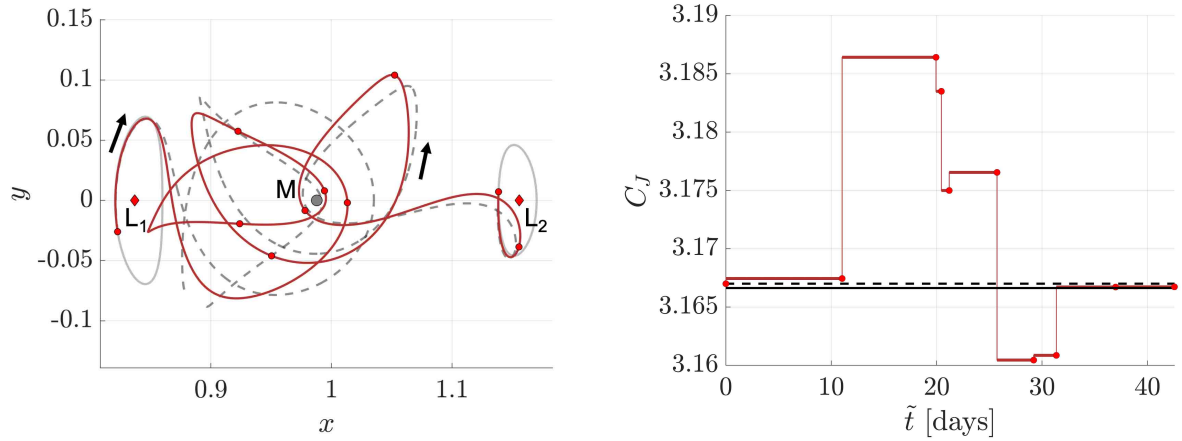

(a) Transfer displayed in the xy-plane of $\mathcal{R}$.

(b) Evolution of C_J along the transfer.

Figure 8.11: Continuous 42.56 day planar transfer from an L_1 Lyapunov orbit to an L_2 Lyapunov orbit in the Earth-Moon CR3BP, computed at $\boldsymbol{w_{opt}} = [0.1, 0.9]$ using the continuation procedure that varies the weights of the multi-objective optimization problem starting from the transfer displayed in Figure 8.10.

changes in its departure or arrival locations as shown for Transfer 1; however, in other cases, the geometry of a transfer deviates more significantly from the original primitive-based initial guess as

shown for Transfer 11. In either case, the design procedure effectively computes a set of transfers in the local neighborhood of a primitive-based initial guess that varies continuously as $\boldsymbol{w}_{\mathbf{opt}}$ is modified.

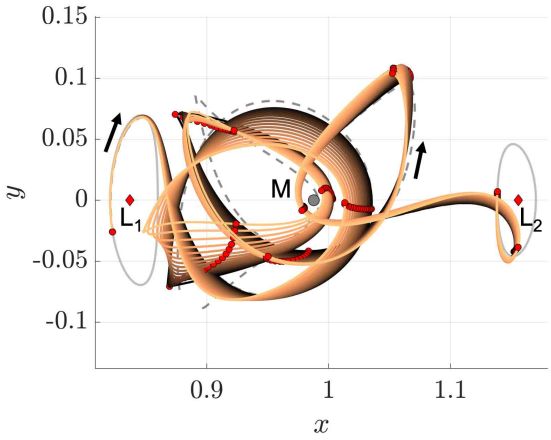

(a) Transfers displayed in the xy-plane of $\mathcal{R}$.

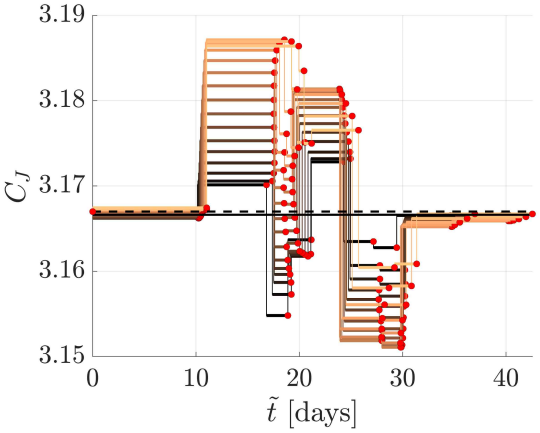

(b) Evolution of C_J along each transfer.

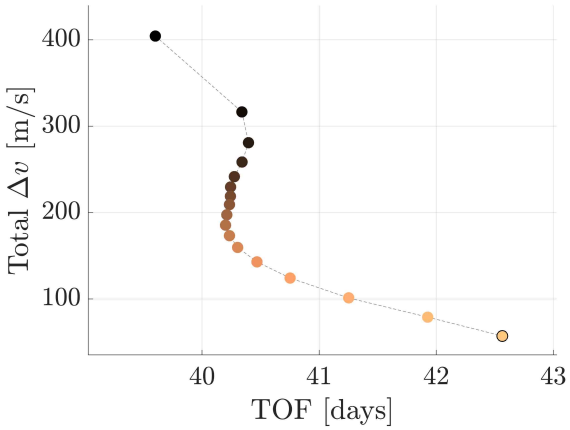

(c) Evolution of the TOF and total Δv for the set of transfers due to changes in $\boldsymbol{w}_{\mathbf{opt}}$.

Figure 8.12: Evolution of the geometry, TOF, and maneuver requirements across transfers in the local vicinity of Transfer 11 from Figure 8.5, computed using the continuation procedure that varies the weights of the multi-objective optimization problem.

8.1.3 Exploring Additional Transfers

A motion primitive graph is used to generate a discrete representation of the continuous design space for a given transfer scenario. In Section 8.1.1, a variety of initial guesses are constructed by searching the motion primitive graph in Figure 8.2 to produce unique sequences of four, five, and six motion primitives between the initial L_1 Lyapunov orbit and the target L_2 Lyapunov orbit. However, the search process, as described in Section 7.4, can be applied generally between any two given primitives within the graph for sequences of any desired length. The efficiency of the search process depends on the complexity of the motion primitive graph, the algorithm used to conduct the search, the selection of the initial and target nodes in the graph, and finally the desired path length. Using DFS to enumerate all potential paths from an initial node to a target node with a desired length may become intractable as the path length and/or the complexity of the graph is increased. DFS is a brute-force search technique and therefore cannot efficiently handle the combinatorial explosion that may occur due to increases in the desired path length and/or the complexity of the graph structure. An avenue of future work is to use more efficient search algorithms in this design framework to address this challenge; however, DFS is the only search algorithm used in this investigation and therefore a waypoint search process may be formulated to mitigate the computational challenge of constructing initial guesses comprised of longer motion primitive sequences.

A preliminary exploration of the design space may lead to the identification of base paths in the motion primitive graph that warrant further exploration. Given a selected base path, the final node in the path is considered a waypoint node. Then, the motion primitive graph may be searched from the waypoint node to the desired target node using the same process described in Section 7.4: Figure 8.13 provides a conceptual depiction of the waypoint search process in which a human analyst may specify a base path and then the graph is searched for paths of a desired length between the waypoint node and the target node. Using this procedure, longer motion primitive sequences may be recovered from the motion primitive graph between the initial node and the

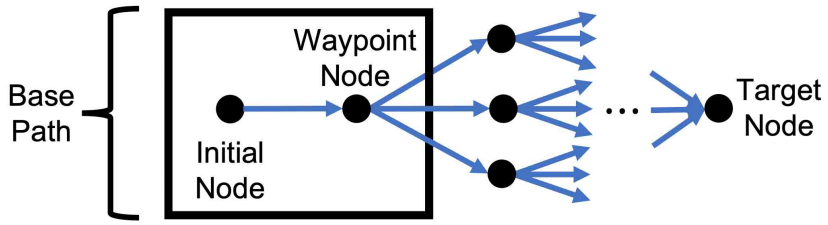

Figure 8.13: Conceptual depiction of the waypoint search process used to find paths in a motion primitive graph from a waypoint node to a target node.

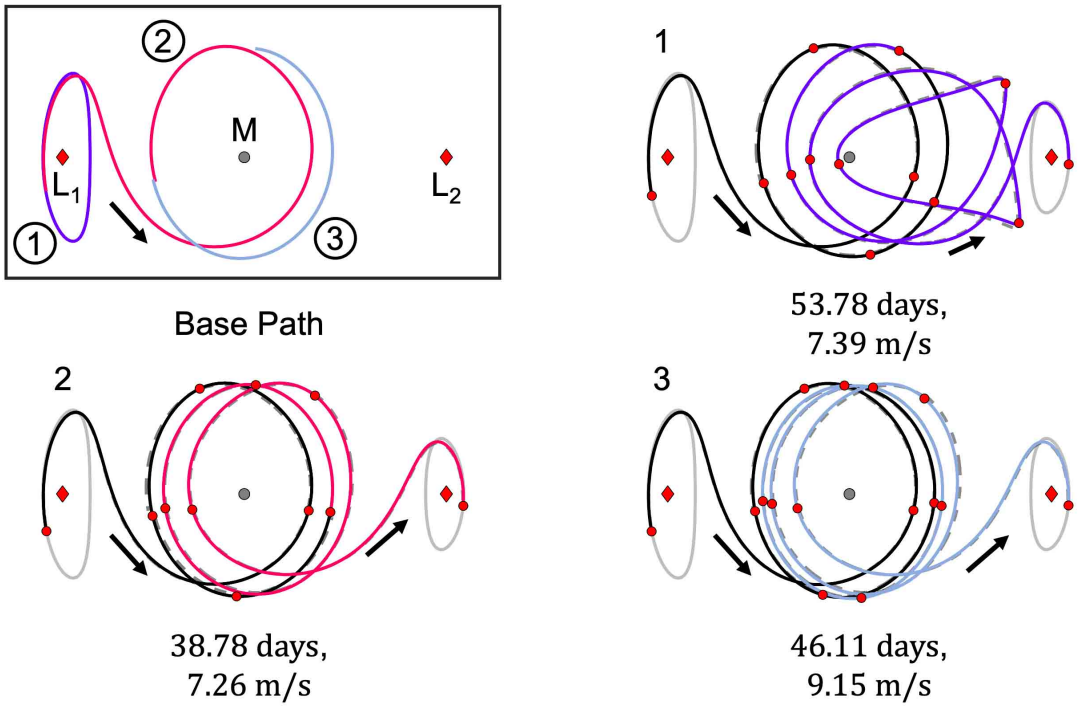

Figure 8.14: Planar transfers computed from primitive-based initial guesses that contain a common base path (black) between an L_1 and L_2 Lyapunov orbit in the Earth-Moon CR3BP, displayed in the xy-plane of $\mathcal{R}$. Note: The base path in each transfer may exhibit variations due to the morphing and trimming process used to refine each initial guess before applying the corrections procedure.

target node without significantly increasing the complexity of the search process.

In the context of the L_1 to L_2 Lyapunov orbit transfer design scenario, consider the base path displayed in Figure 8.14 comprised of three motion primitives (including the initial orbit). This base path is derived from Transfer 7 in Figure 8.5 and the third primitive is considered the

waypoint primitive. The motion primitive graph is then searched from the waypoint primitive to the target orbit for sequences composed of five primitives. The resulting sequences are then combined with the fixed base path to produce longer motion primitive sequences. In this case, each resulting path is composed of seven motion primitives from the initial orbit to the target orbit. Figure 8.14 displays continuous transfers constructed from the top $Q = 3$ paths stemming from the base path denoted in black. The first initial guess is used to recover a similar solution as Transfer 14 displayed in Figure 8.5 and the remaining two transfers are similar to Transfers 5-7 displayed in Figure 8.5 but include additional revolutions around the Moon. Transfers 2 and 3 displayed in Figure 8.14 present two additional transfer geometries that were not previously recovered in the design space exploration conducted in Section 8.1.1. Leveraging this waypoint search process enables a trajectory designer to efficiently construct longer sequences of motion primitives and identify additional transfer geometries after conducting a preliminary design space exploration.

8.1.4 Transitioning Transfers to a Point Mass Ephemeris Model

A continuous trajectory computed in the CR3BP is used as an initial guess to attempt to recover a similar solution in a point mass ephemeris model. The process of transitioning a trajectory from the CR3BP into a point mass ephemeris model is outlined in Chapter 4. In this subsection, this procedure is applied to Transfers 1 and 11 displayed in Figure 8.5 for the L_1 to L_2 Lyapunov orbit transfer design scenario. The reference epoch for both transfers is selected arbitrarily as January 1, 2023, at 00:00:00.000 UTC for demonstration purposes. During the corrections process, the initial epoch of each transfer is allowed to vary relative to this selected reference epoch. Finally, the primary bodies included in the point mass ephemeris model are the Moon, Earth, and Sun.

A periodic orbit does not retain its periodic structure when transitioned from the CR3BP into a point mass ephemeris model; instead, the resulting path may resemble quasi-periodic motion. Therefore, the boundary constraints described in Section 7.6 for the CR3BP are not applicable in an ephemeris model. Instead, multiple revolutions of the initial and target orbits are included in the initial guess to approximately retain the structure of the periodic orbits at each boundary of

the transfer where possible [26]. For each transfer, 5 revolutions of the initial orbit and a partial revolution that terminates at the departure state along the initial orbit are included at the beginning of the transfer. Similarly, a partial revolution of the target orbit that begins at the arrival state along the target orbit and an additional 5 revolutions are included at the end of each transfer. Due to the incorporation of these periodic orbit revolutions, the flight time of the initial guess may increase significantly. Therefore, in some cases, the time variables in the free variable vector may be scaled by the total TOF of the initial guess and inequality constraints may be introduced to enforce positive implicit integration times along each arc to improve the numerical conditioning of the corrections problem.

Using this configuration and $\boldsymbol{w}_{\mathbf{opt}} = [0.1, 0.9]$, Transfers 1 and 11 are corrected in $\mathcal{E}$ ($\mathcal{E}$ is a Moon-centered inertial frame because P_1 is selected as the Moon in the ephemeris model) and transformed back into $\mathcal{R}$ for comparison with the solutions in the CR3BP. Figure 8.15 displays Transfer 1 computed in the Earth-Moon CR3BP (dashed black) with respect to the resulting solution computed in a Moon-Earth-Sun point mass ephemeris model (blue). The transfer generated in the ephemeris model extends out of the xy-plane; however, only the projection of the transfer onto the xy-plane is displayed because the maximum extension in the z-coordinate is minimal. The initial epoch of the corrected trajectory is January 2, 2023, at 02:35:50.693 UTC, the flight time is approximately 23.93 days, and the total Δv is 15.27 m/s. In this case, the transfer time increased by 0.63 days and the total Δv increased by 3.74 m/s compared to the associated solution in the CR3BP. Similarly, Figure 8.16 displays Transfer 11 computed in the Earth-Moon CR3BP (dashed black) with respect to the resulting solution computed in a Moon-Earth-Sun point mass ephemeris model (blue). As discussed for Figure 8.15, only the projection of the transfer onto the xy-plane is displayed. The initial epoch of the corrected trajectory is January 2, 2023, at 21:23:16.294 UTC, the flight time is approximately 43.27 days, and the total Δv is 50.91 m/s. In this case, the transfer time increased by 0.71 days and the total Δv decreased by 6.19 m/s compared to the associated CR3BP solution. In both cases, the geometry of the transfer as well as the initial and final orbits are well preserved in the ephemeris model. These solutions demonstrate the utility of using the

CR3BP for preliminary trajectory design.

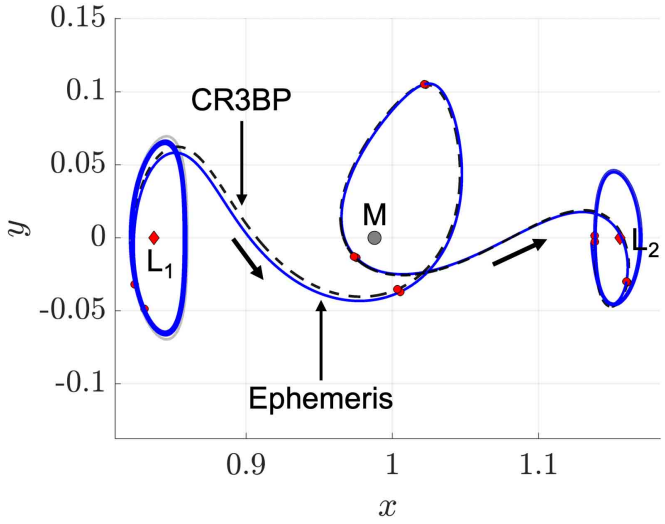

Figure 8.15: Continuous 23.93 day transfer from an L_1 Lyapunov orbit to an L_2 Lyapunov orbit in a Moon-Earth-Sun point mass ephemeris model with an initial epoch of January 2, 2023, at 02:35:50.693 UTC, computed from Transfer 1 displayed in Figure 8.5 using $\boldsymbol{w}_{\mathbf{opt}} = [0.1, 0.9]$. Note: The spatial transfer generated in the ephemeris model is displayed as a projection onto the xy-plane.

8.2 Spatial Transfers from an L_1 to L_2 Northern Halo Orbit in the Earth-Moon System

8.2.1 Constructing Transfers with Distinct Geometries

The primitive-based trajectory design framework is used to construct spatial transfers from an L_1 northern halo orbit at $C_J \approx 3.0635$ to an L_2 northern halo orbit at $C_J \approx 3.0669$ in the Earth-Moon CR3BP with impulsive maneuvers. Figure 8.17 displays the selected northern halo orbits in $\mathcal{R}$ and Table 8.2 lists the properties of each orbit. In this scenario, Poincaré maps capturing spatial motion at high energy levels may be difficult to analyze due to the complexity of the solution space and higher-dimensional description of the map crossings. As a result, it may be challenging to use existing dynamical systems techniques alone to construct point solutions and explore the broader design space spanned by geometrically dissimilar solutions. Thus, this challenging scenario

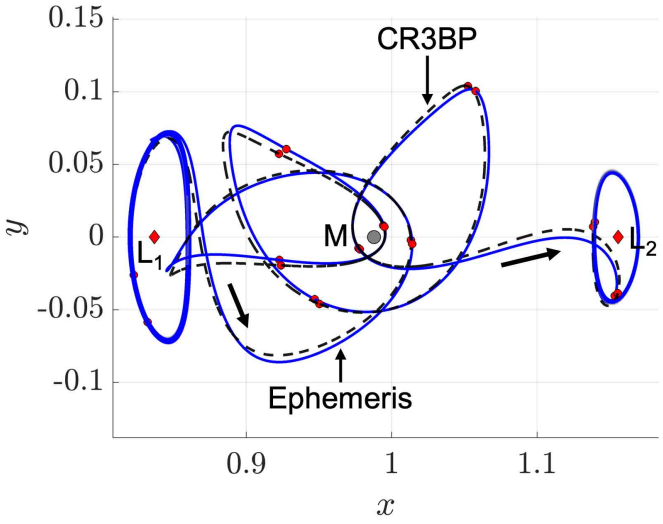

Figure 8.16: Continuous 43.27 day transfer from an L_1 Lyapunov orbit to an L_2 Lyapunov orbit in a Moon-Earth-Sun point mass ephemeris model with an initial epoch of January 2, 2023, at 21:23:16.294 UTC, computed from Transfer 11 displayed in Figure 8.5 using $\boldsymbol{w}_{\mathbf{opt}} = [0.1, 0.9]$. Note: The spatial transfer generated in the ephemeris model is displayed as a projection onto the xy-plane.

Table 8.2: Properties of the initial L_1 northern halo orbit and the target L_2 northern halo orbit for the northern halo orbit transfer design scenario in the Earth-Moon CR3BP.

	Initial Orbit	Target Orbit
Orbit Type	L_1 northern halo	L_2 northern halo
C_J	3.063534530378191	3.066884796159840
T_{PO}	2.777323978103622 ($\approx$ 12.06 days)	3.165890567984349 ($\approx$ 13.75 days)
s_1	218.429599140514	-0.226466014391004
s_2	-0.813864903041833	180.278208268368

supports demonstration of the utility of the presented motion primitive framework for trajectory design in a multi-body system.

To construct a motion primitive graph in this scenario, the high-level itinerary graph is designed to possess the same structure as in Figure 8.2 but uses primitives of the selected northern halo orbit families and their stable and unstable manifolds. Consistent with the Lyapunov transfer design scenario, each manifold is generated for up to 15 apses relative to the Moon and sampled to produce shorter arcs that span up to 4 apses relative to the Moon. The entire set of motion

primitives generated to summarize arcs along these stable and unstable manifolds are provided in Appendix A and all components of the motion primitive library are listed in Table 8.3. Furthermore, the high-level itinerary graph is depicted in Figure 8.18. To construct the motion primitive graph, the following configuration parameters are specified: $k_{\text{nn}} = 15$, $\alpha_{\text{pos}} = 100$, and $\alpha_{\text{vel}} = 1$. These selections place a much stronger emphasis on position discontinuities between primitives compared to the previous transfer design scenario, consistent with an observed increase in sensitivity for higher energy spatial transfers with close lunar passes. Additionally, the set of representative trajectories associated with each motion primitive, excluding the selected initial and target orbit primitives, is incorporated into the edge weight computations and the average edge weight is used to evaluate the quality of each primitive sequence. The computation time for constructing the motion primitive graph in this scenario is on the order of 10^0 minutes using an iMac with a 3GHz 6-Core Intel Core i5 processor.

The motion primitive graph is searched to produce unique sequences of four, five, and six primitives that each form an initial guess for a transfer from the L_1 northern halo orbit to the L_2

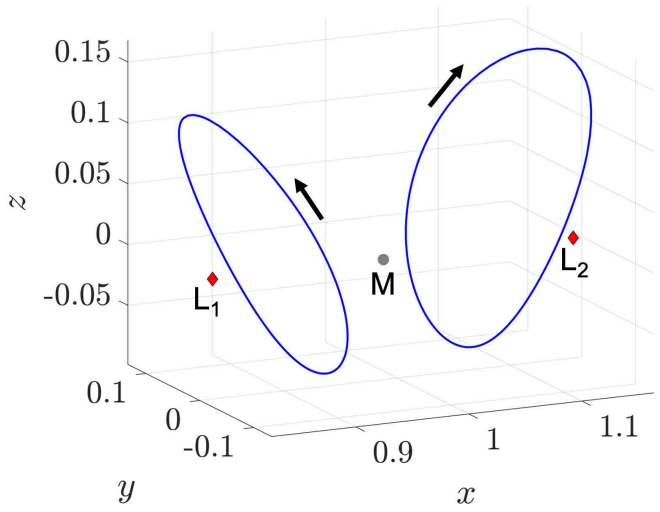

Figure 8.17: Configuration of the initial L_1 northern halo orbit at $C_J \approx 3.0635$ and the target L_2 northern halo orbit at $C_J \approx 3.0669$ in $\mathcal{R}$ for the northern halo orbit transfer design scenario in the Earth-Moon CR3BP.

northern halo orbit. There are a total of 331, 19,764, and 1,148,147 primitive sequences from the initial node to the target node in the graph consisting of four, five, and six primitives, respectively. However, using the filtering process presented in Section 7.4, the $Q = 10$ top-ranked sequences that begin with a unique primitive are examined for each path length. A smaller value of Q is selected for this scenario compared to the previous example because the quality of the initial guesses degrades more significantly as additional sequences are considered. This approach produces 30 unique primitive sequences that are each refined to produce an initial guess.

Each initial guess is corrected with several unconstrained impulsive maneuvers distributed

Table 8.3: Motion primitives in the library for the spatial transfer design scenario from an L_1 to L_2 northern halo orbit.

Fundamental Solution	Number of Primitives	Approx. C_J
L_1 northern halo orbit	1	3.0635
L_1 northern halo orbit unstable manifold	198	3.0635
L_1 northern halo orbit stable manifold	194	3.0635
L_2 northern halo orbit	1	3.0669
L_2 northern halo orbit unstable manifold	226	3.0669
L_2 northern halo orbit stable manifold	223	3.0669

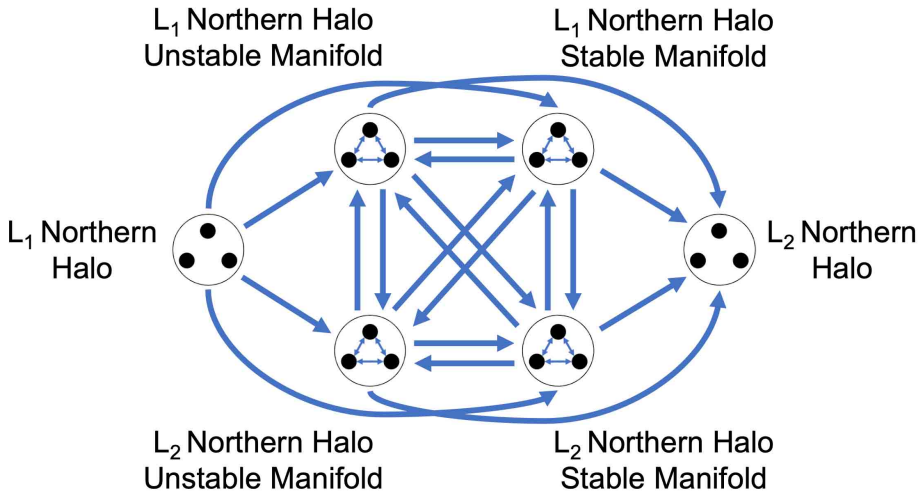

Figure 8.18: High-level itinerary graph for a spatial L_1 to L_2 northern halo orbit transfer design scenario in the Earth-Moon CR3BP.

along the transfer using the same maneuver placement scheme as in the previous example. All 30 primitive-based initial guesses are successfully corrected using $\boldsymbol{w_{opt}} = [0.9, 0.1]$ to produce continuous transfers from the desired initial L_1 northern halo orbit to the target L_2 northern halo orbit. However, 6 of the corrected transfers impact a spherical approximation of the Moon. Continuation is then used to gradually vary the weights of the the multi-objective optimization problem described in Section 7.6 from $\boldsymbol{w_1} = [0.9, 0.1]$ to $\boldsymbol{w_2} = [0.1, 0.9]$. Following this process, only 27 of these transfers are successfully corrected with $\boldsymbol{w_{opt}} = \boldsymbol{w_2}$.

An initial summary of the transfers that solve the multi-objective optimization problem with each value of $\boldsymbol{w_{opt}}$ is presented. In Figure 8.19a, the total Δv of each of the 30 transfers that is corrected with $\boldsymbol{w_{opt}} = \boldsymbol{w_1}$ is displayed with respect to the normalized average potential for sequential composability, $\Delta\check{q}_{\text{avg}}$, of its initial guess; this figure uses the same configuration as Figure 8.3. In Figure 8.19b, however, this information is presented for the 27 transfers that are corrected with $\boldsymbol{w_{opt}} = \boldsymbol{w_2}$ to prioritize minimizing maneuver requirements. Across the set of 30 transfers computed with $\boldsymbol{w_{opt}} = \boldsymbol{w_1}$ to emphasize recovering transfers that are geometrically similar to their initial guesses, the total Δv ranges from 86.05 m/s to 1705.78 m/s. However, when prioritizing minimizing maneuver requirements, the 27 transfers corrected with $\boldsymbol{w_{opt}} = \boldsymbol{w_2}$ require a total Δv ranging from 44.06 m/s to 342.99 m/s. Furthermore, the transfers summarized in Figure 8.19b no longer exhibit a clear correlation between $\Delta\check{q}_{\text{avg}}$ and the total Δv requirements compared to the planar Lyapunov orbit transfers presented in Section 8.1.

The 27 corrected transfers that prioritize minimizing maneuver requirements are grouped based on geometry to extract the distinct types of transfers that connect the selected northern halo orbits. When applying the k-NN graph approach described in Section 7.7, $k_{\text{nn}} = 3$ and $l_{\Delta\text{TOF}} = 5\%$ are selected empirically and produce 18 groups of geometrically distinct transfers. The resulting properties of each transfer are plotted in Figure 8.20 using the same configuration as Figure 8.4 where the minimum Δv solution in each group is circled and numbered. These transfers require flight times ranging from 18.79 days to 60.80 days and total Δv requirements ranging from 44.06 m/s to 342.99 m/s when placing more emphasis on recovering maneuver-efficient transfers.

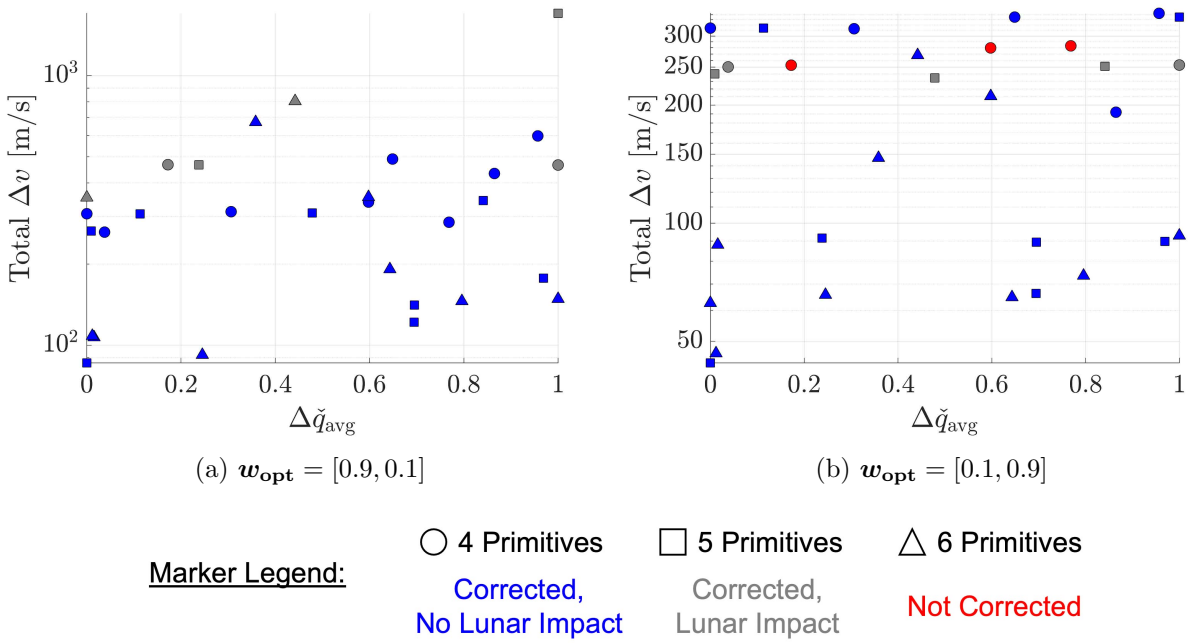

(a) $\boldsymbol{w}_{\mathbf{opt}} = [0.9, 0.1]$ (b) $\boldsymbol{w}_{\mathbf{opt}} = [0.1, 0.9]$

Figure 8.19: Total Δv of spatial transfers computed from an L_1 northern halo orbit to an L_2 northern halo orbit in the Earth-Moon CR3BP as a function of $\Delta\check{q}_{\text{avg}}$.

Figure 8.20b displays the evolution of the flight time and total Δv for each of the transfers circled in Figure 8.20a as the weights of the multi-objective optimization problem are varied, resulting in significant reductions in total Δv. However, some transfers exhibit decreases in TOF while others exhibit increases in TOF. As the objective function weights are adjusted, the specific evolution of each transfer in the TOF-Δv trade space depends on the geometry of the initial guess, the placement of maneuvers, and how the departure and arrival locations along the initial and target orbit, respectively, are adjusted to reduce the total maneuver requirements.

The minimum Δv transfer in each group is visualized in the configuration space of the Earth-Moon CR3BP; specifically, Figures 8.21 and 8.22 display each transfer in $\mathcal{R}$ of the Earth-Moon system. Figure 8.21 displays the transfers as a projection onto the xz-plane of $\mathcal{R}$ and Figure 8.22 displays the transfers as a projection onto the xy-plane of $\mathcal{R}$. In these figures, each corrected transfer geometrically resembles its initial guess (dashed gray) but with more noticeable deviations than

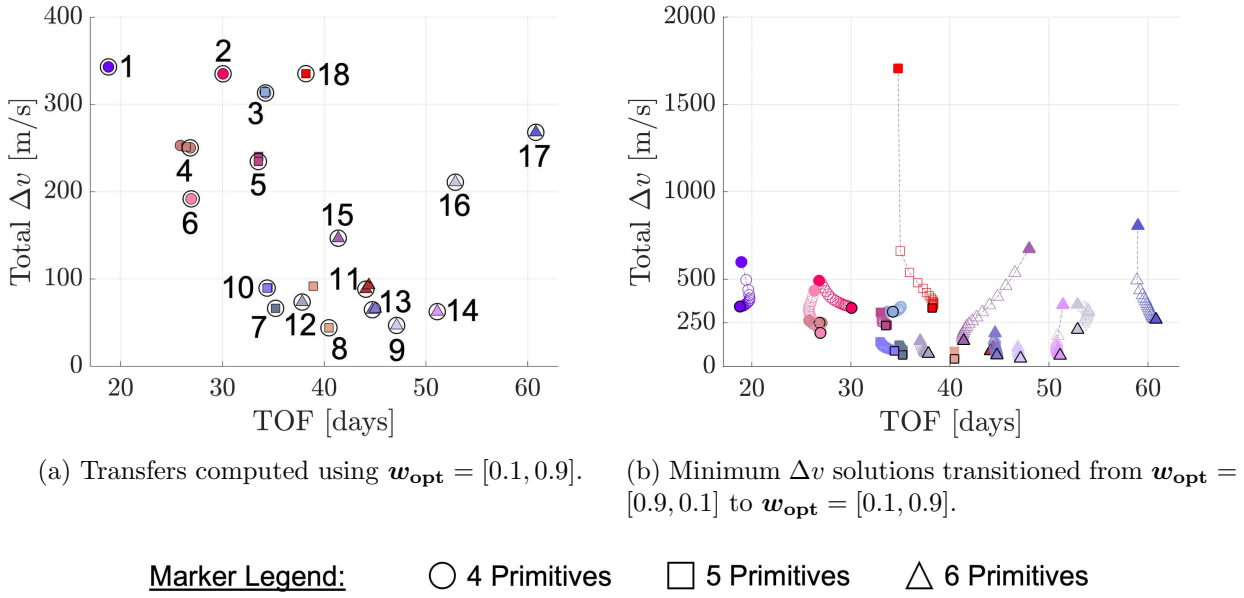

(a) Transfers computed using $\boldsymbol{w}_{\mathbf{opt}} = [0.1, 0.9]$.

(b) Minimum Δv solutions transitioned from $\boldsymbol{w}_{\mathbf{opt}} = [0.9, 0.1]$ to $\boldsymbol{w}_{\mathbf{opt}} = [0.1, 0.9]$.

Figure 8.20: Total Δv and TOF of spatial transfers computed from an L_1 northern halo orbit to an L_2 northern halo orbit in the Earth-Moon CR3BP, where geometrically similar transfers are denoted in the same color and the minimum Δv solution for each transfer geometry is highlighted.

in the planar transfers constructed in Section 8.1. As discussed in Section 8.1, more significant deviations from the primitive-based initial guesses are observed throughout the natural parameter continuation procedure for transfers that are constructed from initial guesses with larger discontinuities. Furthermore, the computed transfers all exhibit distinct transfer geometries in the vicinity of the Moon with several close approaches and apolunes at high z-amplitudes above the plane of the primaries. The exceptions are Transfers 7-9 and Transfers 12-14: both groups of transfers could potentially each be combined into a single group because these transfers exhibit only slight differences in geometry during the transit phase of the itinerary. Each of these transfers exhibits more distinct geometries during the departure and arrival phases of the itinerary. As a comparison with a previous result, Transfers 7-9 geometrically resemble a 51.2 day transfer computed by Haapala between two northern halo orbits at similar energy levels but with a lower total maneuver magnitude of 11.9 m/s [39]; this difference is likely due to alternative corrections problem formulations,

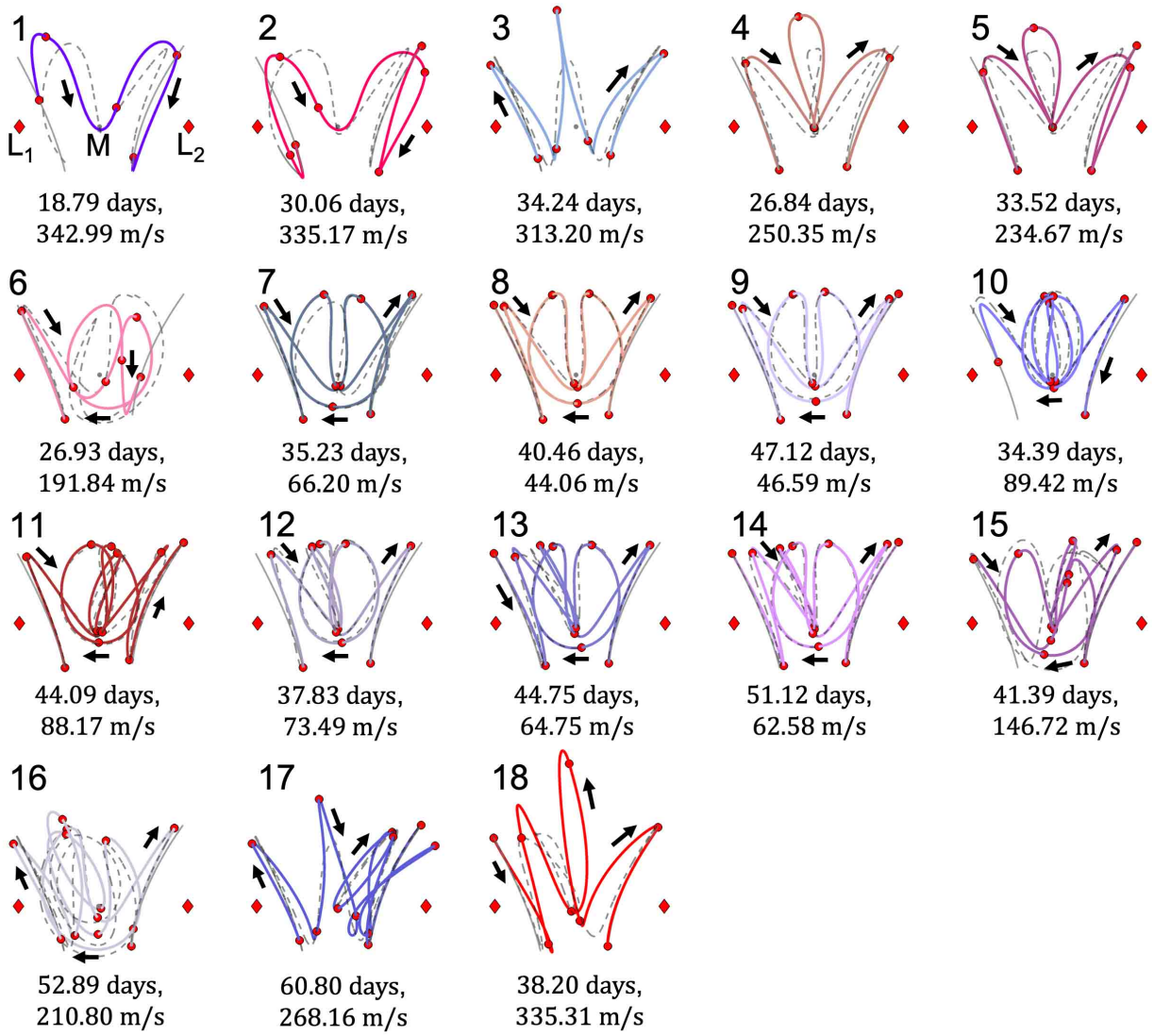

Figure 8.21: Spatial transfers with distinct geometries computed from primitive-based initial guesses between an L_1 and L_2 northern halo orbit in the Earth-Moon CR3BP, displayed as a projection onto the xz-plane of $\mathcal{R}$.

an alternative number and location of maneuvers, and the explicit use of manifold arcs that gradually approach or depart each periodic orbit. Nevertheless, the recovered transfers demonstrate the capability to achieve a significant reduction in total maneuver magnitude while still preserving the approximate geometry of a coarsely-constructed primitive-based initial guess.

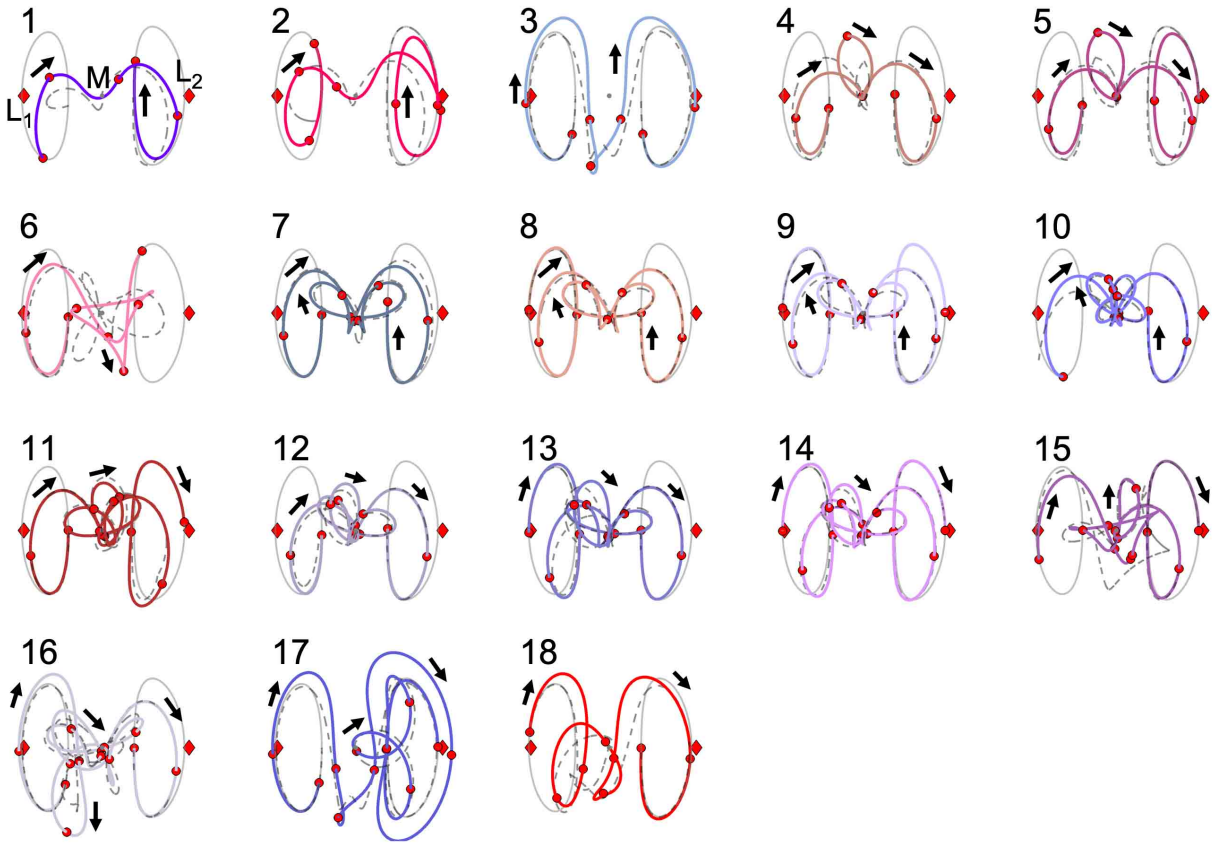

Figure 8.22: Spatial transfers with distinct geometries computed from primitive-based initial guesses between an L_1 and L_2 northern halo orbit in the Earth-Moon CR3BP, displayed as a projection onto the xy-plane of $\mathcal{R}$.

8.2.2 Examining the Local Neighborhood of Transfers

To understand the evolution of each transfer during the natural parameter continuation process, some insight can be obtained from continuous thrust trajectory optimization. The primary objective considered in the continuous thrust problem is commonly either to minimize propellant mass usage or to minimize control effort [96, 91, 42, 83]. Minimizing propellant mass usage along a trajectory often results in a "bang-bang" thrust profile that is comprised of trajectory segments that alternate between thrusting and coasting; in the impulsive case, minimizing propellant mass usage equates to minimizing the sum of the impulsive maneuver magnitudes along a trajectory [42, 83]. However, minimizing control effort often results in smoother thrust profiles where the thrust mag-

nitude varies but the spacecraft is continuously thrusting; in the impulsive case, minimizing control effort is similar to minimizing the sum of the squared impulsive maneuver magnitudes [42, 83]. In this investigation, the maneuver requirement term of the objective function is defined as the sum of the squared impulsive maneuver magnitudes along a trajectory (Equation 7.4). Consequently, during the continuation process, it is observed that increasing w_{man} typically translates to smoother trajectory profiles in the configuration space and more evenly distributed maneuver magnitudes along a trajectory. Transfer 2 from Figure 8.21 is examined in more detail as an example.

Figures 8.23-8.25 display the evolution of Transfer 2 throughout the natural parameter continuation process using a similar format as the Lyapunov transfer design analysis. In addition, Table 8.4 lists the maneuver magnitudes for the transfers displayed in Figures 8.23 and 8.24. The transfer displayed in Figure 8.23 exhibits sharp changes in direction during the departure phase of the transfer, particularly at each of the first three maneuvers. However, as shown in Figures 8.24 and 8.25, these sharp changes in direction are gradually smoothed during the continuation process and results in more significant geometric variations from the primitive-based initial guess. This change in structure is also apparent in the evolution of C_J along each transfer. Finally, Table 8.4 demonstrates that the largest maneuver magnitudes decreased while the smallest maneuver magnitudes increased between the transfers computed using $\boldsymbol{w_{\text{opt}}} = [0.9, 0.1]$ and $\boldsymbol{w_{\text{opt}}} = [0.1, 0.9]$. A similar evolution is observed for many of the transfers computed throughout this investigation that initially exhibit sharp changes in direction of motion and large velocity discontinuities along the corresponding primitive-based initial guess. Although the maneuver requirement term of the objective function formulated in this work does not directly minimize the total Δv of a transfer, the solutions obtained as w_{man} is increased during the continuation procedure generally exhibit significant reductions in total Δv and may serve as starting points to compute nearby local minimum total Δv solutions.

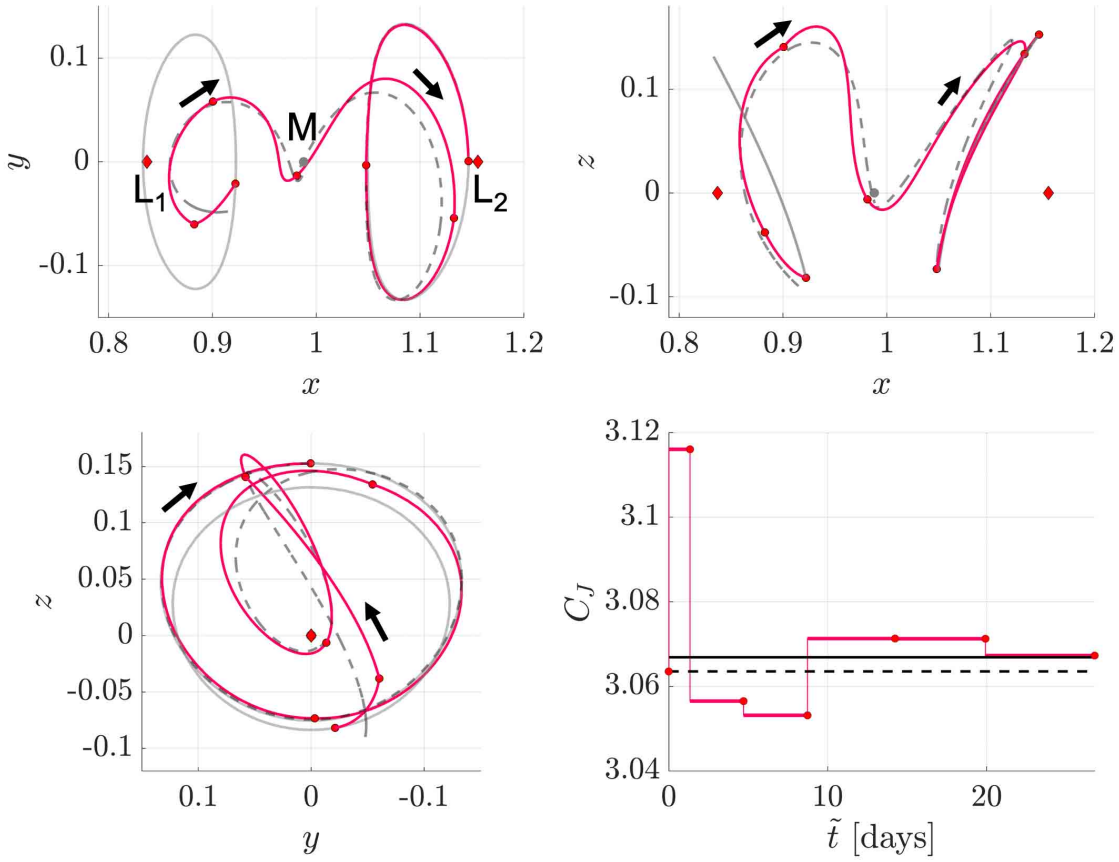

Figure 8.23: Continuous 26.80 day spatial transfer from an L_1 northern halo orbit to an L_2 northern halo orbit in the Earth-Moon CR3BP, computed from a primitive-based initial guess using $\boldsymbol{w}_{\mathbf{opt}} = [0.9, 0.1]$.

Table 8.4: Maneuver magnitudes for the transfers displayed in Figures 8.23 and 8.24 from an L_1 northern halo orbit to an L_2 northern halo orbit in the Earth-Moon CR3BP.

	Δv_i [m/s]							Total Δv [m/s]
Maneuver Index	1	2	3	4	5	6	7	-
$\boldsymbol{w}_{\mathbf{opt}} = [0.9, 0.1]$	182.74	148.05	79.25	31.74	22.83	21.46	4.87	490.94
$\boldsymbol{w}_{\mathbf{opt}} = [0.1, 0.9]$	54.01	53.20	70.58	31.49	50.66	34.14	41.09	335.17

8.2.3 Transitioning Transfers to a Point Mass Ephemeris Model

As discussed in Section 8.1.4, transitioning a trajectory from the CR3BP into a point mass ephemeris model demonstrates the value of using a lower fidelity dynamical model for preliminary

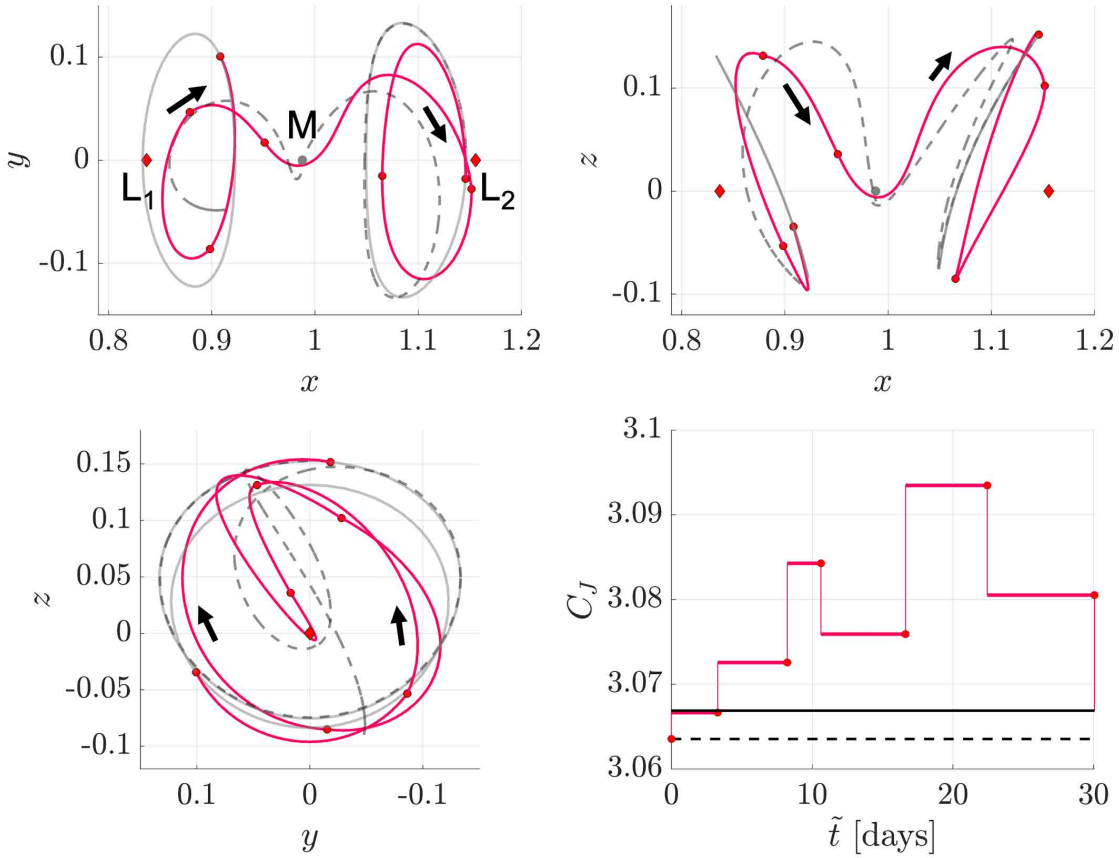

Figure 8.24: Continuous 30.06 day spatial transfer from an L_1 northern halo orbit to an L_2 northern halo orbit in the Earth-Moon CR3BP, computed at $\boldsymbol{w}_{\mathbf{opt}} = [0.1, 0.9]$ using the continuation procedure that varies the weights of the multi-objective optimization problem starting from the transfer displayed in Figure 8.23.

trajectory design. In this subsection, the same point mass ephemeris model including the Moon, Earth, and Sun is used. Furthermore, the reference epoch is specified as January 1, 2023, at 00:00:00.000 UTC and the exact same process used in the Lyapunov case is leveraged for recovering transfers between the selected northern halo orbits in a Moon-Earth-Sun point mass ephemeris model.

The transition procedure is applied to Transfers 2 and 8 displayed in Figure 8.21 for the L_1 to L_2 northern halo orbit transfer design scenario. Figures 8.26a and 8.26b display Transfer 2 com-

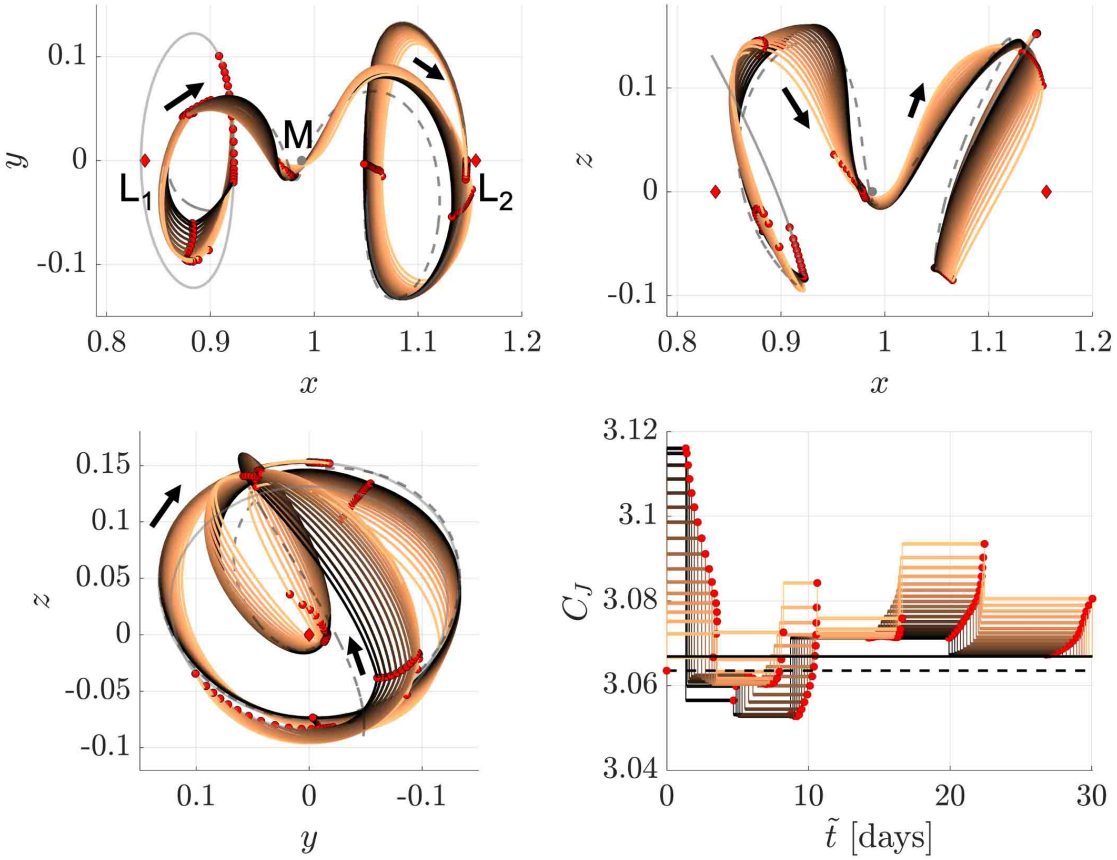

Figure 8.25: Evolution of the geometry and TOF across transfers in the local vicinity of Transfer 2 from Figure 8.21, computed using the continuation procedure that varies the weights of the multi-objective optimization problem.

puted in the Earth-Moon CR3BP (dashed black) with respect to the resulting solutions computed in a Moon-Earth-Sun point mass ephemeris model (blue) using $\boldsymbol{w}_{\mathbf{opt}} = [0.5, 0.5]$ and $\boldsymbol{w}_{\mathbf{opt}} = [0.1, 0.9]$, respectively. The initial epochs of the ephemeris solutions displayed in Figures 8.26a and 8.26b are December 30, 2022, at 19:53:32.074 UTC and December 30, 2022, at 11:16:57.730 UTC, respectively. Furthermore, the flight time is approximately 30.69 days and the total Δv is 323.14 m/s for the ephemeris solution displayed in Figure 8.26a; on the other hand, the flight time is approximately 30.40 days and the total Δv is 268.48 m/s for the ephemeris solution displayed in Figure 8.26b. Both ephemeris solutions resemble the transfer constructed in the CR3BP; however, the solution

computed using $\boldsymbol{w_{opt}} = [0.5, 0.5]$ more closely retains the geometry of the transfer as expected. The solution computed using $\boldsymbol{w_{opt}} = [0.1, 0.9]$ achieves a significant reduction in total Δv but only loosely captures the geometry of the initial L_1 northern halo orbit. Finally, Figure 8.27 displays Transfer 8 computed in the Earth-Moon CR3BP (dashed black) with respect to the resulting trajectory in the ephemeris model (blue). The initial epoch of the trajectory is December 30, 2022, at 20:15:52.791 UTC, the flight time is approximately 41.21 days, and the total Δv is 41.44 m/s. For this case, the transfer time increased by 0.75 days and the total Δv decreased by 2.62 m/s compared to the associated solution in the CR3BP. These transfers demonstrate the ability to recover spatial transfers in a point mass ephemeris model from initial guesses constructed in the CR3BP.

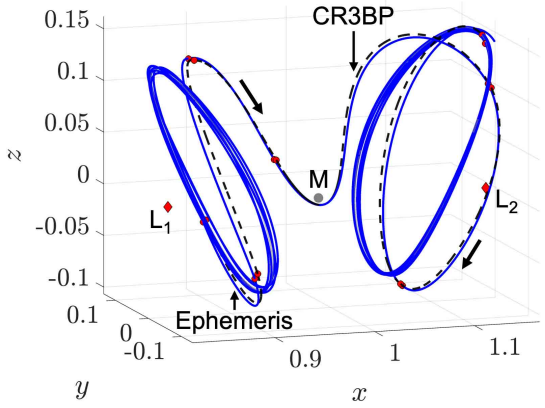

(a) 30.69 day transfer with an initial epoch of December 30, 2022, at 19:53:32.074 UTC, computed using $\boldsymbol{w_{opt}} = [0.5, 0.5]$.

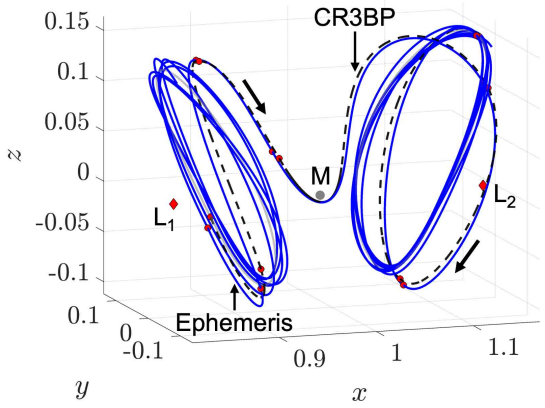

(b) 30.40 day transfer with an initial epoch of December 30, 2022, at 11:16:57.730 UTC, computed using $\boldsymbol{w_{opt}} = [0.1, 0.9]$.

Figure 8.26: Continuous transfers from an L_1 northern halo orbit to an L_2 northern halo orbit in a Moon-Earth-Sun point mass ephemeris model, computed from Transfer 2 displayed in Figure 8.21.

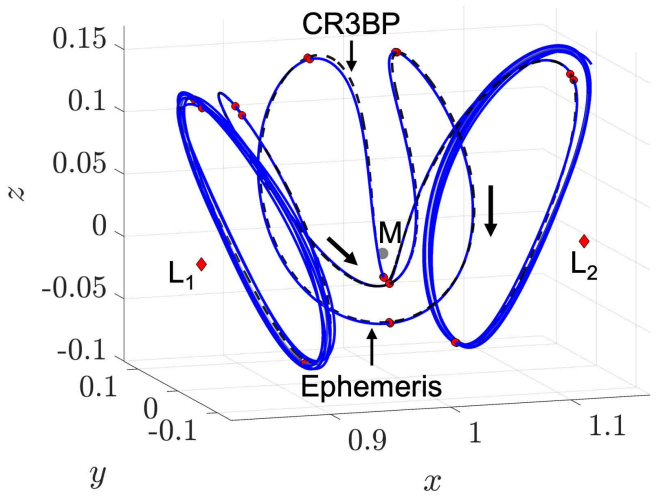

Figure 8.27: Continuous 41.21 day transfer from an L_1 northern halo orbit to an L_2 northern halo orbit in a Moon-Earth-Sun point mass ephemeris model with an initial epoch of December 30, 2022, at 20:15:52.791 UTC, computed from Transfer 8 displayed in Figure 8.21 using $\boldsymbol{w}_{\mathbf{opt}} = [0.1, 0.9]$.

8.3 Transfers from an L_2 Southern NRHO to DROs in the Earth-Moon System

8.3.1 Transfer Scenario Overview

Gateway is an orbital outpost that is planned to operate in an L_2 southern NRHO within cislunar space and expected to support NASA's Artemis program [114, 64]. The currently selected NRHO is in an approximate 9:2 synodic resonance with the orbit of the Moon around the Earth, i.e., 9 revolutions in the NRHO correspond to 2 revolutions of the Moon around the Earth. Therefore, the period of the L_2 southern NRHO selected for Gateway is approximately 6.56 days. The L_2 NRHOs in the Earth-Moon system are nearly stable and require low station-keeping costs over long time intervals; furthermore, these orbits exhibit favorable geometries for Earth communications and eclipse avoidance [64, 77, 19]. In addition, L_2 southern NRHOs provide long communication windows with regions located at the south pole of the Moon, which is desirable because regions at the south pole of the Moon are places of high interest for future science-driven lunar surface operations [34, 113]. Finally, the selection of an L_2 southern NRHO for Gateway provides a suitable

staging orbit for lunar surface access, explorations of cislunar space, and interplanetary transfers [114, 64, 115]. An Earth-Moon DRO is one potential target destination in cislunar space for demonstrating the transit capability of Gateway [71]. This future use of an L_2 southern NRHO as a staging orbit near the Moon motivates the application of the primitive-based initial guess construction framework to an L_2 southern NRHO to DRO transfer scenario in the Earth-Moon system.

Transfers are constructed from an L_2 southern NRHO to two different DROs in the Earth-Moon CR3BP with impulsive maneuvers. To select the initial orbit as well as the target orbits, motion primitives are first generated to summarize the L_2 southern halo orbit family and the DRO family in the Earth-Moon CR3BP using the motion primitive construction process presented in Section 6.2. A total of 9 and 8 primitives are generated to summarize the L_2 southern halo orbit family and the DRO family, respectively. One of the primitives extracted from the L_2 southern halo orbit family corresponds to an L_2 southern NRHO that is near the 9:2 resonant NRHO selected for Gateway; therefore, this primitive is selected as the initial orbit in the transfer design scenario. Furthermore, two DRO primitives of significantly different sizes and energies are arbitrarily selected as the candidate target orbits. The properties of the selected orbits are listed in Tables 8.5 and 8.6. Figures 8.28 and 8.29 display the initial L_2 southern NRHO and the target DROs, respectively, with respect to the other primitives constructed along each periodic orbit family. The selected primitives are denoted in bold and the region of the configuration space spanned by the associated small set of representative trajectories for each primitive is depicted as a transparent surface. Finally, Figure 8.30 displays the configuration of the initial L_2 southern NRHO and the target DROs in $\mathcal{R}$.

This scenario presents a challenging transfer design problem for a few different reasons. As indicated in Tables 8.5 and 8.6, there is a large C_J difference between the initial orbit and each target orbit, the L_2 southern NRHO is nearly stable and therefore motion along its associated unstable manifold is slow to depart the orbit, and the target DROs do not possess stable and unstable manifolds. Furthermore, as evident in Figure 8.30, a large plane change is required to transfer from the L_2 southern NRHO to either planar DRO. As a result, this challenging scenario

Table 8.5: Properties of the initial L_2 southern NRHO selected for the NRHO to DRO transfer design scenario in the Earth-Moon CR3BP.

	Initial Orbit
Orbit Type	L_2 southern NRHO
C_J	3.044579150514986
T_{PO}	1.537096058488171 ($\approx$ 6.67 days)
s_1	-2.751814321511511
s_2	1.324781749745638
Min. Perilune Distance	3560.42 km

Table 8.6: Properties of the target DROs selected for the NRHO to DRO transfer design scenario in the Earth-Moon CR3BP.

	Target Orbit #1	Target Orbit #2
Orbit Type	DRO	DRO
C_J	2.910973011179179	2.765366500505031
T_{PO}	3.764504057199413 ($\approx$ 16.35 days)	5.796982607490156 ($\approx$ 25.17 days)
s_1	-1.520428870861199	-0.251101993988295
s_2	0.454523709953394	1.899399734056896
Min. Perilune Distance	81453.39 km	164326.42 km

further demonstrates the utility of the presented motion primitive framework for complex trajectory design in a multi-body system.

The high-level itinerary graph constructed for the NRHO to DRO transfer design scenario possesses a larger variety of dynamical structures than the Lyapunov and northern halo orbit transfer design scenarios explored in Sections 8.1 and 8.2. The high-level itinerary graph design is displayed in Figure 8.31. Table 8.7 summarizes the sets of motion primitives constructed in the motion primitive library for the design scenario; the $p : q$ nomenclature for referring to resonant orbits indicates that p revolutions of the resonant orbit are completed around the Earth in the approximate time it takes for the Moon to complete q revolutions around the Earth [43, 108]. In Figure 8.31, the periodic orbit primitive sets are displayed next to their corresponding subgraph icons while the general structure of the hyperbolic invariant manifolds are depicted next to their corresponding subgraph icons. The entire set of motion primitives generated to summarize arcs

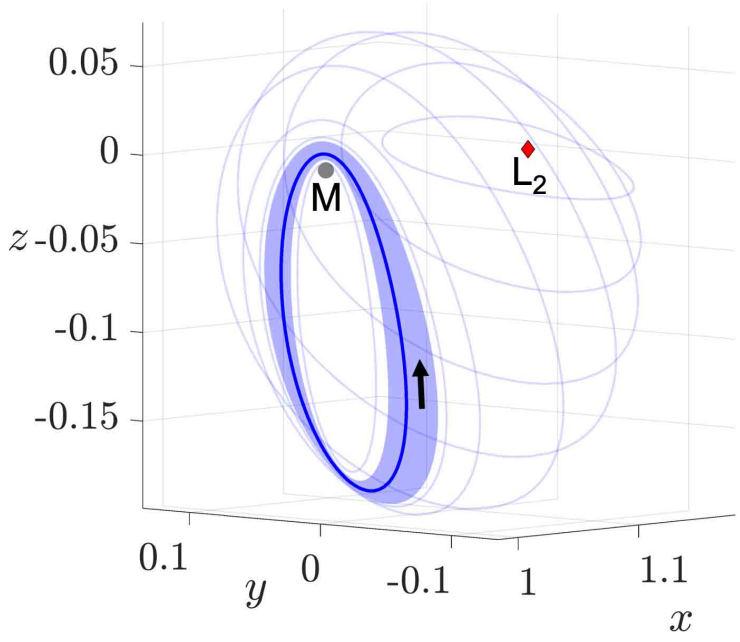

Figure 8.28: Motion primitives constructed for the L_2 southern halo orbit family in the Earth-Moon CR3BP with the initial L_2 southern NRHO selected for the NRHO to DRO transfer design scenario denoted in bold.

along each stable and unstable manifold included in the motion primitive graph is provided in Appendix A.

A diverse set of potential avenues for connecting the selected initial and target orbits are available given the high-level itinerary graph design displayed in Figure 8.31. This graph design exhibits a more complex structure than the graphs constructed for the Lyapunov and northern halo orbit transfer design scenarios. The initial L_2 southern NRHO is contained within the "L_2 SHalos" subgraph and the target DROs are contained within the "DROs" subgraph. Both of these subgraphs are internally connected and therefore allow multiple periodic orbits from each family to be chained together within a sequence. Paths between the initial orbit and the target orbits may also leverage primitives generated along an unstable manifold of the initial L_2 southern NRHO; an unstable manifold of an L_2 southern halo orbit that traverses the exterior region of the system away from the Earth and Moon; a stable manifold of an L_2 southern halo orbit near L_2; a stable

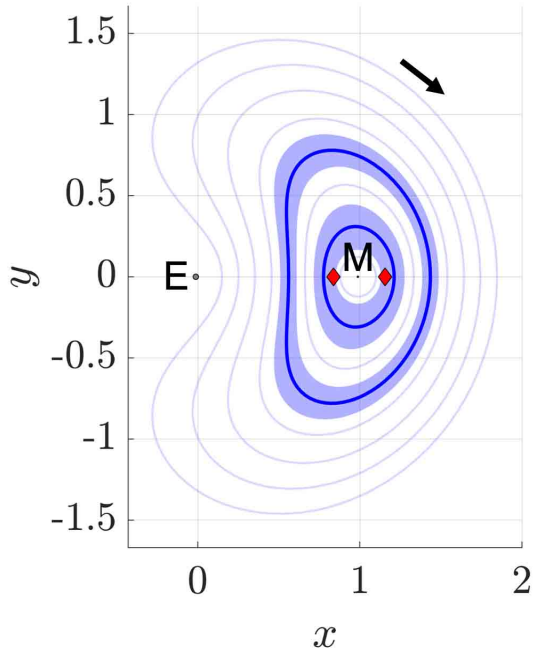

Figure 8.29: Motion primitives constructed for the DRO family in the Earth-Moon CR3BP with the target DROs selected for the NRHO to DRO transfer design scenario denoted in bold.

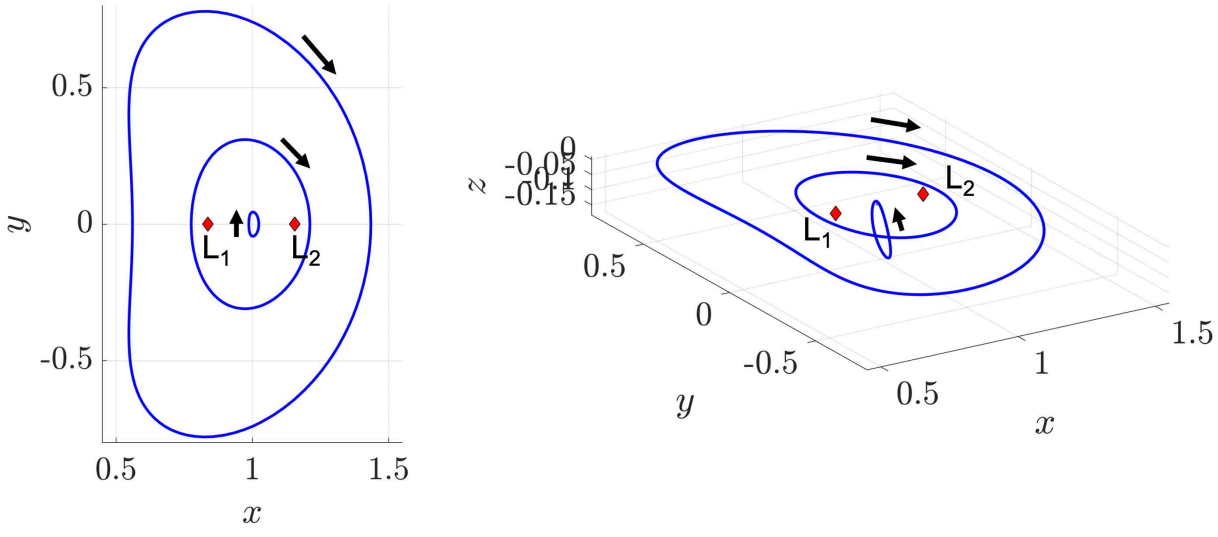

Figure 8.30: Configuration of the initial L_2 southern NRHO and the target DROs in $\mathcal{R}$ for the NRHO to DRO transfer design scenario in the Earth-Moon CR3BP.

Table 8.7: Motion primitives in the library for the NRHO to DRO transfer design scenario in the Earth-Moon CR3BP.

Fundamental Solution	Number of Primitives	Approx. C_J
L_2 southern halo orbits (L_2 SHalos)	9	[3.0152,3.1521]
1:2 resonant orbits (1:2)	10	[1.2692,2.8995]
1:3 resonant orbits (1:3)	12	[1.1338,2.8404]
3:4 resonant orbits (3:4)	10	[2.1410,2.9537]
4:3 resonant orbits (4:3)	12	[2.2422,3.0127]
Distant retrograde orbits (DROs)	8	[1.9138,3.0374]
L_2 southern NRHO unstable manifold (L_2 SNRHO UMani)	55	3.0446
L_2 southern halo orbit unstable manifold (L_2 SHalo UMani - Ext.)	11	3.0188
L_2 southern halo orbit stable manifold (L_2 SHalo SMani - Near L_2)	41	3.1250
L_1 northern halo orbit stable manifold (L_1 NHalo SMani - Near L_1)	118	3.1224

manifold of an L_1 northern halo orbit near L_1; and a variety of resonant orbits (1:2, 1:3, 3:4, and 4:3) that all exhibit retrograde motion in the lunar vicinity with respect to the Moon.

Despite the absence of hyperbolic invariant manifolds associated with the target DROs, the selected manifold structures and periodic orbit families guide motion towards the plane of the primaries and exhibit retrograde motion in the lunar vicinity with respect to the Moon. Furthermore, as indicated in Table 8.7, the sets of motion primitives included in the high-level itinerary graph provide a large range of C_J values relative to the C_J values of the desired initial and target orbits. Finally, in this section, the motion primitive graph is only searched for motion primitive sequences between the initial L_2 southern NRHO and the target DROs displayed in Figure 8.30; however, this graph structure provides a discrete representation of the solution space that could be leveraged to design a larger variety of transfers or it could be further expanded with additional dynamical structures across various energy levels. For example, transfers may be constructed between distinct L_2 southern halo orbits, from an L_2 southern halo orbit to intermediate resonant orbits, from a variety of L_2 southern halo orbits to a variety of DROs, and so forth. This demonstrates the value

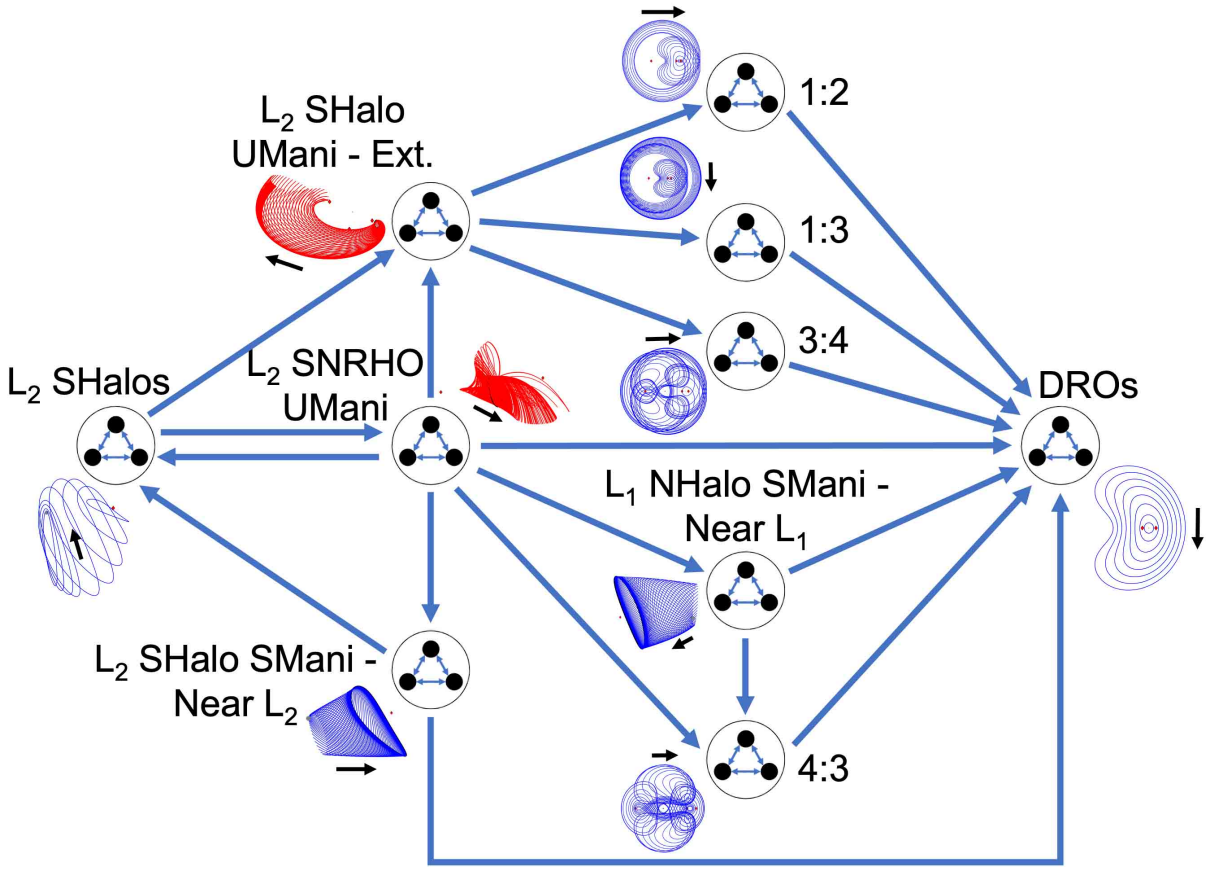

Figure 8.31: High-level itinerary graph developed for a NRHO to DRO transfer design scenario in the Earth-Moon CR3BP.

and versatility of leveraging a motion primitive graph to explore the transfer design space in a multi-body system.

A motion primitive graph is constructed based on the high-level itinerary graph design displayed in Figure 8.31. The following configuration parameters are specified to construct the motion primitive graph: $k_{\text{nn}} = 8$, $\alpha_{\text{pos}} = 10$, and $\alpha_{\text{vel}} = 1$. As specified in the previous design scenarios, each periodic orbit primitive included in the motion primitive graph is discretized into 50 states equally spaced in arclength while each manifold arc primitive is discretized into apses with respect to the Moon as well as its boundary states. However, there is one exception due to the larger variety of dynamical structures included in this scenario. Each manifold arc primitive in the "L_2 SHalo UMani - Ext." subgraph is discretized into apses with respect to the Earth as well as its

boundary states because these arcs leave the vicinity of the Moon and traverse exterior regions of the system. The default measure types specified in Section 7.3 are then used to construct each subgraph as well as the connections between each subgraph. As a reminder, Measure 1 is used to construct the internal edges within a subgraph, Measure 2 is used to construct the external edges between two subgraphs when the source primitive is a periodic orbit and the target primitive is a manifold arc, and Measure 3 is used to construct the external edges between two subgraphs in all other cases. The only design change made in this transfer design scenario is to use Measure 3 instead of Measure 1 when constructing the internal edges for each subgraph comprised of periodic orbits. Finally, the set of representative trajectories associated with each motion primitive is incorporated into the edge weight computations and the average edge weight is used to evaluate the quality of each primitive sequence. The computation time for constructing the motion primitive graph in this scenario is on the order of 10^0 minutes using an iMac with a 3GHz 6-Core Intel Core i5 processor. Using the resulting motion primitive graph, initial guesses are generated to construct transfers between the desired initial L_2 southern NRHO and the target DROs.

8.3.2 Constructing Transfers from an L_2 Southern NRHO to a DRO at $C_J \approx 2.9110$

The motion primitive graph constructed for the NRHO to DRO transfer design scenario is searched to produce unique sequences of four, five, and six primitives that each form an initial guess for a transfer from the initial L_2 southern NRHO described in Table 8.5 to the first target DRO described in Table 8.6. There are a total of 568, 17,073, and 373,315 primitive sequences from the selected initial node to the selected target node in the graph consisting of four, five, and six primitives, respectively. However, using the filtering process presented in Section 7.4, the $Q = 15$ top-ranked sequences that begin with a unique primitive are examined for each path length. As in the previous design scenarios, the sets of representative trajectories associated with the initial orbit and the target orbit are not included in the refinement process presented in Section 7.5 because the exact orbits are desired. This approach produces 45 unique primitive sequences that are each

refined to produce an initial guess.

Each initial guess is corrected with several unconstrained impulsive maneuvers distributed along the transfers using the same maneuver placement scheme as described for the Lyapunov and northern halo orbit transfer design scenarios. Due to the longer flight times associated with the initial guesses for this scenario, the bounds on each Δt_j^i variable are adjusted to $[10^{-5}, 5.0]$. In addition, it is observed that correcting an initial guess using Newton's method first and then optimizing the solution using IPOPT may facilitate more robust convergence in some cases [87]. This behavior is primarily observed for transfers that depart the lunar vicinity and are comprised of trajectory segments that span large regions of the configuration space, which may present numerical challenges in the geometric term of the objective function. Further investigation into this behavior is warranted; however, Newton's method may be used to compute an initial continuous solution from a primitive-based initial guess which is then used to compute a locally optimal solution with $\boldsymbol{w_{opt}} = [0.9, 0.1]$ in the optimization procedure. Using the corrections procedure, 43 of the 45 primitive-based initial guesses are successfully generated with $\boldsymbol{w_{opt}} = [0.9, 0.1]$ to produce continuous transfers from the desired initial L_2 southern NRHO to the target DRO at $C_J \approx 2.9110$. However, one of the corrected transfers impacts a spherical approximation of the Moon. The natural parameter continuation procedure is then used to gradually vary the weights of the multi-objective optimization problem described in Section 7.6 from $\boldsymbol{w_1} = [0.9, 0.1]$ to $\boldsymbol{w_2} = [0.1, 0.9]$. Following this process, only 40 of these transfers are successfully corrected using $\boldsymbol{w_{opt}} = \boldsymbol{w_2}$.

An initial summary of the transfers that solve the multi-objective optimization problem with each value of $\boldsymbol{w_{opt}}$ is presented. In Figure 8.32a, the total Δv of each of the 43 transfers corrected using $\boldsymbol{w_{opt}} = \boldsymbol{w_1}$ is displayed with respect to the normalized average potential for sequential composability, $\Delta\check{q}_{\text{avg}}$, of its initial guess; this figure uses the same configuration as Figures 8.3 and 8.19. In Figure 8.32b, however, this information is presented for the transfers that are corrected using $\boldsymbol{w_{opt}} = \boldsymbol{w_2}$ to prioritize minimizing maneuver requirements. The required total Δv ranges from 488.47 m/s to 2164.01 m/s for the transfers computed using $\boldsymbol{w_{opt}} = \boldsymbol{w_1}$ and from 291.90 m/s to 736.12 m/s for the transfers computed using $\boldsymbol{w_{opt}} = \boldsymbol{w_2}$, excluding the transfers that did

not converge. As observed in the previous design scenarios, there is a gradual increase in total Δv requirements with increasing values of $\Delta\check{q}_{\text{avg}}$ for the solutions computed using $\boldsymbol{w_{opt}} = \boldsymbol{w_1}$; however, the transfers computed using $\boldsymbol{w_{opt}} = \boldsymbol{w_2}$ no longer exhibit a clear direct correlation between total Δv requirements and $\Delta\check{q}_{\text{avg}}$. Finally, significant reductions in total Δv requirements are observed for each computed transfer throughout the continuation procedure.

The 40 corrected transfers that prioritize minimizing maneuver requirements are grouped based on geometry to extract the distinct types of transfers that connect the initial L_2 southern NRHO and the target DRO in the Earth-Moon CR3BP. When applying the k-NN graph approach described in Section 7.7, $k_{\text{nn}} = 4$ and $l_{\Delta\text{TOF}} = 6.5$ days are selected empirically and produce 25 groups of geometrically distinct transfers. The value of $l_{\Delta\text{TOF}}$ is selected to distinguish between transfers that share similar transfer geometries yet exhibit a distinct number of revolutions near the initial NRHO, which has a period of approximately 6.67 days. The resulting properties of each

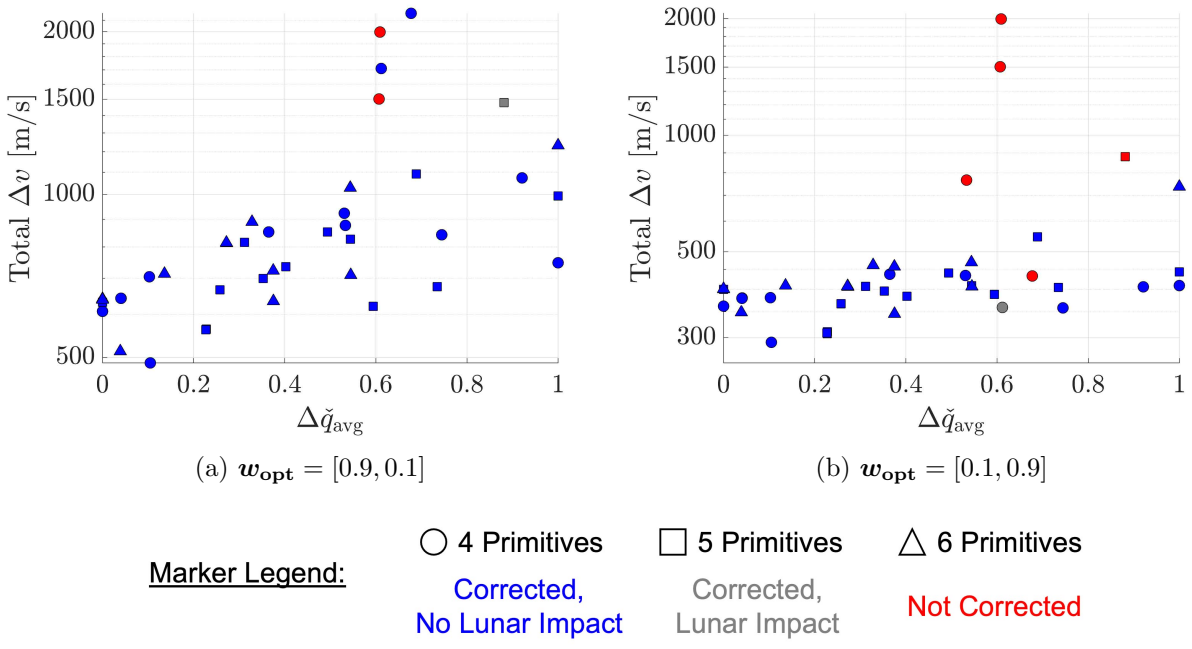

(a) $\boldsymbol{w_{opt}} = [0.9, 0.1]$ (b) $\boldsymbol{w_{opt}} = [0.1, 0.9]$

Figure 8.32: Total Δv of transfers computed from an L_2 southern NRHO to a DRO in the Earth-Moon CR3BP as a function of $\Delta\check{q}_{\text{avg}}$.

transfer are plotted in Figure 8.33 using the same configuration as Figures 8.4 and 8.20 where the minimum Δv solution in each group is circled and numbered. For visual clarity, Figures 8.33b and 8.33c provide zoomed in views of different regions of the TOF-Δv trade space. These transfers require flight times ranging from 23.92 days to 235.75 days and total Δv requirements ranging from 291.90 m/s to 736.12 m/s when placing more emphasis on recovering maneuver-efficient transfers. Figure 8.33d displays the evolution of the flight time and total Δv for each of the transfers circled in Figure 8.33a as the weights of the multi-objective optimization problem are varied. The evolution of these transfers exhibit significant reductions in total Δv and relatively small variations in TOF. Finally, there is a clear separation in the TOF-Δv trade space between transfers possessing flight times less than 100 days and transfers possessing flight times greater than 100 days.

The minimum Δv transfers for groups 1-16 are visualized in the configuration space of the Earth-Moon CR3BP; specifically, Figures 8.34 and 8.35 display each transfer as a projection onto the xy-plane of $\mathcal{R}$. In these figures, each corrected transfer loosely resembles its associated primitive-based initial guess (dashed gray) but with significant deviations due to large velocity discontinuities present in the original primitive-based initial guesses. A similar behavior is observed and discussed for the Lyapunov and northern halo orbit transfer design scenarios during the natural parameter continuation procedure. In addition, Table 8.8 lists the TOF and total Δv for each minimum Δv transfer.

Overall, Transfers 1-16 provide a variety of distinct geometries with flight times less than 100 days that depart the initial L_2 southern NRHO and arrive onto the target DRO. These transfers are constructed from initial guesses that leverage a variety of primitives along the manifolds and intermediate periodic orbits included in the motion primitive graph. Transfers 1-13 remain close to the Moon, L_1, and L_2 while Transfers 14-16 traverse slightly away from this region. Despite these differences, all of these transfers provide design options that remain relatively close to the Moon. As displayed in Figure 8.34, Transfers 2 and 3 exhibit similar geometries that depart the vicinity of the Moon towards the DRO; however, Transfer 3 possesses additional revolutions around the Moon near the initial NRHO before transferring towards the DRO. This behavior is also evident in

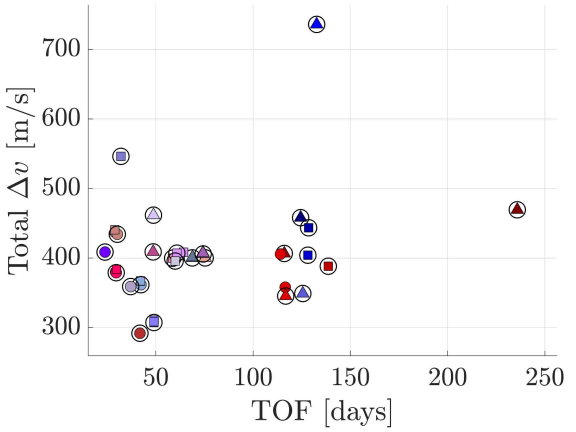

(a) Transfers computed using $\boldsymbol{w_{opt}} = [0.1, 0.9]$.

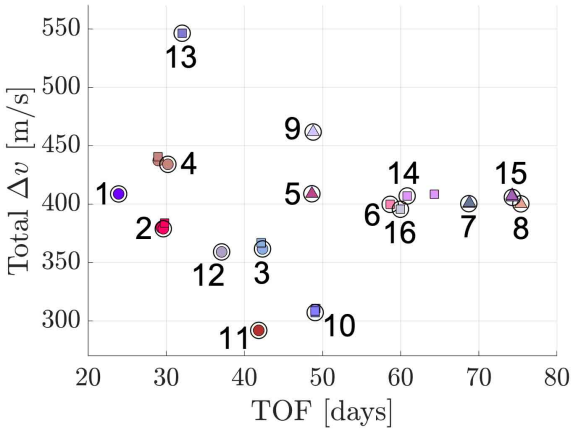

(b) Transfer groups 1-16 computed using $\boldsymbol{w_{opt}} = [0.1, 0.9]$.

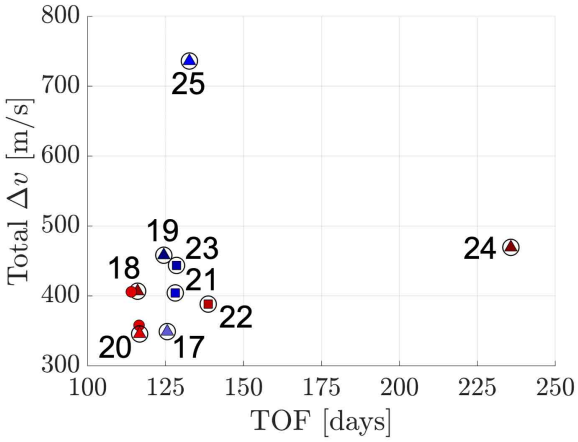

(c) Transfer groups 17-25 computed using $\boldsymbol{w_{opt}} = [0.1, 0.9]$.

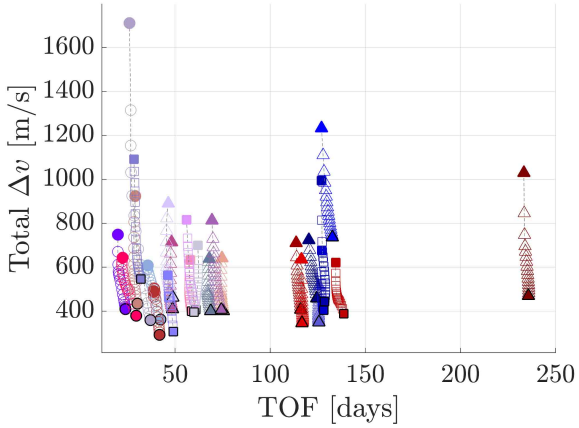

(d) Minimum Δv solutions transitioned from $\boldsymbol{w_{opt}} = [0.9, 0.1]$ to $\boldsymbol{w_{opt}} = [0.1, 0.9]$.

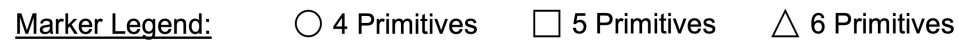

Figure 8.33: Total Δv and TOF of transfers computed from an L_2 southern NRHO to a DRO in the Earth-Moon CR3BP, where geometrically similar transfers are denoted in the same color and the minimum Δv solution for each transfer geometry is highlighted.

the TOF-Δv trade space, as displayed in Figure 8.33b for Transfers 2 and 3. A similar observation holds for Transfers 5-8, Transfers 10-11, and Transfers 14-15: the identified transfers within each set admit similar total Δv requirements and overall transfer geometries but possess a distinct number

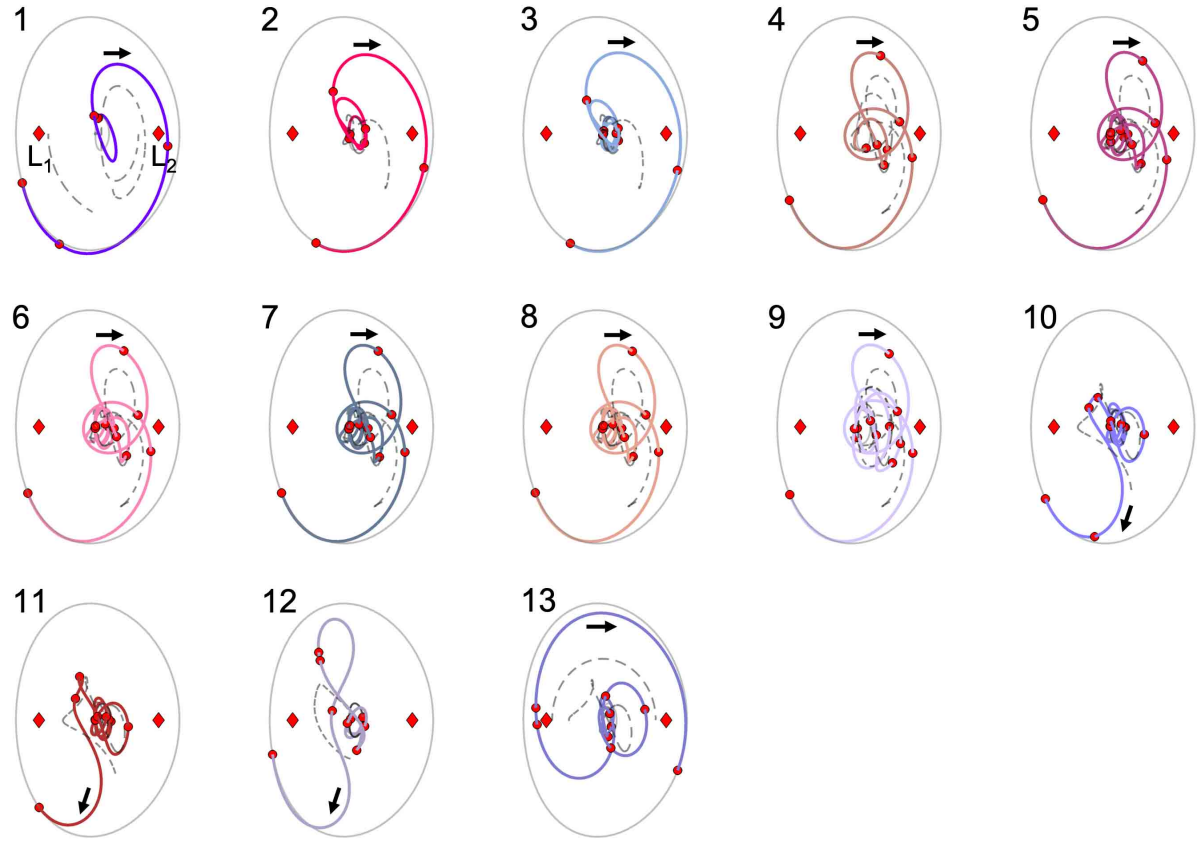

Figure 8.34: Transfers 1-13 (from Figure 8.33) with distinct geometries computed from primitive-based initial guesses between an L_2 southern NRHO and a DRO in the Earth-Moon CR3BP, displayed as a projection onto the xy-plane of $\mathcal{R}$.

of revolutions near the initial NRHO. Trajectories along the unstable manifold associated with the initial L_2 southern NRHO are slow to depart from the orbit due to its stability properties. Therefore, a variety of similar transfer geometries are identified in this design space exploration that only differ based on completed number of revolutions around the Moon in the vicinity of the initial NRHO. This result is valuable in the trajectory design process because it provides a human analyst with insight into the flexibility of the departure conditions from the initial orbit relative to the resulting transfer geometry.

Transfer 11 displayed in Figure 8.34 is examined in more detail because it requires the lowest total Δv among all of the transfers computed for this design scenario. Figures 8.36-8.38 display

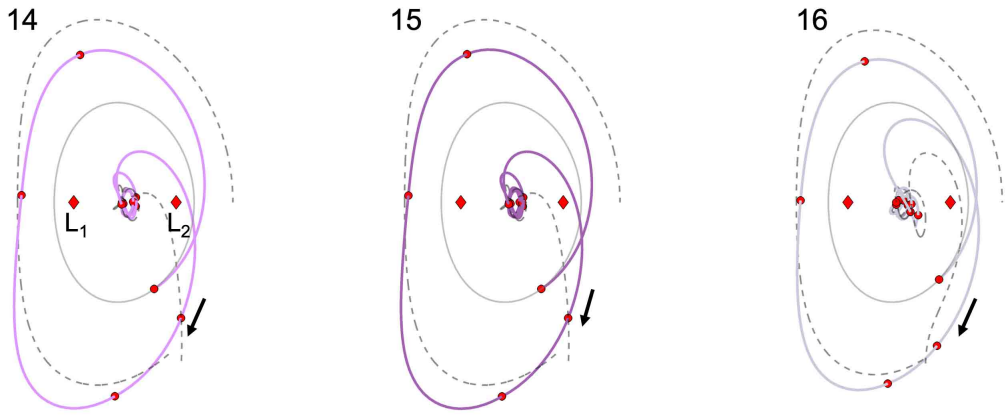

Figure 8.35: Transfers 14-16 (from Figure 8.33) with distinct geometries computed from primitive-based initial guesses between an L_2 southern NRHO and a DRO in the Earth-Moon CR3BP, displayed as a projection onto the xy-plane of $\mathcal{R}$.

Table 8.8: Total Δv and TOF of Transfers 1-16 (from Figure 8.33) computed from primitive-based initial guesses between an L_2 southern NRHO and a DRO in the Earth-Moon CR3BP.

Transfer Index	TOF [days]	Total Δv [m/s]
1	23.92	408.73
2	29.62	379.00
3	42.32	361.69
4	30.22	434.17
5	48.65	408.90
6	58.67	399.80
7	68.73	400.37
8	75.39	400.30
9	48.80	461.71
10	49.07	307.20
11	41.85	291.90
12	37.10	359.09
13	32.05	546.31
14	60.84	407.01
15	74.30	405.83
16	59.97	395.67

the evolution of Transfer 11 throughout the natural parameter continuation process using the same format as the northern halo orbit transfer design analysis. The solution computed using $\boldsymbol{w}_{\mathbf{opt}} = [0.9, 0.1]$ is displayed in Figure 8.36 and closely resembles the primitive-based initial guess.

The primitive-based initial guess used to construct this transfer only leverages primitives along the unstable manifold associated with the initial L_2 southern NRHO as evident in the evolution of C_J along the corrected transfer. As displayed in Figure 8.36, the primary change in C_J is achieved through the final maneuver used to insert onto the DRO and the total Δv requirement is 488.47 m/s. The solution computed using $\boldsymbol{w_{opt}} = [0.1, 0.9]$ is then displayed in Figure 8.37 after applying the continuation procedure and requires a total Δv of 291.90 m/s. As observed in previous results, the geometry of the transfer evolves throughout the continuation process and the final computed solution observes a smoother insertion onto the target DRO. This smoother insertion is evident

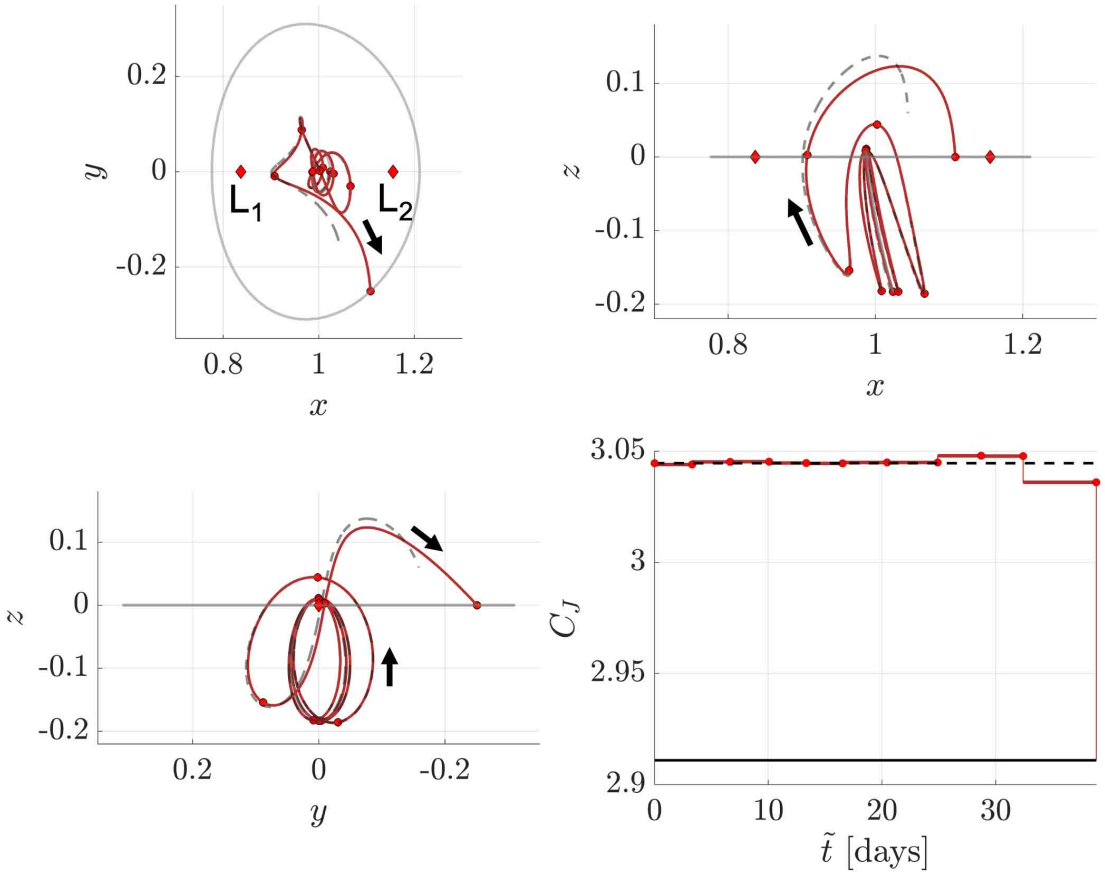

Figure 8.36: Continuous 38.85 day spatial transfer from an L_2 southern NRHO to a DRO in the Earth-Moon CR3BP, computed from a primitive-based initial guess using $\boldsymbol{w_{opt}} = [0.9, 0.1]$.

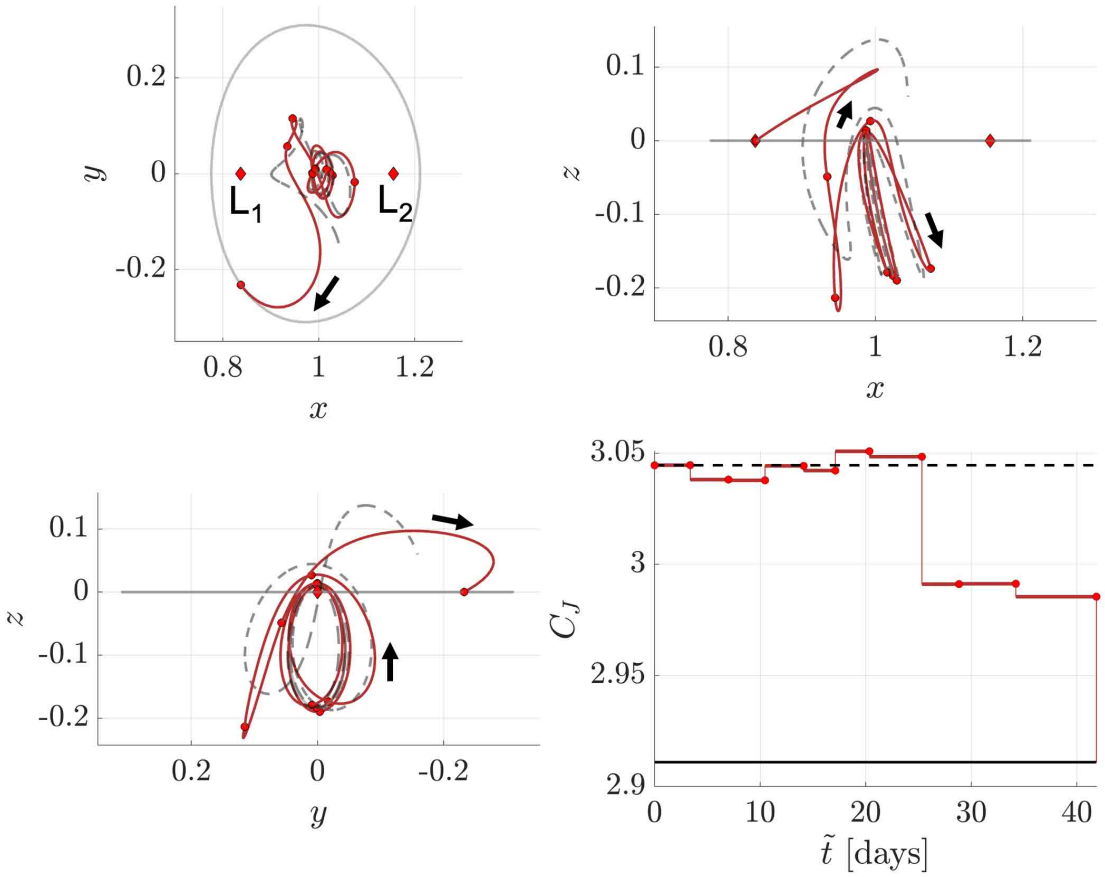

Figure 8.37: Continuous 41.85 day spatial transfer from an L_2 southern NRHO to a DRO in the Earth-Moon CR3BP, computed at $\boldsymbol{w}_{\mathbf{opt}} = [0.1, 0.9]$ using the continuation procedure that varies the weights of the multi-objective optimization problem starting from the transfer displayed in Figure 8.36.

in the evolution of C_J along the corrected transfer displayed in Figure 8.37 because it exhibits an intermediate step in C_J between the initial and target values of C_J. However, the transfer displayed in Figure 8.37 varies more significantly from the geometry of the primitive-based initial guess as expected. The evolution of the transfers during the continuation process are displayed in Figure 8.38 and exhibit a relatively smooth evolution in geometry towards a more maneuver-efficient solution.

The remaining minimum Δv transfers associated with groups 17-25 are visualized in the configuration space of the Earth-Moon CR3BP; specifically, Figure 8.39 displays each transfer as

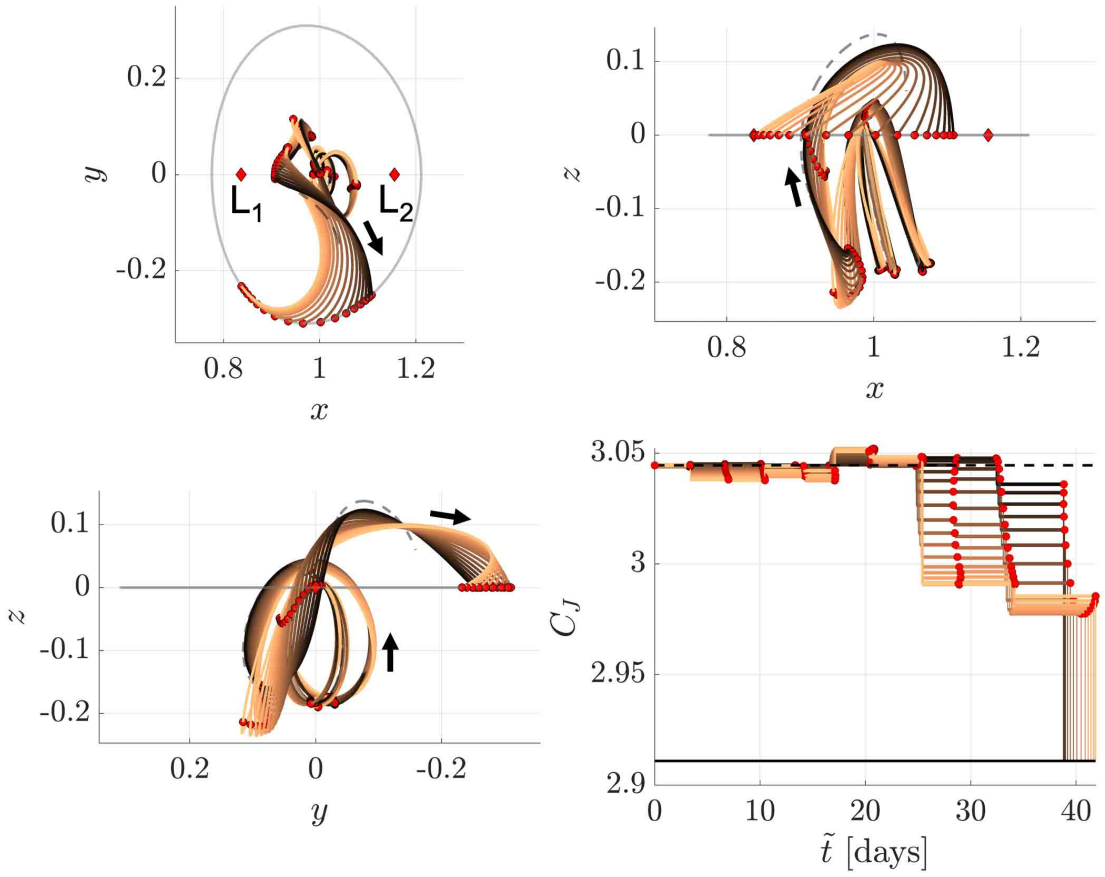

Figure 8.38: Evolution of the geometry and TOF across transfers in the local vicinity of Transfer 11 from Figure 8.34, computed using the continuation procedure that varies the weights of the multi-objective optimization problem.

a projection onto the xy-plane of $\mathcal{R}$ and Figure 8.40 provides a zoomed in view of each transfer in the vicinity of the Moon. In these figures, each corrected transfer geometrically resembles its associated primitive-based initial guess (dashed gray) with less significant deviations than Transfers 1-16. In addition, Table 8.9 lists the TOF and total Δv for each minimum Δv transfer. Each of these transfers has a flight time greater than 100 days and presents a geometry that departs the vicinity of the Moon and circumnavigates the system before returning to the lunar vicinity and inserting onto the target DRO.

Transfers 17-24 each leverage trajectory segments along a 3:4 resonant orbit primitive while

Transfer 25 leverages a trajectory segment along a 1:3 resonant orbit primitive. During the transfer grouping process, Transfers 17 and 19 are originally grouped together due to their global similarities in geometry and similar flight times. However, as displayed in Figure 8.40, Transfers 17 and 19 exhibit significantly different departure geometries from the initial NRHO and arrival geometries onto the target DRO. To visualize Transfer 17 in more detail, Figures 8.41-8.43 display the evolution of Transfer 17 throughout the natural parameter continuation process using the same format as Transfer 11 earlier in this subsection. Consequently, Transfers 17 and 19 are manually separated and placed into separate transfer geometry groups. This result demonstrates a drawback of the transfer geometry grouping procedure presented in Section 7.7. The global similarities between Transfers 17 and 19 dominate the modified Hausdorff distance computation and do not effectively capture their geometric differences near the Moon. Furthermore, the $l_{\Delta \text{TOF}}$ parameter is ineffective in this case because both transfers possess similar flight times. Despite this need for Transfers 17 and 19 to be manually separated, Transfers 17-25 provide a variety of distinct geometries that leverage primitives generated from the unstable manifolds, southern halo orbits, resonant orbits, and DROs included in the motion primitive graph for the transfer design scenario.

Previous research investigations have also explored the transfer design space between an L_2 southern NRHO and a DRO in the Earth-Moon CR3BP using different design methods. Some investigations have focused on the construction of impulsive transfers while others have focused on

Table 8.9: Total Δv and TOF of Transfers 17-25 (from Figure 8.33) computed from primitive-based initial guesses between an L_2 southern NRHO and a DRO in the Earth-Moon CR3BP.

Transfer Index	TOF [days]	Total Δv [m/s]
17	125.58	348.96
18	116.06	406.68
19	124.45	458.10
20	116.72	345.46
21	128.16	404.17
22	138.69	388.17
23	128.53	443.48
24	235.75	469.48
25	132.70	736.12

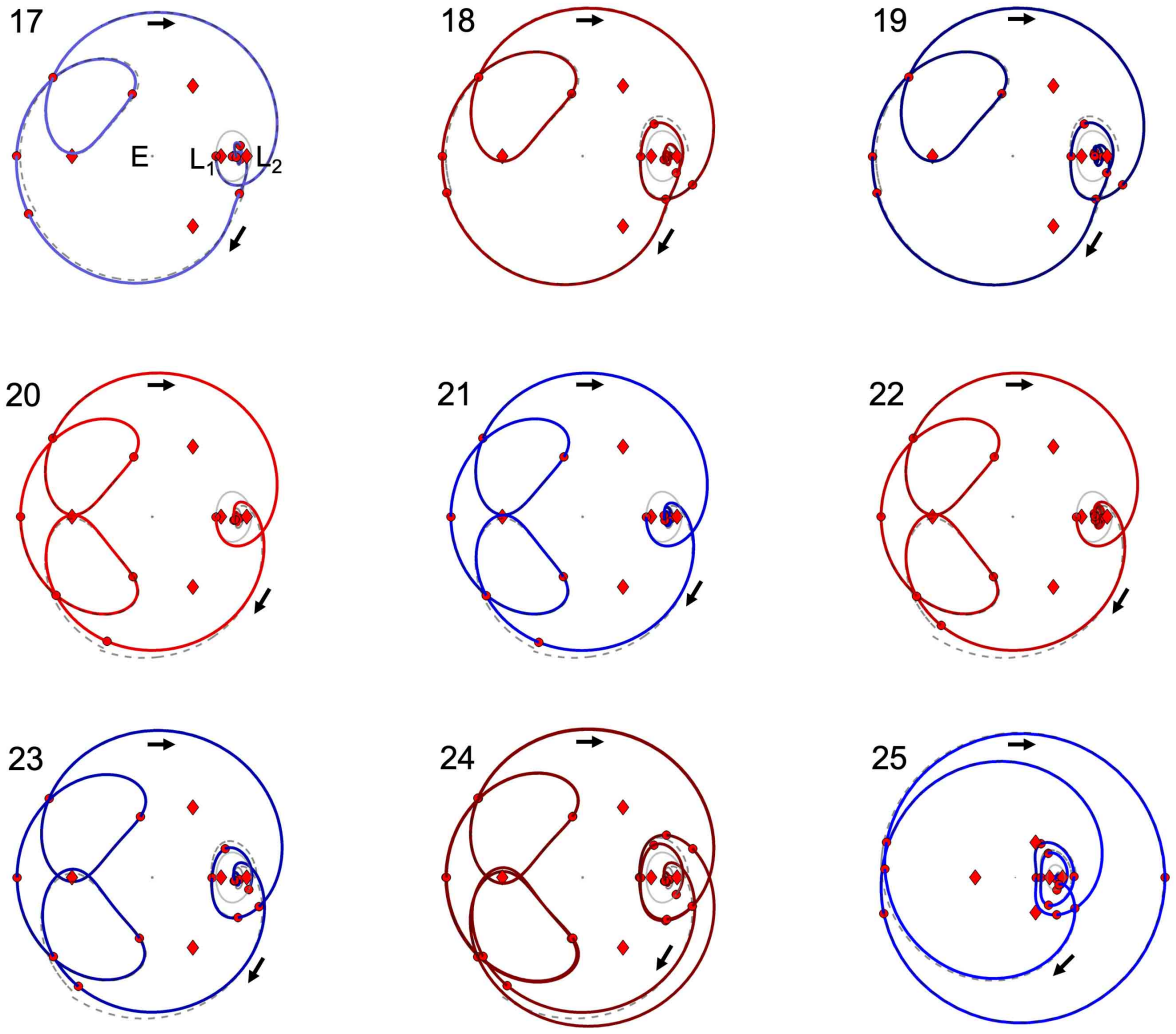

Figure 8.39: Transfers 17-25 (from Figure 8.33) with distinct geometries computed from primitive-based initial guesses between an L_2 southern NRHO and a DRO in the Earth-Moon CR3BP, displayed as a projection onto the xy-plane of $\mathcal{R}$.

the construction of low-thrust transfers [73, 121, 70, 87]. The low-thrust transfers often leverage similar fundamental dynamical structures as the impulsive solutions but exhibit more gradual approaches into the target DRO with a large number of revolutions around the Moon [70, 87]. Furthermore, transfers for this design scenario are often classified as either interior or exterior transfers where the exterior transfers often leverage arcs resembling resonant periodic orbits as presented in this subsection. As a comparison with a previous result, Muralidharan and Howell

[73] computed a set of 6 transfers between an L_2 southern NRHO and a DRO with total Δv values ranging from 142.88 m/s to 372.23 m/s and total flight times ranging from 51.39 days to 167.15 days. Similar ranges of total Δv and total flight time are recovered in this investigation; however, the geometry of the transfers recovered in this investigation are distinctly different than the transfers recovered by Muralidharan and Howell [73]. In their investigation, initial guesses are constructed from sets of trajectories generated by applying impulses to depart from the initial orbit and arrive onto the target orbit based on computed maximum stretching directions. Therefore, the resulting departure and arrival trajectories exhibit fundamentally different types of motion than the

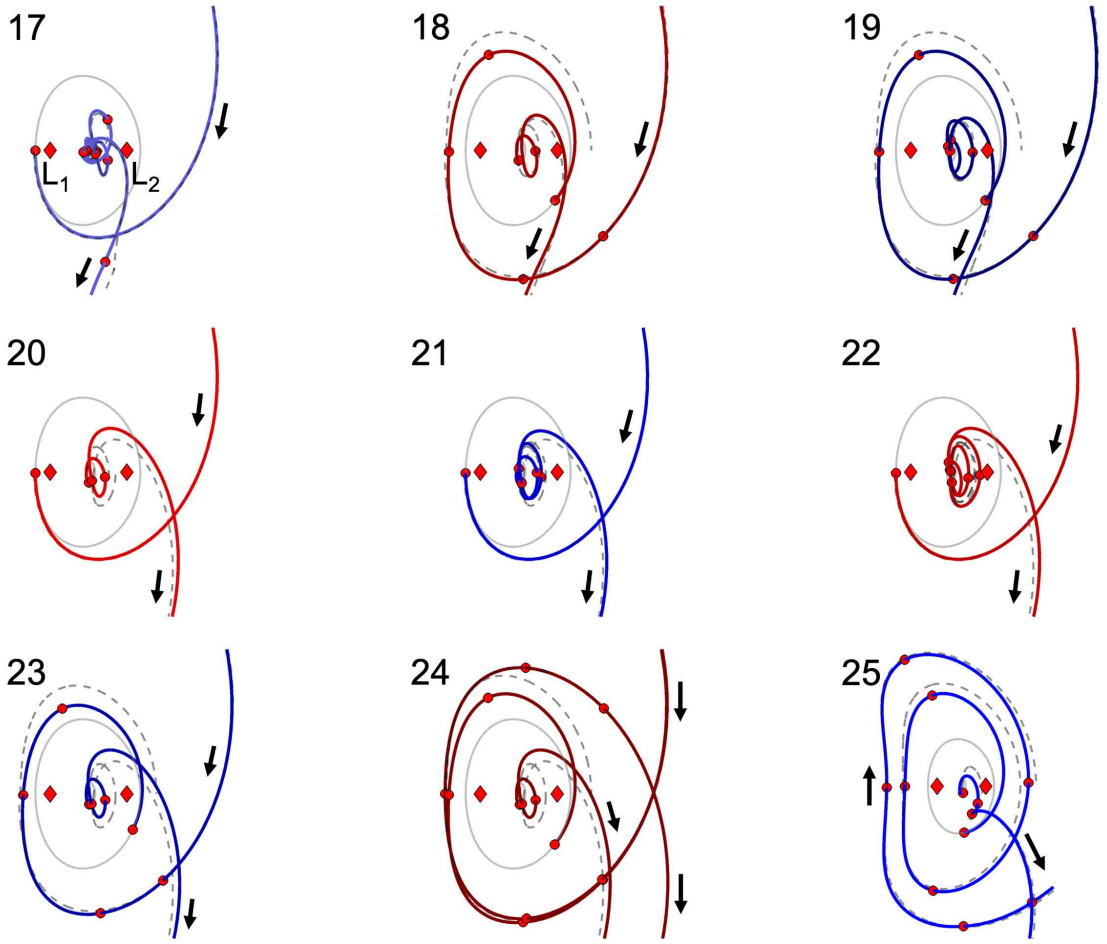

Figure 8.40: Zoomed in view of Transfers 17-25 (from Figure 8.33) in the vicinity of the Moon, displayed as a projection onto the xy-plane of $\mathcal{R}$.

manifold structures and resonant orbits leveraged in this investigation. It is also important to note that Muralidharan and Howell computed transfers that locally minimize total Δv and therefore utilized a different objective function than the objective function used in this investigation [73]. Despite these differences, the transfers constructed in this work possess similar magnitudes of total Δv and TOF.

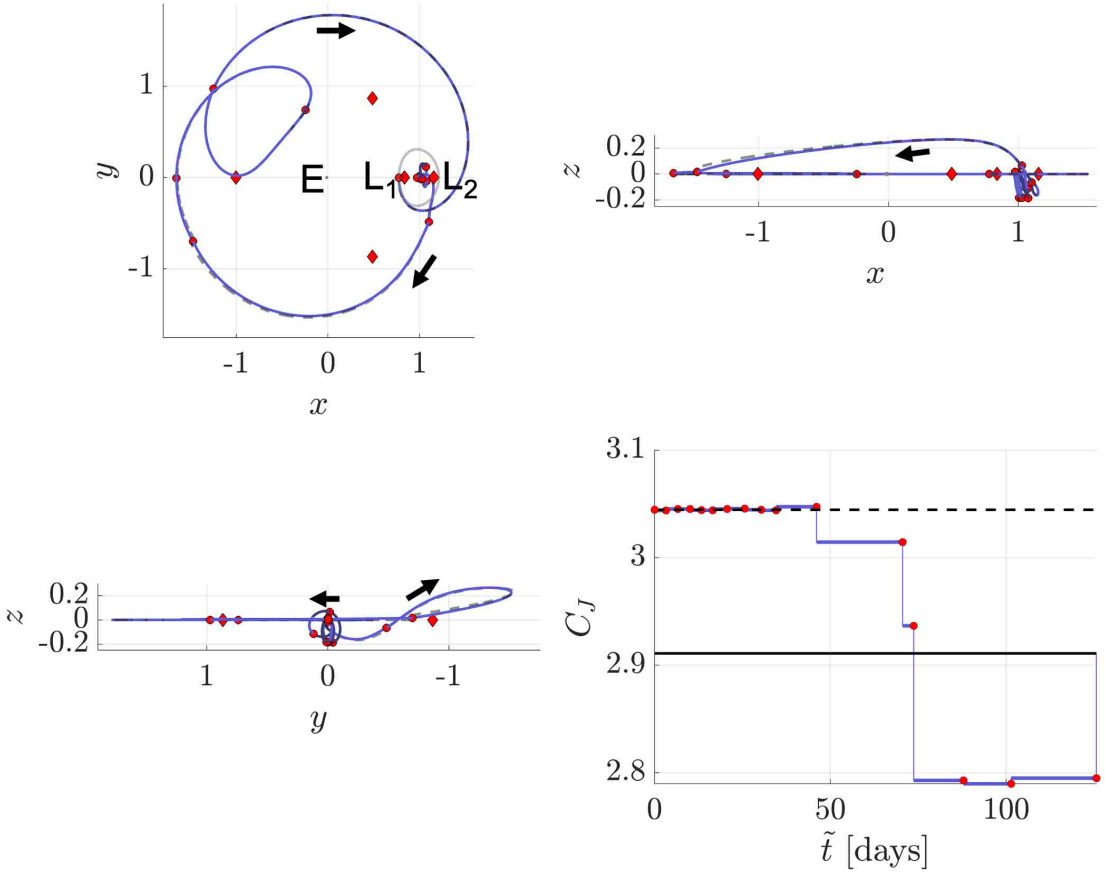

Figure 8.41: Continuous 125.66 day spatial transfer from an L_2 southern NRHO to a DRO in the Earth-Moon CR3BP, computed from a primitive-based initial guess using $\boldsymbol{w}_{\mathbf{opt}} = [0.9, 0.1]$.

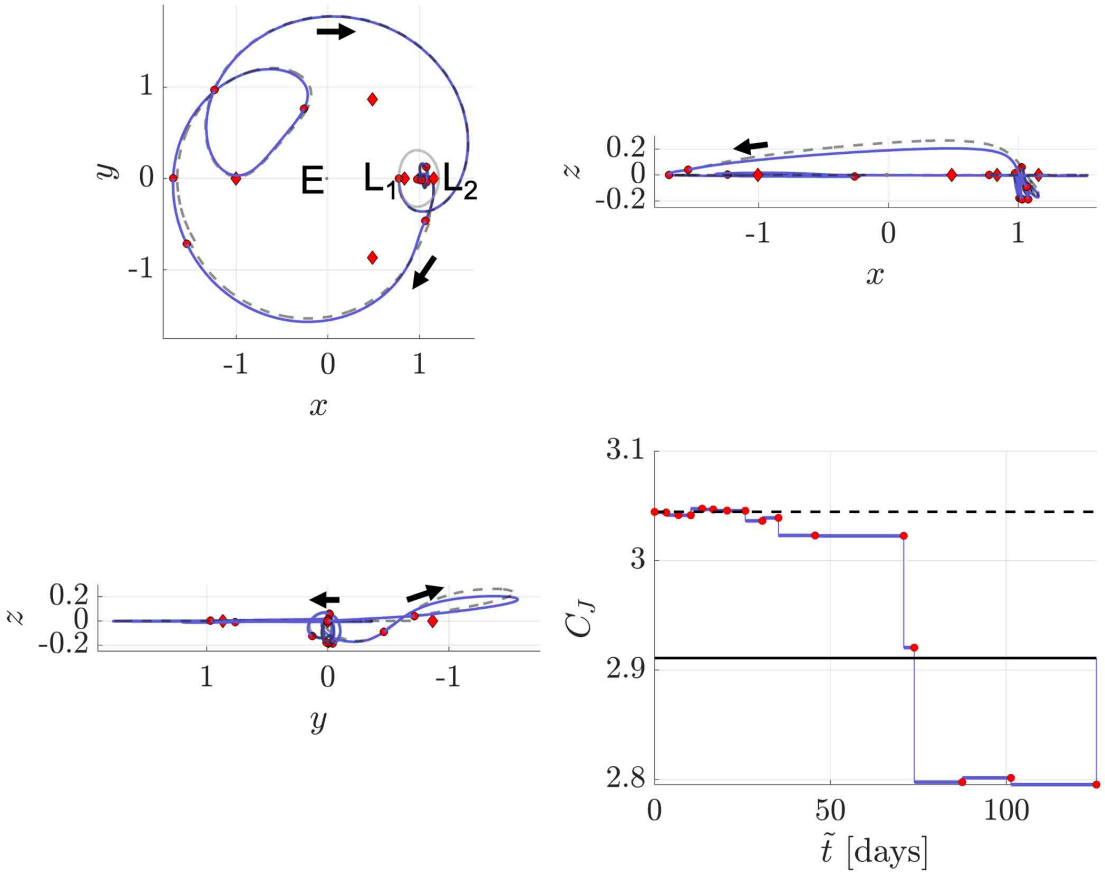

Figure 8.42: Continuous 125.58 day spatial transfer from an L_2 southern NRHO to a DRO in the Earth-Moon CR3BP, computed at $\boldsymbol{w}_{\mathbf{opt}} = [0.1, 0.9]$ using the continuation procedure that varies the weights of the multi-objective optimization problem starting from the transfer displayed in Figure 8.41.

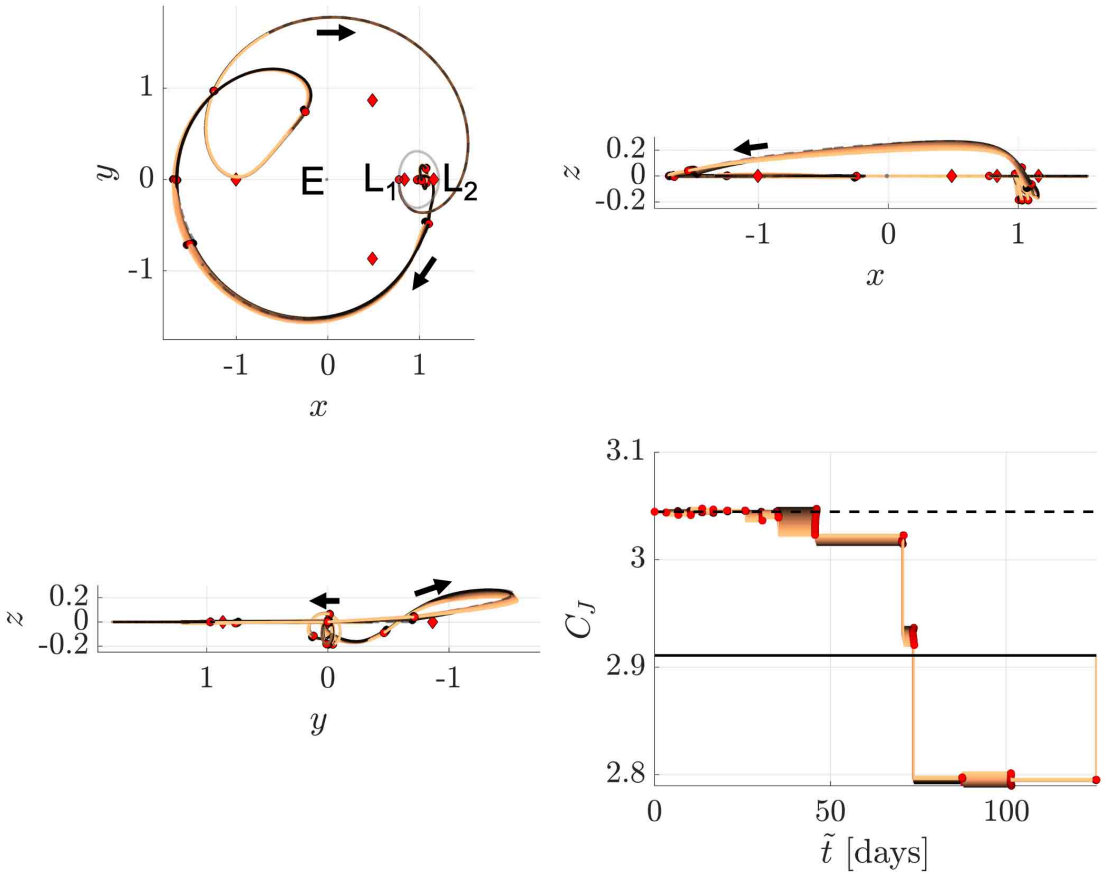

Figure 8.43: Evolution of the geometry and TOF across transfers in the local vicinity of Transfer 17 from Figure 8.39, computed using the continuation procedure that varies the weights of the multi-objective optimization problem.

8.3.3 Constructing Transfers from an L_2 Southern NRHO to a DRO at $C_J \approx 2.7654$

To demonstrate the capability to construct motion primitive sequences between any two selected nodes in a motion primitive graph, the motion primitive graph constructed for the NRHO to DRO transfer design scenario is searched to produce unique sequences of six primitives that each form an initial guess for a transfer from the initial L_2 southern NRHO to the second target DRO described in Table 8.6. There are a total of 373,315 primitive sequences from the selected initial node to the newly selected target node in the graph consisting of six primitives. Using the filtering process presented in Section 7.4, the $Q = 15$ top-ranked sequences that begin with a unique primitive are examined and corrected using the exact same process described in Section 8.3.2.

Following the corrections process, all 15 transfers are successfully corrected using $\boldsymbol{w_{opt}} = [0.9, 0.1]$ and then transitioned to $\boldsymbol{w_{opt}} = [0.1, 0.9]$. The 15 corrected transfers computed using $\boldsymbol{w_{opt}} = [0.1, 0.9]$ are grouped based on geometry to extract the distinct types of transfers that connect the initial L_2 southern NRHO and the target DRO at $C_J \approx 2.7654$ in the Earth-Moon CR3BP. When applying the k-NN graph approach described in Section 7.7, $k_{\text{nn}} = 2$ and $l_{\Delta\text{TOF}} = 6.5$ days are selected empirically and produce 11 groups of geometrically distinct transfers. The resulting properties of each transfer are plotted in Figure 8.44 using the same configuration as Figure 8.33 where the minimum Δv solution in each group is circled and numbered. These transfers require flight times ranging from 45.24 days to 127.66 days and total Δv requirements ranging from 365.54 m/s to 625.57 m/s when placing more emphasis on recovering maneuver-efficient transfers.

The minimum Δv transfer in each group is visualized in the configuration space of the Earth-Moon CR3BP; specifically, Figures 8.45 and 8.46 display each transfer as a projection onto the xy-plane of $\mathcal{R}$. In addition, Figure 8.47 provides a zoomed in view of Transfers 7-11 in the vicinity of the Moon. Similar to the transfers constructed in Section 8.3.2 for the first target DRO, some of the computed transfers remain in the lunar vicinity while other transfers circumnavigate the system. The transfers displayed in Figure 8.45 remain in the lunar vicinity and most of these transfers

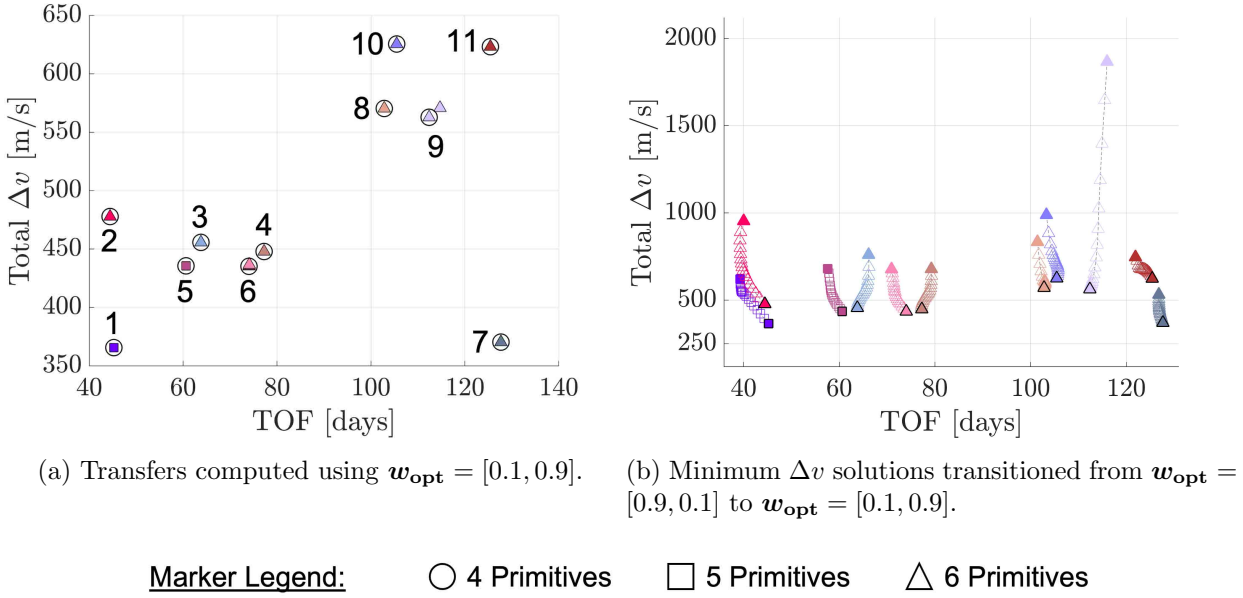

(a) Transfers computed using $\boldsymbol{w}_{\mathbf{opt}} = [0.1, 0.9]$.

(b) Minimum Δv solutions transitioned from $\boldsymbol{w}_{\mathbf{opt}} = [0.9, 0.1]$ to $\boldsymbol{w}_{\mathbf{opt}} = [0.1, 0.9]$.

Figure 8.44: Total Δv and TOF of transfers computed from an L_2 southern NRHO to a DRO in the Earth-Moon CR3BP, where geometrically similar transfers are denoted in the same color and the minimum Δv solution for each transfer geometry is highlighted.

leverage intermediate DROs. Similar to the transfer properties observed in Section 8.3.2, Transfers 3 and 4 each exhibit similar geometries but possess a different number of revolutions around the Moon in the vicinity of the initial NRHO; a similar observation holds for Transfers 5 and 6. To visualize one of these transfers in more detail, Figures 8.48-8.50 display the evolution of Transfer 4 throughout the natural parameter continuation process using the same format as in the previous subsection. Finally, Transfers 7-11 each leverage trajectory segments along either a 3:4 resonant orbit primitive or a 1:3 resonant orbit primitive. These transfer possess significantly longer flight times than Transfers 1-6. A fewer number of transfers are constructed from the initial L_2 southern NRHO to the second target DRO in this subsection compared to Section 8.3.2; however, even this smaller set of results further demonstrates the versatility of rapidly exploring a design space in a multi-body system via a systematic primitive-based initial guess construction framework.

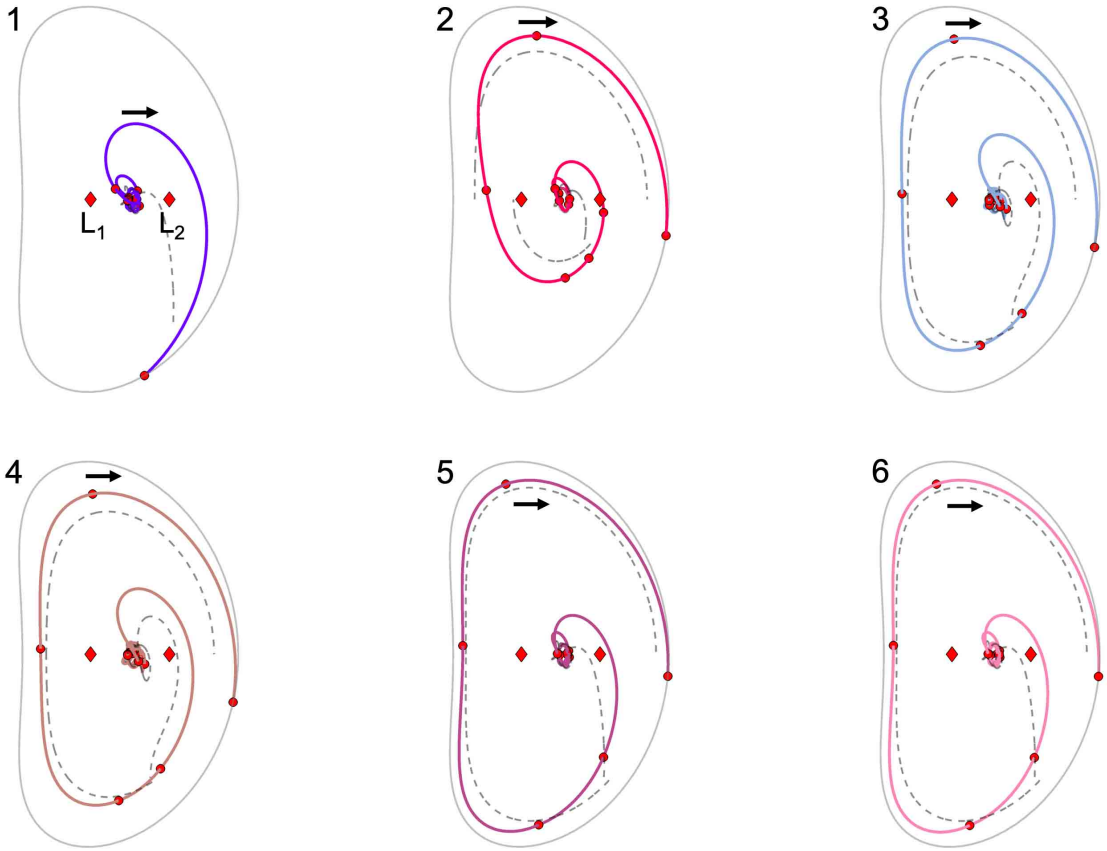

Figure 8.45: Transfers 1-6 (from Figure 8.44) with distinct geometries computed from primitive-based initial guesses between an L_2 southern NRHO and a DRO in the Earth-Moon CR3BP, displayed as a projection onto the xy-plane of $\mathcal{R}$.

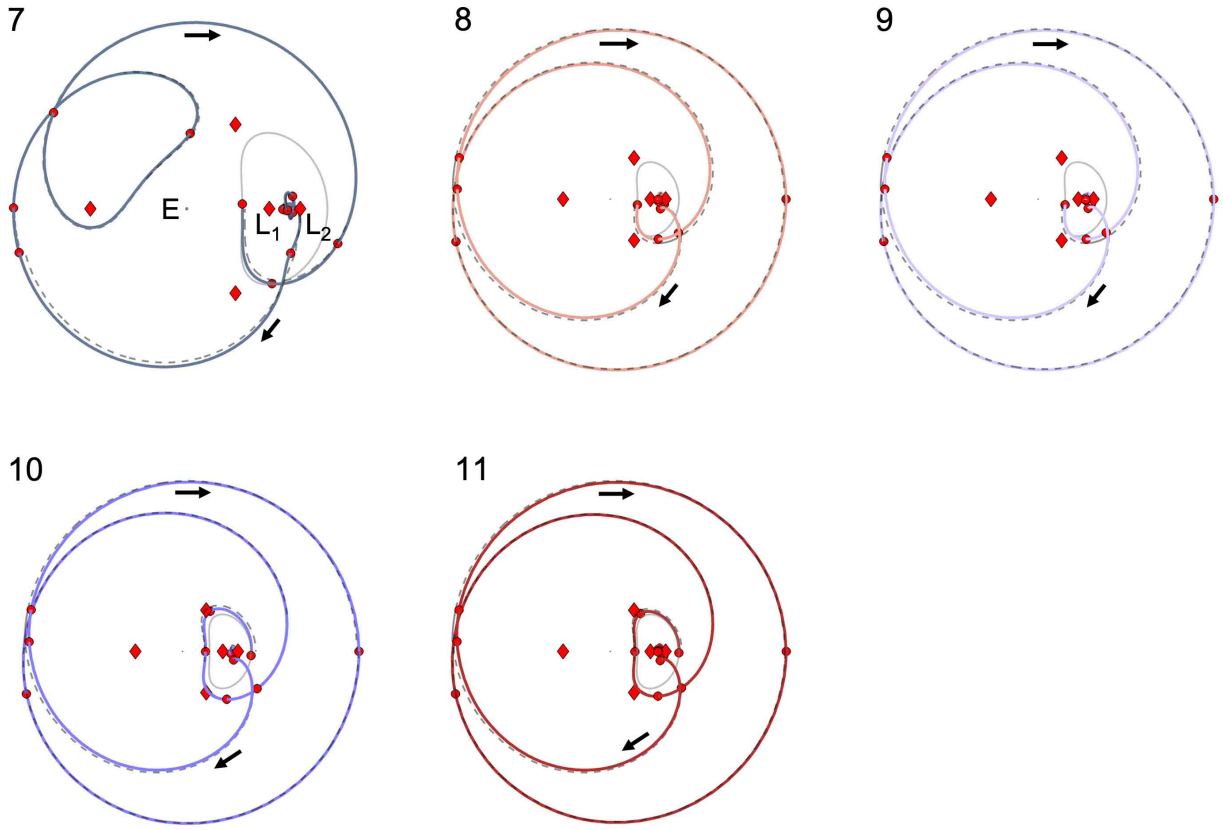

Figure 8.46: Transfers 7-11 (from Figure 8.44) with distinct geometries computed from primitive-based initial guesses between an L_2 southern NRHO and a DRO in the Earth-Moon CR3BP, displayed as a projection onto the xy-plane of $\mathcal{R}$.

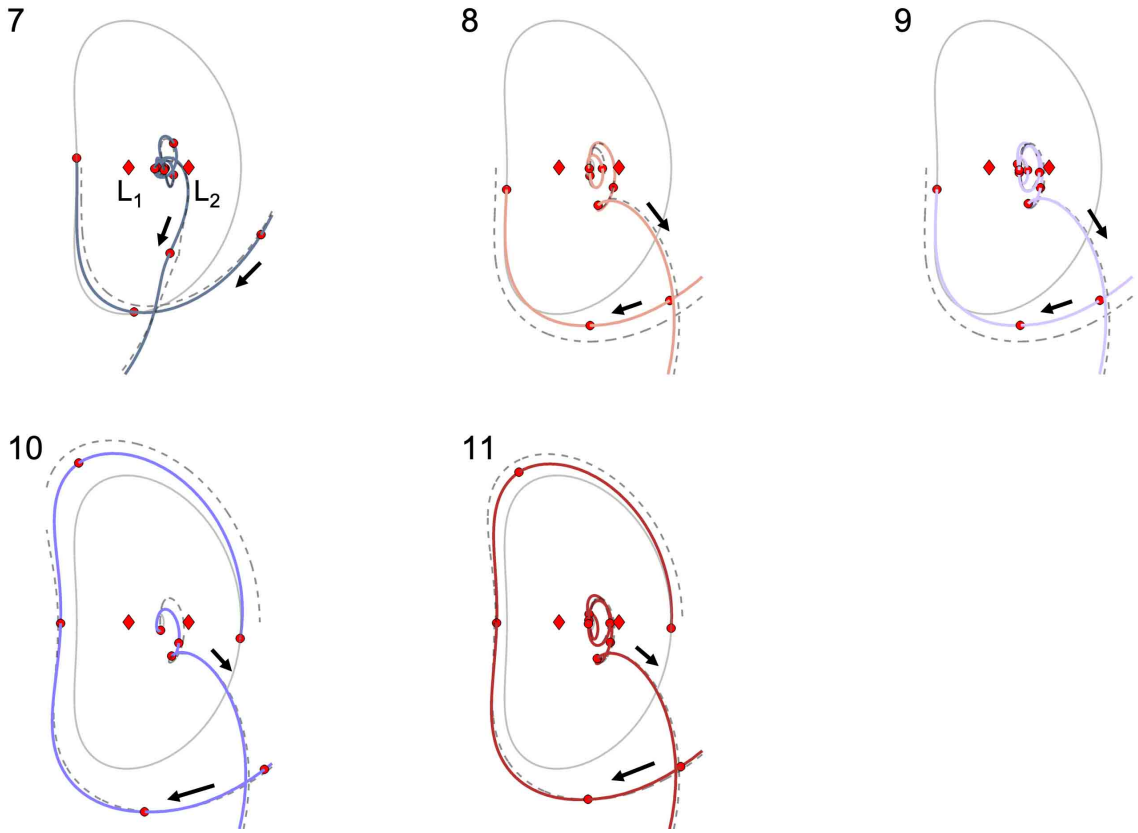

Figure 8.47: Zoomed in view of Transfers 7-11 (from Figure 8.44) in the vicinity of the Moon, displayed as a projection onto the xy-plane of $\mathcal{R}$.

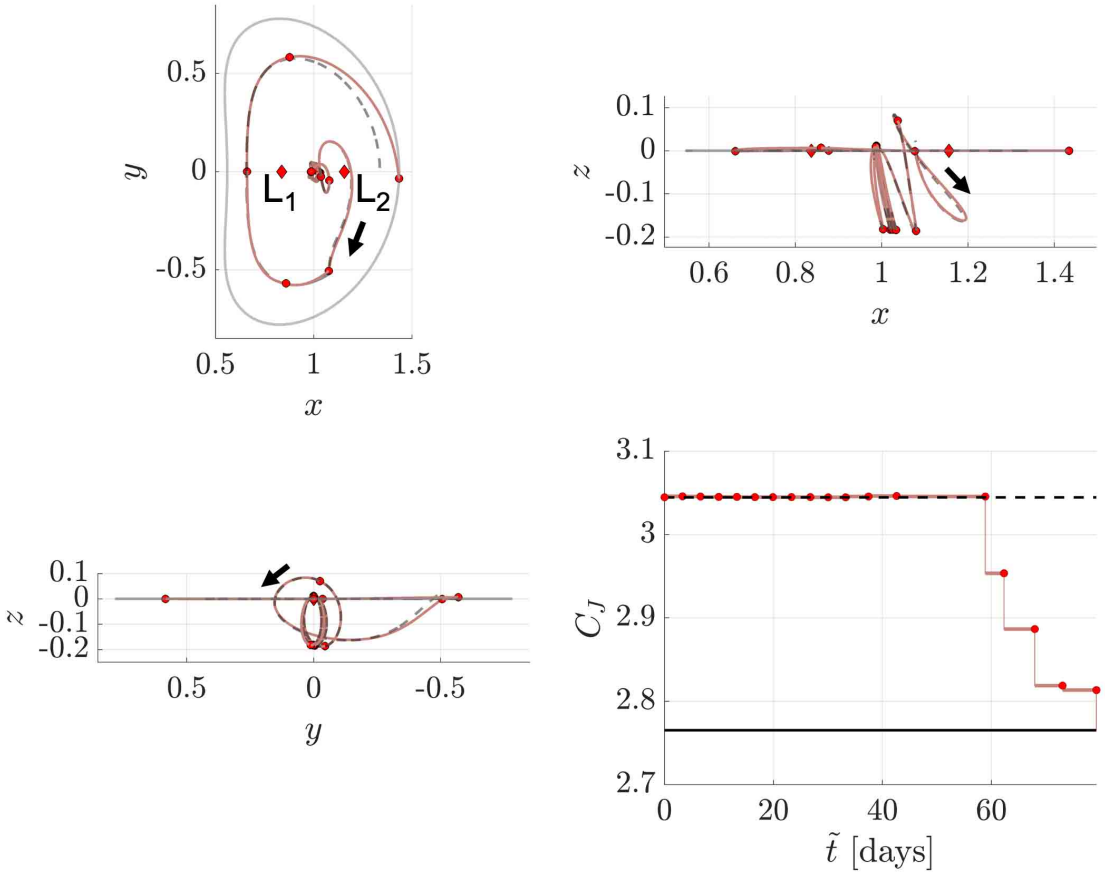

Figure 8.48: Continuous 79.25 day spatial transfer from an L_2 southern NRHO to a DRO in the Earth-Moon CR3BP, computed from a primitive-based initial guess using $\boldsymbol{w}_{\mathbf{opt}} = [0.9, 0.1]$.

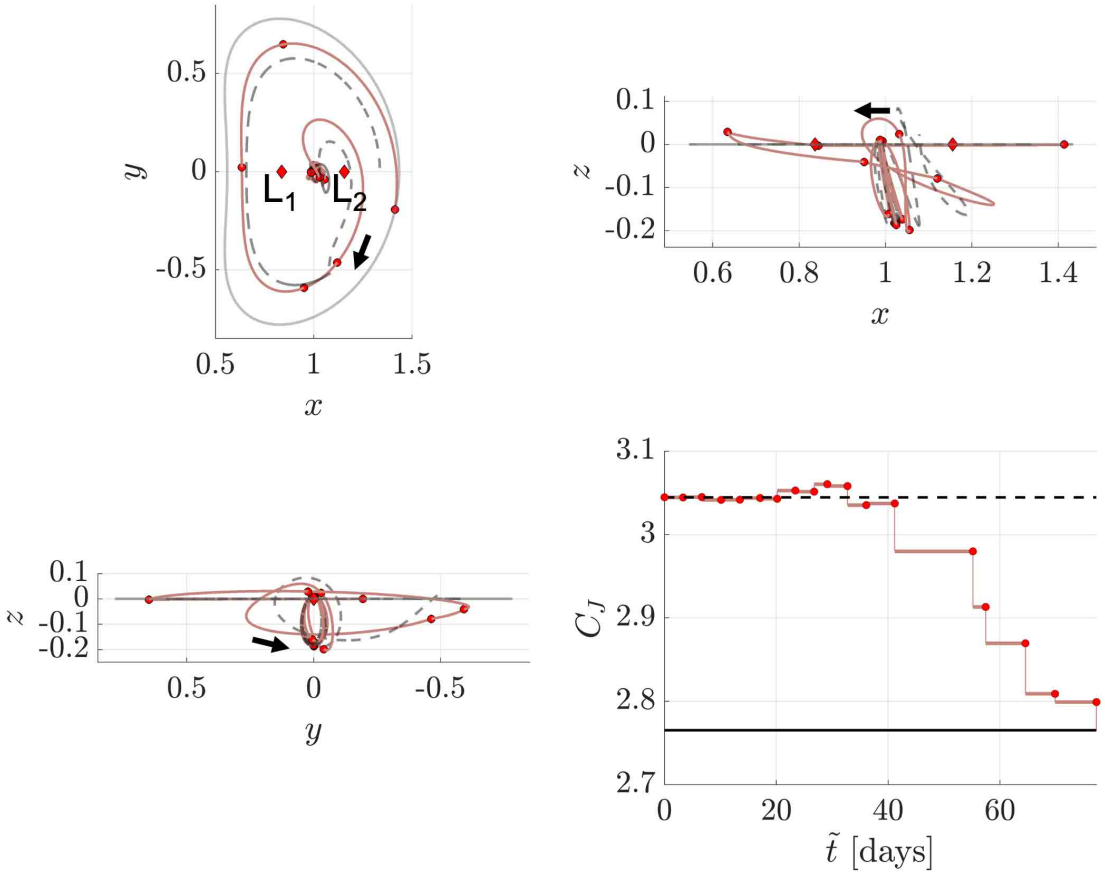

Figure 8.49: Continuous 77.24 day spatial transfer from an L_2 southern NRHO to a DRO in the Earth-Moon CR3BP, computed at $\boldsymbol{w}_{\mathbf{opt}} = [0.1, 0.9]$ using the continuation procedure that varies the weights of the multi-objective optimization problem starting from the transfer displayed in Figure 8.48.

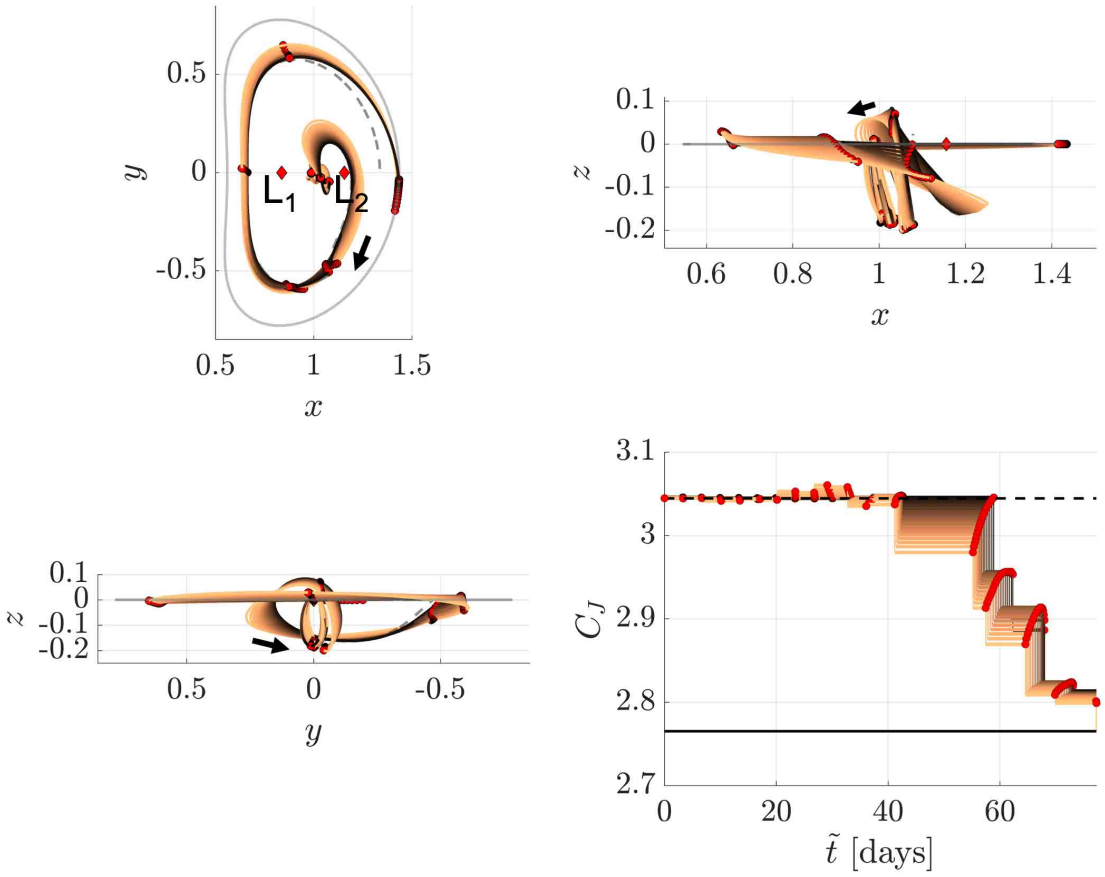

Figure 8.50: Evolution of the geometry and TOF across transfers in the local vicinity of Transfer 4 from Figure 8.45, computed using the continuation procedure that varies the weights of the multi-objective optimization problem.

Chapter 9

Conclusions and Recommendations

9.1 Concluding Remarks

In this investigation, the concept of a motion primitive is used to summarize fundamental dynamical structures in a multi-body system with the goal of reducing the complexity of analysis required for trajectory design. Across a variety of disciplines, a motion primitive is a fundamental building block of complex motion in a dynamical environment that represents a range of similar solutions. In this work, a motion primitive set is defined as a set of arcs that capture the characteristics of a larger set of trajectories and support assembly of an initial guess for a more complex path in a multi-body system. A data-driven procedure is presented for extracting primitives from a set of trajectories without the need for significant human intervention or analytical separation criteria. A set of trajectories is first encoded in a feature space description that captures common design parameters of interest such as geometry, stability, and energy. Then, an ensemble of clustering results is computed for the dataset using k-means and agglomerative clustering evaluated for a variety of input parameters. WEAC, a consensus clustering method, is leveraged to generate the final clustering result from the ensemble. A set of motion primitives is then extracted as the medoids of the clusters. Using a consensus clustering algorithm in conjunction with traditional clustering approaches produces results without requiring significant intervention from a human; rather, this approach learns from an ensemble of accumulated evidence to numerically uncover the natural groupings within a set of trajectories.

Using the presented data-driven procedure, motion primitives are constructed to summarize

families of periodic orbits and hyperbolic invariant manifolds in the Earth-Moon CR3BP as well as the Sun-Earth CR3BP. A set of motion primitives is constructed for the planar family of distant prograde orbits in the Earth-Moon CR3BP, the spatial family of L_1 northern halo orbits in the Earth-Moon CR3BP, and a variety of other periodic orbit families; in each case, the motion primitive sets capture the complex variations in geometry, stability, and energy along each family. A similar clustering approach is also employed to summarize a set of trajectories along an unstable half-manifold of an L_1 Lyapunov orbit in the Earth-Moon CR3BP. Each trajectory along the manifold is discretized into a series of smaller arcs to identify the fundamental variations in geometry of arcs along the manifold. This approach effectively summarizes the departure geometries from the L_1 Lyapunov orbit toward the Moon, motion around the Moon, and trajectories that either directly impact the Moon or leave the lunar vicinity. For both the periodic orbit families and the manifold trajectories, the outputs of the developed approach include: (1) a set of fundamental trajectories that summarize larger sets of natural motions in a multi-body system, and (2) information about the regions in which the motion primitives exist within the solution space. These outputs serve as a key, fundamental step towards leveraging motion primitives for rapidly generating initial guesses for complex trajectories within multi-body systems.

Using the motion primitive construction process, a modular primitive-based trajectory design framework is developed to enable rapid generation of trajectories with distinct geometries and efficient design space exploration in multi-body systems. First, a library of motion primitives is constructed using clustering to summarize periodic orbit families and arcs along stable/unstable manifolds for a transfer design scenario. Then, a graph is constructed to capture the potential for sequential composability of motion primitives in this library and, therefore, offer a discrete representation of part of the solution space. Searching this graph produces sequences of motion primitives that support coarsely constructing initial guesses for transfers with distinct geometries. Finally, each primitive sequence is refined and corrected using direct collocation and multi-objective optimization to produce transfers that balance geometrically resembling the primitive-based initial guess with reducing maneuver requirements.

The primitive-based initial guess construction framework is demonstrated by computing a variety of transfers in the Earth-Moon CR3BP between an L_1 and L_2 Lyapunov orbit, an L_1 and L_2 northern halo orbit, and an L_2 southern NRHO and DRO. Each of these transfer design scenarios showcases different capabilities of the presented framework: the Lyapunov and northern halo orbit scenarios demonstrate the ability to design both planar and spatial transfers, respectively; whereas, the L_2 southern NRHO to DRO transfer scenario demonstrates the ability to design transfers between mission orbits with large energy and orbit plane differences. In each scenario, unique primitive sequences and numerical continuation lead to the recovery of a set of transfers with a variety of distinct geometries, flight times, and maneuver requirements. To demonstrate the utility of using the CR3BP for preliminary trajectory design, some of the constructed transfers are also transitioned into a point mass ephemeris model that incorporates the gravitational influence of the Sun, Earth, and Moon. These examples demonstrate that motion primitives can support initial guess construction for spacecraft trajectories in a multi-body system as well as rapid exploration of the associated design space.

The primary contributions of this investigation to the astrodynamics community are (1) the development of a motion primitive construction process for summarizing periodic orbit families and trajectories along hyperbolic invariant manifolds associated with periodic orbits in the CR3BP; (2) the development of a modular primitive-based initial guess construction framework that enables rapid generation of trajectories with distinct geometries and efficient design space exploration in the CR3BP; and (3) the formulation of a robust corrections procedure that leverages collocation and multi-objective optimization to encourage the recovery of trajectories that geometrically resemble a primitive-based initial guess. Current trajectory design techniques in a multi-body system often leverage natural fundamental solutions for initial guess construction; however, current methodologies require manual exploration of a complex multi-dimensional solution space that is nontrivial, mission specific, and time-consuming for a human analyst. Therefore, the motion primitive construction process presented in this work may support summarizing the complex solution space admitted by a multi-body system and simplifying the analysis process. Furthermore, the

primitive-based initial guess construction framework contributes to addressing the challenges in current design techniques when attempting to identify different geometric solutions for a design scenario, particularly in the case of spatial design scenarios at high energy levels. Finally, the corrections process provides a human analyst with the ability to recover continuous maneuver-enabled trajectories that balance retaining a desired geometry with reducing impulsive maneuver requirements. These contributions built around the concept of a motion primitive may potentially support rapid mission concept development and enhance current trajectory design strategies by reducing the analytical workload of a trajectory designer.

9.2 Recommendations for Future Work

Building upon the proof of concept in this dissertation, the developed primitive-based initial guess construction framework warrants improvement as well as application to more complex trajectory design scenarios. A list of recommendations for future work related to this research include:

- The current motion primitive construction process leverages clustering results produced by k-means and agglomerative clustering within WEAC. However, using additional clustering algorithms may supply more information and diversity in the ensemble of clustering results used within WEAC to generate the final set of clusters for a dataset. Investigating the use of additional clustering algorithms within WEAC may improve clustering results and reduce the need for cluster refinement in some cases, particularly because k-means assumes globular cluster structures and agglomerative clustering is sensitive to the selected linkage type. However, the computational cost of leveraging a larger ensemble must also be considered.

- Investigate potential improvements or alternative methods for cluster refinement. The cluster refinement approach is used to improve clustering results produced by WEAC when applicable. However, as formulated in this work, it requires the selection of three input parameters and relies on the human analyst to develop an intuition for selecting these

parameters. Furthermore, the presented approach may sometimes lead to excessive fragmentation of the original clusters. Therefore, investigating improvements to the procedure or alternative methods may lead to a more robust process that reduces the number of input parameters and further reduces the burden on a human analyst when additional cluster refinement is deemed appropriate.

- Additional and/or alternative information may be incorporated into the feature vector definitions for periodic orbits and trajectories along a hyperbolic invariant manifold. The definitions used in this work focus on describing geometry, stability, and/or energy; however, alternative features may be used to describe these properties as well as additional parameters of interest for trajectory design. Furthermore, the current use of apses for describing the geometry of a trajectory requires the selection of a reference point. Selecting an appropriate reference point for computing the apses may be difficult depending on the trajectory and therefore alternative methods may be investigated that do not require this selection.

- Investigate analytical or numerical methods to describe the volumes of the phase space spanned by a cluster of similar trajectories in order to construct a more complete and accurate approximation of the region of existence associated with a motion primitive.

- In this work, motion primitives are only generated to summarize periodic orbit families and sets of trajectories along hyperbolic invariant manifolds associated with periodic orbits at a single energy level. However, the motion primitive construction process may be adapted to generate motion primitives for a larger variety of trajectory sets. Incorporating primitives generated from additional dynamical structures within a motion primitive library may expand the potential design space for a transfer scenario. For example, motion primitives could be generated to summarize trajectories along hyperbolic invariant manifolds associated with periodic orbits across multiple energy levels, quasi-periodic orbits, hyperbolic invariant manifolds associated with quasi-periodic orbits, sets of trajectories departing an

orbit using an impulsive maneuver, and low-thrust enabled trajectories. Extending the presented approach to a larger variety of trajectory sets will require new feature vector definitions to effectively describe the corresponding trajectories.

- Investigate methods to improve the motion primitive graph construction process. Currently, a single value of k_{nn} is used to generate the edges within a motion primitive graph. However, an adaptive value of k_{nn} based on the size of each subgraph or alternative edge generation processes may be more appropriate. Furthermore, position and velocity difference limits may be incorporated to remove edges in the graph that violate desired thresholds. Finally, the current edge weight computations are based only on state discontinuities; however, additional parameters of interest may be incorporated into the edge weight computations to consider a larger array of criteria related to a transfer scenario.

- Investigate methods to improve the search process for identifying motion primitive sequences with distinct geometries from a motion primitive graph. Currently, a brute force search algorithm is used to enumerate all potential paths between an initial node and a target node with a desired path length. The filtering process presented in this approach helps facilitate an efficient human-driven evaluation of the resulting sequences. Furthermore, the waypoint search process helps mitigate some of the challenges associated with finding longer sequences of motion primitives. However, more powerful and efficient search techniques are needed to effectively search more complex motion primitive graphs for increasingly complex design scenarios. Improved search techniques may also be used to address a similar challenge in the morphing process when refining a long sequence of primitives to generate an initial guess for a transfer.

- Investigate methods to improve the current k-NN graph approach for grouping transfers with similar geometries during the design space exploration for a transfer scenario. As discussed in this investigation, there is a case where two transfers must be manually separated into distinct groups due to limitations of the current grouping procedure. Therefore, alter-

native definitions for evaluating the difference in geometry between two transfers described by a distinct number of nodes may be explored.

- Apply the primitive-based initial guess construction framework to more complex trajectory design scenarios. The framework presented in this work is modular and may be leveraged for a large variety of design applications. Suggestions include transfers to/from low orbits near a primary body, low-thrust transfers, transfers in other multi-body systems, and transfers that incorporate primitives from different multi-body systems. The final listed suggestion may involve patching CR3BP trajectories together from different systems or leveraging primitives constructed in higher-fidelity models.

Bibliography

[1] C. H. Acton. Ancillary Data Services of NASA's Navigation and Ancillary Information Facility. Planetary and Space Science, 44(1):65–70, 1996. DOI: https://doi.org/10.1016/0032-0633(95)00107-7.

[2] C. H. Acton, N. Bachman, B. Semenov, and E. Wright. A Look Towards the Future in the Handling of Space Science Mission Geometry. Planetary and Space Science, 150:9–12, 2018. DOI: https://doi.org/10.1016/j.pss.2017.02.013.

[3] C. C. Aggarwal and C. K. Reddy. Data Clustering Algorithms and Applications. Taylor & Francis Group, Boca Raton, FL, 2014.

[4] J. Barrow-Green. Poincaré and the Three Body Problem. History of Mathematics Vol. 11. American Mathematical Society, 1997. DOI: https://doi.org/10.1090/hmath/011.

[5] E. A. Belbruno and J. K. Miller. Sun-Perturbed Earth-to-Moon Transfers with Ballistic Capture. Journal of Guidance, Control, and Dynamics, 16(4):770–775, 1993. DOI: https://doi.org/10.2514/3.21079.

[6] J. T. Betts. Survey of Numerical Methods for Trajectory Optimization. Journal of Guidance, Control, and Dynamics, 21(2):193–207, 1998. DOI: https://doi.org/10.2514/2.4231.

[7] S. Bonasera and N. Bosanac. Applying Data-Mining Techniques to Higher-Dimensional Poincaré Maps in the Circular Restricted Three-Body Problem. Celestial Mechanics and Dynamical Astronomy, 133(51), 2021. DOI: https://doi.org/10.1007/s10569-021-10047-3.

[8] N. Bosanac. Leveraging Natural Dynamical Structures to Explore Multi-Body Systems. PhD Dissertation, Purdue University, West Lafayette, IN, 2016.

[9] N. Bosanac. Data-Mining Approach to Poincaré Maps in Multi-Body Trajectory Design. Journal of Guidance, Control, and Dynamics, 43(6):1190–1200, 2020. DOI: https://doi.org/10.2514/1.G004857.

[10] N. Bosanac, C. M. Webster, K. C. Howell, and D. C. Folta. Trajectory Design for the Wide Field Infrared Survey Telescope Mission. Journal of Guidance, Control, and Dynamics, 42(9):1899–1911, 2019. DOI: https://doi.org/10.2514/1.G004179.

[11] J. V. Breakwell and J. V. Brown. The 'Halo' Family of 3-Dimensional Periodic Orbits in the Earth-Moon Restricted 3-Body Problem. Celestial Mechanics and Dynamical Astronomy, 20(4):389–404, 1979. DOI: https://doi.org/10.1007/BF01230405.

[12] W. L. Brogan. Modern Control Theory. Prentice-Hall International, Inc., New Jersey, USA, 3 edition, 1991.

[13] R. A. Broucke. Periodic Orbits in the Restricted Three-Body Problem with Earth-Moon Masses. In NASA Technical Report 32-1168. JPL, 1968.

[14] K. L. Bruchko and N. Bosanac. A Preliminary Exploration of Path Planning for Initial Guess Construction in Multi-Body Systems. In AAS/AIAA Astrodynamics Specialist Conference, Virtual, August 2021.

[15] B. Cheetham, T. Gardner, and A. Forsman. Cislunar Autonomous Positioning System Technology Operations and Navigation Experiment (CAPSTONE). In ASCEND 2021, Las Vegas, NV, November 2021. DOI: https://doi.org/10.2514/6.2021-4128.

[16] C. C. Conley. Low Energy Transit Orbits in the Restricted Three-Body Problem. SIAM Journal on Applied Mathematics, 16(4):732–746, 1968. DOI: https://doi.org/10.1137/0116060.

[17] B. A. Conway. Spacecraft Trajectory Optimization. Cambridge University Press, New York, USA, 2010. DOI: https://doi.org/10.1017/CBO9780511778025.

[18] A. Das-Stuart, K. C. Howell, and D. C. Folta. Rapid Trajectory Design in Complex Environments Enabled by Reinforcement Learning and Graph Search Strategies. Acta Astronautica, 171:172–195, 2020. DOI: https://doi.org/10.1016/j.actaastro.2019.04.037.

[19] D. C. Davis, F. S. Khoury, K. C. Howell, and D. J. Sweeney. Phase Control and Eclipse Avoidance in Near Rectilinear Halo Orbits. In AAS Guidance, Navigation, and Control Conference, Breckenridge, CO, January 2020.

[20] K. E. Davis. Locally Optimal Transfer Trajectories Between Libration Point Orbits Using Invariant Manifolds. PhD Dissertation, University of Colorado, Boulder, CO, 2009.

[21] C. De Boor. Good Approximation by Splines with Variable Knots. II. In Conference on the Numerical Solution of Differential Equations, Dundee, Scotland, 1973.

[22] E. Doedel. AUTO: A Program for Automatic Bifurcation Analysis of Autonomous Systems. Congressus Numerantium, 30:265–284, 1981.

[23] M. P. Dubuisson and A. K. Jain. A Modified Hausdorff Distance for Object Matching. In Proceedings of 12th International Conference on Pattern Recognition, Jerusalem, Israel, October 1994. DOI: https://doi.org/10.1109/ICPR.1994.576361.

[24] R. W. Farquhar. Halo-Orbit and Lunar-Swingby Missions of the 1990's. Acta Astronautica, 24:227–234, 1991. DOI: https://doi.org/10.1016/0094-5765(91)90170-A.

[25] R. W. Farquhar, D. P. Muhonen, C. R. Newman, and H. S. Heuberger. Trajectories and Orbital Maneuvers for the First Libration-Point Satellite. Journal of Guidance, Control, and Dynamics, 3(6):549–554, 1980. DOI: https://doi.org/10.2514/3.56034.

[26] D. C. Folta, N. Bosanac, I.L. Elliott, L. Mann, R. Mesarch, and J. Rosales. Astrodynamics Convention and Modeling Reference for Lunar, Cislunar, and Libration Point Orbits. NASA/TP-20220014814, 2022. Version 1.1.

[27] D. C. Folta, N. Bosanac, D. Guzzetti, and K. C. Howell. An Earth-Moon System Trajectory Design Reference Catalog. Acta Astronautica, 110:341–353, 2015. DOI: https://doi.org/10.1016/j.actaastro.2014.07.037.

[28] D. C. Folta, M. Woodard, K. C. Howell, C. Patterson, and W. Schlei. Application of Multi-Body Dynamical Environments: The ARTEMIS Transfer Trajectory Design. Acta Astronautica, 73:237–249, 2012. DOI: https://doi.org/10.1016/j.actaastro.2011.11.007.

[29] E. Frazzoli. Robust Hybrid Control for Autonomous Vehicle Motion Planning. PhD Dissertation, Massachusetts Institute of Technology, Cambridge, MA, 2001.

[30] E. Frazzoli, M. A. Dahleh, and E. Feron. Maneuver-Based Motion Planning for Nonlinear Systems with Symmetries. IEEE Transactions on Robotics, 21(6):1077–1091, 2005. DOI: https://doi.org/10.1109/TRO.2005.852260.

[31] A. L. N. Fred and A. K. Jain. Combining Multiple Clusterings Using Evidence Accumulation. IEEE Transactions on Pattern Analysis and Machine Intelligence, 27(6):835–850, 2005. DOI: https://doi.org/10.1109/TPAMI.2005.113.

[32] G. Gómez, W. S. Koon, M. W. Lo, J. E. Marsden, J. Masdemont, and S. D. Ross. Connecting Orbits and Invariant Manifolds in the Spatial Restricted Three-Body Problem. Nonlinearity, 17:1571–1606, 2004. DOI: https://doi.org/10.1088/0951-7715/17/5/002.

[33] G. Gómez, J. Llibre, R. Martínez, and C. Simó. Dynamics and Mission Design Near Libration Points Vol. I Fundamentals: The Case of Collinear Libration Points. World Scientific, River Edge, NJ, 2001. World Scientific Monograph Series in Mathematics: Volume 2, DOI: https://doi.org/10.1142/4402.

[34] D. J. Grebow, M. T. Ozimek, K. C. Howell, and D. C. Folta. Multibody Orbit Architectures for Lunar South Pole Coverage. Journal of Spacecraft and Rockets, 45(2):344–358, 2008. DOI: https://doi.org/10.2514/1.28738.

[35] D. J. Grebow and T. A. Pavlak. MCOLL: MONTE Collocation Trajectory Design Tool. In AAS/AIAA Astrodynamics Specialist Conference, Stevenson, WA, August 2017.

[36] M. Greenhouse. The James Webb Space Telescope: Mission Overview and Status. In IEEE Aerospace Conference, Big Sky, MT, March 2019. DOI: https://doi.org/10.1109/AERO.2019.8742209.

[37] D. J. Grymin, C. B. Neas, and M. Farhood. A Hierarchical Approach for Primitive-Based Motion Planning and Control of Autonomous Vehicles. Robotics and Autonomous Systems, 62(2):214–228, 2014. DOI: https://doi.org/10.1016/j.robot.2013.10.003.

[38] D. Guzzetti, N. Bosanac, A. F. Haapala, K. C. Howell, and D. C. Folta. Rapid Trajectory Design in the Earth-Moon Ephemeris System via an Interactive Catalog of Periodic and Quasi-Periodic Orbits. Acta Astronautica, 126:439–455, 2016. DOI: https://doi.org/10.1016/j.actaastro.2016.06.029.

[39] A. F. Haapala. Trajectory Design in the Spatial Circular Restricted Three-Body Problem Exploiting Higher-Dimensional Poincaré Maps. PhD Dissertation, Purdue University, West Lafayette, IN, 2014.

[40] A. F. Haapala, K. C. Howell, and D. C. Folta. Incorporating the Evolution of Multi-Body Orbits Into the Trajectory Trade Space and Design Process. Acta Astronautica, 112:1–18, 2015. DOI: https://doi.org/10.1016/j.actaastro.2015.02.024.

[41] A. F. Haapala, M. Vaquero, T. Pavlak, K. C. Howell, and D. C. Folta. Trajectory Selection Strategy for Tours in the Earth-Moon System. In AAS/AIAA Astrodynamics Specialist Conference, Hilton Head, SC, August 2013.

[42] T. Haberkorn, P. Martinon, and J. Gergaud. Low-Thrust Minimum-Fuel Orbital Transfer: A Homotopic Approach. Journal of Guidance, Control, and Dynamics, 27(6):1046–1060, 2004. DOI: https://doi.org/10.2514/1.4022.

[43] J. D. Hadjidemetriou. Resonant Motion in the Restricted Three-Body Problem. Celestial Mechanics and Dynamical Astronomy, 56:201–219, 1993. DOI: https://doi.org/10.1007/BF00699733.

[44] A. Hadjighasem, D. Karrasch, H. Teramoto, and G. Haller. Spectral-Clustering Approach to Lagrangian Vortex Detection. Physical Review E, 93(6), 2016. DOI: https://doi.org/10.1103/PhysRevE.93.063107.

[45] N. Hale and A. Townsend. Fast and Accurate Computation of Gauss-Legendre and Gauss-Jacobi Quadrature Nodes and Weights. SIAM Journal on Scientific Computing, 35(2):A652–A674, 2013. DOI: https://doi.org/10.1137/120889873.

[46] J. Han, M. Kamber, and J. Pei. Data Mining Concepts and Techniques. Morgan Kaufmann Publishers, Waltham, MA, 3 edition, 2012. DOI: https://doi.org/10.1016/C2009-0-61819-5.

[47] R. M. Holladay and S. S. Srinivasa. Distance Metrics and Algorithms for Task Space Path Optimization. In IEEE/RSJ International Conference on Intelligent Robots and Systems, Daejeon, Korea, October 2016. DOI: https://doi.org/10.1109/IROS.2016.7759814.

[48] K. C. Howell. Three-Dimensional, Periodic, 'Halo' Orbits. Celestial Mechanics and Dynamical Astronomy, 32(1):53–71, 1984. DOI: https://doi.org/10.1007/BF01358403.

[49] K. C. Howell, B. T. Barden, and M. W. Lo. Application of Dynamical Systems Theory to Trajectory Design for a Libration Point Mission. The Journal of the Astronautical Sciences, 45(2):161–178, 1997. DOI: https://doi.org/10.1007/BF03546374.

[50] K. C. Howell and M. Kakoi. Transfers Between the Earth-Moon and Sun-Earth Systems Using Manifolds and Transit Orbits. Acta Astronautica, 59:367–380, 2006. DOI: https://doi.org/10.1016/j.actaastro.2006.02.010.

[51] HSL. A Collection of Fortran Codes for Large Scale Scientific Computation. http://www.hsl.rl.ac.uk/.

[52] D. Huang, J. H. Lai, and C. D. Wang. Combining Multiple Clusterings via Crowd Agreement Estimation and Multi-Granularity Link Analysis. Neurocomputing, 170:240–250, 2015. DOI: https://doi.org/10.1016/j.neucom.2014.05.094.

[53] M. C. E. Huber and O. von der Lühe. Coronal Observations with SOHO. Advances in Space Research, 11(1):339–348, 1991. DOI: https://doi.org/10.1016/0273-1177(91)90130-C.

[54] O. C. Jenkins and M. J. Mataric. Deriving Action and Behavior Primitives from Human Motion Data. In IEEE/RSJ International Conference on Intelligent Robots and Systems, Lausanne, Switzerland, 10 2002. DOI: https://doi.org/10.1109/IRDS.2002.1041654.

[55] Z. Jiang, M. Evans, D. Oliver, and S. Shekhar. Identifying K Primary Corridors from Urban Bicycle GPS Trajectories on a Road Network. Information Systems Journal, 57:142–159, 2016. DOI: https://doi.org/10.1016/j.is.2015.10.009.

[56] G. Karypis, E. H. Han, and V. Kumar. Multilevel Refinement for Hierarchical Clustering. Technical Report TR-99-020, Department of Computer Science, University of Minnesota, Minneapolis, MN, 1999.

[57] L. Kaufman and P. J. Rousseeuw. Finding Groups in Data: An Introduction to Cluster Analysis. John Wiley & Sons, Hoboken, NJ, 2005.

[58] H. B. Keller. Numerical Solution of Bifurcation and Nonlinear Eigenvalue Problems. In P. H. Rabinowitz, editor, Applications of Bifurcation Theory, pages 359–384. Academic Press, New York, 1977.

[59] M. Kelly. An Introduction to Trajectory Optimization: How to Do Your Own Direct Collocation. SIAM Review, 59(4):849–904, 2017. DOI: https://doi.org/10.1137/16M1062569.

[60] W. S. Koon, M. W. Lo, J. E. Marsden, and S. D. Ross. Heteroclinic Connections Between Periodic Orbits and Resonance Transitions in Celestial Mechanics. Chaos, 10(2):427–469, 2000. DOI: https://doi.org/10.1063/1.166509.

[61] W. S. Koon, M. W. Lo, J. E. Marsden, and S. D. Ross. Dynamical Systems, The Three-Body Problem, and Space Mission Design. Springer, New York, USA, 2011.

[62] M. Lara and R. P. Russell. On the Family "g" of the Restricted Three-Body Problem. Monografías de la Real Academia de Ciencias de Zaragoza, 30:51–66, 2006.

[63] S. M. LaValle. Planning Algorithms. Cambridge University Press, 2006. DOI: https://doi.org/10.1017/CBO9780511546877.

[64] D. E. Lee. White Paper: Gateway Destination Orbit Model: A Continuous 15 Year NRHO Reference Trajectory. Technical Report TP-20190030294, NASA, 2019.

[65] J. Llibre, R. Martínez, and C. Simó. Transversality of the Invariant Manifolds Associated to the Lyapunov Family of Periodic Orbits near L_2 in the Restricted Three-Body Problem. Journal of Differential Equations, 58(1):104–156, 1985. DOI: https://doi.org/10.1016/0022-0396(85)90024-5.

[66] M. W. Lo. Libration Point Trajectory Design. Numerical Algorithms, 14:153–164, 1997. DOI: https://doi.org/10.1023/A:1019108929089.

[67] M. W. Lo, B. G. Williams, W. E. Bollman, D. Han, Y. Hahn, J. L. Bell, E. A. Hirst, R. A. Corwin, P. E. Hong, K. C. Howell, B. Barden, and R. Wilson. Genesis Mission Design. The Journal of the Astronautical Sciences, 49(1):169–184, 2001. DOI: https://doi.org/10.1007/BF03546342.

[68] A. Majumdar and R. Tedrake. Funnel Libraries for Real-Time Robust Feedback Motion Planning. The International Journal of Robotics Research, 36(8):947–982, 2017. DOI: https://doi.org/10.1177/0278364917712421.

[69] MathWorks. MATLAB®, 2021. [Online]. Available: https://www.mathworks.com/products/matlab.html.

[70] S. L. McCarty and D. J. Grebow. Missed Thrust Analysis and Design for Low Thrust Cislunar Transfers. In AAS/AIAA Astrodynamics Specialist Conference, Virtual, August 2020.

[71] M. L. McGuire, L. M. Burke, S. L. McCarty, K. J. Hack, R. J. Whitley, D. C. Davis, and C. Ocampo. Low Thrust Cis-Lunar Transfers Using a 40 kW-Class Solar Electric Propulsion Spacecraft. In AAS/AIAA Astrodynamics Specialist Conference, Stevenson, WA, August 2017.

[72] K. R. Meyer and D. C. Offin. Introduction to Hamiltonian Dynamical Systems and the N-Body Problem. Springer, Cham, CH, 3 edition, 2017.

[73] V. Muralidharan and K. C. Howell. Departure and Trajectory Design Applications using Stretching Directions. In AAS/AIAA Astrodynamics Specialist Conference, Virtual, August 2021.

[74] N. Nakhjiri and B. F. Villac. Automated Stable Region Generation, Detection, and Representation for Applications to Mission Design. Celestial Mechanics and Dynamical Astronomy, 123(1):63–83, 2015. DOI: https://doi.org/10.1007/s10569-015-9629-0.

[75] NASA. General Mission Analysis Tool (GMAT), 2018. [Online]. Available: https://software.nasa.gov/software/GSC-18094-1.

[76] NASA JPL - The Navigation and Ancillary Information Facility. SPICE Toolkit, 2022. [Online]. Available: https://naif.jpl.nasa.gov/naif/index.html.

[77] C. P. Newman, D. C. Davis, R. J. Whitley, J. R. Guinn, and M. S. Ryne. Stationkeeping, Orbit Determination, and Attitude Control for Spacecraft in Near Rectilinear Halo Orbits. In AAS/AIAA Astrodynamics Specialist Conference, Snowbird, UT, August 2018.

[78] M. Ozimek, D. J. Grebow, and K. C. Howell. A Collocation Approach for Computing Solar Sail Lunar Pole-Sitter Orbits. The Open Aerospace Engineering Journal, 3:65–75, 2010. DOI: https://doi.org/10.2174/1874146001003010065.

[79] A. A. Paranjape, K. C. Meier, X. Shi, S. J. Chung, and S. Hutchinson. Motion Primitives and 3D Path Planning for Fast Flight Through a Forest. The International Journal of Robotics Research, 34(3):357–377, 2015. DOI: https://doi.org/10.1177/0278364914558017.

[80] J. S. Parker and G. H. Born. Modeling a Low-Energy Ballistic Lunar Transfer Using Dynamical Systems Theory. Journal of Spacecraft and Rockets, 45(6):1269–1281, 2008. DOI: https://doi.org/10.2514/1.35262.

[81] J. S. Parker, K. E. Davis, and G. H. Born. Chaining Periodic Three-Body Orbits in the Earth-Moon System. Acta Astronautica, 67(5):623–638, 2010. DOI: https://doi.org/10.1016/j.actaastro.2010.04.003.

[82] N. L. Parrish. A* Pathfinding Continuous-Thrust Trajectory Optimization. In AAS 37th Annual Guidance & Control Conference, Breckenridge, CO, January 2014.

[83] N. L. Parrish and D. J. Scheeres. Low-Thrust Trajectory Optimization with No Initial Guess. In International Symposium on Space Flight Dynamics, Matsuyama, Japan, June 2017.

[84] F. Pedregosa, G. Varoquaux, A. Gramfort, V. Michel, B. Thirion, O. Grisel, M. Blondel, P. Prettenhofer, R. Weiss, V. Dubourg, J. Vanderplas, A. Passos, D. Cournapeau, M. Brucher, M. Perrot, and E. Duchesnay. Scikit-learn: Machine Learning in Python. Journal of Machine Learning Research, 12:2825–2830, 2011.

[85] L. Perko. Differential Equations and Dynamical Systems. Springer, New York, USA, 3 edition, 2001.

[86] G. Petit and B. Luzum. "IERS Conventions (2010)". International Earth Rotation and Reference Systems Service, Technical Note 36, 2010.

[87] R. E. Pritchett. Strategies for Low-Thrust Transfer Design based on Direct Collocation Techniques. PhD Dissertation, Purdue University, West Lafayette, IN, 2020.

[88] GNU Project. GNU Scientific Library, 2021. [Online]. Available: https://www.gnu.org/software/gsl/.

[89] J. E. Prussing and B. A. Conway. Orbital Mechanics. Oxford University Press, New York, USA, 2 edition, 2013.

[90] L. Reng, T. B. Moeslund, and E. Granum. Finding Motion Primitives in Human Body Gestures. In Gesture in Human-Computer Interaction and Simulation: 6th International Gesture Workshop, pages 133–144, Berder Island, France, 05 2005. DOI: https://doi.org/10.1007/11678816_16.

[91] I. M. Ross. Space Trajectory Optimization and L^1-Optimal Control Problems. Elsevier Astrodynamics Series, 1:155–188, 2006. DOI: https://doi.org/10.1016/S1874-9305(07)80008-2.

[92] R. D. Russell and J. Christiansen. Adaptive Mesh Selection Strategies for Solving Boundary Value Problems. SIAM Journal on Numerical Analysis, 15(1):59–80, 1978.

[93] H. Schaub and J. L. Junkins. Analytical Mechanics of Space Systems. American Institute of Aeronautics and Astronautics, Reston, VA, 4 edition, 2018.

[94] W. R. Schlei. Interactive Spacecraft Trajectory Design Strategies Featuring Poincaré Map Topology. PhD Dissertation, Purdue University, West Lafayette, IN, 2017.

[95] P. Sharer and T. Harrington. Trajectory Optimization for the ACE Halo Orbit Mission. In AIAA/AAS Astrodynamics Conference, San Diego, CA, July 1996. DOI: https://doi.org/10.2514/6.1996-3601.

[96] A. Shirazi, J. Ceberio, and J. A. Lozano. Spacecraft Trajectory Optimization: A Review of Models, Objectives, Approaches and Solutions. Progress in Aerospace Sciences, 102:76–98, 2018. DOI: https://doi.org/10.1016/j.paerosci.2018.07.007.

[97] M. Smith, D. Craig, N. Herrmann, E. Mahoney, J. Krezel, N. McIntyre, and K. Goodliff. The Artemis Program: An Overview of NASA's Activities to Return Humans to the Moon. In IEEE Aerospace Conference, Big Sky, MT, March 2020. DOI: https://doi.org/10.1109/AERO47225.2020.9172323.

[98] T. R. Smith and N. Bosanac. A Motion Primitive Approach to Trajectory Design in a Multi-Body System. In AAS/AIAA Astrodynamics Specialist Conference, Charlotte, NC, August 2022.

[99] T. R. Smith and N. Bosanac. Constructing Motion Primitive Sets to Summarize Periodic Orbit Families and Hyperbolic Invariant Manifolds in a Multi-Body System. Celestial Mechanics and Dynamical Astronomy, 134(7), 2022. DOI: https://doi.org/10.1007/s10569-022-10063-x.

[100] A. Strehl and J. Ghosh. Cluster Ensembles - A Knowledge Reuse Framework for Combining Multiple Partitions. Journal of Machine Learning Research, 3:583–617, 2002.

[101] V. Szebehely. Theory of Orbits: The Restricted Problem of Three Bodies. Academic Press, London, UK, 1967. DOI: https://doi.org/10.1016/B978-0-12-395732-0.X5001-6.

[102] F. Topputo, M. Vasile, and F. Bernelli-Zazzera. Low Energy Interplanetary Transfers Exploiting Invariant Manifolds of the Restricted Three-Body Problem. The Journal of the Astronautical Sciences, 53(4):353–372, 2005. DOI: https://doi.org/10.1007/BF03546358.

[103] F. Topputo and C. Zhang. Survey of Direct Transcription for Low-Thrust Space Trajectory Optimization with Applications. Abstract and Applied Analysis, 2014, 2014. DOI: https://doi.org/10.1155/2014/851720.

[104] E. Trumbauer and B. Villac. Heuristic Search-Based Framework for Onboard Trajectory Redesign. Journal of Guidance, Control, and Dynamics, 37(1):164–175, 2014. DOI: https://doi.org/10.2514/1.61236.

[105] G. A. Tsirogiannis. A Graph Based Methodology for Mission Design. Celestial Mechanics and Dynamical Astronomy, 114:353–363, 2012. DOI: https://doi.org/10.1007/s10569-012-9444-9.

[106] D. A. Vallado. Fundamentals of Astrodynamics and Applications. Microcosm Press, Hawthorne, CA, 4 edition, 2013.

[107] M. Van der Laan, K. Pollard, and J. Bryan. A New Partitioning Around Medoids Algorithm. Journal of Statistical Computation and Simulation, 73(8):575–584, 2003. DOI: https://doi.org/10.1080/0094965031000136012.

[108] M. Vaquero. Spacecraft Transfer Trajectory Design Exploiting Resonant Orbits in Multi-Body Environments. PhD Dissertation, Purdue University, West Lafayette, IN, 2013.

[109] M. Vaquero and J. Senent. Poincare: A Multi-Body, Multi-System Trajectory Design Tool. In 7th International Conference on Astrodynamics Tools and Techniques, Oberpfaffenhofen, Germany, November 2018.

[110] B. F. Villac, R. L. Anderson, and A. J. Pini. Computer Aided Ballistic Orbit Classification Around Small Bodies. The Journal of the Astronautical Sciences, 63(3):175–205, 2016. DOI: https://doi.org/10.1007/s40295-016-0089-x.

[111] A. Wächter and L. T. Biegler. On the Implementation of an Interior-Point Filter Line-Search Algorithm for Large-Scale Nonlinear Programming. Mathematical Programming, 106(1):25–57, 2006. DOI: https://doi.org/10.1007/s10107-004-0559-y.

[112] B. Wang, J. Gong, R. Zhang, and H. Chen. Learning to Segment and Represent Motion Primitives from Driving Data for Motion Planning Applications. In 21st International Conference on Intelligent Transportation Systems, pages 1408–1414, Maui, HI, 11 2018. DOI: https://doi.org/10.1109/ITSC.2018.8569913.

[113] R. J. Whitley, D. C. Davis, L. M. Burke, B. P. McCarthy, R. J. Power, M. L. McGuire, and K. C. Howell. Earth-Moon Near Rectilinear Halo and Butterfly Orbits for Lunar Surface Exploration. In AAS/AIAA Astrodynamics Specialist Conference, Snowbird, UT, August 2018.

[114] R. J. Whitley and R. Martinez. Options for Staging Orbits in Cis-Lunar Space. In 2016 IEEE Aerospace Conference, Big Sky, MT, March 2016.

[115] J. Williams, D. E. Lee, R. J. Whitley, K. A. Bokelmann, D. C. Davis, and C. F. Berry. Targeting Cislunar Near Rectilinear Halo Orbits for Human Space Exploration. In 27th AAS/AIAA Space Flight Mechanics Meeting, San Antonio, TX, February 2017.

[116] P. Williams. Hermite-Legendre-Gauss-Lobatto Direct Transcription in Trajectory Optimization. Journal of Guidance, Control, and Dynamics, 32(4):1392–1395, 2009. DOI: https://doi.org/10.2514/1.42731.

[117] A. Wolek and C. A. Woolsey. Model-Based Path Planning. In T. I. Fossen, K. Y. Pettersen, and H. Nijmeijer, editors, Sensing and Control for Autonomous Vehicles: Application to Land, Water and Air Vehicles, volume 474 of Lecture Notes in Control and Information Sciences, pages 183–206. Springer International Publishing, 2017. DOI: https://doi.org/10.1007/978-3-319-55372-6_9.

[118] C. G. Zagouras and P. G. Kazantzis. Three-Dimensional Periodic Oscillations Generating from Plane Periodic Ones around the Collinear Lagrangian Points. Astrophysics and Space Science, 61:389–409, 1979. DOI: https://doi.org/10.1007/BF00640540.

[119] S. Zhao. Time Derivative of Rotation Matrices: A Tutorial. Computing Research Repository, 2016. DOI: https://doi.org/10.48550/arXiv.1609.06088.

[120] Y. Zheng. Trajectory Data Mining: An Overview. ACM Transactions on Intelligent Systems and Technology, 6(3), 2015. DOI: https://doi.org/10.1145/2743025.

[121] E. M. Zimovan Spreen. Trajectory Design and Targeting for Applications to the Exploration Program in Cislunar Space. PhD Dissertation, Purdue University, West Lafayette, IN, 2021.

Appendix A

Motion Primitives Constructed along Hyperbolic Invariant Manifolds in the Earth-Moon CR3BP

In this work, motion primitives are constructed along hyperbolic invariant manifolds in the Earth-Moon CR3BP which are then leveraged in the primitive-based initial guess construction framework. This appendix presents the set of motion primitives constructed to summarize each half-manifold in the Earth-Moon CR3BP that is utilized in this work. Table A.1 lists the identifying properties for each half-manifold. Furthermore, Table A.2 lists the parameters used to generate a set of trajectories along each half-manifold and Table A.3 lists the parameters used to generate sets of motion primitives from these trajectories. Finally, Figures A.1-A.12 display the set of motion primitives generated to summarize each manifold structure. In each of these figures, the motion primitives are depicted in blue and the initial position of each primitive is denoted with a filled black circle; the associated sets of representative trajectories for the primitives are depicted in gray and the initial position of each representative trajectory is denoted with an empty black circle; the Earth and/or Moon is plotted to scale as a gray sphere; and the libration points are marked with red diamonds. Additional relevant plotting specifications are denoted in the caption for each figure. These figures provide a visual representation of the motion primitives utilized to construct the large variety of transfers presented in this work.

Table A.1: Hyperbolic invariant manifolds in the Earth-Moon CR3BP that are utilized in this work. Note: Direction is abbreviated as "Dir.".

Index	Source Orbit	Source Orbit Stability Index	C_J	Type	Initial x Dir.
1	L_1 Lyapunov	$s_1 = 2206.969701740854$	3.167002726384443	Unstable	+
2	L_1 Lyapunov	$s_1 = 2206.969701740854$	3.167002726384443	Stable	+
3	L_2 Lyapunov	$s_1 = 1383.837551141560$	3.166629662653735	Unstable	-
4	L_2 Lyapunov	$s_1 = 1383.837551141560$	3.166629662653735	Stable	-
5	L_1 northern halo	$s_1 = 218.4295991405137$	3.063534530378191	Unstable	+
6	L_1 northern halo	$s_1 = 218.4295991405137$	3.063534530378191	Stable	+
7	L_1 northern halo	$s_1 = 889.3831605316448$	3.122412735785743	Stable	+
8	L_2 northern halo	$s_2 = 180.2782082683678$	3.066884796159840	Unstable	-
9	L_2 northern halo	$s_2 = 180.2782082683678$	3.066884796159840	Stable	-
10	L_2 southern halo	$s_1 = -2.751814321511511$	3.044579150514986	Unstable	+
11	L_2 southern halo	$s_2 = 12.678124806969251$	3.018783209603037	Unstable	+
12	L_2 southern halo	$s_2 = 734.8166117276289$	3.124978276981083	Stable	-

Table A.2: Parameters used to generate trajectories along the hyperbolic invariant manifolds in the Earth-Moon CR3BP that are utilized in this work. Note: The manifold index is obtained from Table A.1, the nondimensional radius of a spherical approximation of the Moon is 0.004519771071800, and the nondimensional radius of a spherical approximation of the Earth is 0.016592446930281.

Index	Orbit Node Spacing Type	Number of Trajectories	Step Size ($\tilde{d}$)	Termination Criteria
1, 2	Equal time	500	40 km	15 apses wrt Moon, Lunar impact, $x = 0.820176824506134$, $x = 1.155682164448510$
3, 4	Equal time	500	40 km	15 apses wrt Moon, Lunar impact, $x = 0.836915127047076$, $x = 1.178795807737480$
5, 6, 8, 9	Equal time	500	40 km	15 apses wrt Moon, Lunar impact, $x = 0.80$, $x = 1.17$, $y = -0.30$, $y = 0.30$
7	Equal arclength	500	40 km	Max. propagation time = 14.73, Lunar Impact, $x = 0.80$, $x = 1.20$, $y = -0.30$, $y = 0.30$
10	Equal arclength	1000	40 km	60 apses wrt Moon, Lunar impact, $x = 0.80$, $x = 1.75$, $y = -0.50$
11	Equal arclength	500	40 km	10 apses wrt Earth, Earth or Lunar Impact, $x = 1.75$, $y = 0.20$
12	Equal arclength	500	40 km	20 apses wrt Moon, Lunar impact, $x = 0.80$, $x = 1.20$, $y = -0.30$, $y = 0.30$

Table A.3: Parameters used to generate motion primitives along the hyperbolic invariant manifolds in the Earth-Moon CR3BP that are utilized in this work. Note: The last two columns provide the number of shorter arcs generated along each half-manifold based on the parameter selections and the resulting number of primitives constructed to summarize each half-manifold.

Index	n_{window}	n_{shift}	refPt	cenPt	k	$d_{\min}$	l_{csize}	l_{sim}	k_{nn}	# of Arcs	# of Prims
1	4	1	Moon (P_2)		[10,75]	0.4	5	0.90	2	1196	69
2	4	1	Moon (P_2)		[10,75]	0.4	5	0.90	2	1196	68
3	4	1	Moon (P_2)		[20,100]	0.4	5	0.90	3	1865	88
4	4	1	Moon (P_2)		[10,100]	0.4	5	0.90	3	1865	89
5	4	1	Moon (P_2)		[80,175]	0.4	5	0.99	2	2102	198
6	4	1	Moon (P_2)		[70,175]	0.4	5	0.99	2	2102	194
7	4	2	Moon (P_2)		[30,100]	0.4	10	0.90	2	1371	118
8	4	1	Moon (P_2)		[75,175]	0.4	5	0.99	2	2028	226
9	4	1	Moon (P_2)		[70,175]	0.4	5	0.99	2	2028	223
10	6	4	Moon (P_2)		[10,75]	0.4	25	0.75	10	8178	55
11	4	2	Earth (P_1)		[5,20]	0.4	5	0.75	5	1459	11
12	4	2	Moon (P_2)		[10,50]	0.4	5	0.90	2	813	41

A.1 L_1 Lyapunov Orbit Unstable Half-Manifold Primitives at $C_J \approx 3.1670$

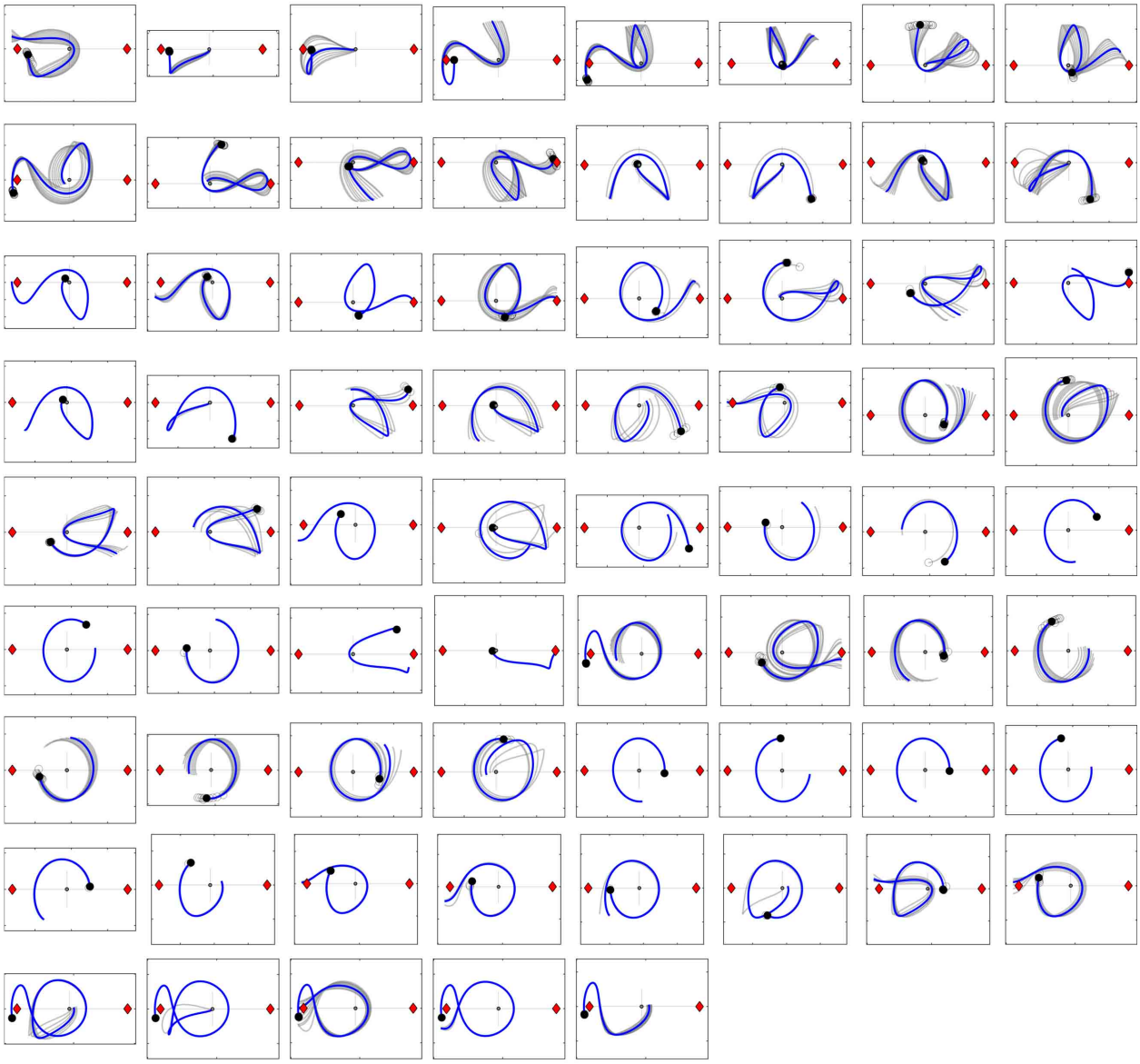

Figure A.1: Motion primitives and the associated sets of representative trajectories computed from an L_1 Lyapunov orbit unstable half-manifold in the Earth-Moon CR3BP at $C_J \approx 3.1670$; trajectories are displayed in the xy-plane of $\mathcal{R}$ and L_1 (L_2) is marked with a red diamond on the left (right) in each subfigure.

A.2 L_1 Lyapunov Orbit Stable Half-Manifold Primitives at $C_J \approx 3.1670$

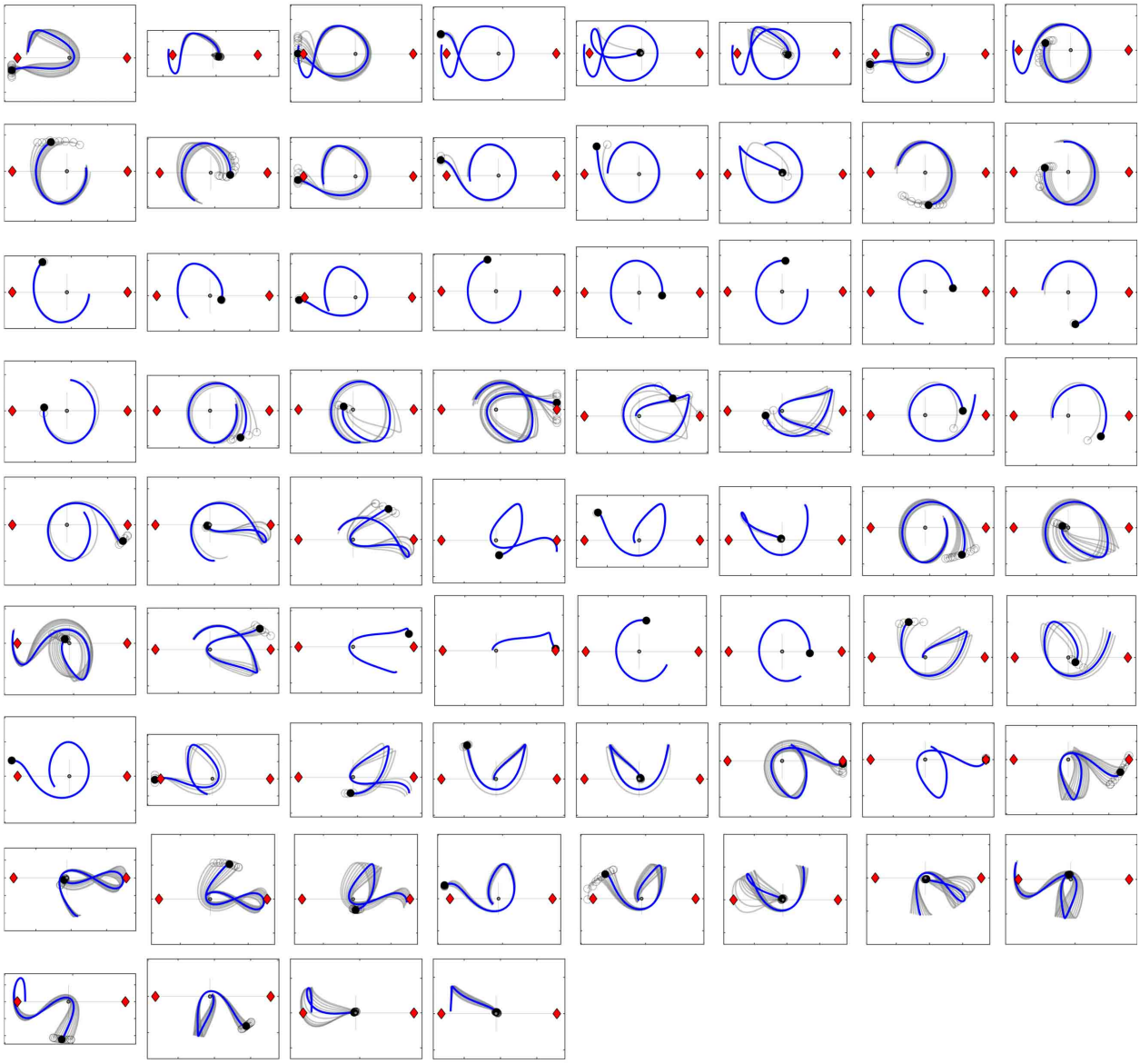

Figure A.2: Motion primitives and the associated sets of representative trajectories computed from an L_1 Lyapunov orbit stable half-manifold in the Earth-Moon CR3BP at $C_J \approx 3.1670$; trajectories are displayed in the xy-plane of $\mathcal{R}$ and L_1 (L_2) is marked with a red diamond on the left (right) in each subfigure.

A.3 L_2 Lyapunov Orbit Unstable Half-Manifold Primitives at $C_J \approx 3.1666$

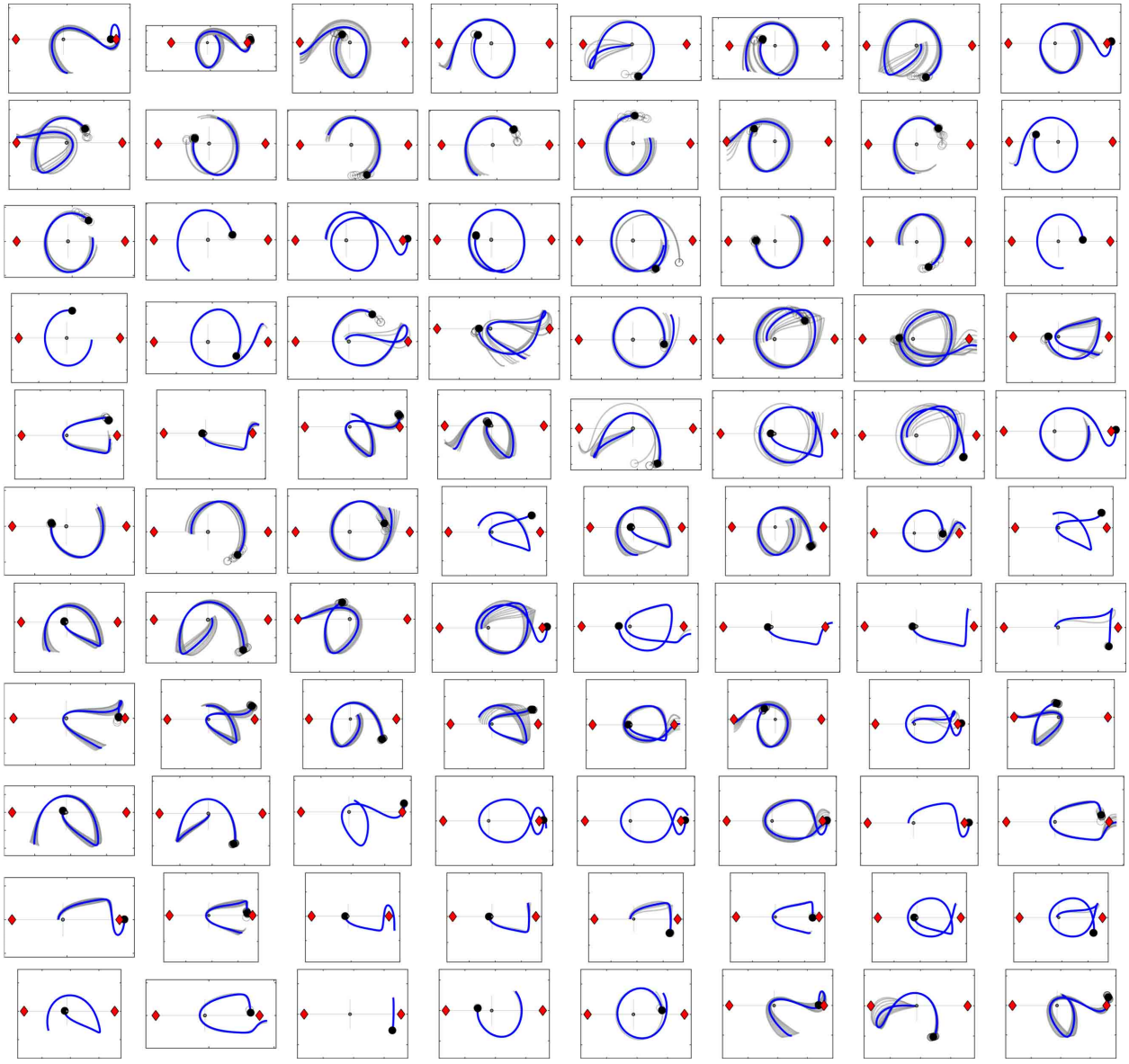

Figure A.3: Motion primitives and the associated sets of representative trajectories computed from an L_2 Lyapunov orbit unstable half-manifold in the Earth-Moon CR3BP at $C_J \approx 3.1666$; trajectories are displayed in the xy-plane of $\mathcal{R}$ and L_1 (L_2) is marked with a red diamond on the left (right) in each subfigure.

A.4 L_2 Lyapunov Orbit Stable Half-Manifold Primitives at $C_J \approx 3.1666$

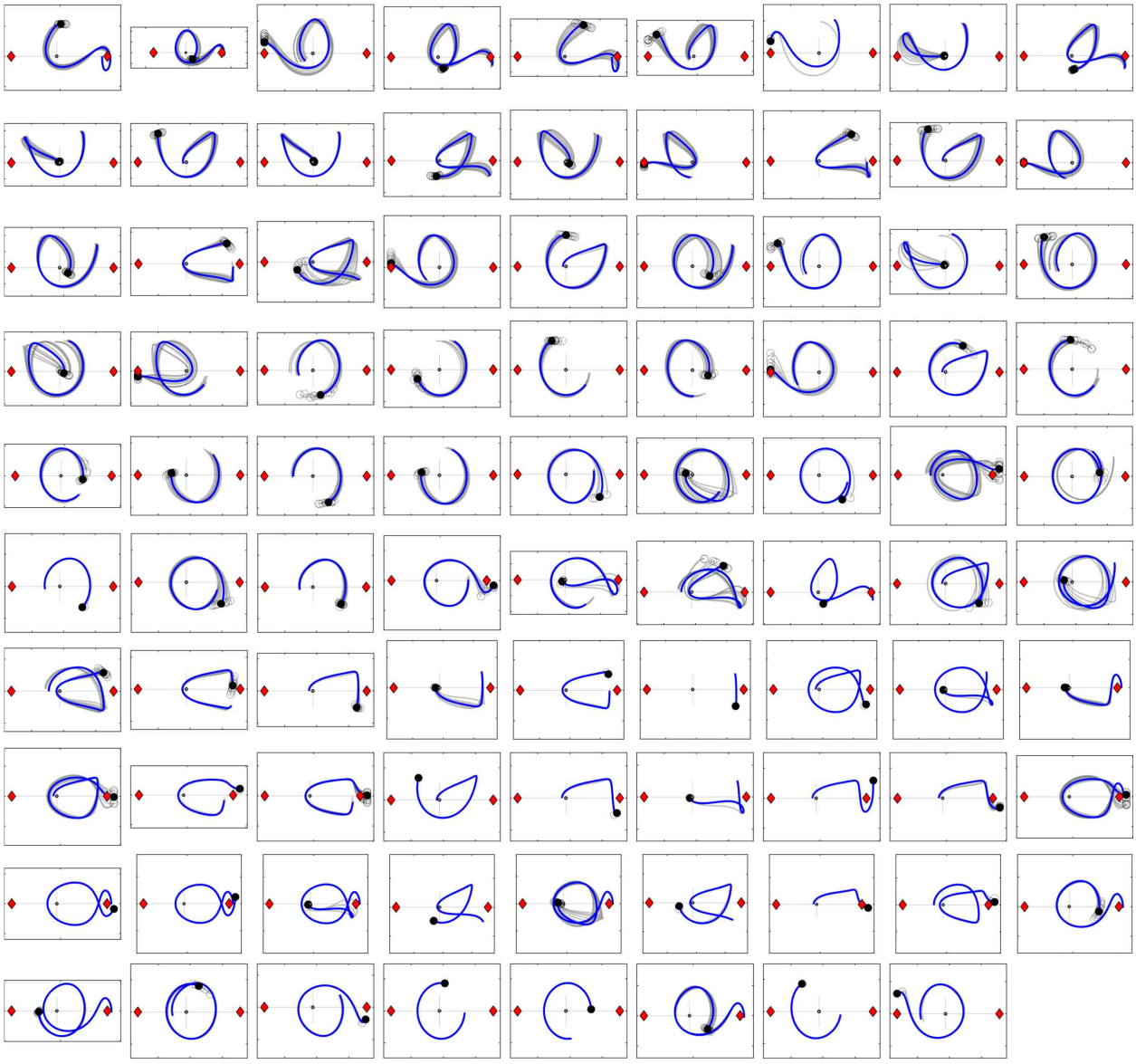

Figure A.4: Motion primitives and the associated sets of representative trajectories computed from an L_2 Lyapunov orbit stable half-manifold in the Earth-Moon CR3BP at $C_J \approx 3.1666$; trajectories are displayed in the xy-plane of $\mathcal{R}$ and L_1 (L_2) is marked with a red diamond on the left (right) in each subfigure.

A.5 L_1 Northern Halo Orbit Unstable Half-Manifold Primitives at $C_J \approx 3.0635$

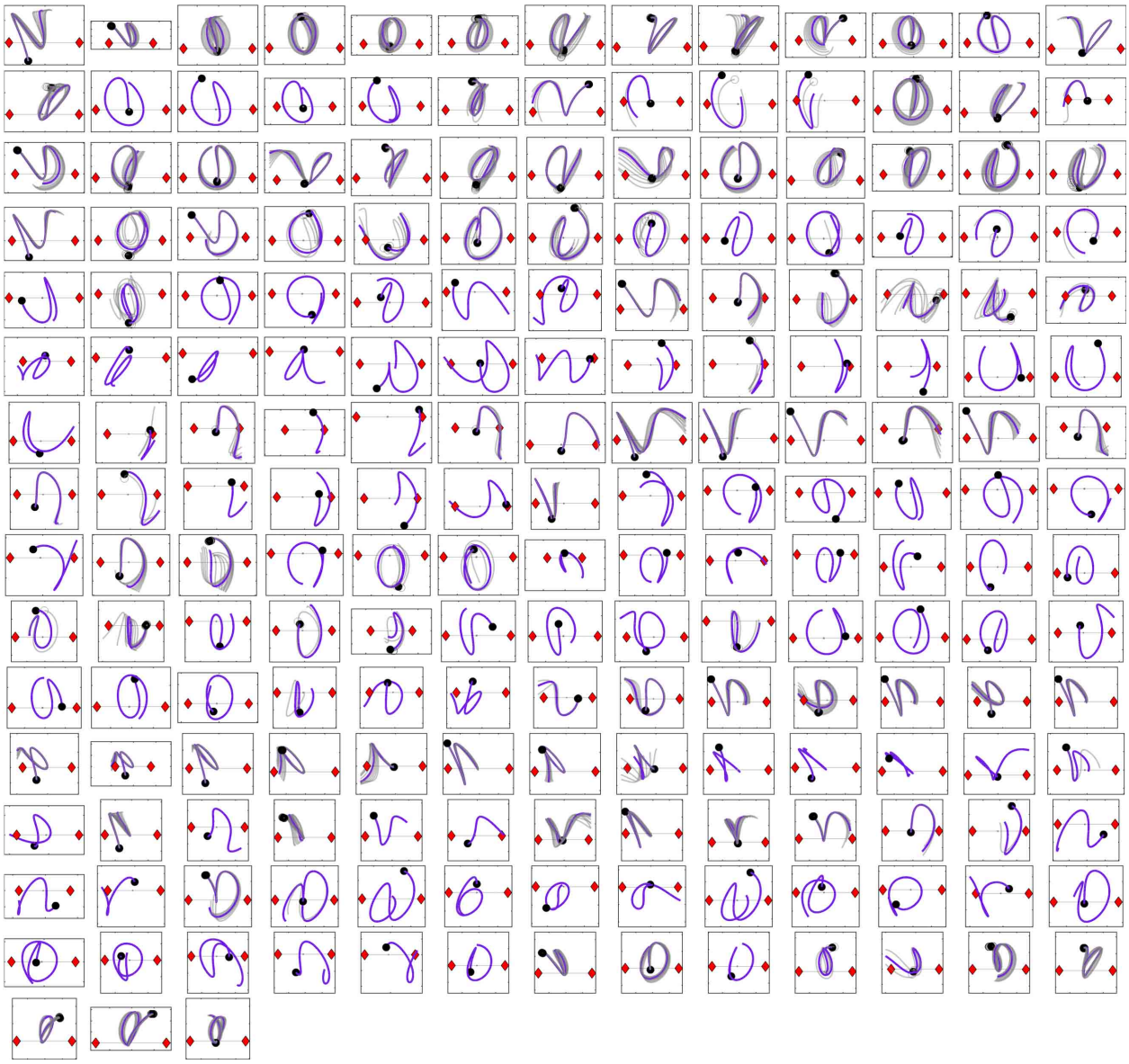

Figure A.5: Motion primitives and the associated sets of representative trajectories computed from an L_1 northern halo orbit unstable half-manifold in the Earth-Moon CR3BP at $C_J \approx 3.0635$; trajectories are displayed as a projection onto the xz-plane of $\mathcal{R}$ and L_1 (L_2) is marked with a red diamond on the left (right) in each subfigure.

A.6 L_1 Northern Halo Orbit Stable Half-Manifold Primitives at $C_J \approx 3.0635$

Figure A.6: Motion primitives and the associated sets of representative trajectories computed from an L_1 northern halo orbit stable half-manifold in the Earth-Moon CR3BP at $C_J \approx 3.0635$; trajectories are displayed as a projection onto the xz-plane of $\mathcal{R}$ and L_1 (L_2) is marked with a red diamond on the left (right) in each subfigure.

A.7 L_1 Northern Halo Orbit Stable Half-Manifold Primitives at $C_J \approx 3.1224$

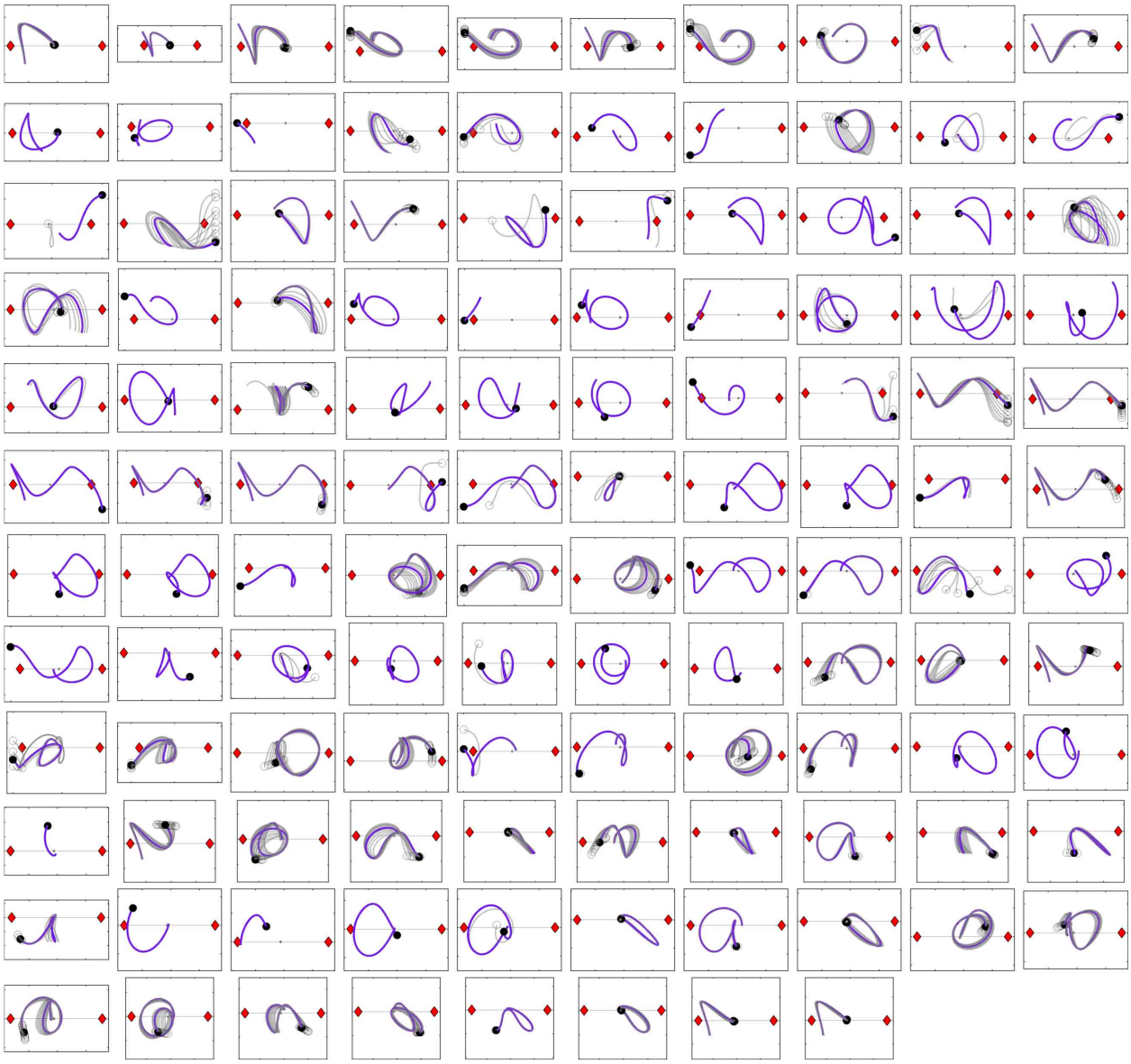

Figure A.7: Motion primitives and the associated sets of representative trajectories computed from an L_1 northern halo orbit stable half-manifold in the Earth-Moon CR3BP at $C_J \approx 3.1224$; trajectories are displayed as a projection onto the xz-plane of $\mathcal{R}$ and L_1 (L_2) is marked with a red diamond on the left (right) in each subfigure.

A.8 L_2 Northern Halo Orbit Unstable Half-Manifold Primitives at $C_J \approx 3.0669$

Figure A.8: Motion primitives and the associated sets of representative trajectories computed from an L_2 northern halo orbit unstable half-manifold in the Earth-Moon CR3BP at $C_J \approx 3.0669$; trajectories are displayed as a projection onto the xz-plane of $\mathcal{R}$ and L_1 (L_2) is marked with a red diamond on the left (right) in each subfigure.

A.9 L_2 Northern Halo Orbit Stable Half-Manifold Primitives at $C_J \approx 3.0669$

Figure A.9: Motion primitives and the associated sets of representative trajectories computed from an L_2 northern halo orbit stable half-manifold in the Earth-Moon CR3BP at $C_J \approx 3.0669$; trajectories are displayed as a projection onto the xz-plane of $\mathcal{R}$ and L_1 (L_2) is marked with a red diamond on the left (right) in each subfigure.

A.10 L_2 Southern Halo Orbit Unstable Half-Manifold Primitives at $C_J \approx 3.0446$

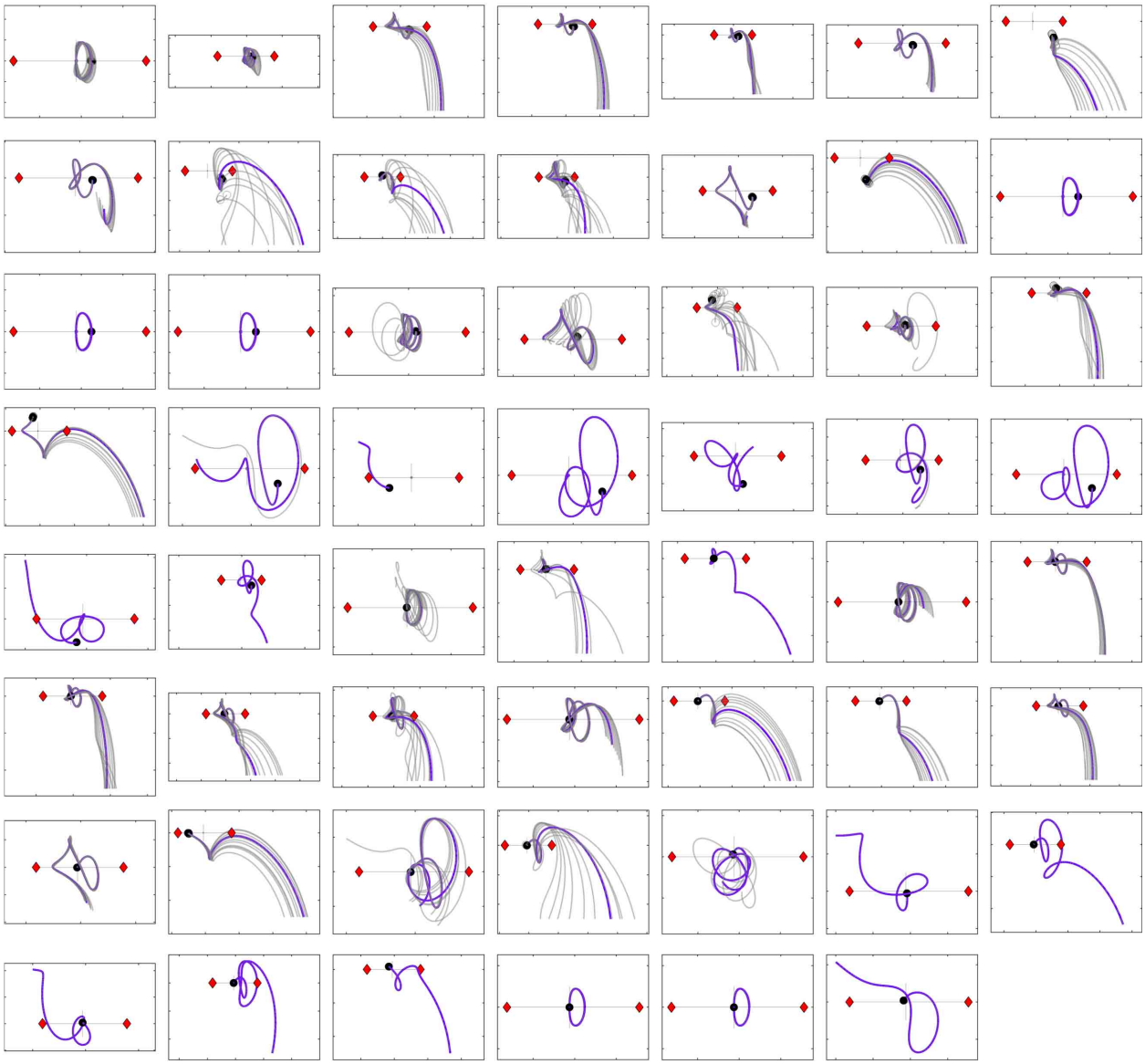

Figure A.10: Motion primitives and the associated sets of representative trajectories computed from an L_2 southern halo orbit unstable half-manifold in the Earth-Moon CR3BP at $C_J \approx 3.0446$; trajectories are displayed as a projection onto the xy-plane of $\mathcal{R}$ and L_1 (L_2) is marked with a red diamond on the left (right) in each subfigure.

A.11 L_2 Southern Halo Orbit Unstable Half-Manifold Primitives at $C_J \approx 3.0188$

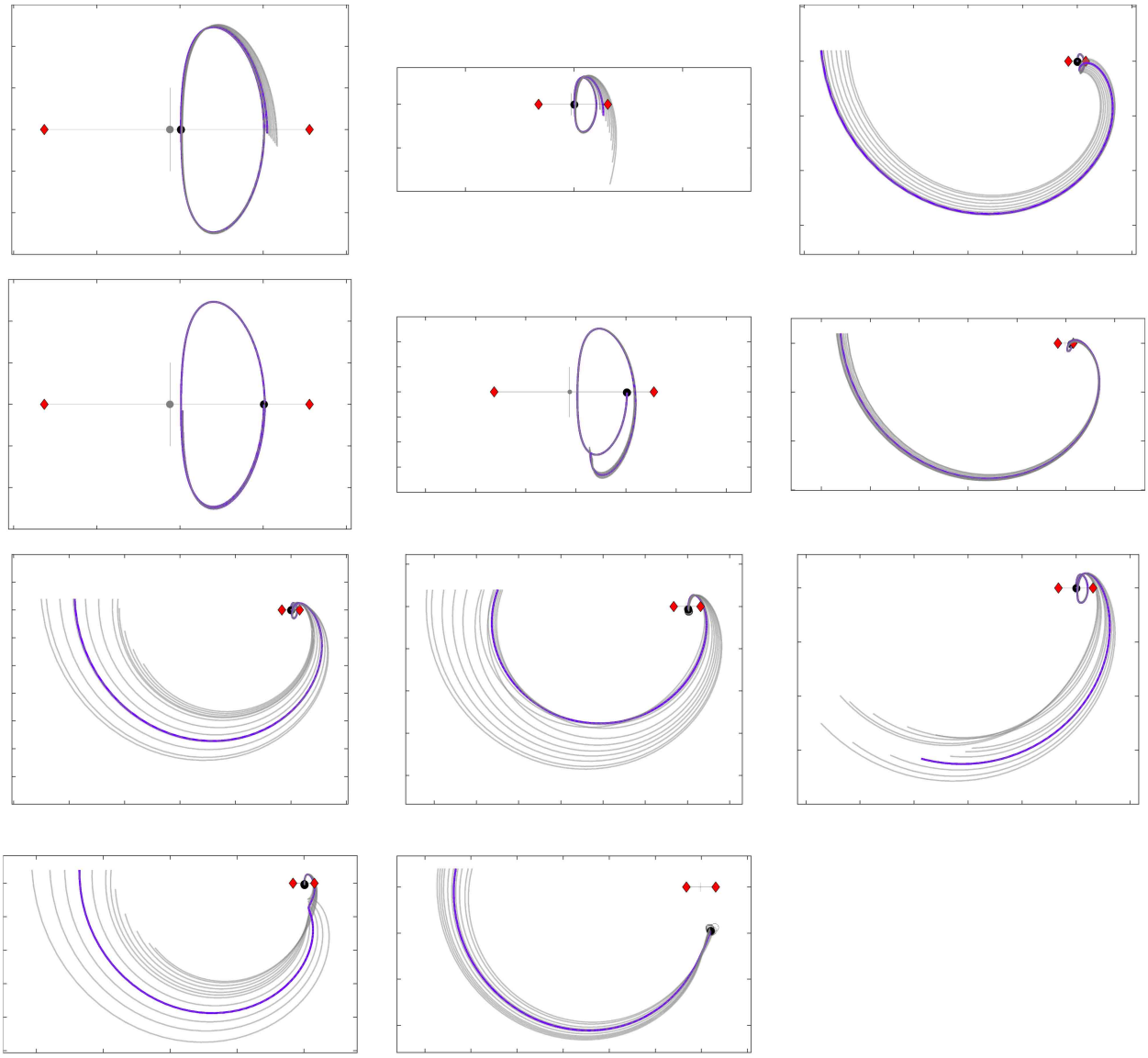

Figure A.11: Motion primitives and the associated sets of representative trajectories computed from an L_2 southern halo orbit unstable half-manifold in the Earth-Moon CR3BP at $C_J \approx 3.0188$; trajectories are displayed as a projection onto the xy-plane of $\mathcal{R}$ and L_1 (L_2) is marked with a red diamond on the left (right) in each subfigure.

A.12 L_2 Southern Halo Orbit Stable Half-Manifold Primitives at $C_J \approx 3.1250$

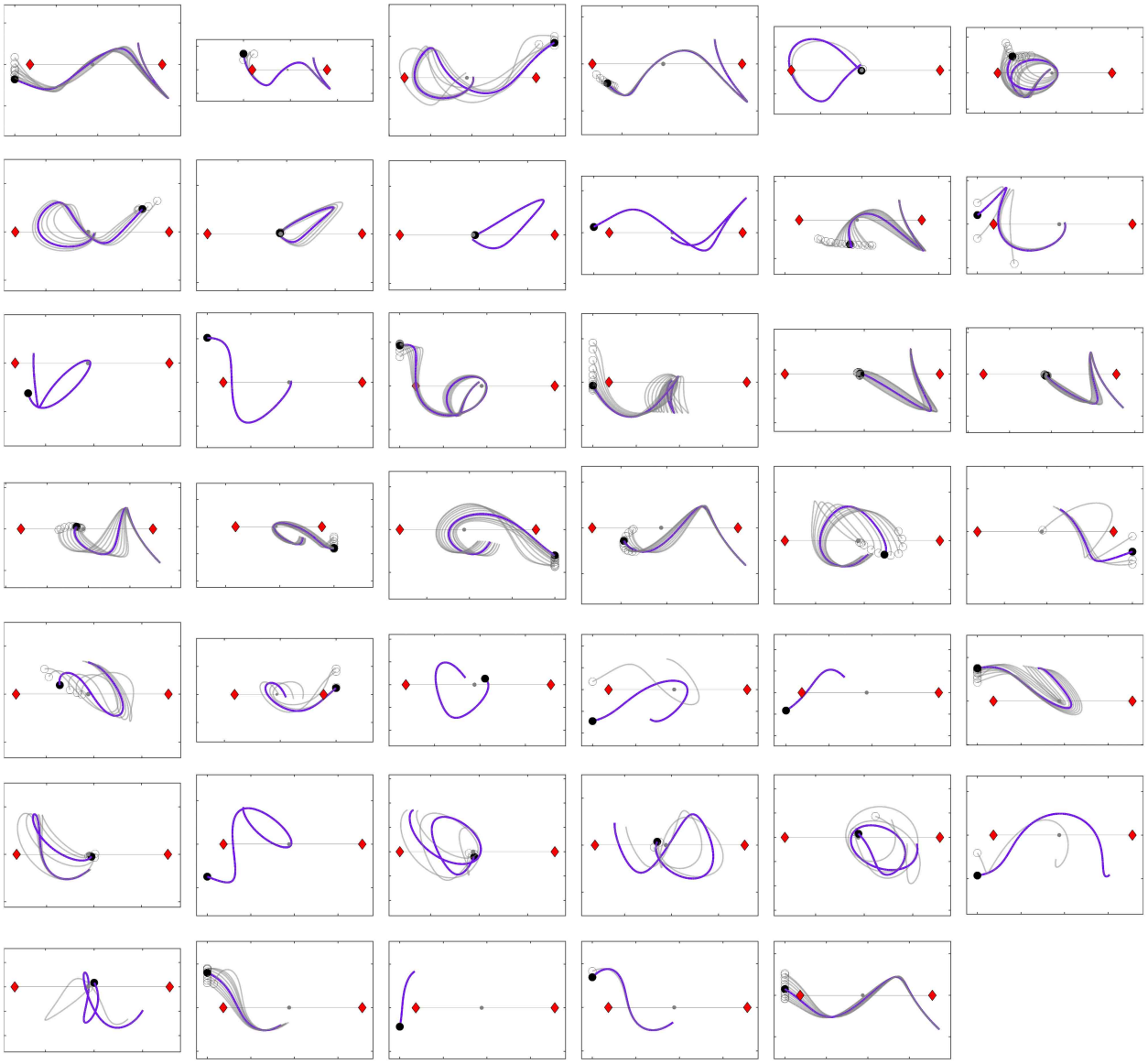

Figure A.12: Motion primitives and the associated sets of representative trajectories computed from an L_2 southern halo orbit stable half-manifold in the Earth-Moon CR3BP at $C_J \approx 3.1250$; trajectories are displayed as a projection onto the xz-plane of $\mathcal{R}$ and L_1 (L_2) is marked with a red diamond on the left (right) in each subfigure.